UiT The Arctic University of Norway

Faculty of Engineering Science and Technology

Institute of Industrial Technology

Study of Atmospheric Ice Accretion on Wind Turbine Blades

Jia Yi Jin

A dissertation for the degree of Philosophiae Doctor in Engineering Science − March 2021

Jia Yi Jin

Study of Atmospheric Ice Accretion on Wind Turbine Blades

Thesis for the degree of Philosophiae Doctor

Narvik, March 2021

UiT − The Arctic University of Norway
Faculty of Engineering Science and Technology
Institute of Industrial Technology (IIT)

Acknowledgment

This thesis is submitted in partial fulfilment of the requirements for the degree of Philosophiae Doctor (Ph.D.) at the UiT – The Arctic University of Norway. The research work is a result of my doctoral studies from April 2018 to March 2021, which has been conducted at the Arctic Technology & Icing Research Group. The research has been done under supervision of Professor Dr. Muhammad Shakeel Virk and co-supervision of Dr. Yngve Birkelund.

During the Ph.D. study, I received good professional and personal support from my supervision team, my family and friends, colleagues. I would like to take this opportunity to thank all of them, without whom I could never reach my goal of completion of this Ph.D. project with such fruitful outcomes.

First and foremost, I want to express my heartfelt gratitude to my principle supervisor Professor Muhammad Shakeel Virk, who is a humble, moderate, low profile and very knowledgeable person. It has been my pleasure to work with him. Professor Virk has shown me the right attitude towards research work and has inspired and encouraged me in a lot of aspects on both professional development and personal life. I am very grateful for his supervision and good guidance. Professor Virk has provided me with many opportunities to work with him in several R&D projects at both national and international levels, which have significantly improved my knowledge, cogitation and perspective.

Furthermore, I would like to express my heartfelt thanks to my co-supervisor Dr. Yngve Birkelund, as his passion for energetic research has a great influence on me. Thanks to him, and his passion for research, I started to recognize my own willingness for doing research, and gradually grew fond of academic research. I am very grateful to him for his constant encouragement and helpful comments, which helped me significantly. Dr. Yngve has provided me with valuable comments for improving my working activities during my Ph.D. studies, and broadened my horizon on wind resource assessment in Arctic regions.

In addition, I would also like to thank Mr. Pavlo Sokolov from UiT and Dr. David Hammond, Dr. Hugo Pervier and Mr. Peter West from Cranfield University, UK for assisting during the icing tunnel experiments. Furthermore, I would also like to extend my gratitude to Professor Xingliang Jiang and Professor Qin Hu from Chongqing University of China, and Mr. Timo Karlsson in VTT, Finland for their support and research collaboration, which inspired me to broaden my research perspective.

Last but not least, special thanks are reserved to my dear parents and friends who gave me their strong spiritual support throughout the years. Without their silent pray underway, it would have been difficult to maintain the progress. In particular, I would like to mention my good friend Dr. Xu Zhang from Brown University, USA, and Mr. Pavlo Sokolov from UiT, Norway, who gave me very useful suggestions and tremendous support during my Ph.D. study. The largest thanks are reserved for my parents, especially my mother, who is the most important and precious person in my life, who brings me unconditional love and encouragement throughout my life.

Jia Yi Jin
Narvik, March 2021

Abstract

This Ph.D. work concerns itself with the atmospheric ice accretion on wind turbine blades. The wind energy has been at the forefront of the renewable energy generation for the last several decades, with the amount and capacity of installed wind turbines steadily increasing. The cold climate (CC) regions around the world like Finland, Germany, Slovak Republic, Norway, Czech Republic, UK, Sweden, Bulgaria, Hungary, Russia, Canada and USA have great potential of wind resources. Estimated wind energy capacity in CC is about 60 GW. [1] However, due to this steady increase in the installed power capacity, more and more turbines have to be placed in regions with harsh geographical conditions, such as arctic regions, in which the temperatures below the normal operating conditions can result in the atmospheric icing to accumulate on the wind turbines particularly along blades. The icing on wind turbines blades leads to negative effects, such as, decreased lift and increased drag, increased mechanical wear and fatigue, possibility of ice throw, which negatively impacts the personnel and life in the area, aeroacoustics noise, generated from iced wind turbines, etc. The icing on wind turbines occurs when super-cooled water droplets collide with the wind turbine structure in the passing clouds (in-cloud icing) and/or freezing rain or drizzle freezes on the exposed wind turbine structure (precipitation icing). Within the scope of this Ph.D. work, the focus is made on the in-cloud icing on the wind turbines.

While there are existing standards and guidelines for the design and operation of wind turbines in normal, temperate climates, for example, the International Electrotechnical Commission standards for offshore turbines, including IEC 61400-1, IEC 61400-3, and the standards for the processes of type certification, which are commonly used to certify turbines in Europe (IEC 2001, 2005, 2010a, 2010b). However, no such definite framework exists for the design, operation and maintenance of wind turbines in cold, ice-prone regions. Thus, the better understanding of the atmospheric ice accretions on wind turbines and their negative effects, such as losses in power production due to the icing is a critical objective for the successful operation of the wind power in CC, ice-prone regions.

For the purposes of better understanding of the icing physics, involved in the icing on the wind turbines, the analytical, numerical and the experimental tools are used in this project. The analytical modelling is done by using the ISO 12494 standard: "*Atmospheric Icing on Structures"* with some modifications done to it, in order to permit analytical modelling of ice accretion on wind turbines, using basic circular cylinders from ISO 12494 as a reference collector. The numerical modelling scheme employs the usage of modern Computational Fluid Dynamics (CFD) tools such an ANSYS FENSAP-ICE and ANSYS-Fluent which are used to study the ice accretion process on airfoils and blades. These CFD tools allow for the study of icing physics in greater detail than the analytical model allows, for example by simulating the resultant ice shapes and their impact on the aerodynamic performance of the iced airfoils, when compared to the clean ones. The experimental methodology of this work encompasses usage of the icing tunnel experimental data, for the validation purposes of the numerical modelling, and the field measurements data from the Supervisory Control and Data Acquisition (SCADA) system, taken from a wind park operating in the CC region. The main reason for this is to perform a wind resource assessment study in the CC, ice prone region, in addition to the use of supplementary statistical and numerical modelling tools, such as T19IceLossMethod and WindSim.

The results of atmospheric ice accretion on the wind turbine blades show that the aerodynamic performance changes mainly due to difference in droplet freezing fraction as due to low freezing fraction for the glaze ice conditions, higher amount of the water runback and the aerodynamic heat flux along

leading edge is observed which results in the complex horn type ice shapes. The phenomenon of the flow interaction in the third dimension results in the velocity magnitudes being reduced in the 3D simulations, when compared to the 2D simulations. This, in turn, affects the ice accretion process, as the higher velocity magnitudes in the 2D cases result in the higher droplet inertia, collision efficiencies and the maximum impingement angles, which results in more ice mass accreted along the leading edge with the thicker and larger ice shapes present in the 2D simulations.

The results of wind resource assessment of ice prone region show that power production for wind parks can be lower in CC regions when compared to identical wind parks/turbines situated in warmer temperate climates. However, the icing-related issues and the associated power losses need to be solved. It shows that duration and timing of the icing event is different for different wind turbines in a wind park, which clearly indicates that the icing events depend upon the meteorological conditions, airflow behaviour and also the location of the wind turbine. Even in the same wind park, it is not given that ice will accrete on all wind turbines under the same instrumental and on-site conditions. The wind park layout and changes in flow behaviour affects the occurrence of ice accretion, despite the favourable conditions for icing events being present.

Two main topics have been considered in this Ph.D. work: the atmospheric ice accretion on wind turbine blade and the performance losses associated with it; and the wind resource assessment in the ice prone region. Both of these topics are of major importance for the wind industry in CC, ice prone regions, due to the challenges present in the form of potential icing conditions and events and the resultant energy production losses. The results obtained in this Ph.D. thesis can be summarized, in short, as follows: power losses due to icing on wind turbines occur not because of a single reason, but through a combination of effects that need to be taken into account carefully during the wind park design process. These effects include the blade profile surface roughness and heat fluxes, which change significantly during the ice accretion process, and, in turn, affect the airflow and droplet behaviour. The change in the accreted ice shape affects both the airflow behaviour and the aerodynamics performance. With the increase in the atmospheric temperature, the type of accreted ice also changes from dry rime to wet glaze ice, which leads to a change in the ice density and also the accreted ice shapes on the wind turbine blades. Generally, wet ice growth is more damaging for wind turbine operations in icing conditions as compared to dry rime ice growth, due to higher degradation of aerodynamic characteristics under the glaze icing conditions.

The results obtained in this work also provide the need and motivation for improving the understanding about icing effects on the wind turbine blades and the improvement of the existing (or creating new) anti-/de-icing technologies.

List of Included Scientific Papers

Number	Authors	Publications
Paper A	Sokolov, Pavlo; Jin, Jia Yi; Virk, Muhammad Shakeel.	″Accreted ice mass ratio (k-factor) for rotating wind turbine blade profile and circular cylinder″, *Wind Energy*, 2018, Volume 22, p.447 – 457.
Paper B	Jin, Jia Yi; Virk, Muhammad Shakeel.	″Study of ice accretion along symmetric and asymmetric airfoils″, *Journal of Wind Engineering and Industrial Aerodynamics*, 2018, Volume 179, p. 240 – 249.
Paper C	Jin, Jia Yi; Virk, Muhammad Shakeel.	″Experimental study of ice accretion on S826 & S832 wind turbine blade profiles″. *Cold Regions Science and Technology*, 2019, Volume 169.
Paper D	Jin, Jia Yi; Virk, Muhammad Shakeel.	″Study of ice accretion and icing effects on aerodynamic characteristics of DU96 wind turbine blade profile″, *Cold Regions Science and Technology*, 2019, Volume 160. p. 119 – 127.
Paper E	Jin, Jia Yi; Virk, Muhammad Shakeel; Hu, Qin; Jiang, Xingliang.	″Study of Ice Accretion on Horizontal Axis Wind Turbine Blade using 2D and 3D Numerical Approach″. *IEEE Access*, 2020, Volume 8, p. 166236 – 166245.
Paper F	Jin, Jia Yi; Karlsson, Timo; Virk, Muhammad Shakeel.	″Wind Turbine Ice Detection Using AEP Loss Method – A Case Study″. Submitted – Under review, 2021.

BACK TO THE FUTURE:

NO MATTER HOW YOU FEEL — GET UP, DRESS UP, SHOW UP, AND NEVER GIVE UP.

Dannielle Olent

Table of Contents

List of Figures

List of Tables

Nomenclature:

This lists the most commonly used symbols, abbreviations and definitions in this thesis, but is not exhaustive and omits some symbols which are unique to specific chapters.

List of Symbols

$\boldsymbol{A}$	The cross-sectional area of the object with respect to the direction of the particle velocity vector, (m^2).
$\boldsymbol{C}$	The characteristic length, (m).
$\boldsymbol{c}$	The chord length, (m).
$\boldsymbol{C_D}$	The drag coefficient.
$\boldsymbol{C_L}$	The lift coefficient.
$\boldsymbol{C_P}$	The power coefficient.
$\boldsymbol{D}$	The drag force.
$\boldsymbol{d}$	The droplet diameter, (m).
$\boldsymbol{E}$	The total initial energy, (kJ).
$\boldsymbol{Fr}$	The Froude number.
$\boldsymbol{g}$	The gravitational acceleration is approximately 9.81 m/s^2.
$\boldsymbol{H}$	The total initial enthalpy.
$\boldsymbol{K}$	The dimensionless droplet's inertia parameter.
$\boldsymbol{k}$	The turbulent kinetic energy, (kJ).
$\boldsymbol{K_i}$	The droplet inertia parameter of the i^{th} bin.
$\boldsymbol{L}$	The lift force.
$\boldsymbol{M}$	Ice mass, (kg).
m.a.s.l.	Meters Above the Sea Level.
m.a.g.l.	Meters Above the Ground Level.
$\boldsymbol{m_{eva}}$	The mass of evaporating water droplets.
$\boldsymbol{m_{ice}}$	The mass of the ice on the turbine blade.
$\boldsymbol{m_{im}}$	The mass of the supercooled water droplets impinging on the turbine blade.
$\boldsymbol{m_{in}}$	The mass of previous water droplets coming into each grid cells.

m_{out} The mass of water droplets flowing out to the next grid cell.

$\vec{n}$ The surface normal vector.

Q_{adh} The viscous adiabatic heating from the friction indie the boundary layer.

Q_c The convective heat.

Q_{cd} The heat loss of conduction to the interface.

Q_{cv} The heat loss of convective produced by airflow over the surface.

Q_{eva} The heat fluxes of evaporating water droplets.

Q_f The heat of liquid (supercooled water droplets) freezing.

Q_f The friction heat.

Q_{im} The heat fluxes of the supercooled water droplets impinging on the turbine blade.

Q_{in} The heat fluxes of previous water droplets coming into each grid cells.

Q_{kin} The kinetic heating from supercooled water droplets.

Q_{out} The heat fluxes of water droplets flowing out to the next grid cell.

Q_{rad} The heat loss of radiative from the surface.

Q_{ss} The total sensible heat of the liquid water mass to the freezing temperature.

$Q_{sub/evap}$ The heat of liquid sublimation or evaporation.

R The rotor radius for cylinder or the leading-edge radius for airfoil, (m).

T The air static temperature in Kelvin.

T_s The surface temperature in Kelvin.

$\tilde{T}_{wall}$ The wall temperature in Celsius.

u The wind velocity, (m/s).

u^* The friction velocity, (m/s).

V The free stream wind speed, (m/s).

v The relative velocity of the particles, (m/s).

$\overrightarrow{v_a}$ The relative air velocity of the particles, (m/s).

$\overrightarrow{v_d}$ The relative water velocity of the particles, (m/s).

w_i The LWC fraction of the i^{th} bin.

z The coordinate in vertical direction, (m).

$\mathbf{z_0}$	The roughness height, (m).
$\boldsymbol{\alpha}$	Angle of Attack (**AOA**) in degree.
$\boldsymbol{\alpha}$	The water volume fraction, (kg/m^3).
$\boldsymbol{\alpha_1}$	The collision efficiency, is a ratio that describes how many of the water, ice or snow particles impact the structure.
$\boldsymbol{\alpha_{1i}}$	The overall collision efficiency of the i^{th} bin.
$\boldsymbol{\alpha_2}$	The sticking efficiency, is the amount of particles that stick to the object rather than bouncing off.
$\boldsymbol{\alpha_3}$	The accretion efficiency, is based on how much water can be frozen given the thermodynamic conditions of the atmosphere.
$\boldsymbol{\beta}$	The local and overall collision efficiencies.
$\boldsymbol{\kappa}$	The von Kármán constant, $\kappa = 0.435$.
$\boldsymbol{\lambda}$	Tip Speed Ratio (**TSR**).
$\boldsymbol{\mu}$	The dynamic viscosity, (μPa·s).
$\boldsymbol{\nu}$	The kinematic viscosity, (m^2/s).
$\boldsymbol{\tilde{\nu}}$	The modified eddy viscosity, (m^2/s).
$\boldsymbol{\nu_T}$	The effective eddy viscosity coefficient.
$\boldsymbol{\rho_a}$	The air density, (kg/m^3).
$\boldsymbol{\rho_d}$	The droplet density, (kg/m^3).
$\boldsymbol{\sigma^{ij}}$	The stress tensor.
$\boldsymbol{\tau^{ij}}$	The velocity trajectory.
$\boldsymbol{\varphi}$	The dimensionless Langmuir parameter.
$\boldsymbol{\omega}$	The rotational speed of the rotor, (rad/s).

List of Abbreviations

2D	Two-Dimensional
3D	Three-Dimensional
AEP	Annual Energy Production
CAPEX	Capital Expenditure
CC	Cold Climate

CFD	Computational Fluid Dynamics
CoE	Cost of Energy
GHG	Greenhouse Gas
HAWT	Horizontal Axis Wind Turbine
HD	High Definition
HLCC	High Latitude Cold Climate
IC	Icing Climate
IR	Infrared
LTC	Low Temperature Climate
LWC	Liquid Water Content
MVD	Median Volume Diameter
NASA	National Aeronautics and Space Administration
OPEX	Operational Expenditure
P10	10th percentile of power production
P90	90th percentile of power production
PBL	Planetary Boundary Layer
RANS	Reynolds Averaged Naiver-Stokes
Re	Reynolds number
SA	Spalart-Allmaras
SCADA	Supervisory Control and Data Acquisition
SLD	Supercooled Large Droplets
VAWT	Vertical Axis Wind Turbine
WRF	Weather Research and Forecasting
RNG	Re-Normalization Group

List of Definitions

ATIRG	Arctic Technology & Icing Research Group
CEEGE	International Conference on Electrical Engineering and Green Energy
CQU	Chongqing University

CU	Cranfield University
EPE	International Conference on Energy and Power Engineering
EWEA	European Wind Energy Association
ICMEA	International Conference on Material Engineering and Application
ICPRE	International Conference on Power and Renewable Energy
ICREE	International Conference on Renewable Energy and Environment
IEA	International Energy Agency
IEC	International Electrotechnical Commission
IEEE	Institute of Electrical and Electronics Engineers
IRENA	International Renewable Energy Agency
ISO	International Standard Organization
IWAIS	International Workshop on Atmospheric Icing of Structures
NZE2050	The World's Roadmap to Net Zero by 2050
SDG 7	Sustainable Development Goal 7
TCP	Technology Collaboration Programme
UiT	UiT − The Arctic University of Norway
VTT	VTT − Technical Research Centre of Finland

1. Introduction

1.1. Background

From the first standard adopted by United States in 1970s, renewable energy has steadily emerged as an important mechanism to set national and regional economies on the path towards the medium and the long-term expectations of the envisioned sustainability goals in the global energy deployment. [2] International financing for supporting the renewable energy is rising gradually, and the world is making progress towards achieving the UN Sustainable Development Goal 7 (SDG 7) by 2030. [3] According to the European Wind Energy Association (EWEA, [4]), by 2021 the wind energy is likely to account for 14 – 17% of the EU's electricity production, which will lead to a reduction of 333 million tons of CO_2 emitted per year and the total savings in the fuel costs of €28 billion a year. In 2021, the International Energy Agency (IEA) [5] also released the special report – "*The World's Roadmap to Net Zero by 2050 (NZE2050)*", the first comprehensive roadmap to further strengthen its leadership role in the global clean energy transitions. [6] Overall, the electricity generation from the wind, geothermal and solar energy has increased in last decades, and wind power has increased the most in the absolute terms of power generation among all renewable energy sources, as shown in Figure 1.1. [7]

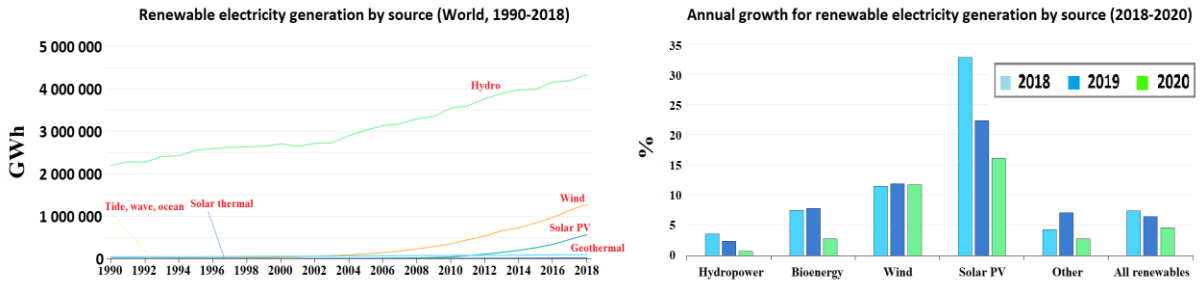

Figure 1.1 – Overview of worldwide electricity generation by the renewable energy sources (1990-2020). [7]

A wind turbine [8] – also called a wind energy converter, is a device that converts the wind's kinetic energy into the electrical energy. Wind power has the lowest greenhouse gas emissions, and the most favourable social impact compared to the solar, hydro, geothermal, coal and gas power generation technologies. [9] According to the International Renewable Energy Agency (IRENA), the global wind energy installed capacity has surged from 180 GW in 2010 to the 622 GW in 2019. The worldwide wind turbine market is expected to grow by 5.34% between 2019 and 2025, and the reduction in the carbon footprint/greenhouse gas (GHG) emissions from the wind turbine industry is projected to decrease ten-fold by 2050 for both the onshore and the offshore wind power industry. [10] Nowadays, onshore wind parks still dominate the global market with Europe being one of the major wind turbine regional markets. Due to high wind speeds, the offshore wind parks offer tremendous potential, and this segment is expected to grow even more in the future.

Cold climate (CC) regions have gained more attention recently from scientific and financial communities, in attempts to reach higher wind energy targets, as the good wind resources, combined with typically low population densities, make the CC regions attractive for future wind market development. However, the icing on wind turbines has been recognized as a hindrance, limiting the wind turbine performance and energy production at elevated cold climate sites, which in some cases have reported to lead up to a 17% decrease in Annual Energy Production (AEP) and a 20 – 50% decrease in the wind turbine's aerodynamic performance. [11] From 2002, IEA began to put more attention on

the wind energy in the CC, in order to address the issues related to the wind turbine operations in the icing conditions. Figure 1.2 shows the trend of wind energy growth in the ice prone cold regions during period from 2015 to 2020. [12, 13]

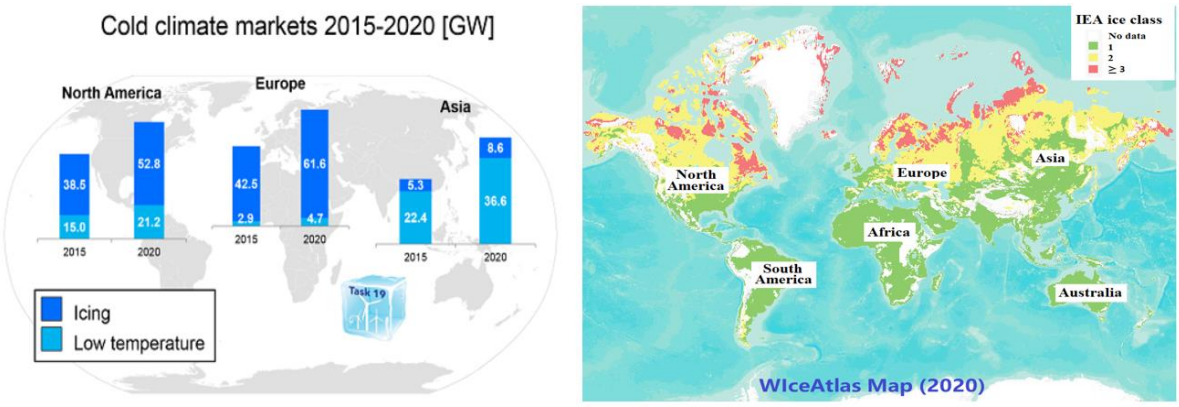

Figure 1.2 – An overview of wind energy growth in ice prone cold regions around the world (2015-2020). [12, 13]

Atmospheric ice accretion and low ambient temperatures pose special challenges for wind energy industry in the CC regions, which leads to the reduction in the energy yield, shortens the mechanical lifespan of wind turbines, increase the total costs, and also increases safety risk due to potential ice throw, etc. [14, 15]

The IEA Wind Task 19 – "*Wind energy in cold climates*" has urged the development of new methods to enable better prediction of the effects of the ice accretion on wind turbines' performance and resultant wind energy production. [5] In addition, the icing on wind turbine blades affect their aerodynamic performance and structural integrity, which consequently affects the AEP. Therefore, there is a growing need to improve the current knowledge about aerodynamic design and performance of wind turbine rotor blades for optimal and cost-effective operations in icing conditions. The potential impacts of icing conditions within CC regions [16] are insufficiently incorporated into the design limits, presently covered by the national and international standards for wind turbine.

The interest in wind energy has increased since the last few decades and has resulted in an increase in the installed wind turbines in the CC regions. Estimated wind energy capacity in ice prone CC is about 60 GW. [1]

A variety of problems due to icing have been documented, including the loss of power production, disrupted blade aerodynamics [17], overloading due to the delayed stall, increased fatigue of components due to imbalance in the ice load [17] and damage caused by the shedding of ice chunks [18]. To improve understanding and addressing these challenges, the IEA has established a task force − the *IEA Wind Task 19*. [19] Atmospheric ice accretion is one of the primary hazards for the design and safety of wind turbine structures. [15, 20] This highlights the need of a better understanding of the ice accretion process on wind turbine blades with the aim of improving safety and reducing the Capital Expenditure (CAPEX) and Operational Expenditure (OPEX) related to wind turbine operations in the ice prone CC areas. Figure 1.3 illustrates the main impacts of icing on the wind turbines.

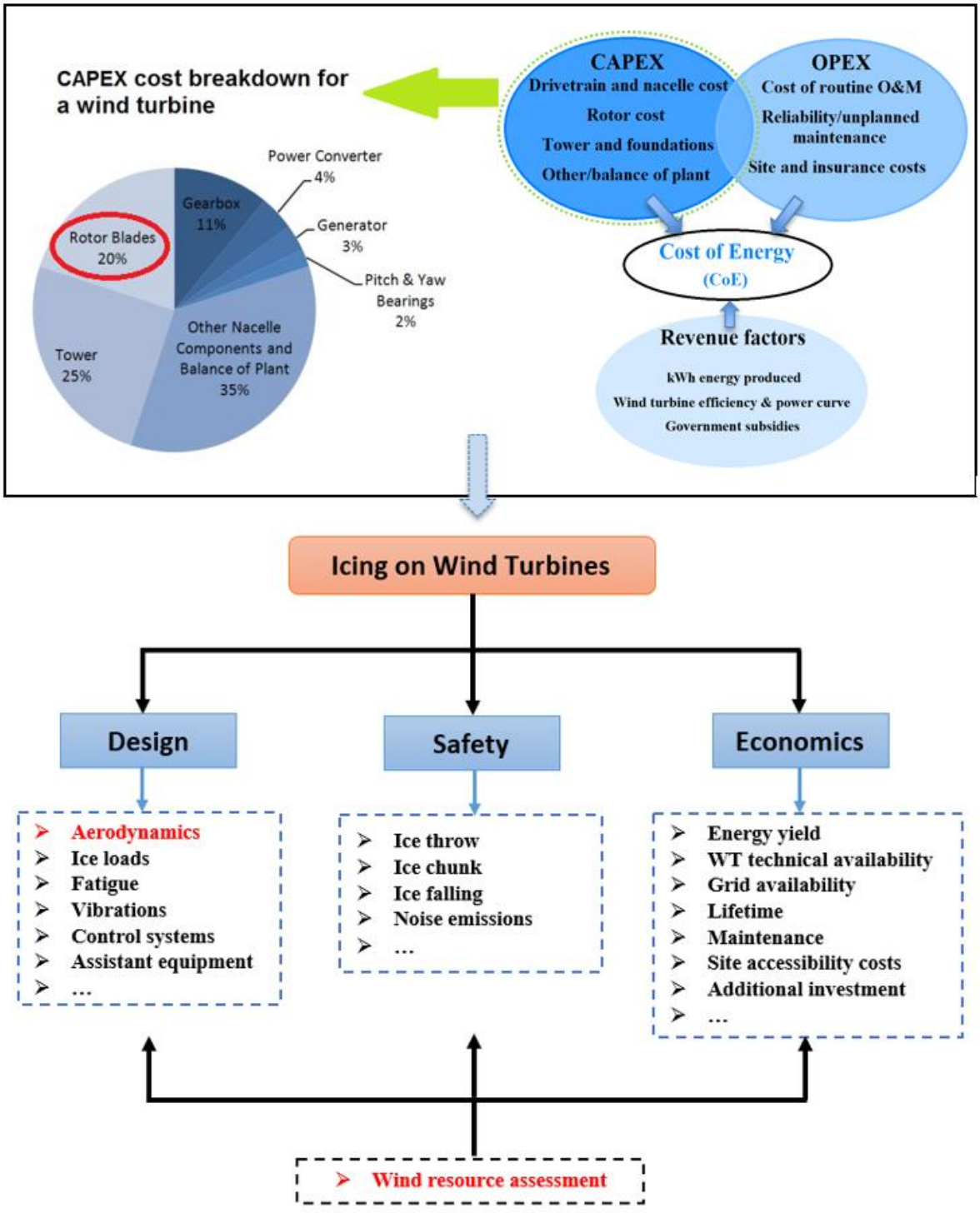

Figure 1.3 – Effect of icing on wind turbines. [21] (The topics addressed in this thesis are marked in red)

Atmospheric ice accretion mainly occurs along leading edge of the wind turbine blade due to the impingement of the super-cooled water droplets, which may freeze on the blade's surface immediately or after a short delay. [21, 22] The accumulated ice changes the blade geometry and increases its surface roughness, thus reducing the aerodynamic performance of wind turbine blades[15, 23] by decreasing the lift and increasing the drag force. The parameters causing negative impact on the wind turbine aerodynamics can be divided into three categories: *small-scale surface roughness, large-scale surface*

roughness and ice geometry. The change in the aerodynamic forces at the leading edge of the blade profile (airfoil) is illustrated in Figure 1.4. [24]

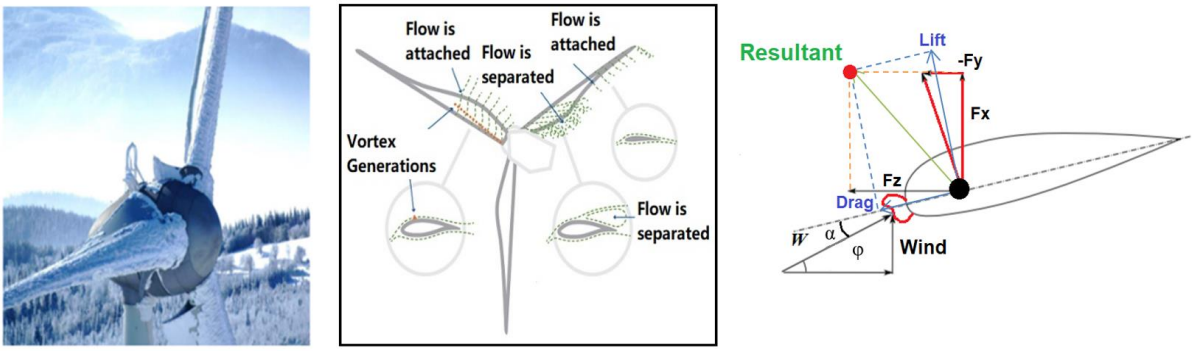

Figure 1.4 – Overview of ice accretion on wind turbine blades and profiles. [24]

Atmospheric ice is mainly classified as dry (rime) and wet (glaze) ice, with glaze ice having a greater impact on the aerodynamic performance, thus resulting in a greater loss of power production when compared with the rime ice. Rime ice is soft and less dense and occurs at lower temperatures, when 100% impinging droplets freeze, whereas glaze ice is harder and denser. Glaze icing events happen close to the freezing temperature, when freezing fraction of impinging droplet is not 100% and some droplets run along the blade surface as a very thin water film. The differences between glaze and rime ice shapes are illustrated in Figure 1.5. Accreted ice has a range of possible shapes depending on different operating conditions, which cause different levels of aerodynamic performance losses. Duncan *et al.* [25] have differentiated between rime and glaze ice shapes and found that the glaze ice caused larger aerodynamic losses than the rime ice. The accreted ice shape along the blade's leading edge also depend upon the geometry of wind turbine blade and operating conditions, with most important being the relative wind velocity, atmospheric temperature, droplet size (Median Volume Diameter, hereafter MVD), droplet distribution spectrum and Liquid Water Content (LWC) [26].

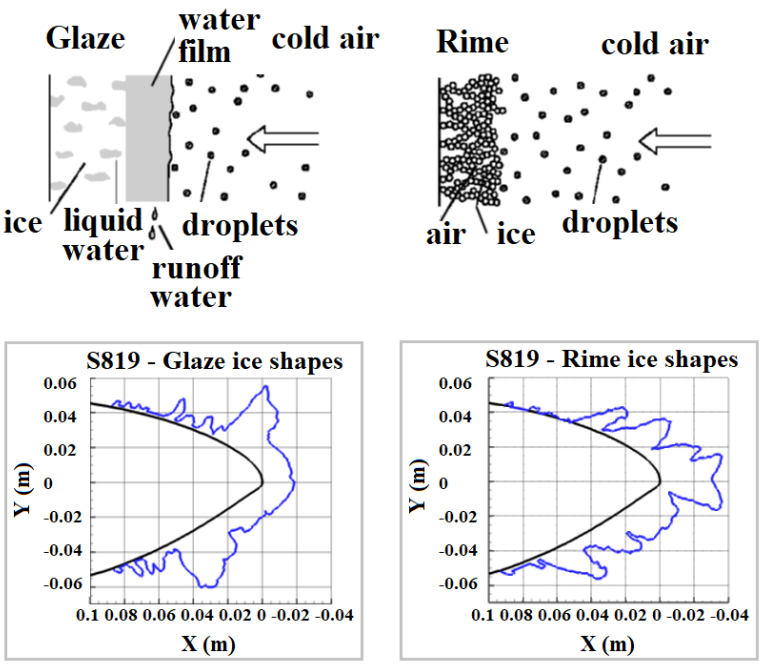

Figure 1.5 – Ice shapes along leading edge of S819 blade profile, for glaze and rime ice [27]).

When developing a wind park in the ice prone CC region, it is important to better estimate the impact that icing may have on its installation, operation and maintenance. Icing events are defined as time periods when the atmospheric temperature is below 0°C and the relative humidity is above 90%. [28] Icing conditions affect the underlying wind resources by reducing the available energy yield that wind turbines are able to capture. [29] Investment decisions for wind park development in CC regions are based on the need for better assessment of the icing conditions and its resultant effects on wind energy production. The severity of icing varies depending on the local weather conditions and the wind park site altitude when compared to the average height of the terrain as the planetary boundary layer (PBL) in the High Latitude Cold Climate (HLCC) regions has significant differences, when compared to lower latitudes, primarily due to reason that in HLCC regions thermal energy is unavailable to drive transport processes for majority of the year and these transport processes modulate the local atmospheric structure. [30]

Different techniques have been used for the wind resource and the icing events assessment in the CC regions involving meteorological field measurements, analytical methods of icing classification and numerical modelling of weather forecast. A combination of validated methodological approach and the on-site measurements of wind resources are used to evaluate the energy yield potential of wind park site. Analytical methods are used to predict icing effects on wind power production, where the aim is to minimize the uncertainties related to the production loss estimates. Numerical modelling approach is also used to develop the wind resource map of the region in order to provide more detailed information about icing intensity, duration of the icing events or their potential impacts to the developers in the planning phase of a wind park project.

In recent years, many advancements have been made in the knowledge of icing on wind turbines. There is a wide range of scales of ice accretion that affect the wind park operation. The relevant research about this topic is mainly divided into three types: *field measurements, lab experiments and numerical simulations*. Field testing has the highest accuracy out of these, counteracted by the highest cost and time investment, while on the other hand, the numerical modelling is cheaper and faster, while being less accurate, as shown in Figure 1.6. [31] Due to the influence of uncertainties such as measurement uncertainties, for example, MVD, LWC etc., in the experimental environment, there are certain constraints in lab-based experiments on wind turbines. Therefore, most lab-based experiments are mainly carried out using wind turbine blade profiles instead of the full-scale blade. In contrast, numerical modelling has more extensive research content and is the most commonly used method for icing research of wind turbine blades when compared with the experiments and field measurements.

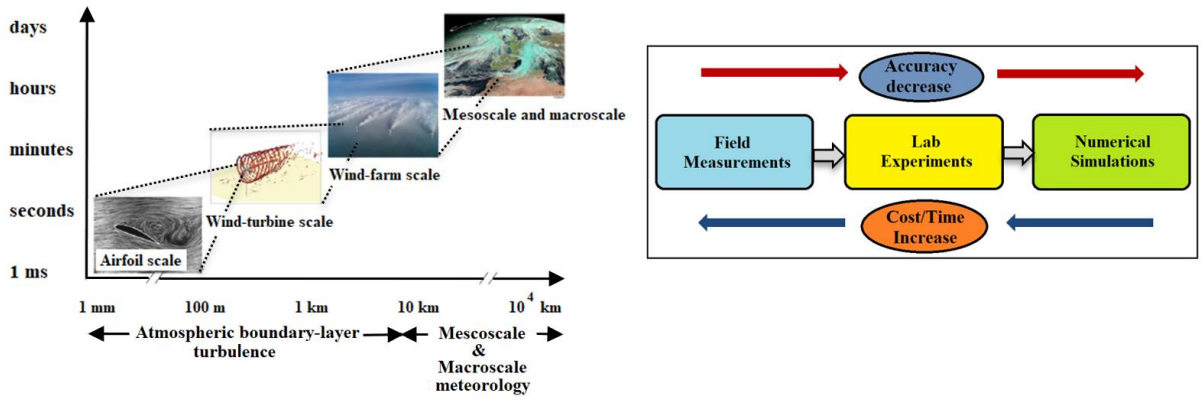

Figure 1.6 – The range of flow scales of wind energy (left) [31] with accuracy and cost/time specified in three aspects (right).

1.2. Motivation of the Ph.D. Project

This Ph.D. work is carried out at the Arctic Technology & Icing Research Group (ATIRG) of UiT – The Arctic University of Norway. Wind turbine operation in icing conditions is one of the main research topic at ATIRG, with an aim to better understand the atmospheric ice accretion on wind turbine blades, minimize the effects of atmospheric ice accretion on wind turbine performance and overall energy production.

The motivation of this Ph.D. project is, "*To study the atmospheric ice accretion on large wind turbine blade profiles, and to better understand the wind resource assessment and wind energy power production losses due to atmospheric ice*".

1.3. Objectives of the Ph.D. Project

A number of methods have been developed for the decision-support systems in optimizing the performance of large wind turbine blades in normal operating conditions, however, these methods are not fully capable to resolve the issues related to wind turbine performance in icing conditions. Therefore, the primary objective of this Ph.D. project is to study the ice accretion on large wind turbine blades. From the theoretical and methodological perspectives, the Ph.D. project aims at better understanding of the ice accretion physics, related aerodynamic and production losses. Another objective of this Ph.D. project is to improve the current knowledge about wind resource assessment in the icing conditions. Wind resource assessment in the CC regions is challenging, but very important, as the decisions about the (potential) wind energy project are based on these estimated results.

The first objective is focused on the ice accretion physics along wind turbine blade and the related performance losses, which includes analytical, numerical and experimental techniques to study the ice accretion physics and aerodynamic. The second objective is the wind resource assessment in the ice prone regions, which includes field measurement data acquisition, analytical modelling and numerical simulations to estimate the power production of the wind park in the ice prone CC region. The work is carried out in the close cooperation with the IEA task 19 members from the VTT − Technical Research Centre of Finland, by using T19IceLossMethod model in this project.

1.4. Problem Statement

Better knowledge of atmospheric ice accretion on wind turbine blade is critical in determining what geometric features of blade profiles (airfoil) contribute most to the aerodynamic performance degradation during ice accretion events and how these may differ for different blade profiles. In recent years, activities regarding wind energy projects in ice prone regions have increased, but atmospheric icing on wind turbine blades is still considered as a potential hazard in proper utilization of these good wind resources. Atmospheric icing affects the wind turbine aerodynamic performance, which leads to a decrease in wind energy production. Thus, aerodynamic performance and ice accretion on the large wind turbine blade profiles are associated with optimal operations of wind park and therefore is a core topic of this Ph.D. project.

This Ph.D. project was started in April 2018 with a focus to address following research questions:

Q1: How the analytical model of the ISO 12494 standard can be applied for modelling of icing on wind turbine blades?

Q2: How the different operating conditions change the accreted ice shapes on different wind turbine blade profiles?

Q3: How to deal with the uncertainties in lab-based experiment ice accretion?

Q4: How the blade geometry affects the ice accretion?

Q5: How the icing events can be detected using SCADA and how these events affect the AEP?

Q6: How to improve the wind energy production in the ice prone CC regions?

Q7: What are the further gains that can be obtained from the numerical methodology in this Ph.D. work?

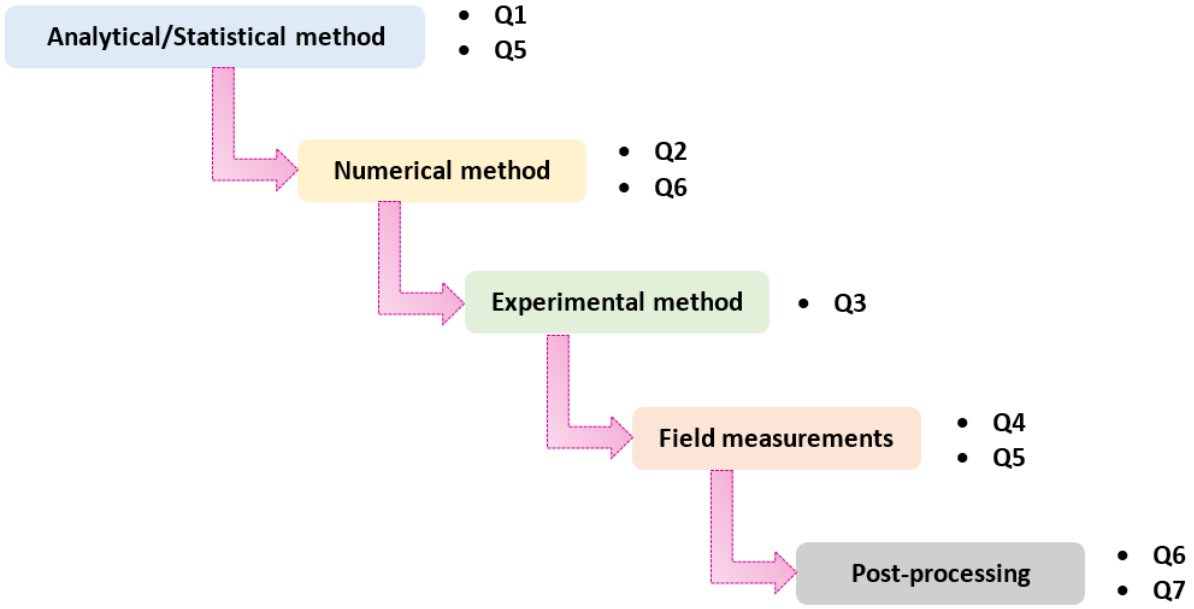

Figure 1.7 – Research questions with respect to analytical/statistical, numerical, experimental, field measurements and post-processing methods in this Ph.D. project.

Figure 1.7 illustrates the domain of the research questions with respect to the analytical, numerical, experimental and field measurements used in this Ph.D. project. As shown in Figure 1.7, the analytical/statistical modelling approach is focused on addressing the questions 1 and 5 in order to implement the existing international standards of icing on structures for wind turbine applications. Numerical modelling is the main focus in the questions 2 and 6 in order to better understand the aerodynamic performance degradation and wind energy production. Question 3 emphasizes on the development of solution for the proposed problems of the lab-based experiments. Field measurements approach is the main focus in answering the question 4 in order to provide better understanding of the ice accretion physics on the wind turbine blades, the question 5 also applied ice classification and energy production of the wind park. Finally, questions 6 and 7 aims to improve the understanding of large wind turbine aerodynamics under icing conditions.

1.5. Thesis Outline

This thesis is divided into four sections: the *first section* gives a general overview of the issues related to the icing on the wind turbines. The *second section* describes the research methodology used in this

Ph.D. work. The *third section* details the results and contributions of this Ph.D. project, including the related scientific publications and applications. The *fourth section* presents the concluding remarks and future work recommendations. Moreover, the bibliography and appendix are also included. Figure 1.8 gives an overview of the methodology and links within, used in the study of the two main topics in this Ph.D. work.

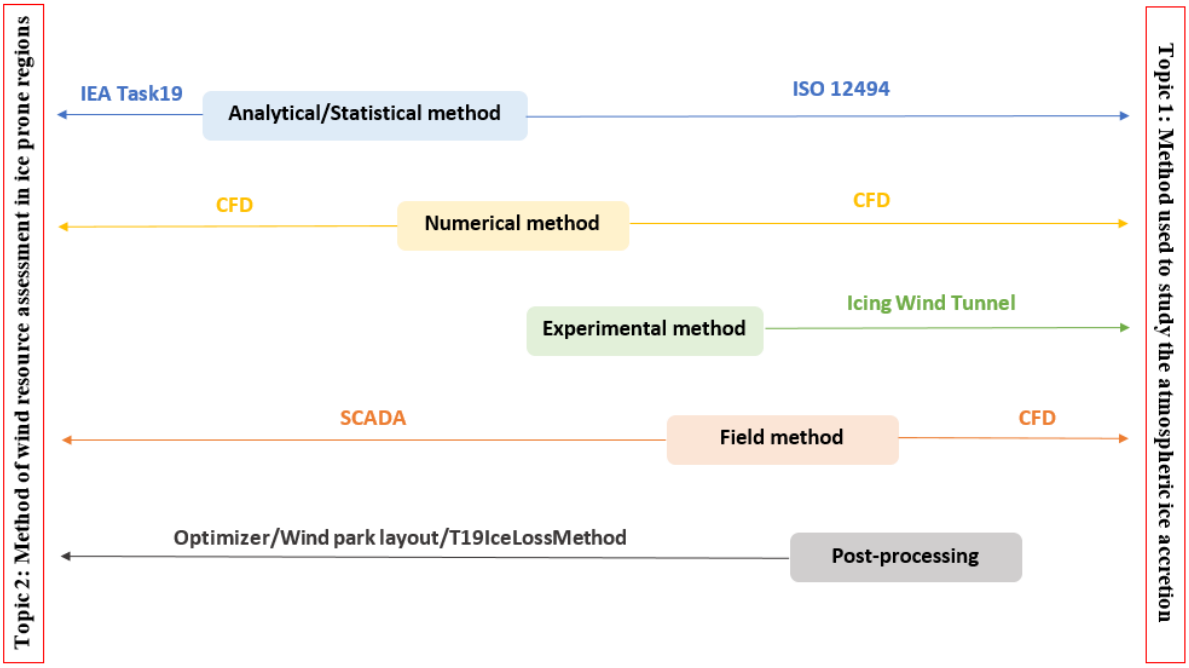

Figure 1.8 – Methodology of this Ph.D. work.

a) The *first* part of the thesis is the analytical method, which is based on the ISO 12494 standard, published by the International Organization for Standardization (ISO), and the IEA Task 19 method developed by the IEA Wind – Task 19 group. This part describes the methodology used in this project to implement the ISO 12494 model for the wind turbine applications, as this ISO model was mainly developed for icing on circular cylinders instead of wind turbines. In this thesis, a fundamental attempt has been made to apply this ISO standard for the wind turbine applications.
b) The *second* part is the numerical modelling, which mainly uses the Computational Fluid Dynamics (CFD) based multiphase analyses to simulate the ice accretion on wind turbine blade profiles at different operating and geometric conditions.
c) The *third* part is the lab-based experiments on ice accretion on different wind turbine blade profiles. Icing tunnel experiments are performed using four different blade profiles (S819, S826, S832 and DU96-W-180) for rime and glaze ice conditions at icing tunnel facility of Cranfield University, UK.
d) The *fourth* part is the field measurements, which uses the data from two wind parks: first wind park is located in Northern Norway, whereas other one is operated by Chongqing University (CQU) national key laboratory – the icing station at Xufeng Mountain in China.
e) The *fifth* part is the post processing, which is used to evaluate the wind resources to improve the power production. In the post processing, the most valued methods in wind resource assessment have been used, such as Supervisory Control and Data Acquisition (SCADA), CFD, and the newest model – the *T19IceLossMethod*, based on international standard IEA Task 19.

Part I

Wind Turbine Blade Ice Accretion Physics

2. An Overview of Wind Turbine Icing

In order to better understand why and how ice accretion on wind turbine occurs, it is necessary to study the physics of icing process. This chapter provides an overview of the basics of atmospheric ice accretion on the wind turbine blade.

2.1. Clouds Physics

Cloud formation and the ice physics has a close relation. In Nordic regions, it is primarily the freezing fog that causes the ice accretion on the wind turbines. Formation of the clouds happens when water evaporates and rises, until it cools and condenses. This means that the observed clouds properties are dynamic, with constant interactions and exchanges within gas, liquid and solid phases of water. Typically, clouds are caused by a rising body of air, however, if the dry air penetrates from the top of the cloud due to turbulence or other movements and mixes with some of the droplets, this causes evaporation of the droplets which further cools the air and accelerates the downward motion.

The formation of clouds is caused by rising air that is driven by several mechanisms: in the first stage, prevailing winds can press the air against mountains and cause it to be driven upwards; in the second stage, frontal lifting can occur when warm and cold air interact, and the warm front is pressed up by the cold front; in the third stage, the heat transfer from warm to cold air can cause it to rise due to its increased buoyancy. When the air rises, the air from different elevations and areas of the cloud mixes due to turbulence, and the two unsaturated quantities (vapor pressure and temperature) of rising and sinking air become supersaturated when mixed. The air mixing process leads to cloud formation consisting of small water droplets.

Droplets can grow through both the continuing condensation, or by the collision and the coalescence with other droplets. The initial water droplets that form are extremely small, and until the size of droplets reaches a critical size, they are classified as stable. Since ice in atmosphere usually forms at temperatures higher than –40°C, it can be deduced that homogenous nucleation is not the primary method of ice formation. [32] Nucleation occurs at higher temperatures, if ice nuclei are present. If the number of active ice nuclei in the atmosphere was as high as the number of condensation nuclei, then supercooled cloud droplets would seldom occur. However, at about –20°C, the number of ice nuclei is estimated to be about a factor of 10^7 lower than the total number of particles in the air, and a factor of 10^5 lower than the number of condensation nuclei. [32] At colder temperatures, the number of active ice nuclei increases exponentially. This relatively low number of ice nuclei means that at temperatures between –20°C and 0°C clouds often form as supercooled water droplets instead of ice. Supercooled droplets are the main cause of the atmospheric ice accretion.

2.2. Atmospheric Icing

With respect to wind park operations, icing conditions mainly affect the wind park site access, wind turbine operations, working and maintenance, finances, noise, health and safety of workers. CC wind energy projects need to take into consideration the high safety standards in addition to other undertakings, present in the normal operating climate. CC regions have good resources of wind energy, but still have issues that might stop financiers from investing in wind energy projects based on uncertainties in the wind resource assessment and ice forecasting methods. To improve this, a better estimation of wind turbine production losses under icing conditions is needed. Figure 2.1 illustrates the

differences among the CC [1], the low temperature climate (LTC) and the icing climate (IC). This Ph.D. work mainly deals with the wind energy in the IC condition.

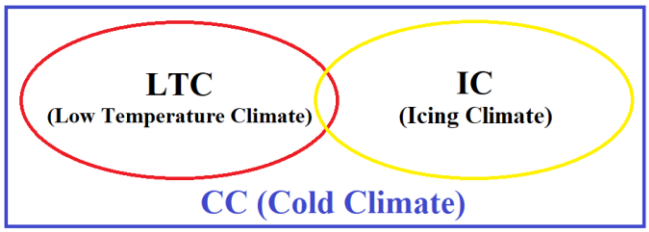

Figure 2.1 – Cold climate classification. [1]

Several decades of studies about atmospheric icing on structures not only show the hazardous consequences of icing [33], but also highlight the damages of infrastructure, such as wind turbines, power lines, transmission towers, radio towers, etc. [34] Atmospheric icing is defined as the (supercooled) water droplets freezing on the existing objects or structures (ISO standard 12494). Atmospheric icing can be classified as either in-cloud icing (rime or glaze ice) or precipitation icing (freezing rain or drizzle, wet snow). Figure 2.2 illustrates a schematic overview of the main meteorological parameters and Table 2.1 shows the differences among various types of atmospheric icing.

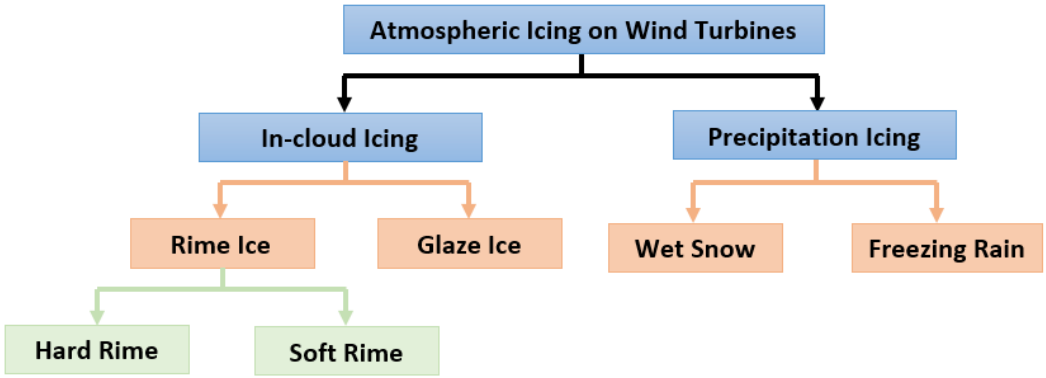

Figure 2.2 – Overview of different types of atmospheric icing on wind turbines.

Table 2.1 – Meteorological parameters of atmospheric icing. [28]

Type of Ice	Temperature (°C)	Wind speed (m/s)	Droplet size	Water content in air	Typical event duration
Precipitation Icing					
Freezing rain (Glaze)	– 0 ~ 0	Any	Large	Medium	Hours
Wet snow	0 ~ + 3	Any	Flakes	Very high	Hours
In-cloud Icing					
Glaze	0 ~ – 6	3-25	Medium	High	Hours
Hard rime	0 ~ – 20	2-25	Medium	Medium	Days
Soft rime		2-25	Small	Low	Days

Atmospheric icing occurs when the supercooled water droplets collide with the surface of structures, and the type of ice which forms is based on the thermal equilibrium, which mainly includes the following terms: heat capacity of the forming ice/water layer, energy released by the freezing droplets, kinetic energy of incoming droplets, radiation, evaporation, conduction, convection, and friction caused by the airflow. The thermodynamic model of the iced surface, used on the control volumes basis, as shown in Figure 2.3 [35, 36], is based on the energy conservation for heat and mass transfer, given in Equation 2.1 [35, 37]:

$$Q_f + Q_{adh} + Q_{kin} = Q_{ss} + Q_{sub/evap} + Q_{cd} + Q_{cv} + Q_{rad} \tag{2.1}$$

where Q_f is the heat of liquid (supercooled water droplets) freezing, Q_{adh} is the viscous adiabatic heating from the friction inside the boundary layer, Q_{kin} is the kinetic heating from supercooled water droplets, Q_{ss} is the total sensible heat of the liquid water mass to the freezing temperature, $Q_{sub/evap}$ is the heat of liquid sublimation or evaporation, Q_{cd} is the heat loss of conduction to the interface, Q_{cv} is the convective heat loss produced by airflow over the surface, Q_{rad} is the heat loss of radiation from the surface.

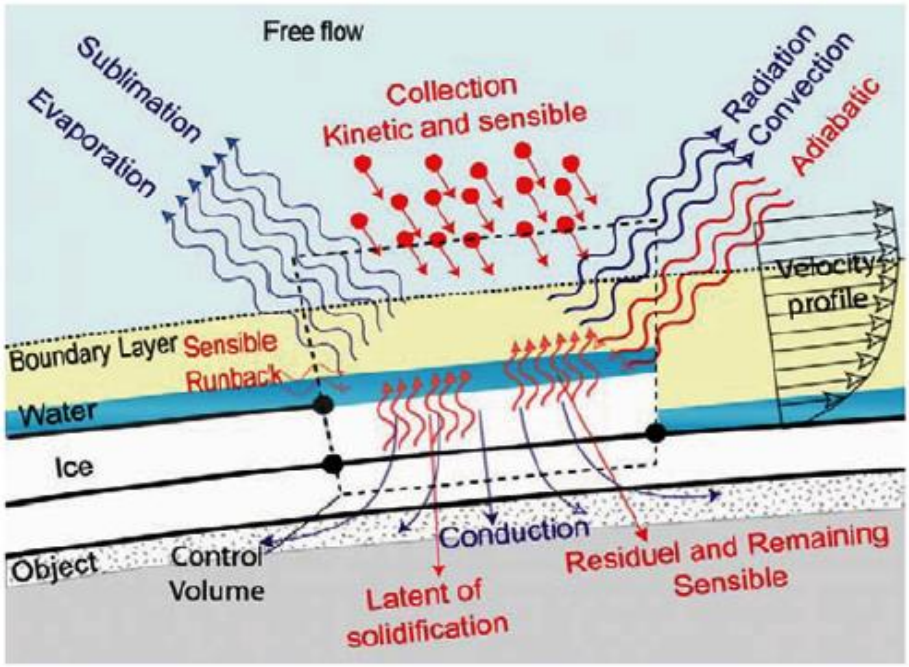

Figure 2.3 – Thermodynamic model of iced surface. [36, 37]

The ice accretion process can become arbitrarily complex depending on the airflow conditions around the structures or objects of intricate shapes. In general, the atmospheric ice accretion on the so-called standard reference collector, which is a 30 mm diameter by 500 mm long rotating circular cylinder, which is defined as a physical model of icing is described by Dr. Lasse Makkonen in 1994 [38], and is extended to use in ISO 12494 standard [39], is given by Equation 2.2:

$$\frac{dM}{dt} = \alpha_1 \alpha_2 \alpha_3 v A w \tag{2.2}$$

Where v (m/sec) is the relative velocity of the particles, A (m^2) is the cross-sectional area of the object with respect to the direction of the particle velocity vector and w is the liquid water content (kg/m^3).

The Makkonen model is based on three ratios, which reduce the incoming mass flux from its maximum possible value (*vAw*): *The collision efficiency* (α_1) which is a ratio that describes how many water, ice or snow particles impact the structure being studied; *The sticking efficiency* (α_2) is the ratio of particles that stick to the surface rather than bouncing off it, which is mostly used for wet snow and ice crystals and its normally assumed that $\alpha_2 = 1$ for water droplets; *The freezing efficiency* (α_3) is the ratio of the particles being frozen, under the given the thermodynamic conditions. It is assumed being equal to 1 for the rime ice accretion (dry growth) but reduced from 1 if the impinging water is lost due to the water runback from the surface. The behaviour of the impinging water droplets is governed by the balance of the inertia and the drag forces, acting on the droplet. Those are primarily the functions of the droplet's mass/size, meaning that larger and heavier droplets tend to collide with the object more easily, while the smaller droplets are being deflected from the object due to following the streamlines due to influence of drag, as shown in Figure 2.4.

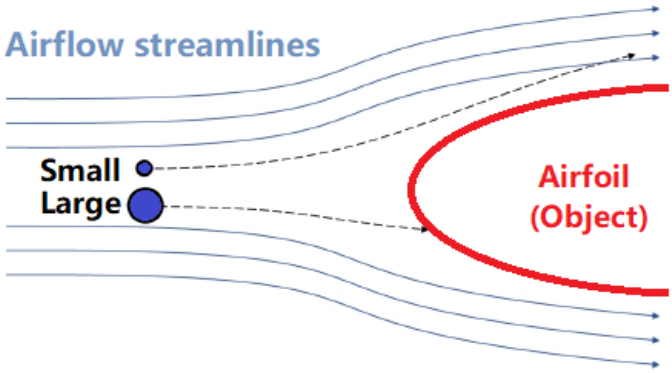

Figure 2.4 – Schematic overview of the behaviour of droplet trajectories around an airfoil.

ISO 12494 standard shows that ice accretion rate has somewhat peculiar dependency on the size/area of the object: as the iced cross-sectional area (*A*) is a function of the ice mass (*M*), the ice growth rate has a positive feedback (increase) with the time as *A* gets larger. However, the droplet collision efficiency has the opposite effects, and it is correlated with the droplet's inertia parameter *K*, which governs the droplet's behaviour (and has the characteristic length in the denominator). With the surface area (*A*) increasing, the airflow prone to deflect incoming water droplets away from the structures more easily.

Several ice types can be defined and depend on thermodynamic behaviour of the object, which are briefly introduced in the section 2.3.

2.3. Icing Classifications

In 2001, the International Organization for Standardization has published the ISO 12494 standard [39] which represents the current aggregated knowledgebase and reference model for icing on structures. According to the method of ice formation (in-cloud or precipitation) and the thermodynamic conditions at the interface, the ice accumulation on the structures can take the different forms. The accumulated ice can be generalized into two categories: the glaze ice (wet-growth) and the rime ice (dry-growth). For the glaze ice conditions, the wet-growth icing can be defined as: the ice growth under the condition which contains a layer of liquid water under the interface, and it normally results in more dense and transparent type of ice. However, for the rime ice conditions, the dry-growth icing defined as: when the interface of structures or objects is completely frozen, the impinging water droplets will freeze immediately, generally resulting in the less dense ice with white and opaque appearance.

In addition, in order to expand the two main categories of ice, presented above, four sub types of icing were classified in COST-727 project [28] in 2006, which are based on the more specific physical characteristics: glaze, wet snow, hard rime and soft rime. If the heat flux balance on the surface results in a slow cooling and freezing process along with a layer of liquid water being present on the interface, which leads to a higher ice density and a larger contact area of surface, then the ice type with a strong adhesion is formed: *glaze ice*. If the process occurs with minimal liquid water present and the high wind speeds and low temperatures, the ice is weakly connected to the interface during formation and leads to a strong ice adhesion, the opaque white ice is formed: *wet snow*. If the heat flux is larger than the cooling flux, the water droplets will freeze slower, and the stronger adhesion and higher density occurs during the ice accretion, then the ice with more opaque appearance is formed: *hard rime*. If the heat flux is small due to freezing and the amount of supercooled water particles is large, the water droplets freeze instantly on the contact with the interface, also containing the air bubbles trapped in-between the frozen ice particles and the ice type which forms is called: *soft rime*.

The typical physical characteristics of accumulated ice and its appearance vary widely with the variations of the operating and on-site conditions during the ice growth, and main preconditions for significant ice accretion are the dimensions of the object exposed, its orientation to the direction of the wind and operating conditions, such as high wind speeds, liquid water concentrations and bigger droplet sizes. The COST-727 project presented a guideline of the main parameters controlling the ice type's formation ranging from low (soft rime ice) to medium (hard rime ice) to high (glaze ice) accumulated ice densities on the spectrum, given in Figure 2.5. The rate at which ice accumulates on the structures depends on meteorological parameters, such as: wind speed, air temperature, LWC and MVD, etc.

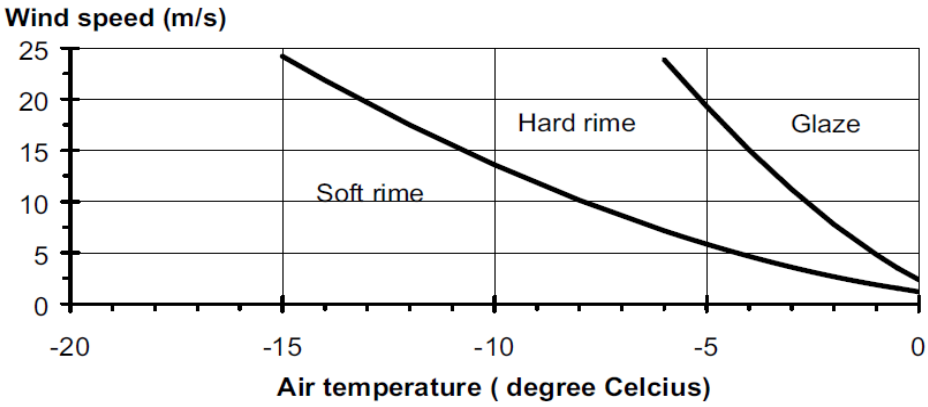

Figure 2.5 – Type of accreted ice as a function of wind speed and air temperature. [28]

2.4. IEA Annexes

The IEA Wind agreement, also known as the "*Implementing Agreement for Co-operation in the Research, Development, and Development of Wind Energy Systems*", is a part of the Technology Collaboration Programme [40] created by the IEA. [5] IEA Wind is a vessel for member countries to exchange the information on the planning and execution of national, large scale wind system projects and to collaborate on research projects, called Tasks or Annexes. Since 2002, IEA has maintained the international working group Task 19 – *"Wind Energy in Cold Climates"* [16], which gathers and disseminates information about wind energy in CC regions and establishes guidelines and state-of-the-art technologies. The purpose of IEA Wind Task 19 is to provide the best available recommendations, reduce the risks involved in undertaking projects [41], and to support/accelerate the growth of wind

energy production in cold climates regions. It also provides preparatory information that should benefit manufacturers, banks and insurance companies. An international collaboration on gathering and providing the information about wind turbine operations under icing and low temperatures has been established in 2003, and the-state-of-art technologies of wind energy in CC regions are presented: knowledge on climatic conditions and resources, techniques in manufacturing and operating wind turbines in CC. [42]

The Available Technologies report [29], published by IEA Task 19 in 2016 and updated to the second edition in 2018, provides a quick and easy interface for available technologies and solutions to the most demanding challenges of wind energy in cold climate. The core of this report consists of summary tables per technology, which not only provides that what solutions are available but also provides an indication of quality or maturity of the solutions based on public information available.

IEA Task 19 groups has also published the international recommendations for icing risk assessment reports [41] in 2018, which provides the best available recommendations for assessing the risk due to ice throw and ice fall from wind turbines, and reducing the uncertainties involved in these assessments. The aim for these reports is to give recommendations, taking into account the national and international laws and standards, regarding the icing risk assessments for wind turbine operations.

Today, the wind energy in the CC regions has high safety and operating requirements. [11] The standardization and certification processes in wind energy are used to ensure safety and performance of wind turbines and other technological equipment. To date, no specific CC wind standard exists, and CC issues are distributed among several different standards. IEA Task 19 is willing to take the lead in proposing prioritized research projects in cold climate regions. Table 2.2 shows the IEA wind park site classification based on icing events [19, 43]:

Table 2.2 – IEA wind park site classification. [19]

IEA Ice class	**Meteorological Icing**	**Instrumental icing**	**Production loss**
	% of year	% of year	% of annual production
5	>10	>20	>20
4	5~10	10~30	10~25
3	3~5	6~15	3~12
2	0.5~3	1~9	0.5~5
1	0~0.5	<1.5	0~0.5

The IEA Wind Task19 group also presented a statistical method to assess production losses due to icing based on standard SCADA data available from modern wind parks in 2015, named the *"T19IceLossMethod"*. [40] T19IceLossMethod is a standardized open source Python code model for assessment of wind power production losses due to ice [29] and comparison of different sites with a systematic analysis method. [44] Within the scope of work used in this Ph.D. work a detailed historical SCADA data analysis, using 10-minute averages from different wind turbine models, and analysis of icing conditions on sites has been carried out. [45]

2.5. Classification of Wind Turbines

There exists a wide range of wind turbine technologies, classified from micro to large wind turbines. A small wind turbine is a wind turbine used for microgeneration, as opposed to large commercial wind turbines, such as those found in modern wind parks, with greater individual power output. The International Electrotechnical Commission [46] has published an international standard 61400-2:2014 [46] which defines the line between the small and the large wind turbines. Small-scale wind turbines produces energy up to 50 kW rated power or less, and they are suitable for homes, farms, small businesses, rural villages, telecommunication systems, etc. On the other hand, large-scale wind turbines have rated energy outputs of greater than 250 kW. For a given survivable wind speed, the mass of a turbine is approximately proportional to the cube of its blade-length. Wind power intercepted by the turbine is proportional to the square of its blade-length times power output from the rotor. Wind turbines are also classified by the aerodynamic force (lift and drag) and the orientation of the axis of rotation to the direction of the wind: Horizontal Axis Wind Turbine (HAWT) and Vertical Axis Wind Turbine (VAWT). The majority of presently installed wind turbines are HAWT and only 3% are VAWT. [47] The overall classification of wind turbines is illustrated in Figure 2.6.

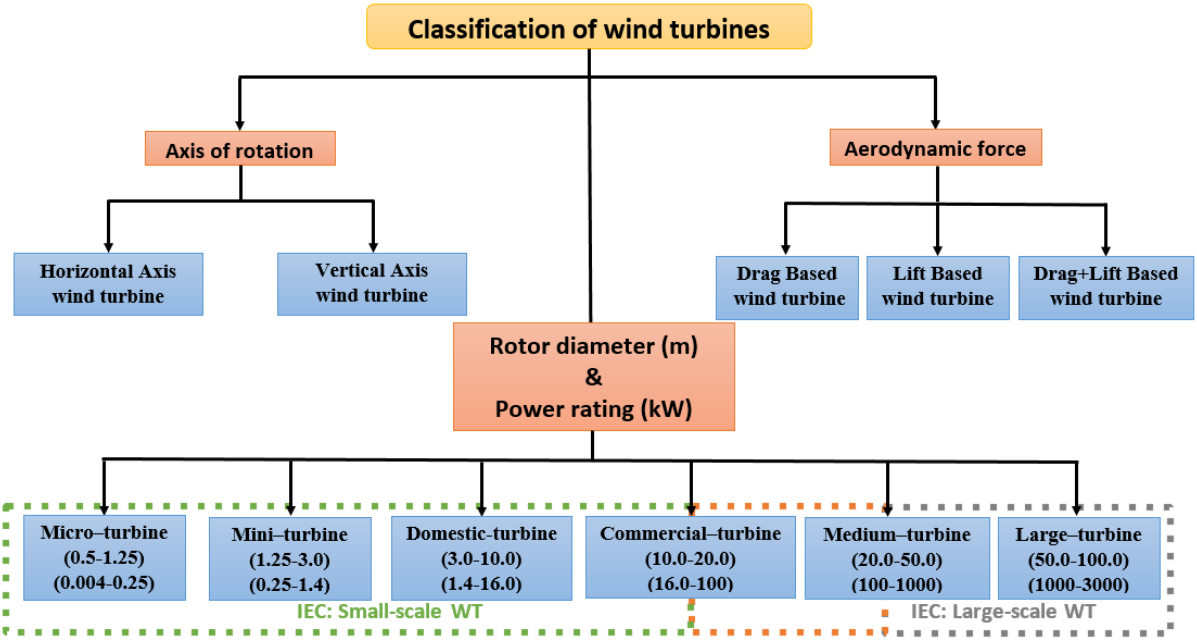

Figure 2.6 – Classification of wind turbines. [48]

Same as with the icing on large-scale wind turbines, the small-scale wind turbines are prone to more severe ice accretion under high wind velocity and low temperature. Due to the lack of feedback loop installed, the small-scale wind turbines can be stopped more easily when they suffer from ice loads compared to the large-scale wind turbines. Thus, compared to the deterioration of aerodynamic performances, ice will accrete more on the rotor of small-scale wind turbines compared to the large-scale wind turbines. [49] With the steady increase of the wind turbine rotor size (Figure 2.7), the CC market is eager to develop new technologies of large wind turbines.

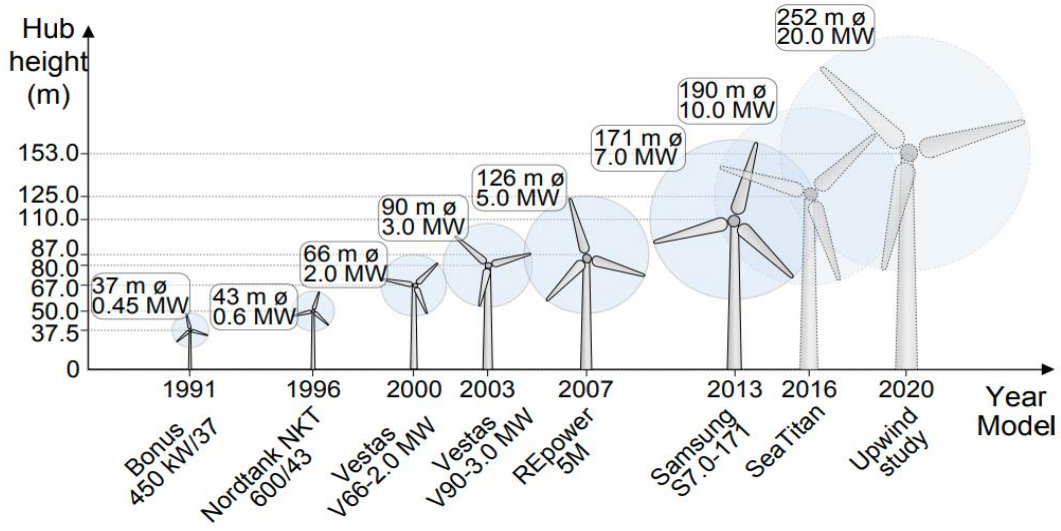

Figure 2.7 – Classification of wind turbines. [50]

On one hand, there are economies of scale in wind turbines, i.e. larger turbines are usually able to deliver electricity at a lower cost than smaller turbines. In addition, the larger turbines are particularly well suited for offshore wind power, and in onshore areas where it is difficult to find sites for more than a single turbine. Furthermore, heating systems are easier to build into large wind turbines, whereas noise, maintenance and safety issues are difficult due to site in different areas with large wind turbines.

2.6. Wind Turbine Geometry and Operation Terminologies

Figure 2.8 illustrates the general nomenclature of wind turbine, which contains several relevant terms, and the airfoil nomenclature, shown in Table 2.3. Whereas Table 2.4 describes the aerodynamic parameters that affect ice accretion on a wind turbine blade.

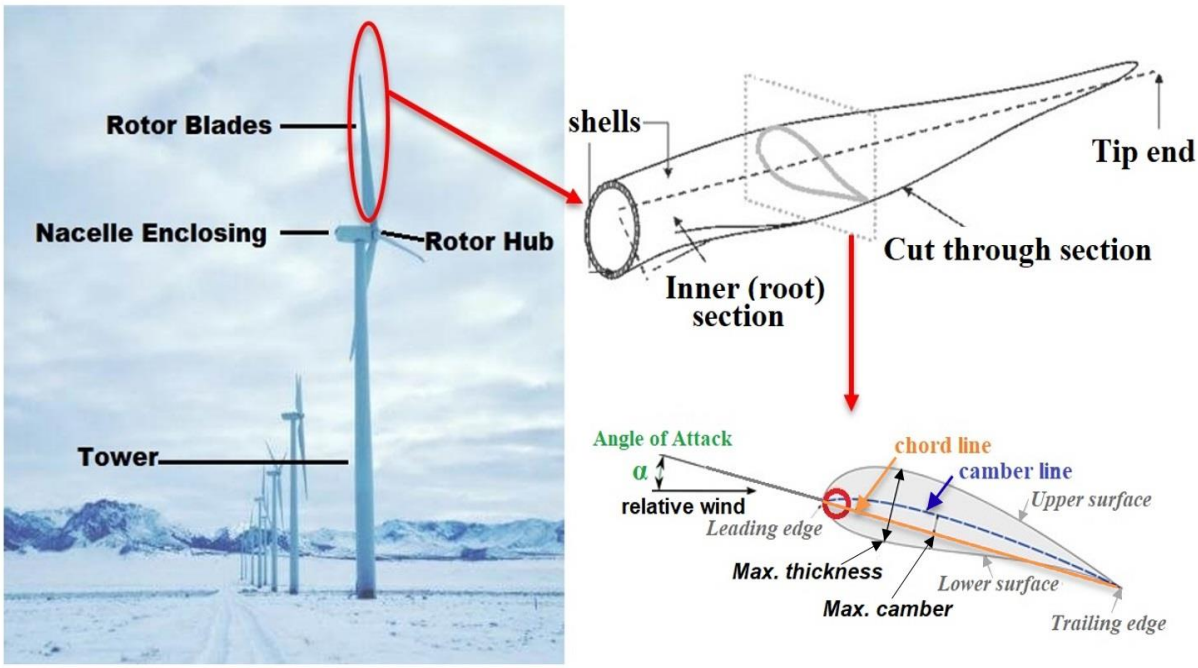

Figure 2.8 – Wind Turbine nomenclature. [51]

Table 2.3 – Definitions of the various terms of airfoil.

Terms	Definition
Angle of attack (AOA, α)	It is the angle between the chord line and the direction of the oncoming flow.
Suction surface (upper surface)	Generally associated with the higher velocity and lower static pressure.
Pressure surface (lower surface)	It has a comparatively higher static pressure than the suction surface. The pressure gradient between these two surfaces contributes to the lift force generated for a given airfoil.
Leading edge	It is the point at the front of the airfoil that has maximum curvature (minimum radius).
Trailing edge	It is defined similarly as the point of maximum curvature at the rear of the airfoil.
Chord line	It is the straight line connecting leading and trailing edges. The chord length, or simply chord, *c* is the length of the chord line. That is the reference dimension of the airfoil section.
Mean camber line (mean line)	It is the locus of point's midway between the upper and lower surfaces. Its shape depends on the thickness distribution along the chord.
Thickness	The thickness of an airfoil varies along the chord. Thickness measured perpendicular to the camber line. This is sometimes described as the "*American convention*"; Thickness measured perpendicular to the chord line. This is sometimes described as the "*British convention*".
Nose circle	At some point on the LE the radius will be a minimum, at which point one could calculate a radius of curvature at that point and draw the radius inward normal to that point and make a circle.
Aerodynamic center	Which is the chord-wise length about which the pitching moment is independent of the lift coefficient and the angle of attack.
Center of pressure	Which is the chord-wise location about which the pitching moment is zero.

Table 2.4 – Definitions of the various aerodynamic parameters.

Terms	Definition
Lift force (*L*)	The component of this force perpendicular to the direction of motion is called lift.
Drag force (*D*)	The component parallel to the direction of motion is called drag.
Stall	It is a reduction in the lift coefficient generated by a foil as angle of attack increases. This occurs when the critical angle of attack of the foil is exceeded.
Reynolds number	It is a measure of the ratio of the inertial force $(\rho v^2)/L$ to the viscous force $\mu v/L^2$ of the fluid, it is a dimensionless quantity, which is defined as in Equation 2.3: $$Re = \frac{\rho_a v C}{\mu} \quad (2.3)$$ where ρ_a (kg/m^3) is air density, v (m/sec) is the air speed, C (m) is the characteristic length and μ (kg/ (m·s)) is the dynamic viscosity.
Tip Speed Ratio (TSR)	It is the ratio between the tangential speed of the tip of a blade and the actual speed of the wind, v. The tip-speed ratio is related to efficiency, with the optimum varying with blade design. $$\lambda = \frac{V}{v} = \frac{\omega R}{v} \quad (2.4)$$

	where *V* is the rotor tip speed (m/s), *v* is the free stream wind speed in metres/second (m/s) at the height of the blade hub.
MVD	It refers to the midpoint droplet size, where half of the volume of spray is in droplets smaller, and half of the volume is in droplets larger than the mean, it is not the average mean values of the droplet sizes.
LWC	It is the measure of the mass of the water in a cloud in a specified amount of dry air, and it is typically measured per volume of air (g/m^3) or mass of air (g/kg).
Supercooled large droplets (SLD)	It defined as those water droplets which exist in liquid form at temperatures below 0°C with a diameter greater than 50 microns. SLD conditions include freezing drizzle drops and freezing raindrops.
The power coefficient (*Cp*)	It is a quantity that expresses what fraction of the power in the wind is being extracted by the wind turbine. It is generally assumed to be a function of both TSR and pitch angle.

2.7. Wind Turbine Icing Environment and Technical Aspects

2.7.1. Icing Environment

Wind turbines in the icing environment can be exposed to the in-cloud icing in one of the following two ways: either wind turbine is tall enough to penetrate into the base of the cloud, or the cloud base is below the ground level in which the wind turbine is suited. [34] The most common observation of the wind turbine in-cloud icing occurs in the cold and mountainous regions, where cloud base levels are frequently close to the ground levels due to frequently occurring processes of the orographic lift and terrain. Under extreme conditions and persistent suitable weather, if those conditions persist, they can cause icing events to last for weeks, resulting in the continuous ice growth and leading to significant ice loads, even potentially destructive [52]. Therefore, there is a growing need to study and better understand the wind turbine operation and performance in the icing conditions.

Icing on wind turbine blades depends on both the operating *(temperature, velocity, MVD and LWC)* and geometric *(size and shape)* characteristics. Different operating and thermodynamic conditions on the wind turbine blades will result in the accreted ice being of different densities and shapes. [53] The change in accreted ice shapes affects the air flow behaviour on the blade profile and its aerodynamic performance, [54]. The drag coefficient of the wind turbine blade has a dependence on the temperature, where it is relatively constant for the dry rime ice, that first increases with the temperature *(due to the transition to formation of horns)* and then drops sharply as the higher temperatures result in the melting of the ice horns. [55] Virk *et al.* [53] showed that the air temperature alone cannot be used to distinguish among the different types of ice and the resultant ice shapes, and that the droplet size, air velocity and LWC can also affect the resultant ice accumulation. Bragg *et al.* [56] categorized four types of ice accretion that affect wind turbine blade aerodynamics differently: dispersed roughness, horn ice, streamwise ice and spanwise-ridge ice, as shown in Figure 2.9.

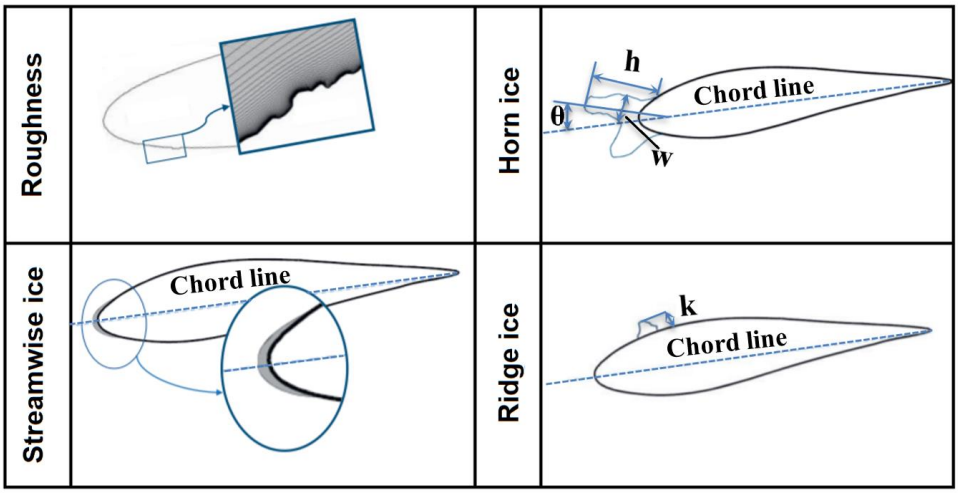

Figure 2.9 – Examples of accreted ice shapes. [56]

Different temperatures and heat fluxes along the blade profile will result in different types of ice accretion. [55] Duncan *et al.* [25] identified the difference between glaze and rime ice causing different levels of production losses. Surface roughness of the blade profile changes during the ice accretion process, which affects the shear stresses and heat fluxes that leads to a change in rate and the shape of the ice accretion. [25] During the ice accretion, the changes in the blade profile surface roughness lead to the changes in the boundary layer development, which influences the convective heat transfer and the droplet freezing efficiency (α_3). Shin [57] and Anderson [58] show that the ice surface roughness can be characterized in the three main zones which develop along the leading edge of airfoil for both the glaze and the rime ice − *the smooth zone, rough zone and feather region*, as illustrated in Figure 2.10. Guy *et al.* [35] have developed a model which combines ice mass and heat balance equations to calculate the surface roughness and masses of remaining, runback and shed liquid water along the blade profile surface.

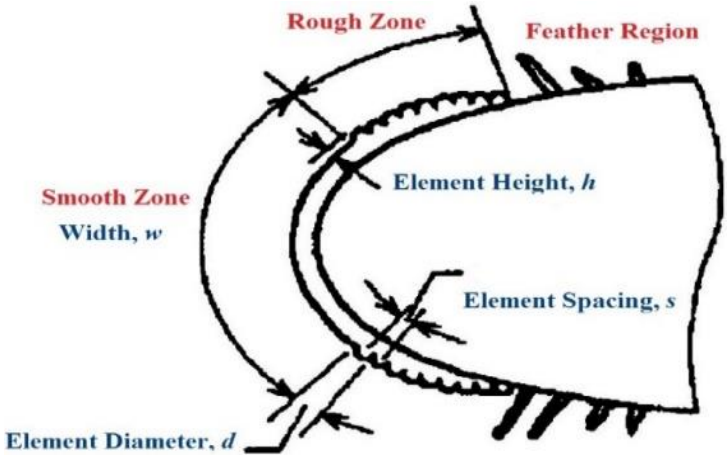

Figure 2.10 – The features of ice roughness. [58]

Better knowledge of the atmospheric ice accretion on the wind turbine blades is critical in determining which geometric features of the blade profile (airfoil) contribute to the performance degradation during the ice accretion events and how these may differ for different blade profiles. Atmospheric ice accretion on wind turbine blade mainly occurs due to collision of super cooled water droplets. These super cooled water droplets may immediately or after some short delay freeze into ice on surfaces. [21, 22] The main

effect of icing on wind turbine blades is generally an altered profile shape which results in a change of its aerodynamic characteristics. This affects the wind turbine torque and power production. The results of such aerodynamic changes can be seen as a decrease in the in-plane (rotating) force because of a decrease in the lift coefficient (C_L) and an increase in the drag coefficient (C_D). [59]

Effects of icing below and above rated wind speed are different. Below the rated wind speed, thrust and especially power of the clean rotor is higher than the iced rotor. When the shaft speed reaches the rated rotor speed, the torque controller adjusts the generator torque to obtain the rated power. But the rated power is shifted to a higher wind speed because of icing, the aerodynamic torque on the iced rotor at rated wind speed is smaller than the clean rotor. Results show that below rated wind speed, power and shaft speed consistency can be used for ice detection, whereas above rated wind speed, thrust is a more reliable signal for ice detection. The change in aerodynamic properties is bigger than the change in the mechanical properties such as change in mass of the rotor, which means that load imbalance of the rotor under icing is mainly due to change in aerodynamic properties. [60]

Different researchers have studied the effects of the atmospheric ice accretion on the airfoil performance. Most of these investigations have been performed using either ordinary wind tunnel with artificial ice templates attached to the blade profile or icing wind tunnel. However, in the recent few decades, the CFD based numerical techniques have begun to play a significant role in simulating and determining the performance of wind turbines under icing conditions. [55] CFD can provide the economical insight into the details of the multiphase flow physics, which is not easily possible using icing wind tunnel. Icing of the wind turbines and its resulting effects on the power production have been simulated for a variety of cases. [61-64] Bak *et al.* [65] and Ferrer *et al.* [66] utilized custom made CFD models to investigate the wind turbine rotor aerodynamics. Chi *et al.* [67] studied several turbulence models to analyse the flow behaviour around the iced airfoils. Kwon *et al.* [68] and Masoud *et al.* [69] compared the experimental and CFD based numerical results about aerodynamic performance analyses of the iced airfoils. Zhu *et al.* [70] used CFD based numerical approach for determining the drag of the iced airfoils. Virk *et al.* [53, 55, 59] and Etemaddar *et al.* [60] studied the effects of different operating and geometric parameters on ice accretion along the wind turbine blade profiles using CFD based numerical approach.

Ice detection and ice measurements are important not only during the project development phase, but also during the wind park operation. The aim of ice detection is to reliably and automatically detect instrumental and meteorological icing periods along rotor blade and measure its severity and intensity. The requirements of the ice detection technology differences depending on the site, project stage and purpose. Moreover, ice detection may also be used for validating icing maps and meteorological models. [29] Despite existence of variety of techniques used to detect the atmospheric ice accretion on wind turbine, still there is no benchmark method accepted by the wind industry. [71]

2.7.2. Technical Aspects

Icing physics on large wind turbines depends on the number of different parameters, including the operating and geometric parameters. Figure 2.11 shows an overview of the operating and geometric parameters which affect the ice accretion on the wind turbine blades. The following is a general overview of the most relevant aspects.

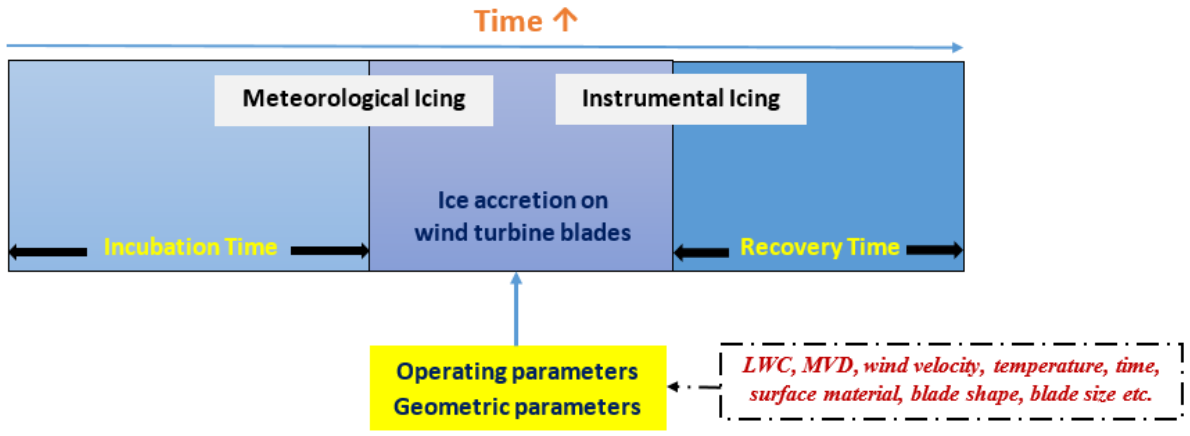

Figure 2.11 – Schematic overview of the operating and geometric parameters affecting the ice accretion on wind turbine blades.

The meteorological icing is defined as the period during which the meteorological conditions (temperature, wind speed, liquid water content, droplet distribution) allow for ice accretion, while the instrumental icing is defined as the period during which the ice is present/visible at a structure and/or a meteorological instrument. Incubation time is the time between the start of meteorological icing and the start of instrumental/rotor icing, dependent on the surface and temperature of the structure. Ice accretion is the period of ice growth (active ice formation) and the period during which the ice remains persistent (no growth and/or ablation). Whereas recovery time is the time duration, during which ice is being removed through ablation and includes melting, erosion, sublimation and shedding of ice. [29]

From the operating parameters, the most important ones are the atmospheric wind speed, rotor RPM, temperature, liquid water content, median volume diameter of the cloud and the droplet spectra, present in the cloud. From the geometric parameters the most important ones are the characteristic length and the cross-sectional area of the object. The maximum icing intensity (mass flux) per some unit of time is a product of the wind speed, cross-sectional area and the liquid water content ($dM/dt = vAw$). The MVD of the cloud and the droplet spectra also play an important role in the icing as the larger droplets, and, as consequence – the cloud spectra having larger value of MVD, tend to collide with the blade more easily. Operating temperature directly influences the thermodynamic balance on the surface, which in turn (depending on the size and speed of the impinging water droplets), determine which type of ice growth will occur – dry or wet, and, as a result determine the type of accreted ice, i.e., soft rime, hard rime or glaze ice.

2.8. Methods of Studying the Atmospheric Ice Accretion on Wind Turbines

Icing on wind turbine can be studied using analytical, numerical and experimental techniques. Following sub-sections will describe an overview of each method used in this Ph.D. work.

2.8.1. Analytical Method

The atmospheric ice accretion process on wind turbines may appear straightforward at first glance; however, a deeper look reveals many layers of complexity in the physical processes involved and serious practical difficulties in the observational, experimental and theoretical aspects of the problem. During the 70's and 80's, many researchers such as Macklin and Payne [72], McComber and Touzot [16],

MacArthur [73], Oleskiw [74], Lozowski, Stallabrass and Hearty [75], Horjen [76], Makkonen [77], Gent and Cansdale [78], and Finstad [79] developed analytical models of ice accretion. Presently, ISO 12494 standard describes the general principles of determining the ice load on structures, but estimation of icing on wind turbines is still a crucial research topic and no analytical model of ice accretion specific for wind turbine has been developed, so far.

Modelling of ice accretion on wind turbines is a complex process that involves airflow simulations, water droplet trajectories calculations, surface thermodynamics and phase changes. The study of water droplet trajectories and their impact on wind turbine blade surface is essential to better understand the mechanism of motion of the water droplets in the air, and their interaction with the blade surface. For many years, the standard analytical reference work on the water droplet trajectories, suspended in an airstream has been the model of Langmuir & Blodgett, developed in 1946 [80]. This was one of the first published treatments of the problem, later Finstad improved on this work in 1986 [79]. The most widely used analytical surface thermodynamic model of the ice accretion process was developed by Messinger in 1953 [81]. Although the Makkonen model [38] for ice accretion is widely being used, it is limited by the fact that it mainly models the ice accretion on circular cylinder shape objects. While it is possible to translate the ice loads from the reference collector to the wind turbine blade, one has to keep in mind that not only the ISO 12494 is limited to circular cylinders (and in the case of airfoil it is parameterized using the leading edge diameter, in order to make it possible to use the ISO 12494 model on it), the ISO 12494 model does not take into account the rotation of the turbine through the domain, and any possible effects caused by it on the ice accretion. The main effect of icing on wind turbine blade is an altered blade profile shape, which results in a change of its aerodynamic characteristics, including a decrease in the toque due to a decrease in the lift coefficient and an increase in the drag coefficient. The change in aerodynamic properties is higher than the change in the mechanical properties such as change in mass of the rotor, due to icing, which means that load imbalance of the rotor under icing is mainly due to change in aerodynamic properties.

The existing ISO 12494 standard is based on the ice accretion on circular cylinder and cannot be used directly as an estimate of ice accretion on rotating wind turbine blades, due to a number of reasons. First and foremost, the analytical formulation for the estimation of the overall collision efficiencies and the accreted ice masses is only really applicable to the geometries conforming to the (rotating) circular cylinder, with “circular” accreted ice shapes, accreted onto it, as a result of continuous, slow rotation around its axis. While it is generally assumed, and as shown by Finstad in her doctoral thesis [79], the analytical formulation can be applied to “non-rotating” circular geometries and accreted ice shapes with small differences in obtained results, compared to the “standard” case of rotating cylinder, this formulation necessitates the (analytical) calculation of impinging droplets trajectories, in order to obtain the distribution of the local collision efficiencies, which, in turn, govern the resultant ice shape. This rather “manual” procedure is considered rather cumbersome. Second, the flow field parameterization in the Finstad (and earlier analytical models), on which ISO 12494 model relies, is a potential flow approximation, characterized by an irrotational velocity field. And lastly, tied to the previous point, it is assumed in the analytical model that the incoming multiphase flow is normal towards the object and two-dimensional. This means, that such finer physical details, which arise in the real airflow around wind turbine blade in three dimensions, are completely ignored in 2D analytical model. For example, due to centrifugal and Coriolis forces the flow in the boundary layer at the root is in spanwise direction, while the flow just outside the layer is chordwise. This effect delays stall, by which much higher lift is achieved compared to two-dimensional data[82]. These factors, combined, make the application of the

ISO 12494 model directly, in order to model the ice accretion of the wind turbines, not a straightforward approach.

In this Ph.D. work a ratio between accreted ice loads on cylinders and wind turbine blade profiles preliminary suggested by the VTT, is used for the analytical modelling of ice accretion on wind turbine blade. [83] There is currently no algorithm, or detailed parametric study, which can translate icing on a cylinder into the icing on a wind turbine blade. [84] As a result, estimation of ice loads using the ISO 12494 standard, while classifying wind park sites, raises some uncertainties in terms of reliable predictions. The ratio between the accreted ice mass on a standard "reference collector" (a *30 mm diameter* × *500 mm* long circular cylinder) and a wind turbine blade in the same weather conditions is represented by the factor *"k"*, which is calculated by dividing the accreted ice mass on the wind turbine blade profile by the ice mass accreted on the reference cylinder. Based upon some preliminary calculations by VTT using TURBICE, an average value of $k = 20$ was obtained [83]. In principle, this means that under the same icing conditions a rotating wind turbine blade collects approximately 20 times more ice per meter than a stationary cylinder "reference collector". This preliminary study needs a detailed parametric study for further validation and refinement. In this Ph.D. work numerical and experimental results are used to further validate and refine this ratio, illustrated in Figure 2.12. In it, the blade as static, fixed and not moving and/or rotating with respect to any reference frame. Instead, the wind turbine hub height value is used in calculations, along with the calculated TSR (in order to obtain the total relative velocity on the blade) value of the blade.

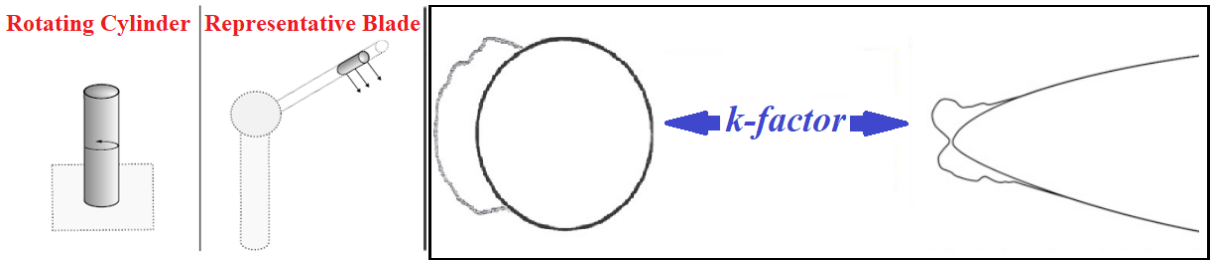

Figure 2.12 – Overview of "k – factor" relation ratio between reference cylinder and airfoil.

2.8.2. Numerical Method

The advanced multiphase CFD numerical simulations have become an important tool for simulating and determining the performance of wind turbine blade profiles under the icing conditions. [85-90] In 2011, Barber *et al.* [91] analysed the ice accretion process on the wind turbine blades and its effects on the turbine performance using both the CFD and the field measurements data, and found that the ice accretion at high altitude sites can cause an AEP lose up to 17%, and the outer section (95 – 100% of the blade length) is the most severely iced. Moreover, Lamaraoui *et al.* [92] found that the majority of power production losses due to atmospheric icing happens at the 80% of the blade extension. Thus, the tip section of the blade is typically used in studying the atmospheric ice accretion and its effects on the wind turbine performance.

The CFD simulations of the atmospheric icing on the wind turbine blades can be performed using both two-dimensional (2D) blade "planes" and three-dimensional (3D) "sections", using either full blade or some section of it. Modern CFD tools such as LEWICE [93-95] and FENSAP-ICE [96, 97] are capable of modelling the icing in both the 2D and the 3D cases, as their main objective is the estimation of the geometry change due to icing. For example, ignoring the rotational effects, Etemaddar *et al.* [60] have

studied the effects of atmospheric and system parameters on the icing simulated with the LEWICE code for different sections along the blade and calculated aerodynamic coefficients using FLUENT, followed by the validation of obtained results against experimental results of NREL 5MW wind turbine. In addition, Switchenko *et al.* [98] have performed a series of 2D and 3D simulations of a complex wind turbine icing events in Canada using the FENSAP-ICE, and compared the results to the available experimental data. Guy *et al.* [99] used CFD technology to simulate the icing process during the rotation of wind turbine blades, and analysed the performance of wind turbine blades after icing. Fu and Farzaneh [100] calculated the two-phase flow of air and water by using Fluent, and simulated the ice shapes and the accreted ice mass of a 3D NREL VI wind turbine operating under the rime ice conditions. Homola *et al.* [55] used CFD to simulate the ice accretion and to compare the aerodynamic performance of NACA64618 airfoil for the clean and the iced cases. Moreover, many researchers developed their own numerical codes, such as Son *et al.* [101] who have carried out a quantitative analysis of ice growth on airfoils simulation.

Numerical modelling of the atmospheric ice accretion mainly includes five modules: grid generation, airflow behaviour simulation, water droplet trajectory calculations, surface thermodynamics and surface mesh displacement after icing, as shown in Figure 2.13.

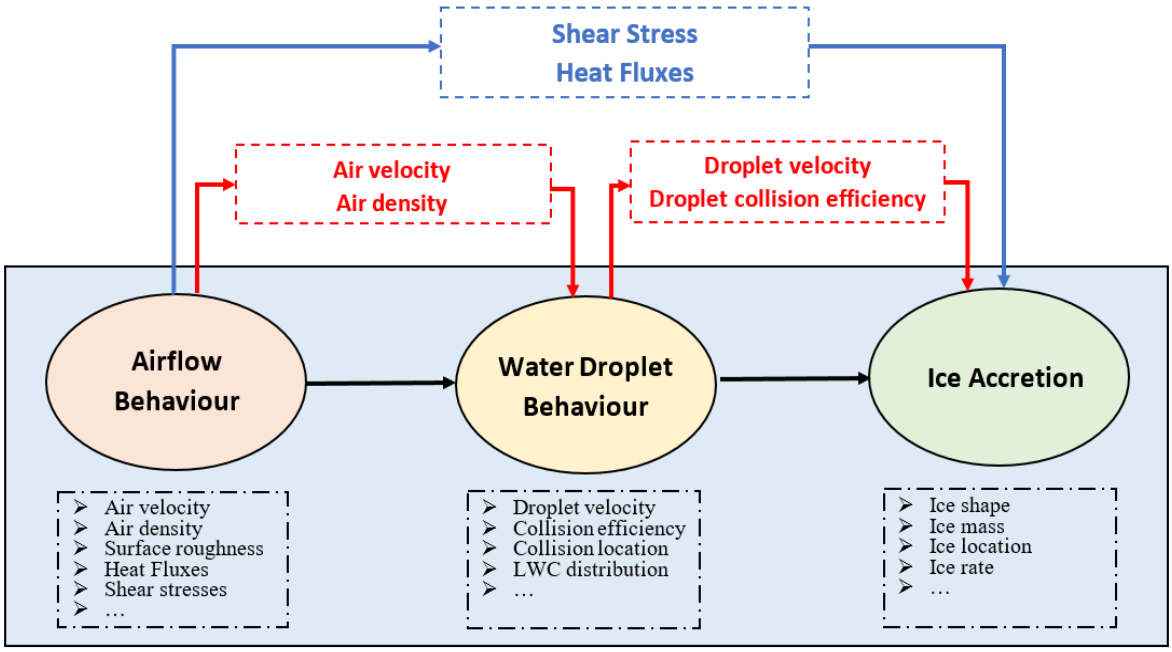

Figure 2.13 – Overview of numerical modelling setup.

A. Airflow Behaviour

The primary parameters of interest in the airflow behaviour are the velocity magnitudes, pressure distributions and heat fluxes. The velocity magnitude distributions will affect the initial "aerodynamic response" of the object, undergoing the atmospheric ice accretion. This is primarily caused by the fluid-structure interaction and the resulting boundary layer response along with the pressure gradients. Strong pressure gradients will indicate the tendency of the boundary layer to "push" the incoming droplets away from the object (such as the wind turbine blade), as the droplets will have to overcome the said pressure gradient in order to collide with the blade first. Moreover, during the continuous ice accretion process, the accreted ice shape will affect the velocity distributions, thus changing the boundary layer response

and flow separation and its behaviour around the wind turbine blade. Primarily, the highly irregular accreted ice shape will increase the drag and reduce the lift, thus making the pressure gradients more adverse. Moreover, such an ice shape can potentially introduce the vorticity forming behind it, which can trap some droplets in it and even can make them collide with the ice shape thus accreting even more complex ice shapes.

Also, the accreted ice will change the distribution of the heat fluxes along the wind turbine blade surface, as the high roughness of accreted ice shape will increase the frictional heating of the air, primarily due to increased skin friction (which is also one of the reasons behind increase of the drag coefficient of the iced blade, as this friction increases the parasitic drag). In the numerical modelling of the ice accretion several equivalent sand-grain roughness models are used, primarily to establish the initial roughness of the wind turbine blade under icing. Generally, for the wind turbine blade profile surface roughness evaluation, two analytical models are mostly being used; *NASA sand-grain roughness model and Shin et al. sand-grain model* [102]. The NASA sand-grain roughness model is computed with an empirical NASA correlation formula for icing, whereas the Shin et al. sand-grain roughness model is a modified the NASA correlation with Shin and Bond correlation formula [96]. These models give an estimate of the initial surface roughness of an order of a several dozen microns. However, the icing roughness due to beading is typically of an order of a fraction of to a several millimeters, thus being at least an order of magnitude higher. This high surface roughness along with the ice shape itself will also change the incoming flow in the significant way, as for the "clean" airfoil it is expected that the incoming flow will be laminar, up to the stagnation point, after which the flow separation will start happening and the flow will become transitional or turbulent. The effects of ice shape and surface roughness will cause the flow to undergo the change from laminar to transitional or turbulent much faster and in a more adverse way, and due to fluid-structure interaction and the boundary layer response and it may even cause the incoming flow to undergo the change from laminar to turbulent to occur a short distance in front of the leading edge. This effect of the surface roughness on the airflow behaviour in the CFD simulations can be both advantageous and disadvantageous. While the main advantage of using the surface roughness model is the possibility of it correctly predicting the laminar-to-turbulent flow transition, its and the surface roughness effects on the resultant ice shape, there lies a similar disadvantage. This disadvantage comes to if the usage of the surface roughness model results in prediction of an incorrect laminar-to-turbulent flow transition in the CFD model. Although it can be fixed, by using the transition equation in the turbulence equation. For example, using the Transition $k - \omega$ SST model, instead of ordinary $k - \omega$ SST model. By extension, it also applies to the heat fluxes on the objects' surface, as they depend on the characteristics of the incoming airflow. In worst-case scenario, the model can incorrectly predict the change from dry to wet ice growth due to increased heat fluxes, associated with the turbulent airflow.

The change in the heat fluxes due to high surface roughness will result in more "heat" available due to frictional heating, in addition to the normal aerodynamic heating, which is counterbalanced by the "cooling" of the surface by a sub-zero temperature in icing events and the loss of heat to the air. The primary interest in studying the heat fluxes on the wind turbine blades in the icing modelling is to answer which type of ice accretion will happen – wet or dry growth. This also has a significant dependence on the impinging droplet sizes, as bigger droplets will take more time to freeze and are more affected by the gravity and airflow forces acting on them. Moreover, air velocity also has a significant impact on the freezing of the water droplets along the surface, as higher wind speeds will result in higher "cooling" heat flux, and thus the droplets will tend to freeze faster. In addition, under wet growth regime the resultant ice type is always a glaze ice which is characterized by its high density and surface roughness.

The reason glaze ice has the maximum possible density from all accretion types is that air bubbles, which can get trapped inside the ice deposit during dry ice growth, will "escape" from the water film while its undergoing cooling and freezing.

B. Water Droplet Behaviour

When it comes to the supercooled droplet behaviour in the multiphase flow, the two primary parameters of interest are the droplet velocity and the droplet size. In general, the incoming droplets follow the airflow streamline perfectly in the far field, however, the closer they become to the object, the more they start to "deviate" from the streamline as their relative Reynolds number starts to increase. Thus, the droplet behaviour is primarily governed by its Reynolds number and droplet's inertia parameter *K*, which shows the "balance" of inertial and drag forces, acting on it.

The "inertia" of the droplet can be estimated using the droplet's inertia parameter, *K*, which is also a definition of Stokes number, and it is defined as:

$$K = \frac{v\rho_d d^2}{18\mu C} \tag{2.5}$$

where v is the wind speed, ρ_d is droplet's density, d is the droplet's diameter, μ is the dynamic viscosity of air and C is the characteristic dimension of the object. As the droplet's inertia parameter directly depends on the particle size as d^2, under the constant operating conditions larger droplets will have significantly higher inertia. Conversely, the droplet's Reynolds number Re_d also depends on the droplet's size as:

$$Re_d = \frac{\rho_a \sqrt{(v-u)^2} d}{\mu} \tag{2.6}$$

where ρ_a is air density and u is the droplet's velocity. Thus, the term under the square root is the relative droplet's velocity with respect to air. However, the droplet's drag coefficient C_D has a non-linear scaling with Re_d, and it tends to decrease as the droplet's Reynolds number increases. For example, FENSAP-ICE uses the following empirical fit for the droplet's drag coefficient:

$$C_D = \left(\frac{24}{Re_d}\right)\left(1 + 0.15 Re_d^{0.687}\right) \quad \text{for} \quad Re_d \leq 1300 \tag{2.7}$$

$$C_D = 0.4 \quad \text{for} \quad Re_d > 1300 \tag{2.8}$$

This parameterization shows that as Re_d increases the drag coefficient C_D will decrease, until it reaches the lower bound of $C_D = 0.4$. The decrease in the droplet's drag will, in turn, decrease the droplet's deceleration, thus allowing them to impinge on the object more easily.

Smaller droplets and/or ones travelling at lower speed will tend to follow the airflow streamlines very closely (perfect advection) and will not collide with the object. On the other hand, bigger droplet and/or travelling at higher velocity, will have more kinetic energy and momentum, and as a result – inertia and will tend to follow more "straight line" trajectories thus more likely colliding with the object. Moreover, when the droplet with a higher inertia approaches the object, it will be less affected by the pressure

gradients and the boundary layer response, as it will require them to exert more “work” on said droplet in order to affect its trajectory in a significant way.

This is the primary reason why typical numerical modelling of the atmospheric ice on structures is carried out using a droplet distribution spectrum. Just as in nature, the different droplet distribution spectra have different proportions of the bigger and smaller droplets, which will be affected by the airflow differently, and the simplified modelling procedures, such as using the monodispersed MVD approximation cannot always effectively resolve the pertaining details, associated with the spectra of droplets sizes.

The droplet component of the multiphase flow primarily affects the local and overall collision efficiencies, the distributions of the local collision efficiencies, impact velocities and the impingement angles. The collision efficiencies show how much of an incoming water flux collides with the object in the first place (the overall collision efficiency) and how this water flux is distributed along the surface of an object (local collision efficiencies and maximum impingement angles). For the dry ice growth, since all droplets freeze on impact, the distribution of the local collision efficiencies and the maximum impingement angles will be exactly corresponding to the accreted ice shape. For the wet ice growth this is not the case, as the water film flow will change the distribution of the impinged water on the surface and can result in the loss of some of it due to runback and evaporation.

The droplet impact velocity primarily influences the accreted ice density in the dry growth regime. Typically, the higher the impact velocities of the droplets are, the higher the accreted ice densities will be, as less air can get trapped inside the ice deposit. Thus, the resultant ice accretion will be a “hard” rime, having density values closer to the glaze ice as opposed to the “soft” rime, which normally results from the ice accretion of smaller droplets, at lower impact velocities and/or at lower surface temperatures.

For the wet ice growth, the droplet impact velocity has primary significance in giving the droplet “initial” velocity, when moving on the surface. Although, its eventual “fate” (freezing or loss due to runback or evaporation) will be the result of heat fluxes and forces, acting on it. Moreover, in such cases, the effects of splashing and bouncing or nucleation can become of an importance, especially for very large droplets, which can act as individual “collectors” thus breaking up to the small droplets which collide with them, or collecting said smaller, unfrozen droplets, when moving across the blade surface.

C. Ice Accretion

For the numerical calculations of the ice accretion, the local water droplet collision efficiencies and the freezing process on the blade surface are usually considered. Two processes [49] of the (ice) mass conservation and the heat transfer, respectively, are given in Equation 2.9 and 2.10:

$$m_{im} + m_{in} = m_{out} + m_{eva} + m_{ice} \tag{2.9}$$

$$Q_{im} + Q_{in} = Q_{out} + Q_{eva} + Q_f + Q_c \tag{2.10}$$

where

m_{im} and Q_{im} are the mass and the heat fluxes of the supercooled water droplets impinging on the turbine blade, m_{in} and Q_{in} are the mass and the heat fluxes of previous water droplets coming into each grid cell,

m_{out} and Q_{out} are the mass and the heat fluxes of water droplets flowing out to the next grid cell, m_{eva} and Q_{eva} are the mass and the heat fluxes of evaporating water droplets, Q_f is the friction heat and Q_c is the convective heat.

In the numerical modelling of the atmospheric ice accretion, the estimations of the water droplets collision efficiency are carried out by simulating the two-phase flow in an either Eulerian or Langrangian framework. The inflowing water droplets are regarded as a continuous term, and the distribution of water droplet in solution domain is reflected by the (local or overall) droplet collision efficiencies. The accreted ice thickness during the time step of each grid is obtained, and the new ice shape needs to be solved for. The ice layer grows along the normal direction of the grid and the ice layer advancement is carried out in the $x-y$ coordinate system. The ice shape along each segment of the blade is respectively calculated and plotted, and finally the sections are connected together to obtain the 3D visualization of the accreted ice shape.

Mesh sensitivity study uses coarse, medium and fine meshes to accurately determine the boundary layer characteristics (shear stresses and heat fluxes). For icing simulations, during mesh sensitivity analysis, the number of mesh elements and the $y+$ value less than 1 for the first cell layer are selected based upon the heat flux calculations, where a numerical check is imposed so that the heat flux computed with the classical formulae dT/dn should be comparable with the heat flux computed with the Gresho's method. Mesh sensitivity study shows that the effect of mesh size on droplet solution is negligible, however air flow quantities including convective heat flux on the blade surface are sensitive to the mesh size. During mesh sensitivity analysis, the first layer thickness is selected for the maximum smooth transition of the inflation layers, and in the case of a 2D airfoil either O-type or C-type structured numerical grid is used, whereas for 3D blade a structured/unstructured numerical grid with the $y+$ value < 1 is used. In addition, this mesh method is unique and can shrink or stretch the grid, which makes it easier to simulate blade profile changes due to ice accretion.

2.8.3. Lab-based Experiments

The icing wind tunnel is an important lab-based experimental approach used to study the icing on wind turbine blade in a controlled environment, where one can study the effect of various operating and geometric parameters on the ice accretion physics. Normally, icing wind tunnels include a spray bar and a cooling system in order to simulate the ice accretion under specific conditions, which include study of the different flow parameters, such as wind speed and turbulence. [29] The amount of ice accretion depends on the liquid water content, wind speed, MVD, droplet distribution and icing time period. The MVD and LWC are two key factors in measurements of icing in the wind tunnel experiment, both of them are critical to the reliability of icing test results from lab-based icing wind tunnel experiments.

2.8.4. Ice Detection and Mitigation Techniques

Ice accretion on wind turbine blades can increase noise emissions, potentially violating the building permit regulations, and ice throw can create a safety hazard for people near the iced turbines, hence the ice throw risks need to be managed and mitigated. Recently, plenty of ice detection and mitigation techniques, borrowed from aviation industry, were improved and applied in the wind turbine industry, including the passive ice protection techniques (hydrophobic/icephobic coating [103-106], the black paint [107] and operational stops [108]) and active ice protection techniques (resistive heaters, hot air injection, microwaves, pneumatic expulsion, ultrasonic waves, and active pitch control) [109]. These techniques can be applied in anti-/de-icing systems, where the anti-icing system is designed to

delay/prevent ice accretion and formation on the wind turbine blades, while the de-icing system goal is to remove the ice accumulation from the blade surfaces.

A. Ice Detection

The aim of ice detection systems/methods is to reliably and automatically detect instrumental and meteorological icing periods, their severity and intensity. The ice detection methods can be divided into two categories: *direct methods and indirect methods*. The direct methods measure changes in weight, reflection characteristics, and electrical or thermal conductivity, caused by the icing. The indirect methods estimate the accreted ice based on the meteorological factors, such as the wind speed, humidity, temperature, and the changes in wind turbine power generation under the icing conditions.

Ice detection and measurements are very important both during the development phase (wind resource assessment) and during the wind park operational phase. In the project development phase, the need to quantify the production losses due to the ice accretion, assess the ice throw and ice chunks, the icing risks and evaluate the need of the ice protection systems is of importance. While in the wind park operational phase, ice detectors can be used for the turbine and the ice protection system to control and to ensure the optimal performance and safety to the people/animals, who live near to the wind park. [29]

B. Ice Mitigation

The difference between the anti-icing and the de-icing methods for wind turbine's ice mitigation is as follows: the former prevents ice from adhering to the blade surface, and the latter removes icing. The specific measures for the anti-icing and the de-icing systems/methods can be divided into passive and active types. The former use the physical properties of the blade surface to eliminate and prevent icing, and the later use the thermal, chemical or pneumatic energy provided by external systems to eliminate and prevent ice coating. [110] Some ice mitigation methods in the aviation field are available, as a reference. [111]

The anti-icing system requires continuous heating to keep the turbine blades above 0 °C to prevent icing, while the de-icing systems require rapid heating to clear the accreted ice. Both methods require a lot of power. Accurate icing detection can effectively reduce the power requirements due to ice melting. In order to reduce the energy consumption, the blade can be divided into multiple heating blocks which are controlled separately. If only the blade tip needs to be equipped with anti-icing and de-icing systems, it can significantly reduce the cost of equipment and energy consumption. [112]

Part II

Research Design and Methodology

3. Methods Used to Study the Atmospheric Ice Accretion

In order to study and better understand the ice accretion on the wind turbine blades and the resultant performance losses, the analytical, numerical and the experimental techniques are used in this Ph.D. work. Following sections give an overview of each technique, used in the scope of this Ph.D. work.

3.1. Design of Experiment

One of the objectives of this Ph.D. work is to better understand the ice accretion on the wind turbine blades and its resultant effects on the aerodynamic performance. In this Ph.D. work, this objective is accomplished using the analytical, the numerical and the experimental techniques. Figure 3.1 gives an overview of the design of experiment which was used to carry out this study.

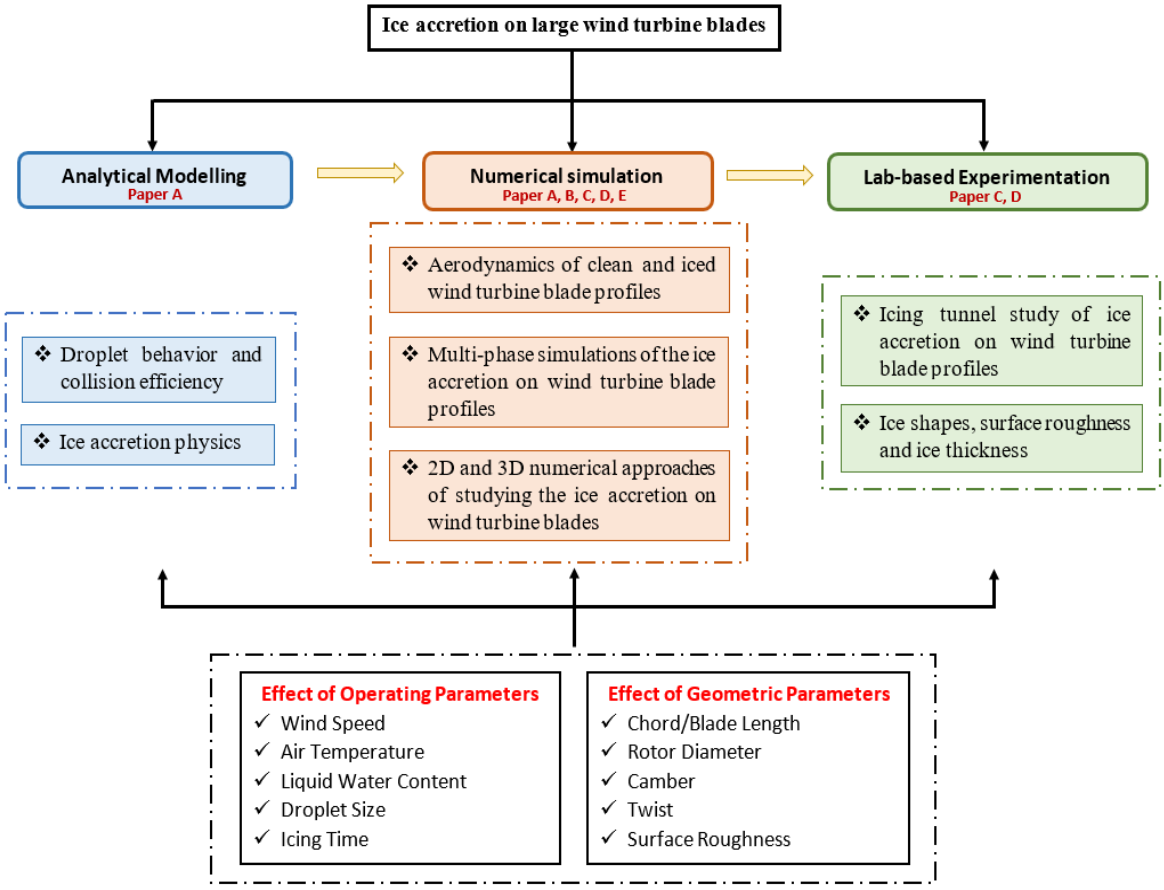

Figure 3.1 – Flowchart of design of experiment used in this study.

3.2. Brief Description of Main Techniques

In this study, three objectives are obtained. The *first* objective is to investigate the aerodynamic performance of the iced blade profiles at high Reynolds numbers ($Re \geq 10^6$). The *second* objective is to use the available icing tunnel experimental data for the validation with the CFD studies using multiple tools, such as ANSYS FENSAP-ICE and ANYSYS FLUENT. *Third*, is to use ISO 12494 analytical model for the purposes of wind turbine applications.

Table 3.1 – Summary of modelling techniques used in each included paper of the Ph.D. project (Part 1).

Techniques	Paper A	Paper B	Paper C	Paper D	Paper E
	2D (airfoil)				*3D (blade)*
Analytical method	√				
Numerical method	√	√	√	√	√
Experimental method			√	√	

3.2.1. Analytical Method

The rate of icing on a structure can be estimated by using the ISO 12494 model, based on expression by Makkonen [38] which is given in Eq. 2.2. This ISO standard is mainly suitable for objects of circular shape and has not been widely used, insofar, for the wind turbine icing applications. The ratio between ice accretion on a rotating wind turbine blade profile and a reference cylinder, known as the *"k–factor"*, which describes the ratio of accreted ice mass on a reference cylinder and wind turbine blade profile. Originally, it was defined by VTT, who proposed the concept of the *k*–factor in the first place, that is the *k*–factor is a constant, with its value being equal to 20 [83]. However, it can vary to significant degree depending on the different geometric and operating parameters.

For the purposes of this Ph.D. work, the effects of blade geometry on the ice accretion, the droplet collision efficiencies, droplet distribution spectra and median volume diameter at different ambient conditions pertaining to the wind speed, as well as tip speed ratios, that can be experienced by both reference cylinder and blade profile are studied. The choice of airfoils has been governed by the need to select a "type" of airfoils having same leading edge radius, thickness and chord length, differing only in the geometric shape and symmetry in order to see if those geometric features have an impact on the *k*–factor or not. The choice of altitude of 10 *m.a.g.l.* is assumed to correspond to the standard mounting height of the reference collector on met mast, as per the ISO 12494 guidelines. The rate of icing on a structure can be calculated according to ISO 12494, based on expression by Makkonen model:

$$\frac{\mathrm{d}M}{\mathrm{d}t} = \alpha_1 \alpha_2 \alpha_3 v A w \tag{3.1}$$

An assumption of "dry ice growth" regime on a reference collector is made in this Ph.D. project, meaning that $\alpha_2 = \alpha_3 = 1$, i.e. all impinging droplets freeze on impact. The overall collision efficiencies and the droplet impingent calculations are carried out in accordance with the Finstad et al. model [113], and are given as:

$$X(K,\phi) = \left[C_{X,1}K^{C_{X,2}}\exp\left(C_{X,3}K^{C_{X,4}}\right) + C_{X,5}\right] - \left[C_{X,6}(\phi - 100)^{C_{X,7}}\right] \times \left[C_{X,8}K^{C_{X,9}}\exp\left(C_{X,10}K^{C_{X,11}}\right) + C_{X,12}\right] \tag{3.2}$$

where X is either the overall collision efficiency E, the stagnation line collision efficiency β_0, the maximum impingement angle α_{max}, or the non-dimensional impact velocity V_0. The constants $C_{X,n}$ are listed in Table 3.2.

Table 3.2 – Coefficient values of cloud impingement parameters [113].

Coefficient	$X = \beta_0$	$X = \alpha_{max}$	$X = E$	$X = V_0$
$C_{X,1}$	1.218	2.433	1.066	1.030
$C_{X,2}$	-6.70×10^{-3}	-4.70×10^{-3}	-6.16×10^{-3}	1.68×10^{-3}
$C_{X,3}$	–0.551	–0.375	–1.103	–0.796
$C_{X,4}$	–0.643	–0.576	–0.688	–0.780
$C_{X,5}$	–0.170	–0.781	–0.028	–0.040
$C_{X,6}$	3.05×10^{-3}	8.50×10^{-3}	6.37×10^{-3}	9.44×10^{-3}
$C_{X,7}$	0.430	0.383	0.381	0.344
$C_{X,8}$	2.220	1.757	3.641	2.657
$C_{X,9}$	–0.450	–0.298	–0.498	–0.519
$C_{X,10}$	–0.767	–0.420	–1.497	–1.060
$C_{X,11}$	–0.806	–0.960	–0.694	–0.842
$C_{X,12}$	–0.068	–0.179	–0.045	–0.029

The collision efficiency, α_1, can be obtained [113] as $X = E$ and filling the constants $C_1 - C_{12}$ from Table 3.2:

$$\alpha_1 = A_1 + C_{X,5} - C_1(B_1 + C_{X,12}) \tag{3.3}$$

where

$$A_1 = C_{X,1}K^{C_{X,2}} \exp\left(C_{X,3}K^{C_{X,4}}\right) \tag{3.4}$$

$$B_1 = C_{X,8}K^{C_{X,9}} \exp\left(C_{X,10}K^{C_{X,11}}\right) \tag{3.5}$$

$$C_1 = C_{X,6}(\varphi - 100)^{C_{X,7}} \tag{3.6}$$

where K is the dimensionless droplet's inertia parameter and φ is the dimensionless Langmuir parameter, respectively, defined as follows:

$$K = \frac{v\rho_d d^2}{18\mu C} \tag{3.7}$$

$$\varphi = \frac{Re^2}{K} \tag{3.8}$$

where v is the wind speed (m/s), ρ_a and ρ_d are densities of air and droplet respectively (kg/m^3), μ is the absolute viscosity of air (μPa·s), d is the droplet diameter (m), Re is droplet's Reynolds number and C is the characteristic length of an object, i.e., cylinder or airfoil (m). When it comes to the estimation of the characteristic length of an object, the typical notion for the cylinder is to use radius, R while for the airfoils the typical notion is to use the leading-edge radius, c as a characteristic length [114, 115]. In other words – the characteristic length of the reference cylinder and blade profile will be the same, provided the cylinder inscribes the leading-edge radius of the airfoil, i.e., $c = R$.

The droplet diameter, *d* is typically a MVD value of a droplet spectrum of a cloud. This is a standard approximation used in the icing studies, first introduced by Langmuir and Blodgett [80] and later verified by Finstad *et al.* [113]. The MVD approximation usage originates from the fact that apart from using a rotating multi-cylinder device, there is currently not many instruments that are capable of measuring the MVD on-site. However, as it has been shown recently [116], the multi-cylinder device may not accurately represent the actual in-cloud distribution using the MVD approximation. Moreover, as noted by Langmuir and Blodgett [80], the different distributions with same MVD will have different collision efficiency, depending on value of inertia parameter, *K*.

As shown in Finstad *et al.* [113], the discrepancy in the overall collision efficiency values between the monodisperse distribution and the actual distribution spectrum under the operating conditions used in that study are typically small enough to be ignored. However, considering vastly different values of the droplet inertia parameter, *K*, for the cylinder and the airfoil, experienced due to the significant differences in the true air speed [5] faced by both the cylinder and the airfoil, it is deemed a reasonable assumption that the differences in the accreted ice mass caused by different distributions at two significantly different values of *K* will be significant. Therefore, in addition to the monodisperse distribution (also referred to as Langmuir A) four progressively wider distributions denoted Langmuir B – E are used in this study. The distributions used in this study and their ratio of diameters, $(d/d_0)^n$ are given in Table 3.3.

Table 3.3 – Langmuir distributions.

LWC fraction	d/d_o **Langmuir B**	$(d/d_o)^{1.5}$ **Langmuir C**	$(d/d_o)^{2.0}$ **Langmuir D**	$(d/d_o)^{2.5}$ **Langmuir E**
0.05	0.56	0.42	0.31	0.23
0.1	0.72	0.61	0.52	0.44
0.2	0.84	0.77	0.71	0.65
0.3	1.00	1.00	1.00	1.00
0.2	1.17	1.26	1.37	1.48
0.1	1.32	1.51	1.74	2.00
0.05	1.49	1.81	2.22	2.71

The overall collision efficiency of the spectrum (spectrum weighted overall collision efficiency) is calculated as:

$$\alpha_1 = \sum w_i \alpha_{1i} \tag{3.9}$$

where α_{1i} is the overall collision efficiency of i^{th} bin and w_i is the LWC fraction of the i^{th} bin. The overall collision efficiency of the i^{th} bin is calculated as in Equations (3.3) – (3.8). Finally, the restriction $\alpha_{1i} = 0.01$ for cases when $K_i \leq 0.17$ is employed, based on Finstad *et al.* [113].

The analytical calculations of cloud impingement on the wind turbine blades follow the same general calculations procedure of the ISO 12494 standard, as presented in this section. However, due to vastly different operating conditions, experienced by the reference collector, mounted on the met mast at 10 *m.a.g.l.* and slowly rotating around its axis, and the rotating wind turbine blade, mounted on the hub at

80 *m.a.g.l.*, for example, some modifications to the calculation procedure of the ISO 12494 model are needed to be done in order to make the results valid for the wind turbine blades.

First, the height factor due to log wind speed profile needs to be taken into the account, as stated in the ISO 12494 standard, section 6.4, page 9 [39]. The height factor accounts for wind speed profile variation due to planetary boundary layer, surface roughness and viscous friction effects between air and surface in planetary boundary layer. This is a relatively well-known phenomenon and is accounted for in governing ISO standard, ISO 12494: "*Atmospheric icing of structures*".

Figure 3.2 shows a typical multiplying factor for ice masses at higher levels above terrain (not above sea level). The factor may be applied for all types of ice, if site-specific data are not available, but reality may in some cases be more complicated than Figure 3.2 shows. The height effect can be expressed also by specifying different ice classes for different levels of a high structure, e.g. mast, towers, ski-lifts, etc. [39].

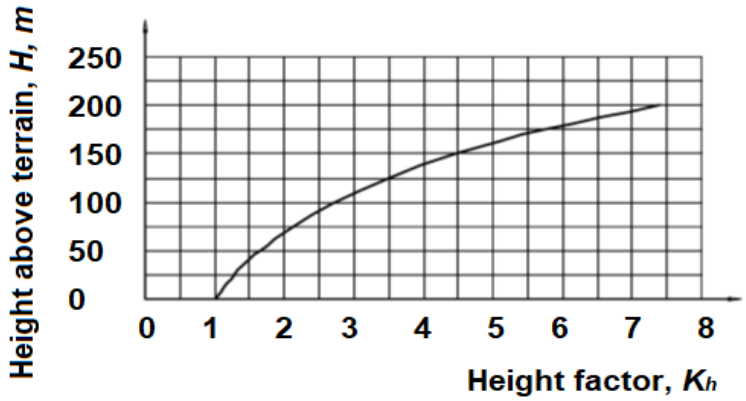

Figure 3.2 – Height Factor from ISO 12494. [39]

The height factor x is defined as:

$$x = e^{0.01H} \tag{3.10}$$

where H is the height above ground level (m). *Second*, is the tip speed ratio (TSR), λ, which is defined as the ratio of the speed of the rotor tip to the free stream wind speed:

$$\lambda = \frac{V}{v} = \frac{\omega R}{v} \tag{3.11}$$

where v is free stream wind speed (m/s), V is the rotor tip speed (m/s), R is the rotor radius (m) and ω is the blade rotational velocity (rad/s). The rotor TSR depends on the blade profile used, the number of blades and the type of wind turbine. In general, three bladed HAWT wind turbines operate at a TSR values between 6 and 8, with 7 being the most typically used value. *Third*, with the values of the height factor and the TSR, the true air speed (TAS), experienced by the rotating blade, needs to be calculated as:

$$V = \sqrt{(xv)^2 + (R\omega)^2} \tag{3.12}$$

where x is height factor, v is freestream velocity, R is the radial distance (for example, at 85% section from blade root) and ω is rotational velocity of the blade in rad/s. *Lastly*, as the ISO 12494 analytical model is only really applicable to the circular sections, the characteristic length C of the blade should be chosen as such, that it is possible to be represented by a circular geometry. For this purpose, the leading edge radius of the blade is used (for example, at 85% section) and thus the cross-sectional area of the object in the "Makkonen model" becomes:

$$A = 2CL = DL \tag{3.13}$$

where C is the leading edge radius, D is the leading edge diameter and L is some length in z-direction. Thus, with these modifications, the "Makkonen model" equation becomes:

$$\frac{\mathrm{d}M}{\mathrm{d}t} = \alpha_1\alpha_2\alpha_3 vAw = 2\alpha_1\alpha_2\alpha_3\sqrt{(xv)^2 + (r\omega)^2}CLw \tag{3.14}$$

and the calculations of the overall collision efficiency α_1 are then carried out as described in this section, with the TAS value used as the operating wind speed.

3.2.2. Numerical Method

Different from the existing numerical codes for the simulations of the atmospheric ice accretion, such as the LEWICE and the CANICE, which were developed strictly for aviation with redundant features analyses, the ANSYS FENSAP-ICE is a robust advanced multiphase flow CFD tool with the second generation, state-of-the-art CFD icing code capable of simulating the icing on wind turbine blades for both 2D and 3D domains. Within the scope of this Ph.D. project, the numerical simulations were carried out in order to study the airflow and droplet behaviour, as well as the resultant ice accretions, using the ANSYS FEMSAP-ICE. Figure 3.3 illustrates the flowchart of multiphase flow calculation for both the single- and the multi-shot simulation approaches used in the coupled FENSAP-DROP3D-ICE3D solvers. As ice grows, the geometric profile of the iced airfoil changes which, in turn, changes the flow of air and water droplets around it. Two approaches are used for icing simulations; *1) single-shot, & 2) multi-shot*:

1) Single-shot: In this approach, the total time of ice accretion is simulated in one shot, meaning that the entire duration of the "icing event" is resolved within one CFD simulation. Thus, the continuous ice accretion, the accreted ice shapes and the changes in those shapes and their influence on the incoming multiphase flow are disregarded. This is the main disadvantage of this method. However, its primary advantages are the numerical robustness and inexpensiveness.
2) Multi-shot: Contrary to the single-shot approach, the ice accretion "event" is split into several steps, called "shots", thus giving the name to this method. Each individual "shot", operates on the same basic principles as a single-shot approach, however, at the end of each shot the accreted ice shapes are being exported to be used as the starting geometry for the next shot in the multi-shot method. The primary advantage of this method is that the continuous ice accretion and the accumulated shapes now do make an impact on the following shots and the end results. Thus, this method is more "physically complete". The disadvantages are certain numerical expensiveness of this method when compared to the single shot and the necessity the re-generate the computational grid after each shot. When using the automatic remeshing tools this may result in the deterioration of the quality of the computational grid, more so for the later shots. In the end, the deteriorating mesh quality can lead to the erroneous results and/or abortion of the simulations due to errors. Therefore, for the complex

ice shapes, manual re-meshing maybe required in order to continue the multi-shot process when using automatic mesh displacement.

Icing simulation results presented in the Papers A, B, C and E are based on the single-shot simulations, whereas results presented in Paper D are based on the multi-shot simulations. For the single shot simulations, both the 2D and 3D results with different airfoils, geometries and operating conditions are used for ice shapes comparison, and how they affect the airflow behaviour and the associated aerodynamic losses. For Paper D, the aim is to focus on the accurate and realistic comparison with the icing tunnel experimental data.

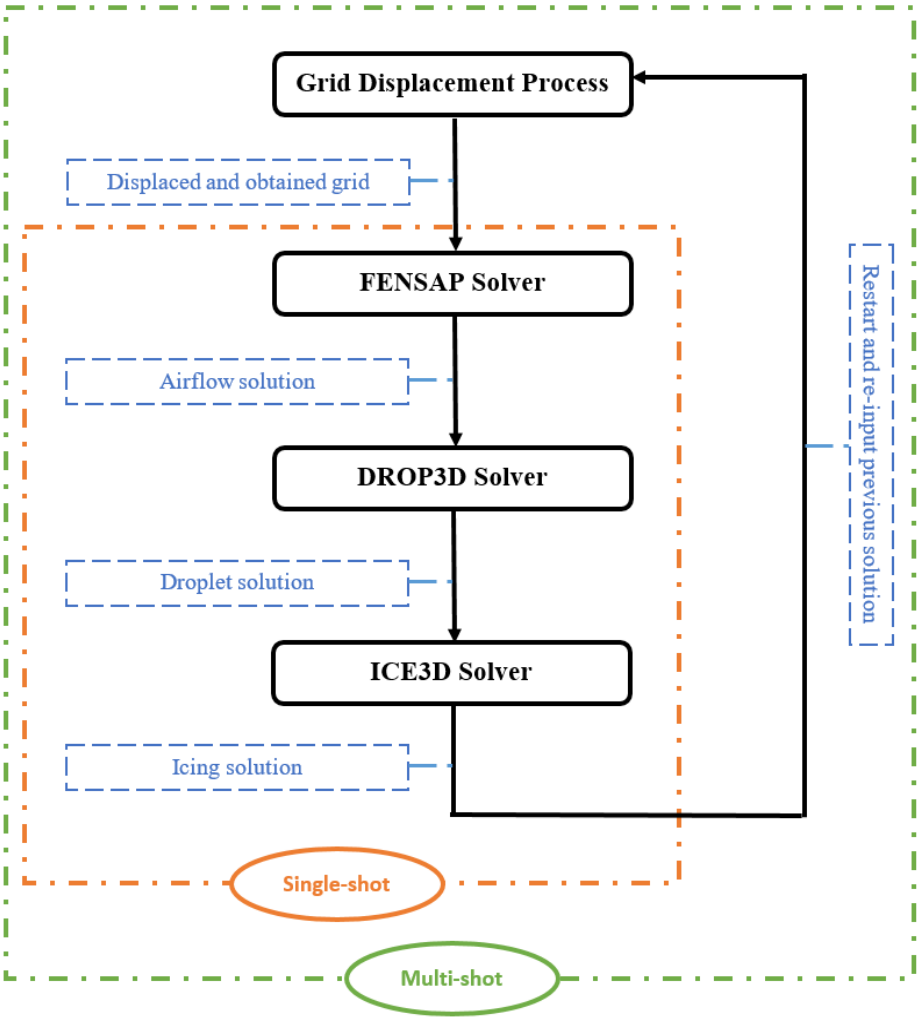

Figure 3.3 – Process flowchart of the ANSYS FENSAP-ICE multiphase simulations.

Atmospheric ice accretion on the wind turbine blades can be numerically simulated by the means of integrated thermo-fluid dynamic models, which involve the air flow simulations, droplet behaviour, surface thermodynamics and phase changes. Following sub-sections provide an overview of each process used in the numerical modelling of icing during this Ph.D. work.

A. Airflow Model

Airflow behaviour is simulated by solving the nonlinear partial differential equations for the conservation of mass, momentum and energy:

$$\frac{\partial \rho_\alpha}{\partial t} + \vec{\nabla}\left(\rho_\alpha \overrightarrow{v_\alpha}\right) = 0 \tag{3.15}$$

$$\frac{\partial \rho_\alpha \overrightarrow{v_\alpha}}{\partial t} + \vec{\nabla}\left(\rho_\alpha \overrightarrow{v_\alpha}\ \overrightarrow{v_\alpha}\right) = \vec{\nabla}\cdot\sigma^{ij} + \boldsymbol{\rho_\alpha}\,\vec{g} \tag{3.16}$$

$$\frac{\partial \rho_\alpha E_\alpha}{\partial t} + \vec{\nabla}\left(\rho_\alpha \overrightarrow{v_\alpha} H_\alpha\right) = \vec{\nabla}\left(\kappa_\alpha\left(\vec{\nabla}\, T_\alpha\right) + v_i \tau^{ij}\right) + \boldsymbol{\rho_\alpha}\,\vec{g}\,\overrightarrow{v_\alpha} \tag{3.17}$$

where ρ is the density of air, v is the velocity vector, and the subscript α refers to the air solution, T refers to the air static temperature in Kelvin, σ^{ij} is the stress tensor and E and H are the total initial energy and enthalpy, respectively.

Airflow through wind turbine is recognized as viscous flow, which can be simulated using the Navier-Stokes equations, and the Equation (3.16), in which the σ^{ij} is the stress tensor, can be described using a set of nonlinear equations, shown here in vector form:

$$\sigma^{ij} = -\delta^{ij} p_a + \mu_a\left[\delta^{jk}\nabla_k v^i + \delta^{ik}\nabla_k v^j - \delta^{ij}\nabla_k v^k\right] = -\delta^{ij} p_a + \tau^{ij} \tag{3.18}$$

$$\tau^{ij} = \mu_a\left[\delta^{jk}\nabla_k v^i + \delta^{ik}\nabla_k v^j - \delta^{ij}\nabla_k v^k\right] \tag{3.19}$$

where p_a is the static pressure and μ_a is the dynamic viscosity.

Turbulence modelling means the formulation of the mathematical relationships required to obtain solutions of the averaged equations of motion. Averaging is necessary because the time-dependent Navier-Stokes equation cannot be solved analytically, and the range of scales occurring in turbulence limits the possibility of numerical solution by supercomputer to simple flow geometries and low Reynolds Numbers. The averaged momentum equations derived by Reynolds do not form a closed set because they contain new terms in the form of the Reynolds stresses, $-\rho\overline{u_i}\overline{u_j}$. Additional equations must be devised to close the system by relating the new terms to known variables. At the lowest level of closure, the $\overline{u_i}\overline{u_j}$ are related to the mean rate of strain through the definition of an "eddy viscosity" analogous to the molecular viscosity of laminar flow. In the simplest models the eddy viscosity is determined from a "mixing length", l, specified at every point in the flow field. One-equation models obtain the intensity of the turbulent velocity fluctuations from a modelled equation for the quantity $k \equiv \overline{u_i}\overline{u_i}/2$, the turbulent kinetic energy per unit mass, but are still limited by their reliance on a specified length scale. This limitation is removed by the introduction of a second modelled equation from which a length scale L can be calculated. Of many such proposals the equation for the rate of turbulent energy dissipation $\varepsilon \equiv k^{3/2}/L$ has gained wide acceptance and the $k - \varepsilon$ model may be regarded as the standard method at the present time.

From its inception by Boussinesq, it has been argued that the eddy viscosity concept is wrong in principle and its limitations have motivated the development of Reynolds-stress-transport models, or second-order closures, in which the $\overline{u_i}\overline{u_j}$ are obtained from their own modelled equations and the eddy-viscosity idea appears only in relating the triple products $\overline{u_i}\overline{u_j}\overline{u_k}$ to the gradients of $\overline{u_i}\overline{u_j}$.

In large-eddy simulations (LES, or sub-grid-scale modelling), only the small-scale motion is modelled. The simulations are performed on grids coarser than those used for direct numerical simulations (DNS),

where the number of nodes needed to discretize all scales increases roughly as the cube of the Reynolds number. Even the low-Re direct simulations currently being attempted require some hundreds of hours of supercomputer time. In addition, specific challenges in the field of atmospheric icing of wind turbines with LES and DNS methods are as follows. For the LES simulations the choice of time step used depends on the problem in question. However, the general rule is that the time step chosen is small enough to satisfy the Courant–Friedrichs–Lewy condition (CFL number) in such a way that CFL is less than 1. This is done is order to preserve the "physicality" of the CFD solution. In practice, it means that the time steps chosen are of an order of a fraction of second (additionally shortened due to additional practice of dividing the time step further by a number of iterations per time step to perform for convergence purposes). Thus, for common icing event (e.g. in this Ph.D. work the icing event duration of 30 minutes is typically used), it means that LES simulations are unpractically time consuming. The problem is further exacerbated with the DNS simulations, as the amount of floating point operations, needed to resolve the DNS flow scales as Re^3. To the best of authors knowledge, the highest resolved DNS simulations had *Re* value 8×10^5 [117]. Even those required the specialized code and supercomputer time. For the practical applications of icing of wind turbines, the operating *Re* number is typically of an order of $10^6 - 10^7$, which makes them prohibitively expensive to run using DNS.

From the vast range of currently available turbulence models, the FENSAP uses the following: Spalart-Allmaras; $k-\omega$ SST; low-Re $k-\omega$; and laminar flow based on the Euler equation. The latter two models are disregarded, as they are deemed to be not applicable to the problems in this thesis, based on the operating values of the Reynolds number used in this work. Out of the remaining models the Spalart-Allmaras is used predominantly for the simple aerodynamic flows, with "predictable" flow separation and in absence of any prominent wake effects, such as extensive vorticity. The $k-\omega$ SST model is used for all other flows. While it is possible to couple FENSAP to Fluent solver and vice-versa, the additional turbulence models, available in Fluent are not used in this work. The remaining models in Fluent can be classified as Scale-Adaptive Simulations (SAS), consisting of Detached Eddy Simulations (DES), Blended Eddy Simulations (BES), Large Eddy Simulations (LES) and their "shielded" variants. These are not used based on the discussion in the previous paragraph.

The other available models in Fluent are the Reynolds Stress Model (RSM) and family of $k-\varepsilon$ models and original $k-\omega$ model. The RSM is not used primarily due to its computational cost, compared to the rest of available RANS models, sensitivity to the operating conditions and numerical stiffness. The $k-\varepsilon$ model as well as the original $k-\omega$ model are not used, as the author deems the $k-\omega$ SST model to be superior to them. The SST $k-\omega$ turbulence model [118] is a two-equation eddy-viscosity model which has become very popular. The shear stress transport (SST) formulation combines the best of $k-\omega$. and $k-\varepsilon$ models. The use of a $k-\omega$ formulation in the inner parts of the boundary layer makes the model directly usable all the way down to the wall through the viscous sub-layer, hence the SST $k-\omega$ model can be used as a Low-Re turbulence model without any extra damping functions. The SST formulation also switches to a $k-\varepsilon$ behaviour in the free-stream and thereby avoids the common $k-\omega$ problem that the model is too sensitive to the inlet free-stream turbulence properties. The SST $k-\omega$ model has a good merit it for its good behaviour in adverse pressure gradients and separating flow. The SST $k-\omega$ model does produce a bit too large turbulence levels in regions with large normal strain, e.g., stagnation regions and regions with strong acceleration. This tendency is much less pronounced than with a normal $k-\varepsilon$ model though.

One of the most challenges for the airflow simulation is the laminar-turbulent transition. Considering the required accuracy of the CFD simulations and need to decrease the needed CPU time, two Reynolds Average Navier-Stokes (RANS) turbulence models were implemented in FENSAP: classical one-equation (eddy-viscosity) Spalart-Allmaras (SA) turbulence model and two equation (turbulence kinetic energy and eddy dissipation rate) k – ω SST turbulence model, furthermore, a transition model is available for both of them. For SA model, free transition is captured based on adverse pressure gradients. Whereas the k – ω SST model uses one equation local correlation-based intermittency transition mode. [96] In general, order of accuracy determines how accurate the solution is. The main disadvantage of using higher order schemes is convergence, potential issues with numerical stiffness and the oscillation of values around some point.

The SA turbulence model based on the transport of a modified eddy viscosity $\tilde{\nu}$, from which the effective eddy viscosity coefficient ν_T is computed. The modified eddy viscosity is related to the effective eddy viscosity:

$$\nu_T = \tilde{\nu} f_{\nu} \tag{3.20}$$

where f_{ν} is defined as:

$$f_{\nu} = \frac{\chi^3}{\chi^3 + c_{\nu}^3} \tag{3.21}$$

where χ is quotient of modified eddy viscosity $\tilde{\nu}$ to laminar kinematic viscosity ν. The eddy/laminar viscosity ratio is used to compute the initial turbulent viscosity coefficient when starting the calculation. For external flow calculations, and if the incoming flow is not turbulent, this parameter should be set to a low (but not zero) value, for example: 10^{-5}.

The k – ω SST turbulence model based on the k – ω with shear stress transport (SST) uses the transport of the turbulent kinetic energy k, and the second transported scalar ω which can be interpreted as a frequency because of its dimension equivalent to reciprocal of time. The eddy/laminar viscosity ratio is used to compute the initial turbulent viscosity coefficient when starting the calculation. For external flow calculations, and if the incoming flow is not turbulent, this parameter should be set to a low (but not zero) value, for example: 1.

Another challenge for the airflow simulation during the process of ice accretion is surface roughness changes. Surface roughness change affects the shear stresses and heat fluxes, which effects the ice accretion in rate and shape. During the process of ice accretion, the blade profile surface roughness leads to changes in the boundary layer growth, which influences the droplet sticking efficiency and the heat transfer. [119]

For example, for a smooth airfoil at low Mach number, transition of the boundary layer usually occurs as a result of the development of Tollmein – Schlichting waves. These linear waves breakdown into nonlinear three-dimensional instabilities and finally form turbulent spots that coalesce to form a turbulent boundary layer. This process takes a finite distance to develop from the initial growth of the Tollmein – Schlichting waves to a fully developed turbulent boundary layer. The introduction of surface roughness into the preceding processes can greatly enhance certain growth regimes or bypass others altogether [119].

There are three types of simulated roughness generally considered: a two-dimensional isolated roughness such as a spanwise two-dimensional trip, an isolated three-dimensional element such as a hemisphere or circular cylinder, and distributed roughness that can include grit or large numbers of densely packed hemispheres or cylinders. The effects of roughness are dependent upon its relative height in the boundary layer. Usually roughness heights are nondimensionalized by the displacement thickness k/δ_* or a roughness Reynolds number Re_k [119].

The sand grain roughness for the iced surface is calculated using Shin *et al.* [102] roughness model:

$$k_s = k_{sNASA}\left[\frac{(k_s/c)}{(k_s/c)_{base}}\right]_{\text{MVD}} \tag{3.22}$$

where the extra factor correlated with droplet mean diameter (MVD, in microns) is:

$$\left[\frac{(k_s/c)}{(k_s/c)_{base}}\right]_{\text{MVD}} = \begin{cases} 1, & \text{MVD} \le 20 \\ 1.667 - 0.0333(\text{MVD}), & \text{MVD} \ge 20 \end{cases} \tag{3.23}$$

Whereas the corresponding value of NASA sand-grain roughness model [98] is obtained with:

$$k_{sNASA} = 0.6839\left[\frac{(k_s/c)}{(k_s/c)_{\text{base}}}\right]_{\text{LWC}}\left[\frac{(k_s/c)}{(k_s/c)_{base}}\right]_{T_s} \left[\frac{(k_s/c)}{(k_s/c)_{base}}\right]_{V}(k_s/c)_{base}c \tag{3.24}$$

where the extra factor correlated with water droplet content (LWC, in g/m^3), surface temperature (T_s, in Kelvin) and free stream velocity (V, in m/s) is correlated with basepoint [102]:

$$\left[\frac{(k_s/c)}{(k_s/c)_{base}}\right]_{\text{LWC}} = 0.5714 + 0.2457(\text{LWC}) + 1.2571(\text{LWC})^2 \tag{3.25}$$

$$\left[\frac{(k_s/c)}{(k_s/c)_{base}}\right]_{T_s} = 0.047(T_s) - 11.27 \tag{3.26}$$

$$\left[\frac{(k_s/c)}{(k_s/c)_{base}}\right]_{V} = 0.04286 + 0.0044139(V_\infty) \tag{3.27}$$

$$(k_s/c)_{base} = 0.001177 \tag{3.28}$$

B. Droplet Impingement Model

DROP3D solves the two-phase flow (air and water droplets) using the Eulerian approach, where the super cooled water droplets are assumed to be spherical. The Eulerian two-phase fluid model consists of the Navier-Stokes equation with the water droplets continuity and momentum equation. The water droplet drag coefficient is based on the empirical correlation for the flow around the spherical droplets described by Clift *et al.* [120]:

$$\frac{\partial \alpha}{\partial t} + \vec{\nabla}\left(\alpha \overrightarrow{V_d}\right) = 0 \tag{3.29}$$

$$\frac{\partial(\alpha\overrightarrow{V_d})}{\partial t} + \vec{\nabla}[\alpha\overrightarrow{V_d} \otimes \overrightarrow{V_d}] = \frac{C_D Re_d}{24K}\alpha(\overrightarrow{V_a} - \overrightarrow{V_d}) + \alpha\left(1 - \frac{\rho_a}{\rho_d}\right)\frac{1}{Fr^2} \tag{3.30}$$

where α is the water volume fraction, v_a and v_d is the airflow and droplet velocity respectively, C_D is the droplet drag coefficient and Fr is the Froude number. The first term on the right-hand-side of the momentum equation represents the drag acting on droplets of mean diameter d. It is proportional to the relative droplet velocity, its drag coefficient C_D and the droplets Reynolds number:

$$Re_d = \frac{\rho_a d V_{a,\infty} \left\| \overrightarrow{V_a} - \overrightarrow{V_d} \right\|}{\mu_a} \tag{3.31}$$

and an inertia parameter:

$$K = \frac{\rho_d d^2 V_{a,\infty}}{18 C \mu_a} \tag{3.32}$$

Where C is the characteristic length of the object, and second term represents buoyancy and gravity forces and is proportional to the local Froude number:

$$Fr = \frac{\left\| V_{a,\infty} \right\|}{\sqrt{Cg}} \tag{3.33}$$

These governing equations describe the same physical droplets phenomenon as Lagrangian particle tracking approach. The droplet drag coefficient is based on an empirical correlation for flow around spherical droplets, or:

$$C_D = \left(\frac{24}{Re_d}\right)(1 + 0.15 Re_d^{0.687}) \quad \text{for} \quad Re_d \leq 1300 \tag{3.34}$$

$$C_D = 0.4 \quad \text{for} \quad Re_d > 1300 \tag{3.35}$$

The local and overall collision efficiencies are calculated as follows:

$$\beta = -\frac{\alpha\overrightarrow{V_d}\cdot\vec{n}}{wV} \tag{3.36}$$

where α is the local volume fraction (kg/m^3) and $\vec{n}$ is the surface normal vector. The overall collision efficiency is an integration of local collision efficiencies over surface area and is given as:

$$\beta_{tot} = \frac{\int \beta \, dA}{L_\infty^2} \tag{3.37}$$

Therefore, in addition to the monodisperse distribution (also referred to as Langmuir A) four progressively wider distributions denoted Langmuir B – E and one custom distribution, built from the data of CU icing tunnel, are used in this study.

C. Thermodynamic and Ice Accretion Model

Surface thermodynamics is calculated using the mass (Equation (3.38)) and energy (Equation (3.39)) conservation equations, considering the heat flux due to convective and evaporative cooling, heat of fusion, viscous and kinetic heating:

$$\rho_f \left[\frac{\partial h_f}{\partial t} + \vec{\nabla}\left(\overline{V}_f h_f\right) \right] = V_\infty \mathrm{LWC}\beta - \dot{m}_{evap} - \dot{m}_{ice} \tag{3.38}$$

Equation (3.39) expresses the conservation of energy:

$$\rho_f \left[\frac{\partial\, h_f c_f \dot{T}_f}{\partial\, t} + \dot{\nabla}\left(\partial\, h_f c_f \dot{T}_f\right) \right] = \left[c_f\left(\tilde{T}_\infty - \tilde{T}_f\right) + \frac{\|\vec{V}_d\|^2}{2} \right] V_\infty \mathrm{LWC}\beta - L_{evap}\dot{m}_{evap} +$$
$$\left(L_{fusion} - c_s\tilde{T}\right)\dot{m}_{ice} + \sigma\varepsilon\left(T_\infty^4\right) - T_f^4 - c_h\left(\tilde{T}_f - \tilde{T}_{ice,rec}\right) + Q_{anti\text{-}icing} \tag{3.39}$$

The coefficients ρ_f, c_f, c_s, σ, ε, L_{evap}, L_{fusion} are physical properties of the fluid. The reference conditions $\tilde{T}_\infty$, V_∞, LWC are the airflow and droplets parameters. Equation (3.40) shows the Jones (glaze) [121] formula (in g/cm^3):

$$\rho_s = \begin{cases} 0.21 R_M^{\,0.53}, & R_M < 10 \\ R_M/(1.15R_M + 2.94), & 10 \le R_M \le 60 \\ 0.84, & R_M \ge 60 \end{cases} \tag{3.40}$$

where R_M is the Macklin parameter, defined as:

$$R_M = \frac{d\|\vec{V}_d\|}{2\tilde{T}_{wall}} \tag{3.41}$$

d is the droplet diameter in microns, $\vec{V}_d$ is the droplet impact velocity (m/s) and $\tilde{T}_{wall}$ is the wall temperature (Celsius). This approach adds the grid speed terms to the Navier-Stokes equations to account for the mesh velocity. [122]

FENSAP-ICE computes heat fluxes in two different manners: one is *Classical*, which is based on temperature gradients on the boundary. The other one is *Gresho*, which is based on Gresho's Consistent Galerkin formulation. The Jones (glaze) ice density model is mainly used in the FENSAP–ICE, while the Jones (rime) ice model is used to solve the special cases in which the reference stagnation temperature is well below freezing point (no water runback), and the ice accretion can be simplified with only the classical heat flux.

FENSAP-ICE has the choice of the following empirical accreted icing density parameterizations: constant (ρ_{ice} = 917 kg/m^3); Macklin (in reality, it follows the Makkonen and Stalalbrass fit to the Macklin equation); "intermediate" version of the Jones empirical icing density parameterization (using the Macklin parameter with the values of constants given in Equation (3.40)); and the "final" version of the Jones parameterization (dubbed Jones (rime)). According to Jones [121], the "intermediate" icing density parameterization accounts for 50% of explained variance using the Mt. Washington Observatory data, while the "final" version of Jones parameterization covers 70% of icing density variance.

The issue with the Jones (rime) parameterization is that it tends to overestimate the accreted icing densities if used with any Langmuir distribution over the monodispersed distribution and changing the source distribution will increase the value of the droplet's inertia parameter *K*, with which this parameterization works directly [123, 124]. When comparing the Macklin (as this model is called in the FENSAP–ICE) analytical icing density parameterization and the Jones (glaze) parameterization, the latter was developed using data from the Mt. Washington Observatory, over the icing wind tunnel data in "Macklin" parameterization. As a result, the author of this work thinks that the former represents the accretions in natural conditions better, and as shown by Sokolov and Virk [124] it produces the better agreement with the experimental data when tested using the results from the Cranfield University experiments.

FENSAP-ICE can output the resultant aerodynamic force acting on the airfoil/blade profile surfaces, which can be decomposed into the lift (*L*) and drag (*D*) forces as follows:

$$L = \frac{1}{2}\rho_a V^2 A C_L \tag{3.42}$$

$$D = \frac{1}{2}\rho_a V^2 A C_D \tag{3.43}$$

where ρ_a is the air density and *A* is the area, which for the 2D cases is equal to the chord length. Moreover, the pressure coefficient C_P distribution is obtained at the selected locations in the 2D and the 3D simulations, and the pressure coefficient is given as:

$$C_p = \frac{p - p_\infty}{\frac{1}{2}\rho_\infty V_\infty^{\,2}} = \frac{p - p_\infty}{p_0 - p_\infty} \tag{3.44}$$

Within this Ph.D. work, several numerical case studies were carried out in order to better understand the effect of varying the blade profile types, domain meshes, turbulence models, surface roughness, droplet distributions and ice densities during icing along different blade profiles at rime and glaze ice conditions. The setup chosen for the numerical modelling in each paper (Paper A, B, C, D and E) is described in Table 3.4.

Table 3.4 – Summary of numerical modelling techniques used in each included paper of the Ph.D. project (Part 1).

Setup		**Paper A**	**Paper B**	**Paper C**	**Paper D**	**Paper E**
		2D (airfoil)				***3D (blade)***
Mesh generation	Structured C type	√	√	√		√
	Structured O type				√	
	Unstructured tetrahedral					√
Turbulence model	SA		√			
	$k-\omega$ SST	√		√	√	√
Surface roughness model	NASA	√	√			
	Shin. et. al.			√	√	√
Droplet distribution model	Langmuir A	√	√			
	Langmuir B	√	√			
	Langmuir C	√	√			
	Langmuir D	√	√			√
	Langmuir E	√	√			
	Custom (CU)			√	√	
Ice density model	Glaze	√	√	√	√	√
	Rime		√	√	√	√

3.2.3. Experimental Method

Experimental investigation of the atmospheric ice accretion on large wind turbine blades can give a unique, hands-on and valuable experience with phenomena and issues that are difficult to investigate in full-scale field measurement. The experimental study in this Ph.D. project is carried out at the icing tunnel laboratory of Cranfield University (CU), U.K. During the experimental runs the values for the pressure, air velocity and temperature in the plenum of the icing tunnel were constantly monitored and recorded. Subsequent analysis of this data has showed that these operating parameters (pressure, air velocity and temperature) didn't fluctuate by more than ±1% from the nominal (operating) values, prescribed in the experimental test matrix. Figure 3.4 shows four different wind turbine blade profiles (listed in Table 3.5) that are used, and Figure 3.5 illustrates the schematic overview of the experimental setup used in CU icing tunnel. Each profile used for icing tunnel experiments in this Ph.D. work has different geometric and aerodynamic features and is suitable for different wind turbine blade's sections, from the inner (root) to the outer (tip). S819 is a thick family airfoil and it is used for 10 to 20 meter long stall-regulated wind turbine blades, S826 and S832 are designed for the mid-scale size wind turbines with variable speed and pitch, and DU96-W-180 is a low-speed airfoil with a thickness-to-length ratio of 0.18. The surfaces of these profiles are made of galvanized steel (VGAL.V.D×SID+Z275) with average surface roughness of 1 μm. Icing tunnel facility at CU has a test section size of 761×761 mm and it can create realistic icing conditions for MVD ranging from 15 to 80 μm, LWC in the range of 0.05 – 3 g/m^3 and air temperature from –30 to +30 °C.

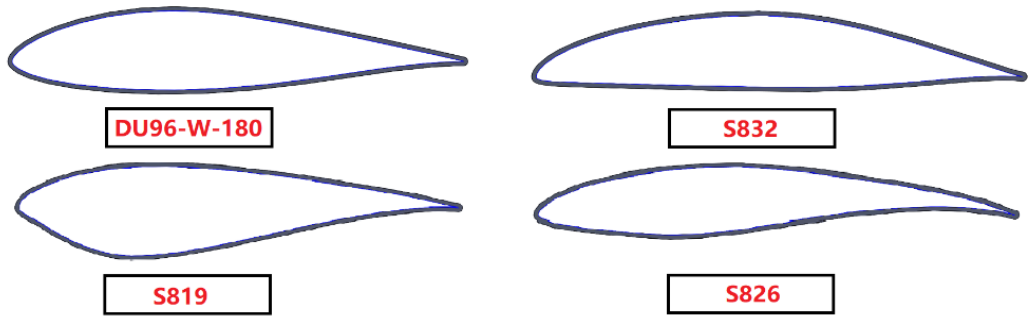

Figure 3.4 – Wind turbine blade profiles used in this study (cross sectional view).

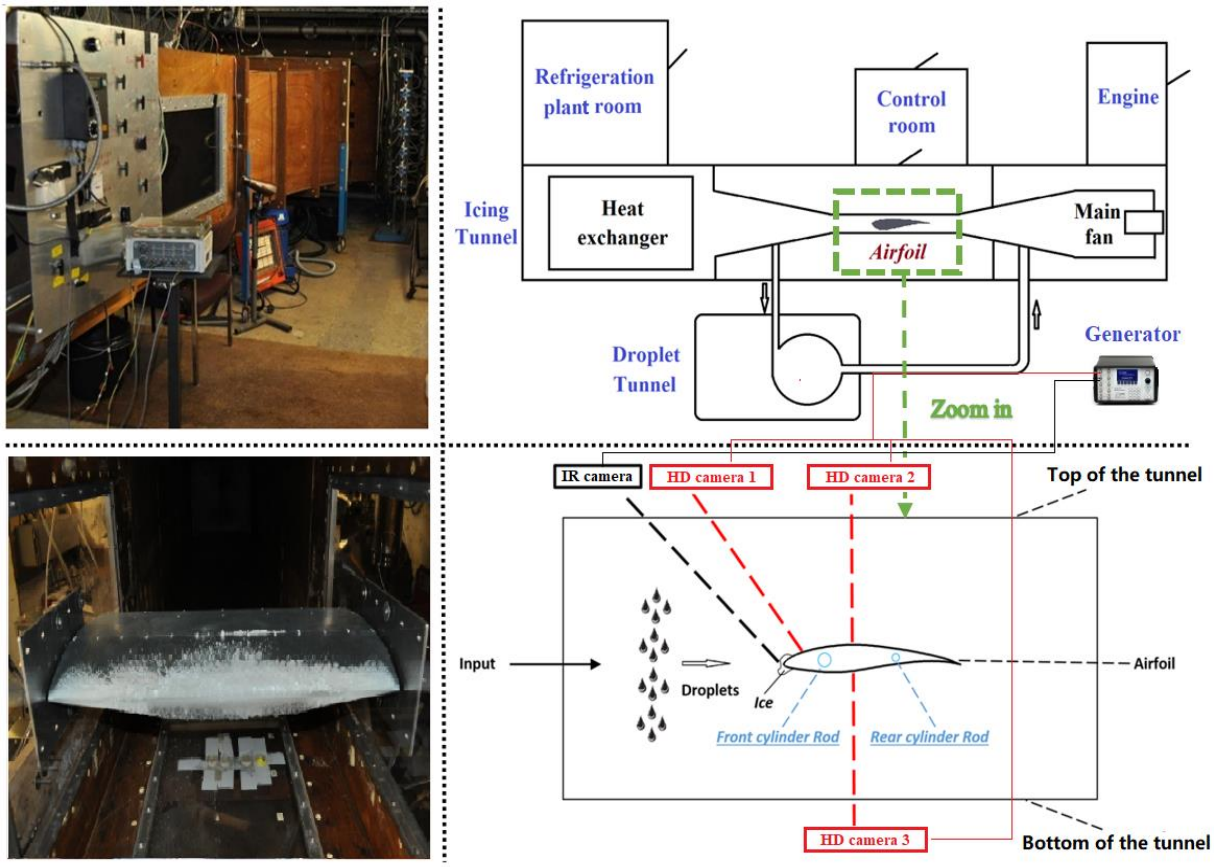

Figure 3.5 – Schematic view of the CU icing tunnel experimental setup.

In order to closely monitor the ice accretion along each profile, three High Definition (HD) cameras were used for video recording and pictures were taking during ice accretion process. One long wavelength thermal infrared camera (IR: FLIR A615) was used. Seven different experiments were carried out at fixed *Re* of 3×10^6 for both dry (rime) and wet (glaze) ice conditions.

The geometric and operating conditions that were chosen for the experimental modelling in each paper (Paper C and D) are shown in Table 3.5.

Table 3.5 – Summary of the experimental modelling techniques used in this Ph.D. project.

Paper	Blade Profile	Test	Ice Type	Air Velocity (m/s)	Temp (°C)	LWC (g/m^3)	MVD (μm)	AOA (°)	Icing duration (mins)
-	**S819**	1	Glaze	77	–5	0.6	20	0	15
		2	Rime	72	–15				
C	**S826**	3	Glaze	77	–5	0.35			
		4	Rime	70	–20				
	S832	5	Glaze	77	–5				
		6	Rime	70	–20				
D	**DU96**	7	Glaze	77	–5				
		8	Rime	70	–20				

4. Methods of Wind Resource Assessment in Ice Prone Regions

In order to better understand the scientific methods used for the wind park operations in icing conditions, it is necessary to study the wind resource assessment in icing conditions. In this Ph.D. work, the wind resource assessment study is carried out using the field measurement data (SCADA), along with the statistical model (T19IceLossMethod – Task19) and the CFD based numerical techniques.

4.1. Design of Experiment

During the planning phase, it is necessary to obtain an estimate of the expected power production from the planned wind park site to determine the project economy and feasibility. If icing occurs at the selected site then the power curve will be reduced during the operating period as long as the icing persists on the wind turbine, which may affect the further wind park operation and maintenance. The research work conducted in this Ph.D. project is aimed to develop an improved understanding of the icing effects on the wind resource assessment of the wind park through the comparison of the field measurements, statistical and numerical models. The flowchart of the design of the experiment of this study is shown in Figure 4.1.

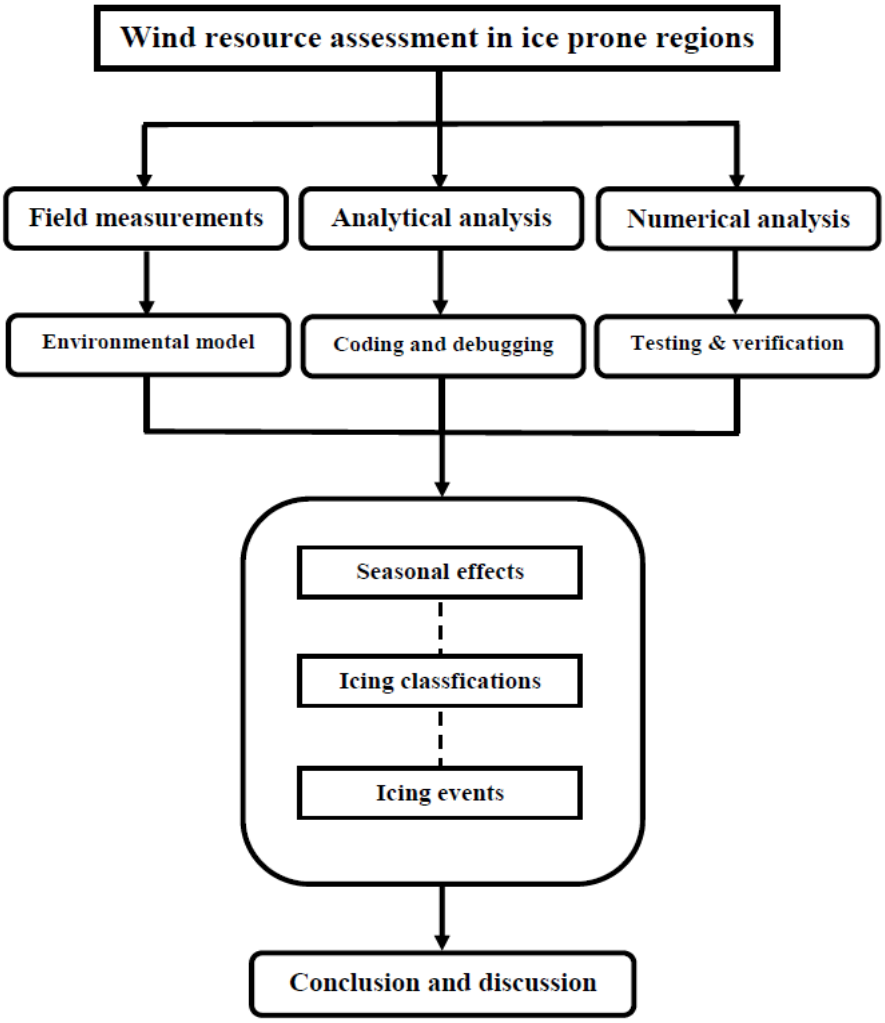

Figure 4.1 – Design of experiment used for the wind resource assessment study.

4.2. Brief Description of Main Techniques

Table 4.1 gives a summary of the modelling techniques used with respect to the included paper in this chapter.

Table 4.1 – Summary of modelling techniques used in paper F (Part 2).

Techniques	Paper F
Field measurements	√
Statistical method	√
Numerical method	√

4.2.1. Field Measurements

The wind park used for study in this Ph.D. project consists of 14 wind turbines which are manufactured by Simens-23-93VS, located at an average elevation of a 400 *m.a.s.l.* in the mountainous arctic region of Norway. The wind turbine rotor diameter is 90 m with 80 m hub height and the annual production capability of the wind park is 104.2 GWh. By using quality control, three years (2013 – 2015) of SCADA data from all wind turbines is collected and sorted. This SCADA data mainly includes wind speed, temperature, direction and power production. Technical details of wind turbines are specified in Table 4.2 and Figure 4.2 shows the terrain/location of the wind park.

Table 4.2 –Technical details of wind turbines.

Turbine Manufacturer	Siemens-23-93VS	Max Production Capacity	104.2 GWh
Tower Height	80 m	Nacelle Weight	83 tons
Rotor Diameter	90 m	Tower Weight	158 tons
Rotor Area	6361 m^2	Rotor Weight	60 tons
Production Speed	3 – 25 m/s	Total Weight	300 tons

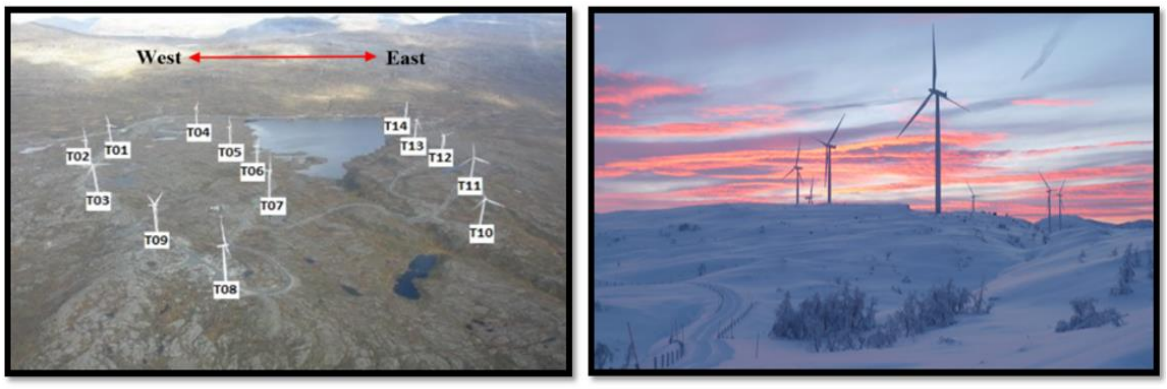

Figure 4.2 – Overview of the wind park site during summer and winter time.

SCADA data system is not only a system of data acquisition and monitoring, but also is a computer based system which allows for a complete process control and automation. By implementing the data acquisition, equipment control, data measurement, parameter adjustment and various signal alarms, it can monitor and control the wind turbine operation. Figure 4.3 shows a schematic overview of the design of experiment used for the field measurements.

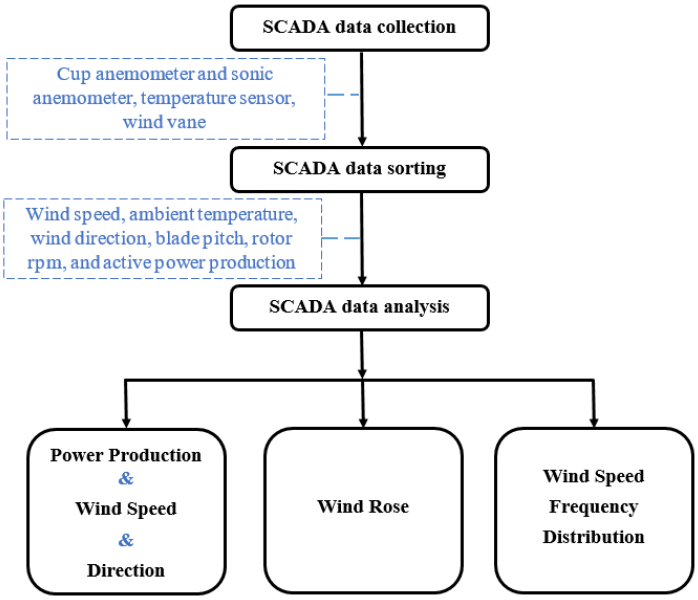

Figure 4.3 – Schematic overview of the design of experiment used for field measurements.

4.2.2. Statistical Method

Wind energy in CC region refers to such sites where the ambient temperatures are below the operational limits of standard working wind turbines, or may experience frequent icing events, or both. [29] Icing can have an adverse effect on wind turbine power production, but this can also be used to detect icing by monitoring the wind turbine power production. The general idea is to compare the power output of a wind turbine operating in icing conditions to a power curve measured in clean, uniced conditions. This Ph.D. work is carried out by using a generic method of detecting icing from a power curve following the IEA Wind Task 19 standardized open-source Python code model: T19IceLossMethod [45]. Figure 4.4 illustrates the flowchart of the ice loss estimation model.

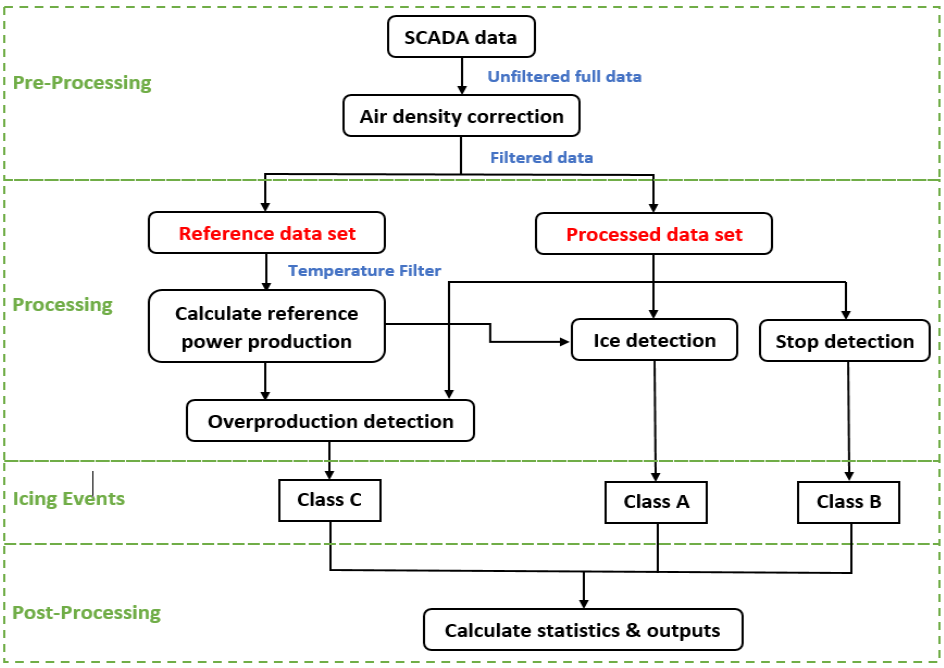

Figure 4.4 – Flowchart of T19IceLossMethod simulation. [45]

The main goal of using the T19IceLossMethod is to minimize the required inputs and to create a solution that would not require any external measurements, such as ice detectors. The ice detection follows the step-by-step process as used in this Ph.D. project: pre-process filtering, process computing, icing events detection and post-processing calculation, as described in following sub-sections A to D.

A. Pre-process Filtering

The first step in pre-process filtering is to clean the input SCADA dataset, such that the time steps of turbine operating in a fault state are removed from the data, if such timestamps are available. This is necessary as these fault states can cause positive detections when the ice detection code is running. However, if the fault state data is unavailable, it will consider each step that happens in icing conditions to be caused by icing. Having the fault log available helps filter out the stops which are caused by unrelated causes and improve the estimation of power loss due to icing.

The second step in pre-process filtering is correlation of air density with the wind speed, in order to compensate for changes in air density caused by temperature differences between summer and winter seasons. This corrected wind speed is then used for all processing steps afterwards.

B. Process Computing

In order to detect the production losses, a baseline needs to be established first. Icing event is defined as a period of time when the output power of the wind turbine is below a set limit in cold temperature. These limits are calculated from a subset of data where temperatures are high enough so that it is reasonable to assume that there is very little icing.

Using only the subset of data above a set threshold temperature (e.g. +1°C), a reference power curve is computed. The data is binned according to a pre-set distribution according to both wind speed and direction. Then for each bin we calculated:

1. Median power in the bin, used to estimate theoretical production of an ideal turbine not affected by icing.
2. 10th percentile of power production (P10 limit). Used as trigger limit for ice detection.
3. 90th percentile of power production (P90 limit). Used as trigger limit for detecting apparent overproduction.
4. Standard deviation of power within the bin, used to estimate the power curve uncertainty.
5. Sample count within the bin. This is monitored to make sure that the sample count in each bin is high enough to be representative.

C. Icing Events Detection

The Task 19 method classifies icing events into three categories based on the behaviour of the wind turbine: reduced power production due to icing, wind turbine stoppage caused by icing, and apparent overproduction. This categorization relies on certain assumptions that are further described below. The detection method has a certain amount of uncertainty, especially when using this kind of approach to estimate the icing frequency on site, since the method only considers icing events that have a large enough impact on the output power. It is also sensitive to the accuracy of the wind speed and temperature measurements. Bias, or other errors in either of them, will affect the results of the ice loss method. However, due to the limitation of the automatic icing detection for all data below the P10 limit some additional checks are performed in order to ensure that this cannot be a false positive Class A icing event.

First category of icing events is reduced power production due to icing, named **Class A**. The production losses are caused by the degraded aerodynamics of the blade profile due to ice accretion. It is assumed that the turbine needs to operate normally without any known fault states, that the output power is below the 10^{th} percentile of the reference power curve continuously for 30 minutes or longer, and that the temperature is below the threshold limit. When all of these applied at the same time it is assumed that reduced power production is caused by the blade icing. The threshold limit is usually set +1 °C to compensate for possible bias in nacelle temperature measurements.

Second category of icing events is wind turbine stoppage caused by icing, named **Class B**. The decreased lift and increased drag, caused by the ice accretion on wind turbine blade, which might cause the wind turbine to stop at a higher wind speed than normal conditions. Meanwhile, the ice accretion on wind turbine blade increases the cut-in speed for the same reason. This will increase turbine standstill time and will lead to large power production losses. A stop is defined as a moment when the wind turbine output power is below a set threshold. If turbine stops during an icing event, it is assumed that the icing event is considered to be a contributing factor to the stop. An icing induced stop is assumed to have ended once turbine output power is above the icing alarm limit once again.

Third category of icing events is due to apparent overproduction, named **Class C**. In some cases, wind turbine seems to be producing more power than expected. This can happen if, for example, an anemometer is experiencing icing. An iced cup anemometer will show lower wind speeds than what the actual wind speeds are. This in turn will result in apparent overproduction in SCADA. It is assumed, similar to the Class A, and unlike in the case of reduced production, the effects of overproduction events in the electricity production of the turbine cannot really be estimated from SCADA data alone. These events are still flagged in the data but the production is taken as-is.

D. Post-processing Calculations

After the power curve has been created, the entire original dataset is compared to the calculated reference power curve. Each individual data point is then flagged as an icing event if it meets the criteria for an icing event. After this, a set of statistics is calculated for the entire dataset and the icing events are classified into three categories. The results show both the energy based availability and time based availability.

4.2.3. Numerical Method

Different from the mesoscale models, such as Weather Research and Forecasting (WRF) model in which it is hard to capture and simulate the flow separation, caused by wind flow over steep slopes and ridges, the CFD based wind resource assessment can provide improved agreement with the field measurements, when compared with analytical models. In this Ph.D. project, the work has been carried out using the 3D terrain model of the wind park and by solving the Reynolds Averaged Naiver–Stokes equations (RANS) using WindSim, where the wind park domain is discretized using structured grid. The energy equation is neglected during this study, as temperature is assumed to be constant in the region close to the ground surface. Therefore, the exchange of heat and water vapour at the Earth's surface is neglected. In order to account for surface roughness in the numerical simulations the Wieringa's classification is used[125]. Re-Normalization Group (RNG) − based $k - \varepsilon$ turbulence model is used due to its better agreement with the flow profiles and length of the separated flow region [125]. The detailed setup is shown in Table 4.3.

Table 4.3 – Solver setting for CFD simulations.

Height of boundary layer (m)	500.0
Speed above boundary layer (m/s)	10.0
Boundary condition at the top	Fixed pressure
Potential temperature	No
Turbulence model	RNG $k - \varepsilon$

The default value of terrain surface roughness height is read from the grid file in WindSim, or, alternatively, a constant roughness height can also be imposed in the model by specifying a non-zero value for the roughness height. The roughness height is used in the log-law velocity profile, given in Equation (4.1):

$$\frac{u}{u^*} = \frac{1}{\kappa} \ln \frac{z}{z_0} \tag{4.1}$$

where u is the wind velocity; u* is the friction velocity, κ is von Kármán constant (κ = 0.435, [126]); z is the coordinate in vertical direction; z_0 is the roughness height. Wind park digital terrain layout used for the CFD simulations is shown in Figure 4.5.

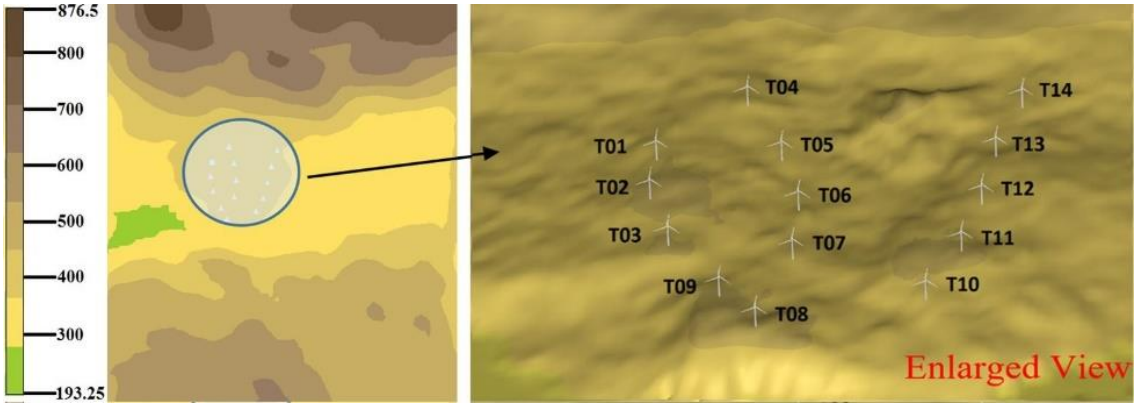

Figure 4.5 – Digital terrain (m) of wind park layout.

In this Ph.D. project, the wind park terrain corresponds to mesoscale topology of the region around the wind park. The areas selected for the wind flow simulations are the sections that involve different sizes in the direction of the flow, to determine the influence of the natural formation of the region on the wind profile. Estimation of latitudinal and longitudinal extension of the domain is quite important because the wind behaviour will be directly affected by the surface shape, following the mass and momentum conservation equations. For a fixed latitude range that cover the top of the mountain, and a more flatter area to the south, three different territorial domains, based on the variation of the starting point of the domain in the longitudinal direction are tested in this numerical study. Mesh sensitivity analysis is carried out, where a final refined mesh is placed in the center of the domain and the cell distribution is uniform within the refined area with an increasing cell size towards the borders with cell resolution of 28 m is selected for the numerical study. Figure 4.6 shows the refined mesh used for this study, the information about the grid spacing and cells is given in Table 4.4.

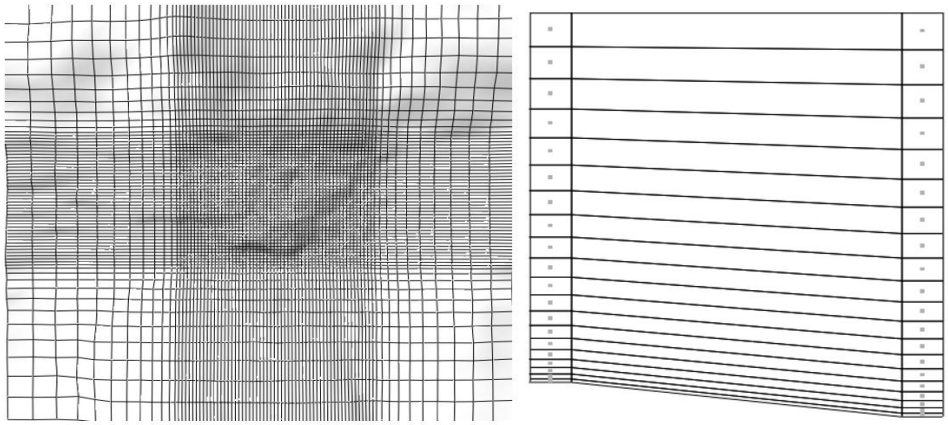

Figure 4.6 – Horizontal layers (left) and vertical layers (right) of the 3D model, used for grid generation.

Table 4.4 – Gird Spacing and cells.

	East	**North**	***Z***	**Total**
Grid spacing (m)	61.8-454.8	61.0-439.0	Variable	-
Number of cells	78	64	20	99840

Three different wake loss models, *1) Jensen et al.; 2) Larsen et al.; 3) Ishihara et al.* [127, 128] are used for this study. These wake loss models are based on calculating the normalized velocity deficit, δv, given as:

$$\delta v = \frac{V - v}{V} \tag{4.2}$$

Where, V is the free stream velocity, and v is air velocity at some point after the turbine rotor. All wake loss models are rotational axisymmetric along the x-axis.

Part III

Results and Contributions

5. Results

In this chapter, the summary of the Ph.D. project' results and contributions is presented via a list of the research publications, together with the potential application of this Ph.D. work, as follows from the main findings and contributions.

5.1. List of Publications

This Ph.D. thesis includes six scientific articles which are published and/or under review in international scientific journals. With the exception of Paper E which is published in an open access journal, all other papers are published in traditional journals and also self-archived at the UiT institutional repository: Munin. In addition, some of the results are also presented at various international conferences including International Conference on Material Engineering and Application (ICMEA 2017), IEEE International Conference on Power and Renewable Energy (ICPRE 2017), International Workshop on Atmospheric Icing of Structures (IWAIS 2017 & 2019), International Conference on Renewable Energy and Environment (ICREE 2018), International Conference on Electrical Engineering and Green Energy (CEEGE 2020), International Conference on Energy and Power Engineering (EPE 2020). In total, the author of this Ph.D. thesis successfully published ***16 peer reviewed scientific papers*** during her Ph.D. period.

This thesis includes preprints of following six scientific papers:

Appendix A: Sokolov, P. Jin, J. Y. and Virk, M. S. *Accreted ice mass ratio (k-factor) for rotating wind turbine blade profile and circular cylinder*. Wind Energy, 2018, 22 (4), DOI: 10.1002/we.2298.

Appendix B: Jin, J. Y. and Virk, M. S. *Study of ice accretion along symmetric and asymmetric airfoils*. Journal of Wind Engineering and Industrial Aerodynamics, 2018, 179, Pp: 240 – 249, DOI: 10.1016/j.jweia.2018.06.004.

Appendix C: Jin, J. Y. and Virk, M. S. *Experimental study of ice accretion on S826 & S832 wind turbine blade profiles*. Cold Regions Science and Technology, 2019, 169, DOI: 10.1016/j.coldregions.2019.102913.

Appendix D: Jin, J. Y. and Virk, M. S. *Study of ice accretion and icing effects on aerodynamic characteristics of DU96 wind turbine blade profile*. Cold Regions Science and Technology, 2019, 160, Pp: 119 – 127, DOI: 10.1016/j.coldregions.2019.01.011.

Appendix E: Jin, J. Y. Virk, M. S. Hu Q. Jiang X. L. *Study of Ice Accretion on Horizontal Axis Wind Turbine Blade using 2D and 3D Numerical Approach*. IEEE Access, 2020, 8, Pp: 166236 – 166245, DOI: 10.1109/ACCESS.2020.3022458.

Appendix F: Jin, J. Y. Karlsson, T. and Virk, M. S. *Wind Turbine Ice Detection Using AEP Loss Method – A Case Study*. Submitted (Under Review), 2021.

In addition to the above mentioned six papers, the following scientific works are related to this thesis:

Paper 1: Sokolov, P. Jin, J. Y. and Virk, M. S. *On the empirical k-factor in ice accretion on wind turbines: A numerical study*. IEEE International Conference on Power and Renewable Energy (ICPRE), 2017, DOI: 10.1109/ICPRE.2017.8390570.

Paper 2: Jin, J. Y. and Virk, M. S. *SCADA data analysis of wind farm in cold climate regions*. Proceedings – Int. Workshop on Atmospheric Icing of Structures (IWAIS), 2017.

Paper 3: Jin, J. Y. Sokolov P. and Virk, M. S. *Wind Resource Assessment in Cold Regions – A Numerical Case Study*. Applied Mechanics and Materials, 2018, 875, Pp: 94 – 99, DOI: 10.4028/www.scientific.net/AMM.875.94.

Paper 4: Jin, J. Y. and Virk, M. S. *Seasonal weather effects on wind power production in cold regions-a case study*. International Journal of Smart Grid and Clean Energy, 2019, 8 (1), Pp: 31 – 37, DOI: 10.12720/sgce.8.1.31 – 37.

Paper 5: Jin, J. Y. Blæsterdalen T. and Virk, M. S. *Icing events assessment of a wind park in high wind speed*. International Journal of Smart Grid and Clean Energy, 2019, 8 (3), Pp: 276 – 281, DOI: 10.12720/sgce.8.3.276 – 281.

Paper 6: Jin, J. Y. and Virk, M. S. *Ice Accretion on Wind Turbine Blade – An Experimental Study of S819 Airfoil*. Proceedings – Int. Workshop on Atmospheric Icing of Structures (IWAIS), 2019.

Paper 7: Yousuf A. Jin, J. Y. Sokolov P. and Virk, M. S. *Study of ice accretion on wind turbine blade profiles using thermal infrared imaging*. Wind Engineering, 2020, 00(0), Pp: 1 – 12, DOI: 10.1177/0309524X20933948.

Paper 8: Jin, J. Y. and Virk, M. S. *Effect of Wind Turbine Blade Profile Surface Roughness on Ice Accretion – A Numerical Case Study*. Cold Regions Science and Technology, 2019, 169, DOI: 10.1016/j.coldregions.2019.102913.

Paper 9: Jin, J. Y. and Virk, M. S. *Effect of Wind Turbine Blade Profile Surface Roughness on Ice Accretion – A Numerical Case Study*. International Conference on Energy and Power Engineering (EPE), 2020, 603 (012045), DOI: 10.1088/1755-1315/603/1/012045.

Paper 10: Jin, J. Y. Karlsson, T. and Virk, M. S. *Wind Resource Assessment using double anemometry method of a Wind Park.* Working paper, 2021.

5.2. Applications of the Ph.D. Work

Table 5.1 illustrates the contribution of the Ph.D. student to the main papers in this Ph.D. project. The topics are reviewed from two perspectives these being the intellectual input and implementation. Then further sub-topics are identified as conceptualization, data curation, formal analysis, investigation, methodology, resources, software, visualization, validation and paper writing.

Table 5.1 – Contribution of the Ph.D. candidate to the papers in the Ph.D. thesis.

Topic	Paper A	Paper B	Paper C	Paper D	Paper E	Paper F
Conceptualization	√	√	√	√	√	√
Data curation	√	√	√	√	√	√
Formal analysis		√	√	√	√	√
Investigation		√	√	√	√	√
Methodology	√	√	√	√	√	√
Resources	√	√	√	√	√	√
Software	√	√	√	√	√	√
Visualization	√	√	√	√	√	√
Validation	√	√	√	√	√	√
Paper Writing		√	√	√	√	√

The structure of the included papers in this Ph.D. project is shown in Figure 5.1, where it can be seen that the papers can be categorized into two groups with different focus: *partial and global*, which uses the state-of-the-art technologies capable of simulating the 2D airfoil, 3D blades, and the wind park icing prediction for a variety of applications. The first group consists of Papers A – E. The Paper A concerns itself with the implementation of ISO 12494 for wind turbine applications, whereas the primary goal in Papers B – E is to develop a better understanding of atmospheric ice accretion physics on the wind turbine blades, and to improve the understanding of large wind turbines aerodynamics under icing conditions. The second group contains Paper F in which the wind park resource assessment is carried out, for the purposes of estimation of wind energy production and wind resource assessment in ice prone cold climate regions. The main findings and contributions for each individual paper are presented in next chapter.

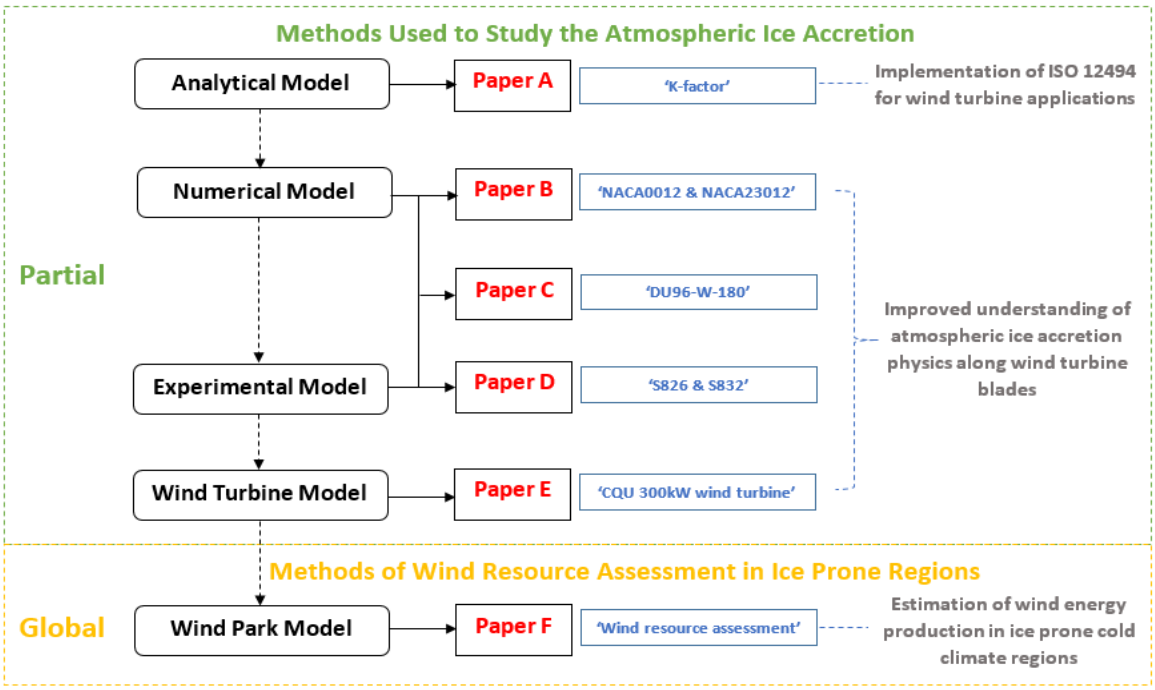

Figure 5.1 – Overview of the included papers in this Ph.D. project.

6. Contributions

In this chapter, the summary of the previously listed papers A to F with focus on the main findings of the Ph.D. project is presented.

Paper A – Accreted ice mass ratio (*k* – factor) for rotating wind turbine blade profile and circular cylinder

In this paper, the investigation into *k*-factor, describing the ratio of ice accretion on reference collector and wind turbine blade profiles, has been carried out by performing a series of numerical simulations using modern CFD software and analytical calculations within the framework of the existing ice accretion theory (ISO 12494). The results show that the *k*-factor is not equal to constant 20, contrary to currently postulated assumption and can vary to a significant degree, depending on a number of different parameters not accounted in present model for it. While the results presented in this paper can be considered somewhat simplistic, the explanation of the *k*-factor variance is established based on effects of MVD, droplet distribution, TSRs, and geometry effects.

Paper B – Study of ice accretion along symmetric and asymmetric airfoils

In this paper, a parametric numerical study of ice accretion on the symmetric and asymmetric airfoils is carried out at different operating and geometric conditions using the CFD based numerical technique. Parametric analysis of ice accretion at different operating and geometric conditions show an increase in the ice growth with the increase in air velocity and droplet size, whereas a change in the atmospheric temperature significantly affects the ice shapes. A significant decrease in accreted ice mass and thickness is observed with the increase of airfoil geometric size. Results show that the airfoil shape has an effect on the rate and shape of the ice accretion. Streamline ice shapes are observed in case of symmetric airfoil compared to asymmetric airfoil. Aerodynamic performance of the iced airfoils decreases as compared to the clean airfoil. The results show that the blade's profile geometric shape affects the ice accretions. More streamlined ice shapes are found in case of a symmetric airfoil, which highlights the possibility of controlling the accreted ice growth by optimizing the blade profile geometry.

Paper C – Experimental study of ice accretion on S826 & S832 wind turbine blade profiles

This paper describes the icing tunnel based experimental study for two different blade profiles (S826 & S832). Results show that difference in geometric characteristics of both airfoils affects the ice accretion and more complex ice shapes are observed in case of S832 profile compared to S826. Analysis show that ice thickness is higher in case of dry rime ice conditions as compared to wet ice, whereas more complex ice shapes are observed in case of glaze ice conditions that affects the aerodynamic performance differently from rime ice conditions. The aerodynamic coefficients of both clean and iced profiles are compared. Results show a decrease in the lift coefficient and increase in drag coefficient for iced profiles. This change is more significant for wet iced profiles, because of higher flow separation due to complex accreted ice shapes along leading edge.

Paper D – Study of ice accretion and icing effects on aerodynamic characteristics of DU96 wind turbine blade profile

This paper describes a case study of ice accretion physics and its effects on aerodynamic performance of DU96-W-180 airfoil for both dry and wet ice conditions. Icing tunnel experiments are carried out at Cranfield University in order to understand and simulate the ice accretion, whereas CFD based numerical analysis are carried out using ANSYS FENSAP-ICE to study the airflow and droplet behaviour and to estimate its aerodynamic performance. Analysis show that ice thickness is higher in case of dry rime ice conditions as compared to wet ice, whereas more complex ice shapes are observed in case of glaze ice conditions that affects the aerodynamic performance differently from rime ice conditions. CFD analysis show a change in airflow behaviour for iced profiles which leads to a decrease in the aerodynamic performance, when compared with the clean profiles. For DU96, results show higher aerodynamic performance degradation for glaze ice conditions particularly at higher angles of attack. A reasonably good agreement is found for the ice shapes particularly for the ice growth along stagnation point of the blade profile for both rime and glaze ice conditions. This ice accretion study for DU96 airfoil showed more streamlined ice shape for dry rime ice conditions, whereas complex horn type ice shape was found for case of glaze ice.

Paper E – Study of ice accretion on horizontal axis wind turbine blade using 2D and 3D numerical approach

This paper is focused on the multiphase CFD based 2D and 3D numerical techniques in order to better understand the ice accretion process and how it affects the wind turbine performance of CQU 300 KW wind turbine blade. CFD simulations of airflow behaviour over iced profiles are carried out and aerodynamic characteristics are calculated and compared with the clean profiles. Most of the existing work in this field is performed using blade profiles (blade sections) and not much work is performed for full scale blade analysis. The icing simulations are carried out using zero AOA, and afterwards these simulated ice shapes at zero AOA are used to further study the change in airflow behaviour at different AOA. The power coefficient (C_p) comparison for the 2D and the 3D numerical simulations is carried out. The aim of this paper is mainly to study and better understand the difference in rate and shape of ice accretion in case of blade profile sections (2D) and full scale blade. The knowledge from this paper can easily be used by other researchers in future to study the effect of change in ice accretion on power coefficient of wind turbine.

Paper F – Wind Turbine Ice Detection Using AEP Loss Method – A Case Study

This paper describes the comparison of analytical and numerical case study of wind resource assessment in cold region. T19IcelossMthod based analytical/statistical analysis and CFD based numerical simulations are carried out in comparison with the three years (2013 – 2015) wind park SCADA data. In order to better understand the wind turbine wake effects on flow behaviour and the resultant power production, Larsen wake model is used to calculate the AEP of each wind turbine before and after wind park layout optimization. Both analytical and numerical results are compared with the field SCADA data, where a good agreement is found. Statistical analysis shows the relative power loss due to icing related stops (Class B) is the main issue for this wind park. In order to better understand the wind flow physics and estimation of the wind turbine wake losses, Larsen wake model is used for the numerical simulations, where results show that it is important to use the wake loss model for CFD simulations of wind resource assessment and AEP estimation of a wind park. A preliminary case study about wind

park layout optimization has been carried out which shows that AEP can be improved by optimizing the wind park layout and CFD simulations can be a good tool in this regards.

Part IV

Epilogue

7. Concluding Remarks and Future Works

This chapter describes the main findings of this Ph.D. work and also includes the recommendations for the future work.

7.1. Concluding Remarks

The available research works show that the atmospheric icing on the wind turbines mainly occurs due to the collision and freezing of the super cooled water droplets with the exposed surfaces of wind turbines. At present, there is a need to develop a better understanding of atmospheric icing physics and its resultant effects on the wind turbines in order to improve the design and safety of wind turbines operating in the cold regions. The goal of this Ph.D. thesis was to investigate the challenge of atmospheric ice accretion on wind turbine blades. Two main topics have been considered: ice accretion and the performance losses caused by it, and wind resource assessment in the ice prone region. Both topics involved in this Ph.D. thesis are important for the wind turbine operations and maintenance, due to challenges present in the icing conditions and the resultant energy production losses. The answers provided through this Ph.D. thesis can be summarized in short as follows: Power losses due to icing on wind turbines occur not because of a single reason, such as icing on assistant equipment, control systems, instruments, aerodynamic degradation, etc. but through a combination of those effects, and they need to be taken into the account carefully during the wind park design process. This also provides the motivation for increasing the understanding about icing effects on wind turbine blades and the improvement of the anti-/de-icing technologies.

In this Ph.D. project, six scientific papers are developed for the purposes of studying the atmospheric ice accretion on the wind turbine blades. Compared with the modelling efforts, given in the introduction, the models developed and used in this project, focus primarily on better understanding of the atmospheric ice accretion on wind turbine blades at different operating and geometric conditions. The aim is to optimize the wind turbine blade aerodynamics in order to minimize the effects of the atmospheric ice accretion on the wind turbine performance and overall energy production. Multiphase computational fluid dynamics based numerical tools are used for this research work, in addition to the experimental and field measurements data.

Based on the research questions for the atmospheric ice accretion and the resultant performance losses, the obtained results show that the aerodynamic performance changes in those cases are mainly due to difference in droplet freezing fraction, as due to low freezing fraction for the glaze ice conditions, higher amount of the water runback and the aerodynamic heat flux along leading edge is observed which results in a complex horn type ice shapes. This phenomenon is difficult to capture during the numerical simulations and requires further improvements in the existing numerical models of the wet ice accretion. (Paper A, B). Numerical results show that the blade profile surface roughness and heat fluxes change significantly during the ice accretion process, which affects the airflow and droplet behaviour. The change in the accreted ice shape affects both the airflow behaviour and the aerodynamic performance (Paper B, C, D). In addition, analysis shows a decrease in the aerodynamic characteristics of the iced airfoils when compared to the clean airfoils. This degradation in aerodynamic performance is higher in case of the glaze ice, when compared to the profiles subjected to the rime icing (Paper B, C, D). As a result of this flow interaction in the third dimension, the velocity magnitudes are reduced in the 3D simulations when compared to the 2D simulations. This, in turn, affects the ice accretion process, as the higher velocity magnitudes in the 2D cases result in the higher droplet inertia, collision efficiencies and

the maximum impingement angles, which results in more ice mass accreted on the blade, along with the thicker and larger ice shapes present in the 2D simulations (Paper E).

Based on the research questions for the wind resource assessment in ice prone region the obtained results show that for wind parks, situated in the cold climate regions, power production can be lower when compared to identical wind parks/turbines situated in warmer temperate climates. Thus, the icing-related issues and the associated power losses need to be solved. With the increase in the atmospheric temperature, the type of accreted ice also changes from dry rime to wet glaze ice, which leads to a change in the ice density and also the accreted ice shapes on the wind turbine blades. In case of wet glaze ice the ice density is higher and more irregular (horn type) ice shapes are observed, which leads to a higher decrease in aerodynamic performance of wing turbines and resultant power production. Generally, wet ice growth is more damaging for wind turbine operations in icing conditions as compared to dry rime ice growth, due to higher degradation of aerodynamic characteristics under the glaze icing conditions. Results show that duration and timing of icing events are different for different wind turbines in a wind park, which clearly indicates that the icing events depend upon the meteorological conditions, airflow behaviour and also the location of the wind turbine. Even in the same wind park, it is not given that ice will accrete on all wind turbines under the instrumental and on-site conditions. The wind park layout and changes in flow behaviour affects the occurrence of ice accretion, despite the favourable conditions for icing events being present (Paper F).

Based on the research questions for both topics pointed out in Chapter 1.2, the answers to these are given in Table 7.1.

Table 7.1 – The answers to the research questions of the Ph.D. project.

Research questions	Papers	Brief answer
Q1: How the analytical model of the ISO 12494 standard can be applied for modelling of icing on wind turbine blades?	Paper A	ISO 12494 standard is only applicable to circular cross sections. The analytical model of the ISO 12494 standard can be applied to the wind turbine blades by parameterizing the characteristic length of it as leading edge diameter and by taking the rotation into account by calculating the true air speed from the known operating wind speed and the TSR.
Q2: How the different operating conditions change the accreted ice shapes on different wind turbine blade profiles?	Paper B	Results show that the operating conditions such as MVD, LWC, droplet distribution spectra, etc. have a pronounced effects on the resultant ice accretions and shapes. Moreover, the airfoil geometry affects the ice accretions. More streamlined ice shapes are found in case of a symmetric airfoil, which highlights the possibility of controlling the accreted ice growth by optimizing the blade profile geometry.
Q3: How to deal with the uncertainties in lab-based experiment ice accretion?	Paper C Paper D	Numerical CFD simulations allow for ease of validation with the experimental data and also permit a greater control over the variables involved in the atmospheric icing, such as droplet distribution spectra, MVD, LWC, which are normally the greatest uncertainties in the lab experiments. Fine control over these variables permits

		deeper understanding of the resultant ice accretion which can be used for the design and operations of the wind turbines.
Q4: How the blade geometry affects the ice accretion?	Paper E	Normally, the study of the atmospheric ice accretions on wind turbines is limited to the simulations of the 2D (or "quasi" 2D) airfoils. By performing a 3D numerical simulations better results can be achieved, as the more intricate multiphase flow behaviour (for example – flow in the *z*-direction due to asymmetry, twist and taper of the blade) can be resolved within the simulations. This will lead to differences in the resultant ice accretions between the 2D and the 3D simulations. These results can be applied for the purposes of better design of the wind turbine blades.
Q5: How the icing events can be detected using SCADA and how these events affect the AEP?	Paper F	Wind resource assessment in cold regions is challenging, but very important, for wind energy projects. SCADA data from a wind park in arctic region is used for this study. T19IceLossMethod based analytical analysis and CFD simulations are carried out for wind resource assessment and estimation of resultant AEP.
Q6: How to improve the wind energy production in the ice prone CC regions?	Paper A Paper E Paper F	The improved methodology of the *k*–factor allows for better analytical estimation of the icing on the wind turbine blades, provided that the wind site is equipped with the reference collector. In addition, the CFD simulations can be a good tool in this regards as they allow one to obtain the pressure distributions and C_P plots for both the 2D airfoils and the 3D blades, which are correlated with the power production. Furthermore, wake models can be used for the numerical simulations, where results show that it is important to use the wake loss model for CFD simulations of wind resource assessment and AEP estimation of a wind park. A preliminary case shows that AEP can be improved by optimizing the wind park layout.
Q7: What are the further gains that can be obtained from the numerical methodology in this Ph.D. work?	Paper B Paper C Paper D	By using the single-shot and multi-shot numerical simulations along with the available experimental data, it is possible to simulate the ice accretion on a very fine time scale, which allows for continuous monitoring of the progressive ice shape in the CFD simulations, how it affects the airflow behaviour and the associated aerodynamic losses. The methodology is applicable to different airfoils, geometries and operating conditions and can be used for further studies.

7.2. Limitations and Future Work

Nevertheless, the research results obtained during this Ph.D. project are not without limitations, and on a more generalized level, there are still many aspects of icing on wind turbines that needs contributions in further research work. Some ideas and suggestions for future improvement are discussed as follows:

First, there are limited standardized methodologies worldwide for wind energy in cold climate. For example, when compared to the European sites, the icing characteristics of the Chinese sites such as the accreted ice shapes, ice density and its adhesion to the surface are quite different, mostly due to different

climatic characteristics [88-90]. Therefore, future research works may need to be performed to address specific technologies for different CC regions.

Second, in this Ph.D. project, the aerodynamic performance degradation on wind turbines is investigated for wind turbine blades under icing conditions, while for the future research work, the modelling and measurements could be extended to the icing on hubs, sensors or other constructions of wind parks of interest.

Third, in this Ph.D. project, both the 2D and the 3D technologies have been used for stationary wind turbine blades. However, the rotational effects of ice accretion on wind turbine blades can be vary from rotor to rotor. Due to this reason, the future research work can focus on the effects of rotational rotors under the icing conditions.

Fourth, in this Ph.D. project, the methodology of icing detection is done only using anemometers. Therefore, development of advanced ice sensors for ice prone regions could be an interesting topic for future research in wind turbines design and operations in the CC regions.

Fifth, there exists many different anti-/de-icing systems, which are used in the modern wind turbines. These systems use various technologies and have different specifications, sometimes with no clear indication of their efficiency. Since the effect of cold climate on wind turbines is complex, not every ice protection system is suitable for a given wind farm. Therefore, the aim of the future work should be to compare the existing ice mitigation solutions and provide an indication on their efficacy.

References

[1] Ian Baring-Gould, René Cattin, Michael Durstewitz, Mira Hulkkonen, Andreas Krenn, Timo Laakso, Antoine Lacroix, Esa Peltola, Göran Ronsten, Lars Tallhaug, and Tomas Wallenius, *IEA Wind Recommended Practice 13: Wind Energy in Cold Climates*, IEA Wind Task XIX, VTT, Finland, 2012.

[2] *Renewable Energy Target Setting*, International Renewable Energy Agency, 2015.

[3] *SDG 7: Ensure access to affordable, reliable, sustainable and modern energy for all*, United Nations General Assembly, 2015.

[4] European Wind Energy Association, http://www.ewea.org/.

[5] *IEA Wind Task 19: Wind Energy in Cold Climates*, https://community.ieawind.org/task19/home.

[6] *IEA to produce world's first comprehensive roadmap to net-zero emissions by 2050*, https://www.iea.org/news/iea-to-produce-world-s-first-comprehensive-roadmap-to-net-zero-emissions-by-2050.

[7] *IEA: Data and Statistics*, http://www.iea.org/statistics/.

[8] *Icing Wind Tunnel (CIRA)*, https://www.cira.it/en/research-infrastructures/icing-wind-tunnel-(iwt)/Icing%20Wind%20Tunnel.

[9] Annette Evans, Vladimir Strezov, and Tim J. Evans, *Assessment of sustainability indicators for renewable energy technologies*, Renewable and Sustainable Energy Reviews, vol. 13, no. 5, pp. 1082 – 1088, 2008.

[10] *Global Wind Turbine Market – Forecasts from 2020 to 2025*, Reseach and Markets, 2020.

[11] Ozcan Yirtici, Ismail H. Tuncer , and Serkan Ozgen, *Ice Accretion Prediction on Wind Turbines and Consequent Power Losses*, Journal of Physics: Conference Series, vol. 753, no. 2, 2016.

[12] *Task 19 Work Plan and Objectives*, https://community.ieawind.org/task19/19workplan.

[13] *Wind Power Icing Atlas – WIceAtlas*, https://projectsites.vtt.fi/sites/wiceatlas/www.vtt.fi/sites/wiceatlas.html.

[14] Muhammad S. Virk, *Atmospheric Ice Accretion on Non-Rotating Circular Cylinder*, The Journal of Computational Multiphase Flows, vol. 3, no. 4, pp. 197 – 205, 2011.

[15] B. Tammelin, A. Böhringer, M. Cavaliere, H. Holttinen, C. Morgan, H. Seifert, K. Säntti, P. Vølund, *Wind energy production in cold climate (WECO)*, Finnish Meteorological Institute, Helsinki, 2000.

[16] Pierre McComber, and Gilbert Touzot., *Calculation of the impingement of cloud droplets in a cylinder by Finite element method*, Journal of atmospheric Science, 1981.

[17] Göran Ronsten, *Sevenska erfarenheter av vindkraft i kallt klimat nedisning*, Elforsk Rapport, 2004.

[18] Adriána Hudecz, *Icing Problems of Wind Turbine Blades in Cold Climates*, Department of Wind Energy, Technical University of Denmark, DTU Wind Energy, 2014.

[19] Timo Laakso, Lars Talhaug, Göran Ronsten, Robert Horbaty, Ian Baring-Gould, Antoine Lacroix, Esa Peltola, Tomas Wallenius, and Michael Durstewitz, *Task 19 wind energy in cold climates final report*, Paris: IEA, 2009: 19.

[20] Neil Davis, *Icing Impacts on Wind Energy Production*, DTU, DTU Wind Energy, 2014.

[21] Kathie Zipp. *Understanding costs for large wind-turbine drivetrains*, https://www.windpowerengineering.com/understanding-costs-for-large-wind-turbine-drivetrains/.

[22] Sohrab Gholahosein Pouryoussefi, Masoud Mirzaei, Mohamed Mahdi Nazemi, Mojtaba Fouladi, Alreza Doostmahmoudi, *Experimental study of ice accretion effects on aerodynamic performance of NACA-23012 airfoil*, Chinese Journal of Aeronautics, vol. 29, no. 3, pp. 585 – 595, 2016.

[23] Fayçal Lamraoui, Guy Fortin, Jean Perron, and Robert Benoit, *Canadian icing envelopes near the surface and its impact on wind energy assessment*, Cold Regions Science and Technology, vol. 120, pp. 76 – 88, 2015.

[24] Joshua Smalley, *Evaluation of VGs on Suzlon S88 turbines shows 2.5% AEP increase*, Windpower Engyneering & Development, 2015.

[25] M. L. T Duncan, C Morgan, L Landberg, *Underestanding Icing Losses and Risk of Ice Trhow at Operating Wind Farms*, in Windterwind 2008, Norrköping, Sweden, 2008.
[26] Drage Peter, *Numerical simulation of Ice Accretion on Wind Turbines*, IWAIS 2009, 2009.
[27] Jia Yi Jin and Muhammad S. Virk, *Ice Accretion on Wind Turbine Blade – An Experimental Study of S819 Airfoil*, IWAIS 2019, 2019.
[28] S. Fikke, G. Ronsten, A. Heimo, S. Kunz, M. Ostrozlik, P.-E. Persson, J. Sabata, B. Wareing, B. Wichura, J. Chum, T. Laakso, K. Säntti, Lasse Makkonen, *COAT 727: Atmospheric Icing on Strutures Measurements and data collection on icing: State of the Art*, MeteoSwiss No. 75, 2007.
[29] Ville Lehtomäki, Andreas Krenn, Pieter Jan Jordaens, Charles Godreau, Neil Davis, Zouhair Khadiri-Yazami, Rolv Erlend Bredesen, Göran Ronsten, Helena Wickman, Saskia Bourgeois, and Till Beckford, *IEA Wind TCP Task 19 – Available Technologies for Wind Energy in Cold Climates, 2nd Edition*, IEA Wind Task 19, 2018.
[30] Shang-Ping Xie, W. Timothy Liu, Qingyu Liu, and Masami Nonaka, *Far-Reaching Effects of the Hawaiian Islands on the Pacific Ocean-Atmosphere System*, Science, vol. 292, no. 5524, pp. 2057 – 2060, 2001.
[31] Fernando Porté-Agel, Majid Bastankhah, and Sina Shamsoddin, *Wind-Turbine and Wind-Farm Flows: A Review*, Boundary-Layer Meteorology, vol. 174, pp. 1 – 59, 2020.
[32] R. R. Rogers and M. K. Yau, *A Short Course in Cloud Physics*, Butterworth-Heinemann, Elsevier, 1989.
[33] *Understanding ice formation to improve aricraft safety*. https://www.cranfield.ac.uk/case-studies/research-case-studies/aircraft-icing.
[34] Kristian Ingvaldsen, *Atmospheric icing in a changing climate – Impact of higher boundary temperatures on simulations of atmospheric ice accretion on structures during the 2015-2016 icing winter in West-Norway*, Department of Geosciences, Master thesis, University of Oslo (UiO), 2017.
[35] Guy Fortin, Jean-Louis Laforte, and Adrian Ilinca, *Heat and mass transfer during ice accretion on aircraft wings with an improved roughness model*, International Journal of Thermal Sciences, vol. 45, no. 6, pp. 595 – 606, 2005.
[36] Hantao Li, *Power Performance and Its Computational Model of Wind Turbines under Icing Conditions*, Electrical Engineering, Doctoral thesis, Chongqing University Chongqing, China, 2018.
[37] Mathew Carl Homola, *Atmospheric icing on wind turbines - Modeling and consequences for energy production*, Department of Engineering Cybernetics, Doctoral thesis, Norwegain University of Science and Technology (NTNU), 2011.
[38] L. Makkonen, *Ice and Construction – Rilem Report 13*, London, England: Chapman & Hall, 1994.
[39] *ISO 12494: Atmopsheric icing of structures*, 2001.
[40] IEAWind – Task19, *T19IceLossMethod: Method for estimating icing losses from wind turbine SCADA data*, https://github.com/IEAWind-Task19/T19IceLossMethod, 2019.
[41] Andreas Krenn, Alexander Stök, Nina Weber, Sten Barup, Thorsten Weidl, André Hoffmann, Rolv Erlend Bredesen, Marine Lannic, Stefan Müller, Nicole Stoffels, Thomas Hahm, Felix Storck, and Frederik Lautenschlager, *IEA Wind TCP Task 19: International Recommendations for Ice Fall and Ice Throw Risk Assessments*, IEA Wind, 2018.
[42] Timo Laakso, Ian Baring-Gould, Michael Durstewitz, Robert Horbaty, Antoine Lacroix, Esa Peltola, Göran Ronsten, Lars Tallhaug, andTomas Wallenius, *State-of-the-art of wind energy in cold climates*, VTT Technical Research Center, 2010.
[43] G. Ronsten, *Swedish cold climate wind energy projects*, 2010.
[44] Ville Lehtomäki, Timo Karlsson, and Simo Rissanen, *Wind Turbine Ice Protection System Benchmark Analysis*, VTT Technical Research Centre of Finland, 2018.
[45] IEA Wind Task 19, *Task 19 Ice Loss Release 2.2 tutorial*, https://github.com/IEAWind-Task19/T19IceLossMethod, 2019.
[46] International Electrotechnique Internationale (IEC), *Wind turbine – Part 2: Small wind turbines, IEC 61400-2:2013*, European Committee for Electrotechnical Standardization (CENELEC), 2014.

[47] A. C. Hansen and C. P. Butterfield, *Aerodynamics of horizontal-axis wind turbines*, Annual Review of Fluid Mechanics vol. 25, pp. 115 – 149, 1993.
[48] K. Giridhar, S. J. Venkata Aravind, and Sana Vani, *Aerodynamic Modelling and Analysis of Wind Turbine*, Soft Computing Techniques and Applications, pp. 139 – 145, Singapore, 2020.
[49] Lichun Shu, Liang Jian, Qin Hu, Xingliang Jiang, Xiaokai Ren, and Gang Qiu, *Study on small wind turbine icing and its performance*, Cold Regions Science and Technology, vol. 134, pp. 11 – 19, 2016.
[50] Silvio Rodrigues, Carlos Restrepo, George Katsouris, Rodrigo Teixeira Pinto, Maryam Soleimanzadeh, Peter Bosman, and Pavol Bauer, *A Multi-Objective Optimization Framework for Offshore Wind Farm Layouts and Electric Infrastructures*, Energies, vol. 9, no. 3, pp. 216 – 258, 2016.
[51] P. Dvork, *Lessons learned from ice-resistant turbine tech*, Windpower Engineering & Development, October 19, 2016.
[52] Bjørn Egil Kringlebotn Nygaard, Jón Egill Kristjánsson, and Lasse Makkonen, *Prediction of In-Cloud Icing Conditions at Ground Level Using the WRF Model*, Journal of Applied Mrteorology and Climatology, vol. 50, 2011.
[53] Muhammad S. Virk, Matthew C. Homola, and Per J. Nicklasson, *Effect of Rime Ice Accretion on Aerodynamic Characteristics of Wind Turbine Blade Profiles*, Wind Engineering, vol. 34, pp. 207 – 218, No. 2, 2010.
[54] Jaiwon Shin, Berkowitz Brian, Chen Hsun, and Cebeci Tuncer, *Prediction of ice shapes and their effect on airfoil performance*, NASA Techical Memorandum 103701, 1991.
[55] Matthew C. Homola, Muhammad S. Virk, Tomas Wallenius, Per J. Nicklasson, and Per A. Sundsbø, *Effect of atmospheric temperature and droplet size variation on ice accretion of wind turbine blades*, Journal of Wind Engineering and Industrial Aerodynamics, vol. 98, no. 12, pp. 724 – 729, 2010.
[56] Sam Lee, Michael B. Bragg, *Investigation of Factors Affecting Iced-Airfoil Aerodynamics*, Journal of Aircraft, vol. 40, no. 3, pp. 499 – 508, 2003.
[57] N. Abuaf , R. S. Bunker, and C. P. Lee, *Effects of surface roughness on heat transfer and aerodynamic performance of turbine airfoils*, J. Turbomachinery, 120(3): 522 – 529, 1998.
[58] David Anderson and Jaiwon Shin, *Characterization of ice roughness from simulated icing encounters*, in American Institute of Aeronautics and Astronautics, Inc. (AIAA), Paper 97-0052, 1997.
[59] Matthew C Homola, Muhammad S Virk, and P. J. Nicklasson., *Performance losses due to ice accretion for a 5 MW wind turbine*, Wind Energy, Vol. 15, no. 3, pp. 379 – 389, 2012.
[60] M. Etemaddar, M. O. L. Hansen, and T. Moan, *Wind turbine aerodynamic response under atmospheric icing conditions*, Wind Energy, vol. 17, no 2, pp. 241 – 265, 2012.
[61] W. J. Jasinski , S. C. Noe, M. S. Selig, and M. B. Bragg, *Wind turbine performance under icing conditions*, Journal of solar energy engineering, vol. 120(1), pp. 60 – 65, 1998.
[62] Tammelin, B. Stuke, M., Seifert, H. and Kimura, S., 1999. *Icing effect on power production of wind turbine*. In: Tammelin, B. et al (eds.), BOREAS IV, Proceeding of an International Meeting, 31 March – 2 April, Hetta, Finland.
[63] Mauri Marjaniemi, and Esa Peltola, *Blade heating element design and practical experiences*, BOREAS IV: Wind Energy Produciton in Cold Climates – Hetta, Enontekiö, 1998, Finland.
[64] Mauri Marjaniemi, Lasse Makkonen, and Timo Laakso, *Turbice – the wind turbine blade icing model*, International Conference BOREAS V: Wind power production in cold climates - Levi, 2000, Finland.
[65] C. Bak, P. Fuglsang, and Niels N. Sørensen, Helge Aagaard Madsen, W.Z. Shen, Jens Nørkær Jens, *Airfoil Characteristics for Wind Turbines*, Roskilde: Risø National Laboratory, 1999, Denmark.
[66] E. Ferrer, and X. Munduate, *Wind turbine blade tip comparison using CFD*, Journal of Physics, Conference Series vol. 75, no. 012005, 2007, Denmark.
[67] X. Chi, Bin Zhu, Tom Shih, H. Addy, and Yung Choo, *CFD Analysis of the Aerodynamics of a Business-Jet Airfoil with Leading-Edge Ice Accretion*, 42nd AIAA Aerospace Sciences Meeting and Exhibit, AIAA 2004-0560, 2004, Nevada.

[68] O. Joon Kwon, and Lakshmi N. Sankar, *Numerical Simulation of the Flow About a Swept Wing With Leading-Edge Ice Accretions*, *Computers & Fluids*, vol. 26, no. 2, pp. 183 – 192, 1997.
[69] Masoud Mirzaei, Mohammad A. Ardekani, and Mehdi Doosttalab, *Numerical and experimental study of flow field charactristics of an iced airfoil*, Aerospace science and technology, vol. 13, no. 6, pp. 267 – 276, 2009.
[70] ZiQiang Zhu, XiaoLu Wang, Jie Liu, and Zhou Liu, *Comparison of predicting drag methods using computational fluid dynamics in 2d/3d viscous flow*, Science in China Series E: Technological Sciences, vol. 50, no. 5, pp. 534 – 549, 2007.
[71] Hao Guo, Kai Zhang, Rye M. Waldman, and Hui Hu, *An experimental study on Icing Physics for Wind Turbine Icing Mitigation*, 35th Wind Energy Symposium, AIAA SciTech Forum, (AIAA 2017-0918), Grapevine, Texas, 2017.
[72] W. C. Macklin, and G. S. Payne., *A theoretical study of the ice accretion process*, Quarterly Journal of the Royal Meteorological Society, vol. 93, no. 396, pp. 195 – 213, 1967.
[73] Charles D. MacArthur, John L Keller, and J. K. Luers, *Mathematical modelling of ice accretion on airfoils*, AIAA 20th Aerospace Sciences Meeting, 82-0284, USA, 1982.
[74] Myron M. Oleskiw, *A computer simulation of time dependent rime icing on airfoils*, Department of Geography, Doctoral thesis, University of Alberta, Alberta, 1982.
[75] E. P. Lozowski, J. R. Stakkabrass, and P. F. Hearty, *The icing of an unheated, non rotating cylinder – Part 1: A simulation model*, Journal of applied meteorology and climatology, vol. 22, no. 12, pp. 2053 – 2062, 1983.
[76] Ivar Horjen, *Icing on offshore structure*, Norwegian Matitime Research, vol. 11, no. 3, pp. 9 – 21, 1983.
[77] Lasse Makkonen, *Modelling of ice accretion on wires*, Journal of Applied Meteorology and Climatology, vol. 23, no. 6, pp.929 – 939, 1984.
[78] R. W. Gent, and J. T. Cansdale, *The development of mathematical modelling techniques for helicopter rotor icing*, AIAA 23rd Aerospace Sciences Meeting 85-0336, U.S.A., 1985.
[79] Karen Joan Finstad, *Numerical and Experimental Studies of Rime Ice Accretion on Cylinders and Airfoils*, Department of Geography, Doctoral thesis, University of Alberta, Alberta, 1986.
[80] Irving Langmuir, and Katherine B. Blodgett, *A mathematical investigation of water droplet trajectories*, Pergamon Press, 1946.
[81] Bernard L. Messinger, *Equilibriuim temperature of an unheated icing surface as a function of air speed*, Journal of the Aeronautical Sciences, vol. 20, no. 1, pp. 29 – 42, 1953.
[82] L.J. Vermeer, J.N. Sørensen, A. Crespo, *Wind turbine wake aerodynamics*, Progress in Aerospace Sciences, Vol.39, no. 6–7, pp. 467-510, 2003.
[83] Ville Turkia, Saasa Huttunen, and Tomas Wallenius., *Methods for estimating wind turbine production losses due to icing*, VTT Technology 114, Finland, 2013.
[84] René Cattin, *Icing of Wind Turbines – Vindforsk projects, a survey of the development and research needs*, 2012.
[85] W. A. Timmer, *Aerodynamic characteristics of wind turbine blade airfoils at high angle-of-attack*, 3rd EWEA Conference-Torque 2010: The Science of Making Torque from Wind, Greece, 2010.
[86] Woobeom Han, Jonghwa Kim, and Bumsuk Kim, *Study on correlation between wind turbine performance and ice accretion along a blade tip airfoil using CFD*, Journal of Renewable and Sustainable Energy, vol. 10, no. 2, 2018.
[87] Gitsuzo Tagawa, François Morency, and Héloïse Beaugendre, *CFD study of airfoil lift reduction caused by ice roughness*, 2018 Applied Aerodynamics Conference, Atlanta, Georgia, 2018.
[88] Jia Yi Jin and Muhammad Shakeel Virk, *Study of ice accretion along symmetric and asymmetric airfoils*, Journal of wind engineering and industrial aerodynamics, vol. 179, pp. 240 – 249, 2018.
[89] Pavlo Sokolov, Jia Yi Jin, and Muhammad S. Virk, *Accreted ice mass ratio (k-factor) for rotating wind turbine blade profile and circular cylinder*, Wind Energy, vol. 22, no. 4, pp. 447 – 457, 2018.
[90] Jian Liang, Maolian Liu, Ruiqi Wang, Yuhang Wang, *Study on the glaze ice accretion of wind turbine with various chord lengths*, Earth and Environmental Science, vol. 121 no. 4, pp. 042026, 2018.

[91] S. Barber, Y. Wang, S. Jafari, N. Chokani, and R. S. Abhari, *The impact of ice formation on wind turbine performance and aerodynamics*, Journal of Solar Energy Engineering, vol. 133, no. 1, 011007, 2011.

[92] Fayçal Lamraoui, Guy Fortin, Robert Benoit, Jean Perron, and Christian Masson, *Atmospheric icing impact on wind turbine production*, Cold Regions Science and Technology, vol. 100, no. 4, pp. 36 – 49, 2014.

[93] William B. Wright, *User manual for the NASA Glenn Ice Accretion code LEWICE version 2.2.2*, NASA/CR 2002-211793, NASA, 2002.

[94] William B. Wright, *Validation results for LEWICE 3.0*, NASA-2005-1243, NASA, 2005.

[95] Colin S. Bidwell and Mark G. Potapczuk, *Users manual for the NASA Lewis three-dimensional ice accretion code (LEWICE3D)*, NASA Technical Memorandum 105974, NASA, 1993.

[96] *ANSYS FENSAP-ICE user manual*, ANSYS, 2016.

[97] Héloïse Beaugendre, François Morency, and Wagdi G. Habashi, *FENSAP-ICE's three-dimensional in-flight ice accretion module : ICE3D*, Jounal of Aircraft, vol. 40, no. 2, pp. 239 – 247, 2003.

[98] David Switchenko, and Wagdi G. Habashi, *Fensap-ice simulation of complex wind turbine icing events, and comparison to observed performance data*, 32nd ASME Wind Energy Symposium, AIAA 2014-1399, Maryland, 2014.

[99] Guy Fortin and Jean Perron, *Wind Turbine Icing and De-Icing*, 47th AIAA Aerospace Sciences Meeting Including The New Horizons Forum and Aerospace Exposition, Orlando, Florida, 2009.

[100] Ping Fu and Masoud Farzaneh, *A CFD approach for modeling the rime-ice accretion process on a horizontal-axis wind turbine*, Journal of Wind Engineering and Industrial Aerodynamics, vol. 98, no. 4 – 5, pp. 181 – 188, 2010.

[101] Chankyu Son, Sejong Oh, and Kwanjung Yee, *Quantitative analysis of a two-dimensional ice accretion on airfoils*, Journal of Mechanical Science and Technology, vol. 26, no. 4, pp. 1059 – 1071, 2012.

[102] Jaiwon Shin and Thomas H. Bond, *Experimental and Computational Ice Shapes and Resulting Drag Increase for a NACA 0012 Airfoil*, vol. 105743, NASA Technical Manual 1992.

[103] Zuo-JiaWang, Dong-Jun Kwon, K. Lawrence DeVries, and Joung-Man Park, *Frost formation and anti-icing performance of a hydrophobic coatingon aluminum*, Experimental Themal and Fluid Science, vol. 60, pp. 132 – 137, 2015.

[104] Qi Liu,Ying Yang, Meng Huang, Yuanxiang Zhou, Yingyan Liu, and Xidong Liang, *Durability of a lubricant-infused Electrospray Silicon Rubber surface as an anti-icing coating*, Applied Surface Science, vol. 346, no. 15, pp. 68 – 76, 2015.

[105] Chaoyi Peng, Suli Xing, Zhiqing Yuan, Jiayu Xiao, Chunqi Wang, and Jingcheng Zeng, *Preparation and anti-icing of superhydrophobic PVDF coating on a wind turbine blade*, Applied Surface Science, vol. 259, no.15, pp. 764 – 768, 2012.

[106] F.Arianpour, M. Farzaneh, and S.A.Kulinich, *Hydrophobic and ice-retarding properties of doped silicone rubber coatings*, Applied Surface Science, vol. 265, no. 15, pp. 546 – 552, 2013.

[107] Henry Seifert, *Technical Requirements for Rotor Blades Operating in Cold Climate*. Environmental Science, pp. 50 – 55, 2004.

[108] Jesús María Pinar Pérez, Fausto Pedro García Márquez, and Diego Ruiz Hernández, *Economic viability analysis for icing blades detection in wind turbines*, Journal of Cleaner Production, vol. 135, no. 1, pp. 1150 – 1160, 2016.

[109] Linyue Gao, Yang Liu, Cem Kolbakir, and Hui Hu, *An Experimental Investigation on an Electric-Thermal Strategy for Wind Turbine Icing Mitigation*, 2018 Atmospheric and Space Environments Conference, Atlanta, Georgia, 2018.

[110] David Anderson, Allen Reich, David Anderson, and Allen Reich, *Tests of the performance of coatings for low ice adhesion*, 35th Aerospace Sciences Meeting and Exhibit, AIAA, U.S.A., 2013.

[111] N. Dalili, A. Edrisy, and R. Carriveau, *A review of surface engineering issues critical to wind turbine performance*, Renewable and Sustainable Energy Reviews, vol. 13, no. 2, pp. 428 – 438, 2009.

[112] Lasse Makkonen, Timo Laakso, Mauri Marjaniemi, and Karen J. Finstad, *Modeling and prevention of ice accretion on wind turbines*, Wind Engineering, vol. 25, no. 1, pp. 3 – 21, 2001.
[113] Karen J. Finstad, Edward P. Lozowski, and Lasse Makkonen, *On the median volume diameter approximation for droplet collision efficiency*, Journal of the Atmospheric Sciences, vol. 45, no. 24, pp. 4008 – 4012, 1988.
[114] Jen-ching Tsao and David N. Anderson, *Additional Study of Water Droplet Median Volume Diameter (MVD) Effects on Ice Shapes*, NASA/CR–2005-213853, 2005.
[115] Jen-Ching Tsao and David N. Anderson, *Evaluation of Icing Scaling on Swept NACA 0012 Airfoil Models*, NASA/CR–2012-217419, NASA, 2012.
[116] Kathleen F. Jones, Gregory Thompson, Keran J. Claffey, and Eric P. Kelsey, *Gamma distribution parameters for cloud drop distributions from multicylinder measurements*, Journal of Applied Meteorology and Climatology, vol. 53, no. 6, pp. 1606 – 1617, 2014.
[117] Markus Zauner, *Direct numerical simulation and stability analysis of transonic flow around airfoils at moderate Reynolds numbers*, Ph.D. thesis, University of Southampton, April 2019.
[118] Florian R. Menter, *Improved Two-Equation k – ω Turbulence Models for Aerodynamic flows*, NASA Technical Memorandum 103975, National Aeronautics and Space Administration, October 1992.
[119] Michael F. Kerho and Michael. B. Bragg, *Airfoil Boundary-Layer Development and Transition with Large Leading-Edge Roughness*. AIAA Journal, Vol. 35, No.1, January 1997.
[120] R. Clift, J. R. Grace, and M. E. Weber, *Bubbles, drops and particles*, Dover publications, INC., New York, U.S.A., 1978.
[121] Kathleen F. Jones, *The density of natural ice accretions related to nondimensional icing parameters*, Quarterly Journal of Royal Meteorological Society, vol. 116, no. 492, pp. 477 – 496, 1990.
[122] N. S. U. Manual, NTI, Washington, DC, USA, 2010.
[123] Pavlo Sokolov, Muhammad S. Virk, *Droplet distribution spectrum effects on dry ice growth on cylinders*, Cold Region Science and Technology, vol. 160, pp. 80 – 88, 2019.
[124] Pavlo Sokolov, Muhammad S. Virk, *An investigation into empirical ice density formulations for dry ice growth on cylinders*, Cold Region Science and Technology, vol. 169, 102906, 2020.
[125] Catherine Meissner, *WindSim-getting started (12th edition)*, WindSim AS, Norway, 2019.
[126] Long Guo, Zixu Wang, Ming Li, and Zhangsong Ni, *2016 cloud calibration of 3m*2m icing wind tunnel*, IWAIS 2017 B1_5, Chongqing, China, 2017.
[127] Gunner C. Larsen, *A Simple Wake Calculation Procedure*, Risø National Laboratory, DK-4000 Roskilde, Denmark, 1988.
[128] Takeshi Ishihara, Atsushi Yamaguchi, and Yozo Fujino, *Development of a New Wake Model Based on a Wind Tunnel Experiment*, Globle Wind Power – Poster, 2004.

Appendix

Paper A

Accreted Ice Mass Ratio (*k*-factor) for Rotating Wind Turbine Blade Profile and Circular Cylinder

Pavlo Sokolov, Jia Yi Jin and Muhammad Shakeel Virk

Wind Energy, 2018, Volume 22, p.447-457.

Doi: 10.1002/we.2298

Author's Contribution

Jia Yi Jin has contributed in the proposal of conceptualization, data curation, methodology, resources, software, visualization and validation of the paper.

A. Accreted ice mass ratio (*k*–factor) for rotating wind turbine blade profile and circular cylinder

This is a reprint

Pavlo Sokolov, Jia Yi Jin and Muhammad Shakeel Virk

Arctic Technology and Icing Research Group
Institute of Industrial Technology
Faculty of Engineering Science and Technology
UiT- The Arctic University of Norway
Norway

Abstract

This paper describes a study to investigate the relation between ice accretion on a rotating wind turbine blade profile (airfoil) and a reference collector (circular cylinder). This relation, known as "*k*–factor" describes the ratio of accreted ice mass on a reference collector and wind turbine blade profile. Analyzes are carried out by performing a series of multiphase numerical simulations and ISO 12494 based analytical calculations. The results show that *k*–factor is not equal to constant 20, contrary to currently postulated assumption and can vary to a significant degree depending on a number of different operating and geometric parameters. These factors include the effects of blade geometry on ice accretion, droplet collision efficiency, droplet distribution spectrum and median volume diameter under different ambient conditions pertaining to wind speed and tip speed ratios experienced by both the reference collector and wind turbine blade. The results presented in this paper provide a simplistic explanation about *k*–factor variance, however, further validation is necessary, in particular when it comes to the ice accretions on different wind turbine blade profiles under different operating and geometric conditions.

Keywords:
Circular cylinder, Droplet collision efficiency, Ice accretion, MVD, Tip speed ratio, Wind turbine.

A.1. Introduction

The interest in energy generated by the wind turbines has been steadily increasing over the last few decades and has resulted in increase of installed wind turbines in ice prone cold climate regions having good wind resources. Icing on wind turbines is an undesirable phenomenon as it causes adverse effects such as loss in power production [1-2]; increased vibrations in structure due to unbalanced loadings, which in turn will lead to increase in fatigue damage of the components; overloading due to delayed stall and ice shedding from the wind turbine. [3] When it comes to these negative effects, the main question posed here is better way of estimation of the icing load on wind turbine blade in order to estimate the magnitude and severity of these undesirable events. However, direct measurements of ice load on wind turbines are difficult, if not impossible, and therefore some simplifications and empirical relations can be employed. In 2013, VTT technical research center of Finland proposed to use a so-called "*k*–factor", [4] a constant conversion ratio of an order of $k = 20$ at 85% of blade length deemed to be a representative value for wind turbine ice accretion.

The practical meaning of k–factor is a ratio of ice mass accreted on a reference collector, i.e. a slowly rotating cylinder 30 mm in diameter by 500 mm in length, mounted on a met mast to the ice mass accreted on a rotating wind turbine blade profile section in question. The k–factor 20 means that rotating wind turbine blade profile, in general, will accrete 20 times more ice in the same time under same operating conditions than a reference collector. However, the VTT model does not explicitly state for what icing conditions it is applicable, as it is expected that reference collector and wind turbine might have differences in ice accretion processes, primarily due to the fact that under ISO 12494 model, it is assumed that velocity vector is normal to the object, i.e., the reference collector, while for wind turbine the velocity vector would not be normal to the blade as the true air speed (TSR) of the turbine blade is a function of normal velocity caused by the wind and tangential velocity as function of blade rotation. However, the precise extent of those possible differences on ice accretion process is not known as to the best of authors' knowledge, and there are no experimental investigations being done for objects rotating in such a way. Nonetheless, the physical reasoning behind k–factor can be explained by several factors.

First, is height factor due to log wind speed profile. The height factor accounts for wind speed profile variation due to planetary boundary layer, surface roughness, and viscous friction effects between air and surface in planetary boundary layer. This is a relatively well-known phenomenon and is accounted for in governing ISO standard, ISO 12494: "Atmospheric icing of structures". [5] The height factor x is defined as

$$x = e^{0.01H} \tag{A.1}$$

where H is the height above ground level (m). *Second*, is the tip speed ratio (TSR), λ, which is defined as the ratio of the speed of the rotor tip to the free stream wind speed:

$$\lambda = \frac{V}{v} = \frac{\omega r}{v} \tag{A.2}$$

where v is free stream wind speed (m/s), V is the rotor tip speed (m/s), r is the rotor radius (m), and ω is the blade rotational velocity (rad/s). The rotor TSR depends on the blade profile used, the number of blades, and the type of wind turbine. In general, three blade wind turbines operate at a TSR value between 6 and 8, with 7 being the most typically used value. *Lastly*, airfoil geometry and droplet distribution size have the possibility to affect the *k*–factor values; however, as of current, the possible

effects of those has not been ascertained in great details and thus are some of the major scopes of the work presented in this paper. In addition, another major scope of current work is to provide better estimate of ice load maps for the wind parks. This case-by-case estimate is believed to be more accurate in nature than the broad generalist approach, as was the case in Turkia et al. [4]

A.2. Models setup

A.2.1. Analytical Model

The operating parameters used for this study are summarized in Table A.1.

Table A.1 – Operating Conditions.

Parameter	Value
Cylinder radius [leading edge radius of airfoil] (mm)	15
Air velocity (m/s)	7 (cylinder), 60 (airfoil)
Air temperature (°C)	–5
Altitude (m.a.g.l)	10 (cylinder), 80 (hub)
MVD (μm)	20
Liquid Water Content (g/m^3)	0.4
Icing duration (min)	60
Chord length (m)	1
Droplet distribution	Langmuir A – E

The airfoils used in this study are: NACA 0012, 4412, 6412, 23012 and N-22, all having the same leading edge radius of 15 mm and maximum thickness of 12 cm. The choice of airfoils has been governed by the need to select a "type" of airfoils having same leading edge radius, thickness, and chord length, differing only in the geometric shape and symmetry in order to see if those geometric features have an impact on *k*–factor or not. The choice of altitude of 10 m.a.g.l. is assumed to correspond to the standard mounting height of the reference collector on met mast, as per ISO 12494 guidelines. Other mounting heights of the reference collector and/or hub height are acceptable, granted the collector measurements are compliant with the ISO 12494 [5] and the height difference between the reference collector and the turbine hub height is properly taken into account in calculations of the height factor. In this study, the pressure difference associated with the height difference between reference collector and turbine hub height is ignored. This is based on reporting in Finstad et al., [6] that the pressure difference between sea level and Mt. Washington (1916.6 m.a.s.l.) caused about 0.5% difference in overall collision efficiency values, and the height difference between assumed cylinder mounting height (10 m.a.s.l.) and typical wind turbine hub height (80 m.a.g.l.) is considerably less than the elevation of Mt. Washington. The choice of cylinder diameter matches the diameter of typical reference collector, [5] while the choice of temperature, LWC, and MVD corresponds to typical conditions of dry growth under moderate icing intensity. The choice of wind speeds is based on reference in Bredesen and Refusm [7] that for global average in-cloud icing conditions ice accretes at a rate of roughly 1 kg/m/hr on a typical wind turbine blade airfoil section at 85 % of the blade span for wind speeds of 7 m/s corresponding to a airfoil section velocity of 60 m/s.

The rate of icing on a structure can be calculated according to ISO 12494, based on expression by Makkonen [8] is given in Equation (A.3):

$$\frac{dm}{dt} = \alpha_1 \alpha_2 \alpha_3 vAw \tag{A.3}$$

where dm is the change in ice mass (g), dt is the change in time (s), α_1, α_2 and α_3 are dimensionless collision, sticking and accretion efficiency of a droplet, respectively, *v* is the wind speed (m/s), *A* is the cross-sectional area of an object (m^2) and *w* is the liquid water content (hereafter, LWC, g/m^3). For this study an assumption of "dry ice growth" regime on a reference collector is made, meaning that $\alpha_2 = \alpha_3 = 1$, i.e. all impinging droplets freeze on impact. The collision efficiency, α_1, can be obtained [5] as

$$\alpha_1 = A - 0.028 - C(B - 0.0454) \tag{A.4}$$

where

$$A = 1.066K^{-0.00616} \exp(-1.103K^{-0.688}) \tag{A.5}$$

$$B = 3.641K^{-0.498} \exp(-1.497K^{-0.694}) \tag{A.6}$$

$$C = 0.00637(\varphi - 100)^{-0.688} \tag{A.7}$$

Where *K* is the dimensionless droplet's inertia parameter and φ is the dimensionless Langmuir parameter, respectively, defined as follows:

$$K = \frac{v\rho_w d^2}{18\mu L} \tag{A.8}$$

$$\varphi = \frac{Re^2}{K} \tag{A.9}$$

in which *v* is the wind speed (m/s), ρ_a and ρ_w are densities of air and water respectively (kg/m^3), μ is the absolute viscosity of air (μPa·s), *d* is the droplet diameter (m), *Re* is droplet's Reynolds number and *L* is the characteristic length of an object, i.e., cylinder or airfoil (m). When it comes to the estimation of the characteristic length of an object, the typical notion for the cylinder is to use radius, *R* while for the airfoils the typical notion is to use the leading-edge radius, *c* as a characteristic length. [9-10] In other words, the characteristic length of the reference cylinder and blade airfoil will be the same, provided the cylinder inscribes the leading edge radius of the airfoil, i.e., c = R.

The droplet diameter, *d*, is typically a median volume diameter (hereafter, MVD) of a droplet spectrum of a cloud. This is a standard approximation used in the icing studies, *first* introduced by Langmuir and Blodgett [11] and later verified by Finstad et al. [12] The MVD approximation usage originates from the fact that apart from using a rotating multicylinder device, there is currently no equipment available to measure MVD or distribution spectra to any degree of precision on-site. However, as it has been shown recently, [13] the multicylinder device may not accurately represent the actual in-cloud distribution using the MVD approximation. Moreover, as noted by Langmuir and Blodgett, [6] the different distributions with same MVD will have different collision efficiency, depending on value of inertia parameter, *K*. As shown in Finstad et al., [12] the discrepancy in the overall collision efficiency

values between the monodisperse distribution and the actual distribution spectrum under operating conditions used in that study are typically small enough to be ignored. However, considering vastly different values of the droplet inertia parameter, *K*, for cylinder and airfoil due to significant differences in the TAS faced by both the cylinder and the airfoil, it is deemed a reasonable assumption that the differences in the accreted ice mass caused by different distributions at two significantly different values of *K* will be significant. Therefore, in addition to the monodisperse distribution (also referred to as Langmuir A) four progressively wider distributions denoted Langmuir B – E (also referred in literature as gamma distributions) are used in this study. The distributions used in this study and their ratio of diameters, $(d/d_0)^n$ are given in Table A.2.

Table A.2 – Langmuir distributions.

LWC fraction	d/d_o **Langmuir B**	$(d/d_o)^{1.5}$ **Langmuir C**	$(d/d_o)^{2.0}$ **Langmuir D**	$(d/d_o)^{2.5}$ **Langmuir E**
0.05	0.56	0.42	0.31	0.23
0.1	0.72	0.61	0.52	0.44
0.2	0.84	0.77	0.71	0.65
0.3	1.00	1.00	1.00	1.00
0.2	1.17	1.26	1.37	1.48
0.1	1.32	1.51	1.74	2.00
0.05	1.49	1.81	2.22	2.71

Taking values from Table A.2, the overall collision efficiency of the spectrum (spectrum weighted overall collision efficiency) is calculated as:

$$\alpha_1 = \sum w_i \alpha_{1i} \tag{A.10}$$

where α_{1i} is the overall collision efficiency of *i*th bin and w_i is the LWC fraction of the *i*th bin. The overall collision efficiency of the *i*th bin is calculated as in Equations (A.4) to (A.9). Finally, the restriction $\alpha_{1i} = 0.01$ for cases when $K_i \leq 0.17$ is employed, based on Finstad et al. [6]

A.2.2. Numerical Model

The multiphase computational fluid dynamics (CFD)-based numerical simulations are carried out using ANSYS FENSAP-ICE, which uses Eulerian water droplet impingement solver. The existing analytical models of the droplet behavior such as Langmuir and Blodgett, Finstad et al. etc. solve the droplet trajectories using the Lagrangian particle tracking approach. The Eulerian method treats the particle phase as a continuum and develops its conservation equations on a control volume basis and in a similar form as that for the fluid phase. The Lagrangian method considers particles as a discrete phase and tracks the pathway of each individual particle. By studying the statistics of particle trajectories, the Lagrangian method is also able to calculate the particle concentration and other phase data. On the other hand, by studying particle velocity vectors and its magnitudes in Eulerian method, it is possible to reconstruct the pathways and trajectories of particles in a phase. The general Eulerian two-phase model for viscous flow consists of the Navier-Stokes equations augmented by the droplets continuity and momentum equations [14]:

$$\frac{\partial \alpha}{\partial t} + \vec{\nabla} \cdot \left(\alpha \overrightarrow{V_d}\right) = 0 \tag{A.11}$$

$$\frac{\partial \left(\alpha \overrightarrow{V_d}\right)}{\partial t} + \vec{\nabla}\left[\alpha \overrightarrow{V_d} \otimes \overrightarrow{V_d}\right] = \frac{C_D Re_d}{24K} \alpha \left(\overrightarrow{V_a} - \overrightarrow{V_d}\right) + \alpha \left(1 - \frac{\rho_a}{\rho_d}\right) \frac{1}{Fr^2} \tag{A.12}$$

where the variables α and $V_{d,a}$ are mean field values of, respectively, the water volume fraction and droplet velocity. The first term on the right-hand-side of the momentum equation represents the drag acting on droplets of mean diameter *d*. It is proportional to the relative droplet velocity, its drag coefficient C_D, and the droplets Reynolds number:

$$Re_d = \frac{\rho_a d V_{a,\infty} \left\| \overrightarrow{V_a} - \overrightarrow{V_d} \right\|}{\mu_a} \tag{A.13}$$

and an inertia parameter:

$$K = \frac{\rho_d d^2 V_{a,\infty}}{18 L_\infty \mu_a} \tag{A.14}$$

Where L_∞ is the characteristic length of the object. The second term represents buoyancy and gravity forces and is proportional to the local Froude number:

$$Fr = \frac{\left\| V_{a,\infty} \right\|}{\sqrt{L_\infty g_\infty}} \tag{A.15}$$

These governing equations describe the same physical droplets phenomenon as Lagrangian particle tracking approach. Only the mathematical form in which these equations are derived changes, using partial differential equations instead of ordinary differential equations. The droplet drag coefficient is based on an empirical correlation for flow around spherical droplets, or:

$$CD = (24/Red)\,(1 + 0.15 Red^{0.687}) \quad \text{for} \quad Red \leq 1300$$

$$CD = 0.4 \quad \text{for} \quad Red > 1300$$

The local and overall collision efficiencies are calculated following a completely different approach, when compared to Finstad et al. The local and overall collision efficiencies are calculated as follows:

$$\beta = -\frac{\alpha \overrightarrow{V_d} \cdot \vec{n}}{w V_\infty} \tag{A.16}$$

where α is the local volume fraction (kg/m^3) and $\vec{n}$ is the surface normal vector. The overall collision efficiency is an integration of local collision efficiencies over surface area and is given as

$$\beta_{tot} = \frac{\int \beta \, dA}{L_\infty^2} \tag{A.17}$$

The turbulence model used in this study if Menster's SST k-ω model. [14-15] The surface roughness model used in CFD simulations is NASA sand-grain roughness which is computed with an empirical NASA correlation for icing. [14, 16]

A.3. Results and discussion

This section describes the results obtained from the CFD-based numerical simulations and the analytical model (ISO 12494) in this study. CFD simulations are mainly used for obtaining the values of *k*–factor, as was the case in original work of Turkia et al. [4] and analyzing the potential effects of the airfoil geometry on the *k*–factor itself. The main reason of using the CFD simulations in this study is the detailed treatment of airflow and the droplet impingement characteristics as compared to the potential flow approximation used in the analytical calculations. The use of analytical tools is governed by the necessity of making the results ISO 12494 compliant, as well as describing the *k*–factor values and any associated changes of it using the currently established framework. Moreover, the use of the ISO 12494 model allows for coupling of the analytical results with the mesoscale modeling, the sheer size of which makes them computationally infeasible for extensive CFD usage. This coupling allows for wind park icing load maps estimations in mesoscale simulations, while making sure that any obtained results are governed by the currently accepted icing modeling framework.

A.3.1. *k*–factor Values

Table A.3 shows the ice mass accretion and *k*–factor values from the CFD based numerical simulations for reference cylinder and the airfoils used in this study. The values of ice accretions are in g/m, and the values of *k*–factor are given with respect to each droplet distribution spectrum. The ice accretion masses on airfoils are given for 60 m/s wind speed, while ice accretion for reference cylinder are given for 7 m/s wind speed.

Table A.3 – Ice mass at 60 m/s and k–factor values from CFD simulations.

Distribution / Object	A, g/m	B, g/m	C, g/m	D, g/m	E, g/m
Cylinder (7 m/s)	44.140	45.692	53.279	59.367	73.432
NACA 0012	1506.483	1520.233	1560.729	1636.556	1735.632
NACA 4412	1525.261	1518.949	1549.694	1625.232	1715.327
NACA 6412	1579.491	1565.593	1613.423	1695.436	1787.881
NACA 23012	1471.361	1500.879	1530.999	1597.035	1660.198
N-22	1519.840	1519.856	1566.159	1639.767	1719.454
k–factor values					
NACA 0012	34.13	33.27	29.29	27.57	23.64
NACA 4412	34.55	33.24	29.09	27.38	23.36
NACA 6412	35.78	34.26	30.28	28.56	24.35
NACA 23012	33.33	32.85	28.74	26.90	22.61
N-22	34.43	33.26	29.40	27.62	23.42

As it can be seen from Table A.3, the values of *k*–factor tend to vary among different distributions and airfoils, with the maximum obtained value being 35.78 and minimum being 17.24, and in general, having the tendency to decrease as distribution becomes progressively "wider". In addition, there is a small difference in the *k*–factor values for all the airfoils in this study. From the results in Table A.3, it can be said that the *k*–factor also depends on the airfoil type/geometry and the droplet distribution spectrum used.

A.3.2. Effect of Airfoil Geometry

The effect of airfoil geometry on the ice accretion and the *k*–factor values are investigated by comparing the overall collision efficiency values for the cylinder and the airfoils at 7 and 60 m/s wind speed conditions using the CFD-based numerical simulations which were carried out for this study. In order to permit the direct comparison, Table A.4 shows the ice masses in the numerical simulations for 7 m/s wind conditions, while the ice masses from 60 m/s conditions are given in Table A.3. Table A.5 shows the overall collision efficiency values in the numerical simulations, in addition to "*Reference*" row showing the overall collision efficiency values for the analytical calculations. The overall collision efficiency values are obtained for the operating conditions in Table A.1 with the droplet distributions given in Table A.2.

Table A.4 – Ice accretion for airfoils at 7 m/s wind speed from CFD simulations.

Distribution / Airfoil	A, g/m	B, g/m	C, g/m	D, g/m	E, g/m
Cylinder	44.140	45.692	53.279	59.367	73.432
NACA 0012	12.991	18.041	23.813	31.536	40.790
NACA 4412	14.512	20.147	25.248	31.786	41.011
NACA 6412	19.713	22.879	27.137	33.722	43.131
NACA 23012	16.724	21.209	26.565	33.852	41.452
N-22	17.126	21.020	26.164	33.921	42.599

Table A.5 – Overall collision efficiency values.

Distribution / Airfoil	Langmuir A	Langmuir B	Langmuir C	Langmuir D	Langmuir E
Wind speed = 60 m/s					
Reference (Analytical)	0.613	0.600	0.589	0.580	0.570
CFD – 60 m/s					
Cylinder	0.519	0.508	0.501	0.494	0.488
NACA 0012	0.581	0.587	0.602	0.631	0.670
NACA 4412	0.588	0.586	0.598	0.627	0.662
NACA 6412	0.609	0.604	0.622	0.654	0.690
NACA 23012	0.568	0.579	0.591	0.616	0.641
N-22	0.586	0.586	0.604	0.633	0.663
Wind speed = 7 m/s					

Reference (Analytical)	0.179	0.182	0.191	0.206	0.220
CFD – 7 m/s					
Cylinder	0.146	0.151	0.176	0.196	0.243
NACA 0012	0.043	0.060	0.079	0.104	0.135
NACA 4412	0.048	0.067	0.083	0.105	0.136
NACA 6412	0.065	0.076	0.090	0.112	0.143
NACA 23012	0.055	0.070	0.088	0.112	0.137
N-22	0.057	0.070	0.087	0.112	0.141

Table A.5 shows an interesting situation. If the geometry would not be important, all values for the respective distribution would be equal, as airfoils with same characteristic length should accrete the same amount of mass as the cylinder with the same characteristic length under same operating conditions, which is the case in the analytical calculations and assumptions. Instead, at 7 m/s wind speed the airfoils tend to accrete significantly less ice mass than the reference collector, while at 60 m/s wind speed conditions, the situation reverses and all airfoils accrete more mass than the reference collector. Furthermore, Table A.5 shows that for wider distributions the reference collector (cylinder) tends to accrete less ice mass as the distributions widen, for 60 m/s wind speed conditions, in full accordance with Langmuir and Blodgett. [11] However, this is not the case for any of the tested airfoils, which tend to accrete more mass with the wider distributions, for both 7 and 60 m/s wind speed conditions. Moreover, if ice accretion on all airfoils should be the same, by extension, the ice shapes should also be the same. Contrary, if there are tangible differences present, such as change in local collision efficiency or maximum impingement angle values, one can see those by investigating ice shapes. Figure A.1 presents comparison of ice shapes of NACA 0012, 23012, 4412 and 6412 airfoils at 60 m/s wind speed conditions for all droplet distribution spectra in this study.

Figure A.1 shows that the ice shape becomes asymmetric, when comparing NACA airfoils, and this asymmetry roughly follows the shape of leading edge of the airfoil. In addition, observe the changes to the maximum impingement angles occurring with the droplet distribution spectrum change, while stagnation line thicknesses are relatively the same across all the droplet distribution spectra. Furthermore, if variance in ice mass is caused by the effects of distribution spectra only, the relative values of the overall collision efficiencies would change by the same factor with the change of the droplet distribution spectrum when using, for example, the monodisperse distribution as a reference, assuming that dry growth assumption of $\alpha_2 = \alpha_3 = 1$ is valid. As it can be seen from Table A.5 the overall collision efficiency values change by different ratios for all objects with the change of droplet distribution spectrum, which clearly indicates the effect of the geometry on the ice accretion. Two possible reasons are identified:

a) The inertia parameter for airfoils is not the same, most likely due to characteristic dimension being different.
b) Different airfoils experience different airflow and thus associated effects, for example, boundary layer effects become important.

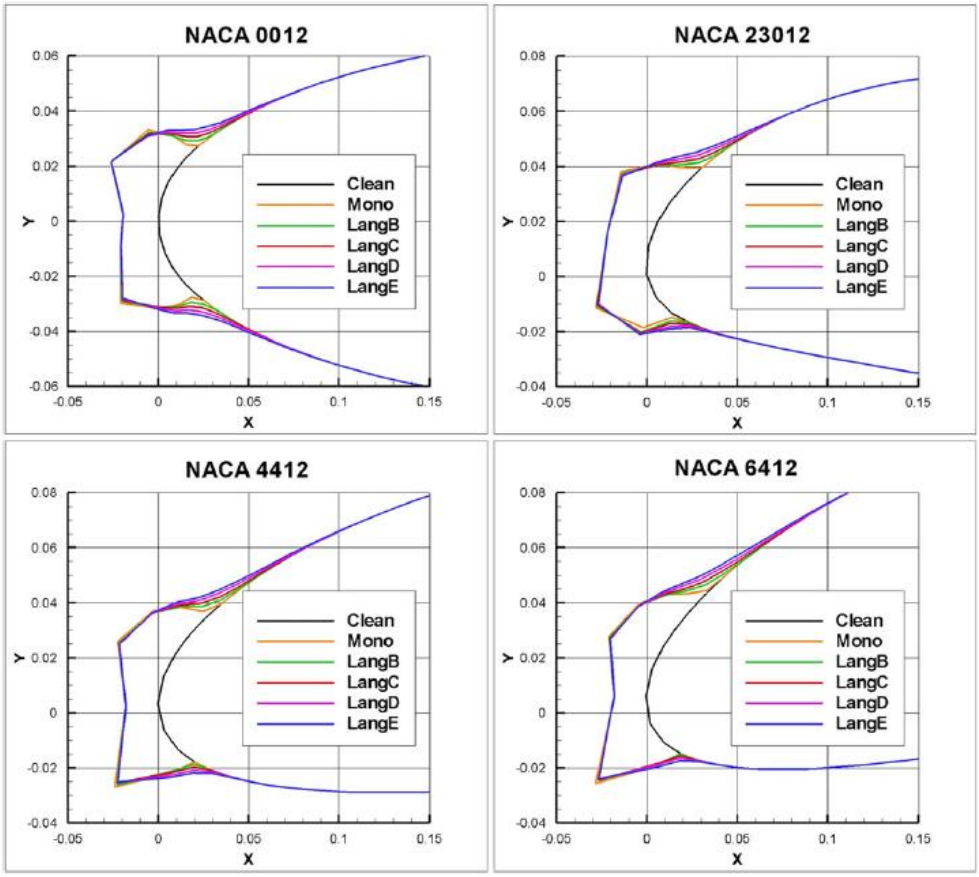

Figure A.1 – Ice shapes of NACA 0012, 4412, 6412 and 23012.

The first reason, while highly logical, seems unlikely as it goes against core concepts of well-established in-flight icing theory. The second possible reason seems more likely, as compared with the cylinder, the airfoil is aerodynamically streamlined object, specifically designed for maximizing lift and minimizing drag, thus creating the possibility of different flow conditions, experienced by different airfoils. However, without experimental study of airfoil ice accretion in similar conditions the verification of this claim is complicated. Finally, note the difference in the overall collision efficiency values between thee analytical results in the "*Reference*" row of Table A.5 and the numerical results elsewhere. The difference in the overall collision efficiency values can be explained by fundamentally different treatment of the fluid flow in the analytical and numerical models. The analytical model treats the fluid flow as inviscid potential flow, while the numerical model treats it as viscid turbulent flow. Thus, the difference in the overall collision efficiency values can be attributed to the potential flow theory approximation limitations.

A.3.3. Effect of Droplet Distribution Spectrum and MVD

As seen from Table A.3 the *k*–factor values depend on the droplet distribution spectrum used both in numerical and analytical results. The effect of the droplet distribution change on the *k*–factor values is investigated within the framework of the analytical model of ISO 12494 standard. Following the analytical procedure from section A.2.1, it is possible to calculate the ratio of the accreted ice between the wind turbine blade and the reference collector as

$$\frac{\left(dm/dt\right)_b}{\left(dm/dt\right)_c} = \frac{(\alpha_1\alpha_2\alpha_3 vAw)_b}{(\alpha_1\alpha_2\alpha_3 vAw)_c} \tag{A.18}$$

where subscript *b* stands for the blade, and subscript *c* stands for the collector, assuming that dry growth conditions are maintained for both the collector and airfoil, thus $\alpha_2 = \alpha_3 = 1$, and eliminating the common variables, the ratio of accreted ice mass in g/m/hr can be obtained as

$$\frac{dm_b}{dm_c} = \frac{\alpha_{1b} v_b}{\alpha_{1c} v_c} = \frac{\alpha_{1b}}{\alpha_{1c}} \frac{v_b}{v_c} = v_r \alpha_{1r} \tag{A.19}$$

where v_r and α_{1r} are ratios of wind speeds and overall collision efficiency. In addition, it can be noted that ratio of wind speeds is equal to the ratio of droplet inertia parameters, under previously mentioned assumptions, between the reference collector and the wind turbine blade, as the droplet inertia parameter *K* is linearly dependent on the wind speed *v*. Thus assuming constant $v_r = 60/7 = 8.571$ under operating conditions from Table A.1 and computing the values of α_{1r} using the analytical model of ISO 12494, one can introduce the "pseudo" *k*–factor, γ calculated as

$$\gamma = v_r \alpha_{1r} \tag{A.20}$$

Again, assuming $v_r = 8.571$ from the operating conditions in Table A.1 and computing α_1 values for the droplet distribution spectra from Table A.2, the resultant values of "pseudo" *k*–factor, γ, for the droplet distributions in this study are given in Table A.6.

The agreement between *k*–factor values in Tables A.6 and A.3 is somewhat reasonable, with the differences in values not exceeding 20%, with agreement having a tendency to improve as the distribution progressively "widens". Again, some of this discrepancy can be explained by the difference in fluid flow modeling between the CFD simulations and the analytical model. Moreover, Table A.7 shows the calculated γ values for conditions in Turkia et al. [4] for comparison purposes. While Turkia et al. have used the monodisperse distribution (distribution A in this study), the results have been tabulated for all distributions in this study. Here the agreement with value $k = 20$ is sufficiently good, and small discrepancies in numbers can be explained by possible differences in handling small connected values, for example pressure or viscosity. However, in their study, Turkia et al. assumed MVD of 25 microns. As MVD being one of the most important parameters in the ice accretion modeling, it is necessary to investigate how the change in the MVD value will affect the *k*–factor values. Table A.8 shows the value of the “pseudo” *k*–factor, γ, for the range of different MVDs under operating conditions from Table A.1. From Table A.8 it can be seen that "pseudo" *k*–factor γ tends to vary significantly, depending on the MVD with maximum value being approximately 60 and smallest being approximately 12, both for Langmuir A distribution, at 15 and 50 microns, respectively. Moreover, observe that for lower values of MVD, the wider distributions tend to have smaller values of γ; however, for bigger MVD sizes, for example, 40 – 50 microns, the situation is opposite, and narrower distributions tend to have smaller values of γ. The only row of values, where γ is close to 20 for all the distributions is for 25 microns MVD, the same value used by Turkia et al. in their study. Turkia et al. used NREL 5 MW reference turbine. An important question here, how the *k*–factor will change for different turbines, as TSR value can change based on hub height and RPM, and TSR and γ are connected values as one can see from preceding discussion.

Table A.6 – Analytical comparison of spectrum-weighted parameter (K), overall collision efficiency (α_{1f}), and "pseudo" k–factor γ for Langmuir distributions at 7 and 60 m/s wind speed for reference collector.

Distribution	MVD (µm)	*K* (7 m/s)	α_1 (7 m/s)	*K* (60 m/s)	α_1 (60 m/s)	α_1 ratio (α_{60}/α_7)	γ
Langmuir A	20.0	0.606	0.179	5.191	0.613	3.425	29.35
Langmuir B	20.0	0.647	0.182	5.542	0.600	3.328	28.26
Langmuir C	20.0	0.714	0.191	6.093	0.589	3.084	26.33
Langmuir D	20.0	0.828	0.206	7.045	0.580	2.816	24.00
Langmuir E	20.0	0.988	0.220	8.366	0.570	2.591	21.94

Table A.7 – Values of "pseudo" k–factor γ for conditions in Turkia et al. [4]

Distribution	A	B	C	D	E
γ	21.44	21.39	20.96	20.17	19.37

Table A.8 – Dependence of "pseudo" k–factor on MVD in analytical calculations.

Distribution / MVD (µm)	A	B	C	D	E
15	59.98	50.08	41.55	33.96	28.63
20	29.35	28.26	26.33	24.00	21.94
25	20.86	20.74	20.19	19.22	18.31
30	17.03	17.14	17.00	16.55	16.09
35	14.89	15.06	15.07	14.90	14.63
40	13.55	13.73	13.80	13.77	13.63
45	12.63	12.81	12.91	12.94	12.90
50	11.97	12.14	12.25	12.32	12.35

A.3.4. Effect of Blade Tip Speed Ratio

For investigation of TSR on values of *k*–factor, two wind turbines have been selected – Siemens SWT-2.3-93 [17] and Vestas V112-3.45 [18]. The operating parameters for those turbines are listed in Table A.9.

Table A.9 – Operating parameters of Siemens SWT-2.3-93 [17] and Vestas V112-3.45 [18] wind turbines.

Parameter	SWT-2.3-93	V112-3.45
Blade length (m)	45	54.65
RPM	6 – 16	6.2 – 17.7
Hub Height (m)	80	80

It should be noted that these wind turbines have options when it comes to hub height, for example, Vestas V112-3.45 has optional hub heights of 80, 94, 119 and 140 meters. The hub height of 80m has been selected for both turbines for consistency purposes. The calculations are performed using the analytical model of ISO 12494, as this allows to estimate the wide range of possible TSRs and their impact on *k*–factor values in quick and concise manner. The operating conditions for this examples are

from Table A.1. It is worth mentioning that the wind speed of 7 m/s is assumed to be the value at the reference collector, being mounted on met mast 10 meters in height. Moreover, for simplicity, following assumptions are being made in the calculations:

- It is assumed that wind direction is always normal to rotor plane.
- It is assumed that the reference collector and the blade at 85% of length have the same value of characteristic length, i.e., cylinder diameter or twice the leading edge radius, respectively.
- It is assumed that RPM of wind turbine is independent of freestream wind speed.

The last assumption is made purely for illustrative purposes, while second assumption is made for simplification purposes. If it is known that reference object and the blade at 85% of the length have different characteristic lengths than the γ ratio has to be modified as

$$\gamma = v_r \alpha_{1r} A_r \tag{A.21}$$

where A_r is the ratio of areas, provided dry growth regime is maintained for both the reference collector and wind turbine blade. It should be noted that in this case the ratio of overall collision efficiency will be more complicated due to its non-linear dependence on inertia parameter, which in turn depends on characteristic length. Noting that first assumption results in that the normal velocity component, which is a product of freestream wind speed and height effect and tangential component, which is a product of blade length and turbine RPM. Thus, the TAS of the blade at 85% section can be obtained as $V = \sqrt{(xv)^2 + (r\omega)^2}$, where x is height factor, v is freestream velocity, r is the radial distance at 85% section and ω is rotational velocity of the blade in rad/s. The value of V is then used to compute the overall collision efficiency and the inertia parameter of the blade. The *k*–factor is computed by dividing previously mentioned values by overall collision efficiency and the inertia parameter of the reference collector. Figure 2 shows the graphical comparison of calculated *k*–factors for the conditions, specified in Table A.9. The dotted horizontal line in Figure A.2 corresponds to value of *k*–factor k = 20. Moreover, Figure A.2 shows the results for all distributions (A – E) in this study to additionally show the effect of droplet distribution spectrum.

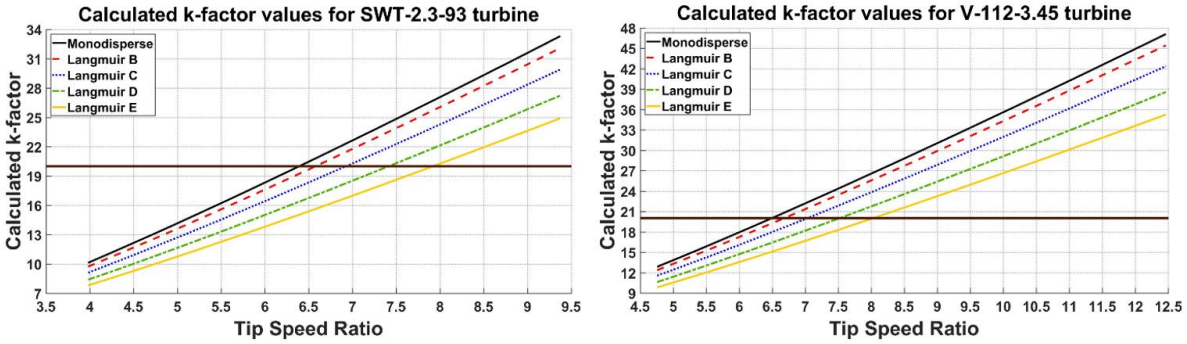

Figure A.2 – k–factor values for Siemens SWT-2.3-93 wind turbine (left) and Vestas V112-3.45 wind turbine (right).

Summarizing the value of k–factor depends on a few critical parameters, namely:

- The droplet distribution used.
- The value of median volume diameter.
- Wind speed ratio and TSR.

- Airfoil geometry.

Since the droplet distribution spectra is somewhat difficult to estimate in practice, the usage of Langmuir distributions is recommended in addition to the monodisperse distribution, and in particular, the Langmuir D distribution, as it is a "standard" distribution for in-flight icing studies. [19-21] In addition, as it is seen from Table A.8, the Langmuir D distribution has the value of the "pseudo" *k*–factor γ = 20.17, which is close to k = 20, as was initially proposed by Turkia et al..

A.4. Conclusion

In this paper the investigation into *k*–factor, describing the ratio of ice accretion on reference collector and wind turbine blade, has been carried out by performing a series of numerical simulations using modern CFD software and analytical calculations within the framework of the existing ice accretion theory (ISO 12494). The results show that *k*–factor is not equal to constant 20, contrary to currently postulated assumption and can vary to a significant degree, depending on a number of different parameters not accounted in present model for it. These factors include the effect of object's geometry on ice accretion, droplet overall collision efficiencies, droplet distribution spectrum and MVD under significantly different ambient conditions, pertaining to wind speed and TSRs experienced by both the reference collector and wind turbine blade. While the results presented in this paper can be considered somewhat simplistic, the explanation of *k*–factor variance is established based on effects of MVD, droplet distribution, TSRs, and geometry effects. However, further numerical experimentations and experimental validation are necessary, in particular, when it comes to the ice accretions on different airfoils under different operating conditions. Despite this, the obtained results still show the shortcomings of current implementation for empirical *k*–factor ratio and as a result modifications and improvements for this ratio are needed. Considering the complexity of the process in question, there is a significant chance that ice accretion on a wind turbine, when compared to ice accretion of reference collector cannot be explained using simple, constant, dimensionless ratio.

References

1. Tammelin B, Cavaliere M, Holttinen H, Morgan C, Seifert H, Säntti K. 2000. Wind energy production in cold climates (WECO), Finnish Meteorological Institute, EUR 19.398.
2. Jasinski WJ, Noe SC, Selig MS, Bragg MB. Wind turbine performance under icing conditions. Trans ASME, J Sol Energy Eng. New York, NY, USA. February. 120:60-65.
3. Seifert H, Westerhellweg A, Kröning J. 2003 Risk analysis of ice throw from wind turbines.
4. Turkia V, Huttunen S, Wallenius T. Method for estimating wind turbine production losses due to icing, VTT, 2013, Finland.
5. ISO 12494:2001(E), 2001. Atmospheric icing of structures. Standard. International Organization for Standardization. Geneva, CH.
6. Finstad KJ, Lozowski EP, Gates EM. A computational investigation of water droplet trajectories. J Atmos Oceanic Tech. 1988;5(1):160-170. https://doi.org/10.1175/1520-0426(1988)005<0160:ACIOWD>2.0.CO;2.
7. Bredesen RE, Refsum H. 2015. IceRisk—methods for evaluating risk caused by ice throw and ice fall from wind turbines and other tall structures, 16th International Workshop on Atmospheric Icing, Uppsala, Sweden.

8. Makkonen L. Models for the growth of rime, glaze, icicles and wet snow on structures. Phil Trans R Soc Lond A. 2000; 358:2913-2939. https://doi.org/10.1098/rsta.2000.0690. Published 15 November 2000.
9. Tsao J-C, Lee S. 2012. Evaluation of icing scaling on swept NACA 0012 airfoil models, NASA/CR–2012-217419, NASA.
10. Tsao J-C, Anderson DN. 2005. Additional study of water droplet median volume diameter (MVD) effects on ice shapes, NASA/CR–2005-213853.
11. Langmuir I, Blodgett K. 1946. A mathematical investigation of water droplet trajectories. Army Air Forces technical report 5418. Army Air Forces Headquarters, Air Technical Service Command.
12. Finstad KJ, Lozowski EP, Makkonen L. On the median volume diameter approximation for droplet collision efficiency. J Atmos Sci.1988b;45(24):4008-4012. https://doi.org/10.1175/1520-0469(1988)045<4008:OTMVDA>2.0.CO;2.
13. Jones KF, Thompson G, Claffey KJ, Kelsey EP. Gamma distribution parameters for cloud drop distributions from multicylinder measurements. J Appl Meteorol Climatol. 2014. https://doi.org/10.1175/JAMC-D-13-0306.1;53(6):1606-1617.
14. FENSAP-ICE Technical Manual.
15. Wilcox DC. Re-assessment of the scale-determining equation for advanced turbulence models. AIAA J. 1988;26(11):1299-1310.
16. Shin J, Bond T. 1992. Experimental and computational ice shapes and resulting drag increase for a NACA 0012 airfoil, NASA Technical Manual 105743, 1992.
17. Siemens SWT 2.3-93 Technical specifications.
18. Vestas V112-3.45 Technical specifications.
19. Wright W., 2008, User's manual for LEWICE version 3.2, NASA/CR–2008-214255, NASA.
20. Bidwell CS. 2012. Particle trajectory and icing analysis of the E3 turbofan engine using LEWICE3D version 3, NASA/TM–2012-217696, NASA.
21. Papadakis M, Wongm S-C, Rachman A, Hung KE, Vu GT, Bidwell CS. 2007. Large and small droplet impingement data on airfoils and two simulated ice shapes, NASA/TM-2007-213959.

Paper B

Study of Ice Accretion along Symmetric and Asymmetric Airfoils

Jia Yi Jin and Muhammad Shakeel Virk

Journal of wind Engineering & Industrial Aerodynamics, 2018, Volume 179, p. 240-249.

Doi: 10.1016/j.jweia.2018.06.004

Author's Contribution

Jia Yi Jin has contributed substantially in the proposal of conceptualization, data curation, formal analysis, investigation, methodology, resources, software, visualization, validation, and writing of the paper.

B. Study of ice accretion along symmetric and asymmetric airfoils

This is a reprint

Jia Yi Jin and Muhammad Shakeel Virk

Arctic Technology and Icing Research Group
Institute of Industrial Technology
Faculty of Engineering Science and Technology
UiT- The Arctic University of Norway
Norway

Abstract

A parametric numerical study of ice accretion along symmetric (NACA-0012) and asymmetric (NACA-23012) airfoils has been carried out at different operating and geometric conditions with the aim to better understand the ice accretion along wind turbine blades. The results show that the airfoil geometric shape and size has an effect on the rate and shape of ice accretion. Streamline ice shapes are observed in the case of symmetric airfoil in comparison to the ones found for the asymmetric airfoil. Aerodynamic characteristics of both airfoils for clean and iced conditions were analyzed at different angles of attack ranging from -16º to +16º. The analysis shows a decrease in the aerodynamic characteristics of the iced airfoils as compared to the clean airfoil. The parametric analysis of the ice accretion at different operating and geometric conditions show an increase in the ice growth with the increase in air velocity and droplet size, whereas a change in the atmospheric temperature significantly affects the accreted ice shapes. A decrease in accreted ice mass and thickness is observed with the increase of airfoil geometric size.

Keywords:
Airfoil; Atmospheric ice; Wind turbine; CFD; Aerodynamics.

B.1. Introduction

Icing on wind turbines has been recognized as a hindrance limiting the wind turbine performance and energy production at elevated cold climate regions [1]. Such losses have been reported to lead up to a 17% decrease in Annual Energy Production (AEP) and 20–50% in the aerodynamic performance [2]. A variety of the problems due to icing have been documented including loss of power production, disrupted blade aerodynamics [3], overloading due to delayed stall, increase fatigue of components due to imbalance in the ice load [3] and damage caused by the shedding of ice chunks [4]. Worldwide, the installed wind energy capacity in the ice prone regions in 2015 was of 86.5 GW and is expected to reach 123 GW by 2020 [5]. This highlights the importance of a better understanding of the ice accretion process on wind turbine with the aim to improve safety and reduce the Capital Expenditure (CAPEX) and Operational Expenditure (OPEX). The international Energy Agency (IEA) Task 19 – *Wind energy in cold climate* has also urged the need for better understanding of ice accretion physics along wind turbines.

Better knowledge of atmospheric ice accretion on wind turbine blades is critical in determining what geometric features of blade profiles (airfoil) contribute to the performance degradation during ice accretion and how these may differ for different airfoils. Atmospheric ice accretion on wind turbine blades mainly occurs due to collision of super cooled water droplets. These super cooled water droplets may immediately or with some short delay freeze into ice on surface [6]. The effect of icing on wind turbine blades is generally an altered profile shape which results in a change of its aerodynamic characteristics. This affects the wind turbine torque and power production. The results of such aerodynamic changes can be seen as a decrease in the in-plane (rotating) force both because of a decrease in the lift coefficient (C_L) and an increase in the drag coefficient (C_D) [7].

Icing on wind turbine blades depends on both its operating *(temperature, velocity, MVD and LWC)* and geometric *(size and shape)* characteristics. Different temperatures and heat balance situations along wind turbine blade will result in accreted ice of different mass and shapes [8]. The change in accreted ice mass and shape effects the flow behaviour along the blade profile and aerodynamic performance [9], where the blade drag coefficient has a temperature dependence that is relatively constant through the dry rime ice region, that increases by increasing the temperature *(due to the transition to formation of horns)* and then drops sharply as the higher temperatures melts the horns [10]. On the basis of various geometric shapes of ice, it can be classified into 5 different groups; *1) roughness ice, 2) horn ice, 3) stream wise ice, 4) span wise ridge ice and 5) runback ice* [6]. Virk et al. [8] showed that the air temperature alone cannot be used to differentiate between different types of ice and resultant ice shapes, but that droplet size, air velocity and liquid water content (LWC) can also effect the icing event.

Different researchers have studied the effects of ice accretion on airfoil performance. Most of the investigations have been performed using either ordinary wind tunnel with artificial ice templates attached to the blade profile or icing wind tunnel. However, for the last decade or so the computational fluid dynamics (CFD) based numerical techniques have begun to play a significant role in simulating and determining the performance of wind turbines under icing conditions [11]. CFD can provide the economical insight details of flow physics, which is not easily possible using icing wind tunnel. Icing of the wind turbines and its resulting effects on power production have been simulated for a variety of cases [12-15]. Bak et al. [16] and Ferrer et al. [17] utilized custom made 3D CFD models to investigate the wind turbine rotor aerodynamics. Chi et al. [18] studied several turbulence models to analyze the flow behavior around the iced airfoils. Kwon et al. [19] and Masoud et al. [20] compared the

experimental and CFD based numerical results about aerodynamic performance analyses of the iced airfoils. Zhu et al. [21] used CFD based numerical approach for determining the drag of the iced airfoils. Virk et al. [7, 10, 22] and Etemaddar et al. [23] studied the effects of different operating and geometric parameters on ice accretion along the wind turbine blade profiles using CFD based numerical approach.

Blade profiles (airfoil) can be divided into two categories: *symmetric and asymmetric*. The camber of an airfoil determines its curvature and its type: symmetric airfoils have zero camber, whereas asymmetric airfoils have non-zero camber. Symmetric and asymmetric airfoils have different aerodynamic characteristics which can possibly lead to different ice accretion process. A change in the airfoil geometric shape can affect the flow behavior along the upper and lower surfaces which also affects the heat fluxes and shear stress distribution. This results in a change in the droplet behavior and the resultant ice accretion along its surface. Not much work has been done so far to better understand and compare the ice accretion along symmetric and asymmetric airfoils, so the objective of this paper is to study the ice accretion along symmetric (NACA-0012) and asymmetric (NACA-23012) blade profiles at different operating and geometric conditions.

B.2. Numerical Setup

CFD based multiphase numerical analysis are carried out to study the airflow and droplet behaviour and simulate the ice accretion at different operating and geometric conditions. Aerodynamic coefficients of these airfoils are calculated and compared for both clean and iced conditions. This numerical study is carried out using ANSYS FENSAP and FLUENT. Prior to this numerical study, the authors performed an unpublished comparison between ice shapes along NACA-0012 obtained from FENSAP-ICE, LEWICE (NASA, Cleveland, Ohio, USA) and icing tunnel experiments. A good agreement was found. Different other researchers have also used FENSAPICE to simulate the ice shapes along different airfoils in comparison to the icing tunnel experimentation data, where they also found a good agreement between simulated and experimental results. The numerical study of atmospheric ice accretion on airfoils includes the computation of the mass flux of icing particles as well as the determination of the icing conditions. These can be numerically simulated by means of integrated thermo-fluid dynamic models, which involve the fluid flow simulation, droplet behavior, surface thermodynamics and phase changes. The numerical study of airflow behavior is carried out by solving nonlinear partial differential equations for the conservation of mass, momentum and energy.

$$\partial \rho_\alpha / \partial t + \vec{\nabla}(\rho_\alpha \overrightarrow{\boldsymbol{v_\alpha}}) = 0 \tag{B.1}$$

$$\partial \rho_\alpha \overrightarrow{\boldsymbol{v_\alpha}} / \partial t + \vec{\nabla}\,(\rho_\alpha \overrightarrow{\boldsymbol{v_\alpha}}\ \overrightarrow{\boldsymbol{v_\alpha}}) = \vec{\nabla} \cdot \sigma^{ij} + \boldsymbol{\rho_\alpha}\, \vec{g} \tag{B.2}$$

$$\partial \rho_\alpha E_\alpha / \partial t + \vec{\nabla}\,(\rho_\alpha \overrightarrow{\boldsymbol{v_\alpha}} H_\alpha) = \vec{\nabla}\left(\kappa_\alpha \left(\vec{\nabla}\, T_\alpha\right) + \nu_i \tau^{ij}\right) + \boldsymbol{\rho_\alpha}\, \vec{g}\, \overrightarrow{\boldsymbol{v_\alpha}} \tag{B.3}$$

Where ρ is the density of air, v is the velocity vector, subscript α refers to the air solution, T refers to the air static temperature in Kelvin, σ^{ij} is the stress tensor and E and H are the total initial energy and enthalpy, respectively. The sand grain roughness height for the iced airfoil surface is calculated using NASA's roughness model from the following equations.

$$[(k_s/c)/((k_s/c)_{base})]_{V_\infty} = 0.4286 + 0.0044139 V_\infty \tag{B.4}$$

$$[(k_s/c)/((k_s/c)_{base})]_{LWC} = 0.5714 + 0.2457(LWC) + 1.2571(LWC)^2 \tag{B.5}$$

$$[(k_s/c)/((k_s/c)_{base})]_{T_s} = 0.047T_s - 11.27 \quad \text{(B.6)}$$

Where LWC is Liquid Water Content, and $(k_s/c)_{base}$=0.001177. Whereas, the corresponding value of NASA sand-grain roughness is obtained:

$$k_s = [(k_s/c)/((k_s/c)_{base})]_{V_\infty}[(k_s/c)/(k_s/c)_{base}]_{LWC}[(k_s/c)/((k_s/c)_{base})]_{T_s}(k_s/c)_{base}c \quad \text{(B.7)}$$

Two phase flow *(air and water droplets)* is simulated using the Eulerian approach, where the super cooled water droplets are assumed to be spherical. The Eulerian two phase fluid model consists of the Navier Stokes equation with the water droplets continuity and momentum equation. The water droplet drag coefficient is based on the empirical correlation for the flow around the spherical droplets described by Clift et al. [24]

$$\partial\alpha/\partial t + \vec{\nabla}\left(\alpha\overrightarrow{V_d}\right) = 0 \quad \text{(B.8)}$$

$$\partial\left(\alpha\overrightarrow{V_d}\right)/\partial t + \vec{\nabla}\left(\rho_\alpha\,\overrightarrow{V_d}H_d\right) = C_D Re_d/24k\;\alpha\left(\overrightarrow{V_a} - \overrightarrow{V_d}\right) + \alpha(1-\rho_a/\rho_d)\,1/(Fr^2)\,\vec{g} \quad \text{(B.9)}$$

Where α is the water volume fraction, V_d is the droplet velocity, C_D is the droplet drag coefficient and Fr is the Froude number. The numerical analysis is carried out for different droplet distribution spectrums (Langmuir A–E) at a constant droplet median volume diameter (MVD). Surface thermodynamics is calculated using the mass and energy conservation equations, considering the heat flux due to convective and evaporative cooling, heat of fusion, viscous and kinetic heating. For the conservation of mass, the partial differential equation on solid surfaces shows as follow:

$$\rho_f\left[\partial h_f/\partial t + \vec{\nabla}\left(\bar{V}_f h_f\right)\right] = V_\infty LWC\beta - \dot{m}_{evap} - \dot{m}_{ice} \quad \text{(B.10)}$$

Equation B.11 expresses conservation of energy:

$$\rho_f\left[\left(\partial h_f c_f \dot{T}_f\right)/\partial t + \dot{\nabla}\left(\partial h_f c_f \dot{T}_f\right)\right] = \left[c_f\left(\tilde{T}_\infty - \tilde{T}_f\right) + \left(\left\|\vec{V}_d\right\|^2\right)/2\right]V_\infty LWC\beta$$
$$-L_{evap}\dot{m}_{evap} + \left(L_{fusion} - c_s\tilde{T}\right)\dot{m}_{ice} + \sigma\varepsilon(T_\infty^4) - T_{f^4} - c_h\left(\tilde{T}_f - \tilde{T}_{ice,rec}\right) + Q_{anti-icing} \quad \text{(B.11)}$$

The coefficients ρ_f, c_f, c_s, σ, ε, L_{evap}, L_{fusion} are physical properties of the fluid and of the solid. The reference conditions$\tilde{T}_\infty$, V_∞, LWC are the airflow and droplets parameters. ALE (Arbitrary Langrangian Eulerian) formulation is used for the mesh displacement due to ice accretion in time. This approach adds the grid speed terms to the Navier–Stokes equations to account for the mesh velocity [25]. C–type structured numerical grid having 55000 elements was used for both airfoils. Detailed mesh sensitivity analysis were carried out to accurately determine the boundary layer characteristics *(shear stress and heat fluxes)*, a y+ values of less than 1 is used near the wall surface. Number of mesh elements and y+ value was selected based upon the heat flux calculations, where a numerical check was imposed that the heat flux computed with the classical formulae dT/dn should be comparable with the heat flux computed with the Gresho's method. The roughness height for the iced surface was calculated using NASA model. The one equation Spalart–Allmaras turbulence model is used. The numerical simulations are carried out at operating and geometric conditions specified in Table B.1.

Table B.1 – Operating & geometric conditions used.

Airfoil	**NACA-0012 and NACA-23012**
Chord length (m)	1
Angle of attack (AOA, degree)	-16,-12,-8,-4,0,4,8,12,16
Air velocity (m/s)	5,10,30,50,53.7
Temperature (Celsius)	-1, -5,-15
MVD (microns)	15,20,40,60
Droplet distribution	Langmuir A, B, C, D and E
LWC (g/m^3)	0.4
Simulation time (min)	10

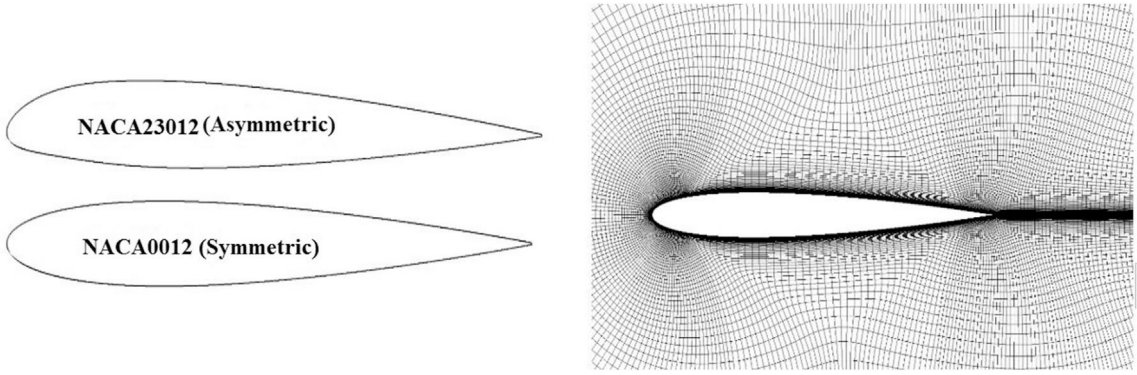

Figure B.1 – Numerical grid used for the simulations.

B.3. Results and Discussion

B.3.1. Effects of Operating Parameters

To study the effects of operating parameters variation on the rate and shape of ice accretion along symmetric and asymmetric airfoils, parametric analyses are carried out at different wind velocity, air temperature and MVD.

a) Effect of wind velocity

To study the effects of wind velocity, numerical analyses are carried out using four different wind velocities (5, 10, 30 & 50 m/s) (see Fig. B.1). This parametric study is carried out at a constant air temperature of -5 °C, a median volume diameter (MVD) of 20 µm for Langmuir D droplet distribution, a liquid water content (LWC) 0.4 g/m^3 and an incoming wind angle of attack of 0º. Results show a significant change in the air flow behavior along both profiles at different wind velocities, which also effects the droplets behavior and resultant ice shapes. A droplet moving in the free stream air is influenced by its drag and inertia, when neglecting the gravity and buoyancy. If drag dominates the inertia, the droplet follows the streamline whereas, for the case where inertia dominates, the droplet collides with the airfoil surface. The ratio of droplet inertia to drag depends on the wind velocity. The results show an increase in the droplet collision efficiency with an increase of wind velocity. This is mainly due to an increase in the droplet inertia (that dominates the droplet drag in this case) and leads

to an increase in the droplet collision efficiency. Fig. B.2 shows a comparison of droplet collision efficiency for NACA-0012 and NACA-23012 airfoils. The analyses show that for the symmetric airfoil (NACA-0012) the droplet collision efficiency is the same along the lower (pressure) and upper (suction) sides whereas, for the asymmetric (NACA-23012) airfoil, the droplet collision efficiency is higher along the suction side as compared to the pressure side. The rate and shape of accreted ice along both airfoils depends on the efficiency and location of the droplet collision. The analyses show that the droplet impingement area along the airfoil increases significantly with the increase of wind velocity. Results show that the ice shapes are symmetric along NACA-0012, whereas for NACA-23012 airfoil, more ice is accreted along the suction side of the airfoil, as compared to the pressure side. Fig. B.3 shows the accreted ice shapes along both airfoils.

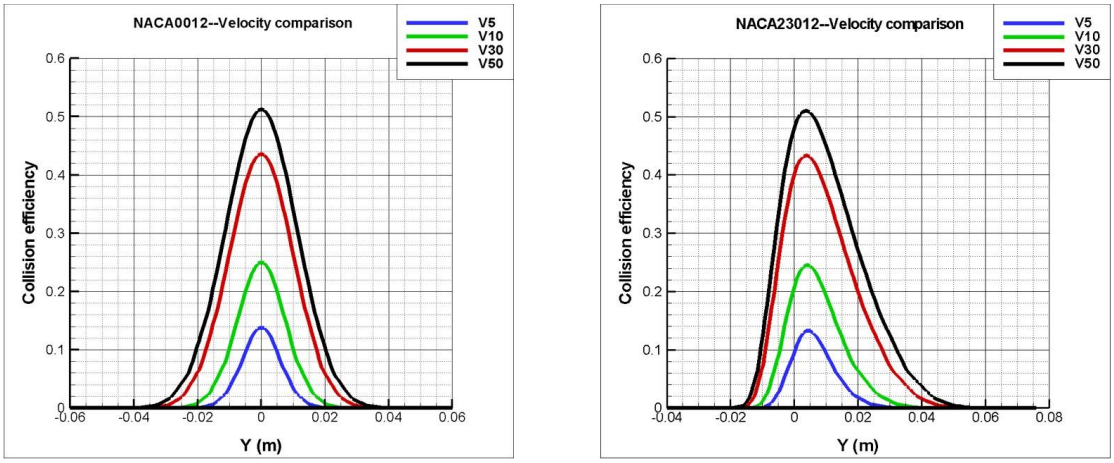

Figure B.2 – Droplet collision efficiency at different wind velocities.

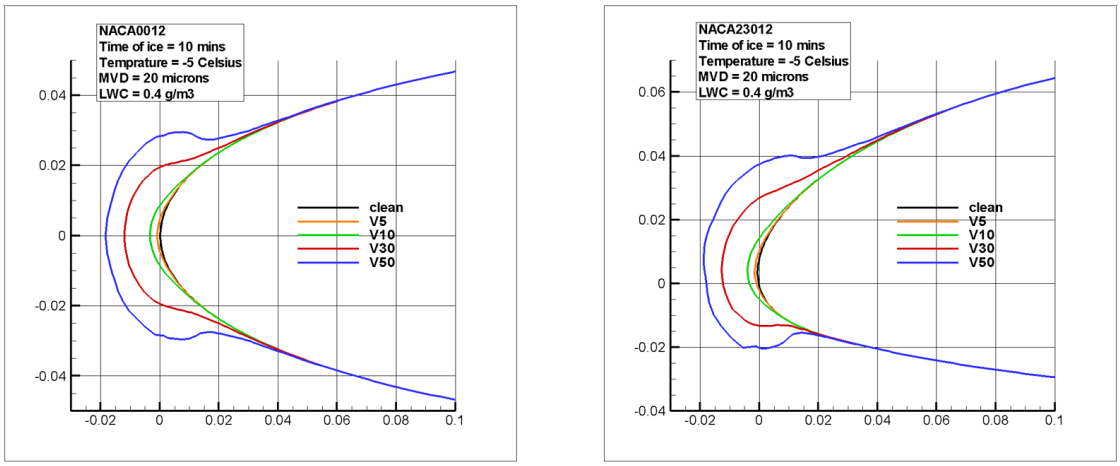

Figure B.3 – Accreted ice shapes at different wind velocities.

b) Effect of atmospheric temperature

To study the effect of atmospheric temperature, numerical analyses are carried out at three different atmospheric temperatures (-1, -5 and -15 °C). This parametric study is carried out at a constant wind velocity of 10 m/s, MVD of 20 microns for Langmuir D droplet distribution, LWC of 0.4 g/m^3 and an incoming air angle of attack of 0 degrees. Results show that accreted ice shape changes with the air temperature. The change in air temperature has no effect on the droplet collision efficiency, but the rate and shape of ice does change with the change in air temperature mainly due to change of surface heat

fluxes. At very low temperatures, such as -15 °C, the droplet freezing fraction is almost 100%. Because of this, all colliding droplets freeze into ice. For higher temperature, such as -1 °C, the droplet freezing fraction is lower than 100% due to which most of the colliding droplets do not freeze along the airfoil surface and run back as thin layer of water. Such change in the droplet freezing fraction due to surface heat fluxes results in different ice accretion process and also results in different accreted ice densities. The analyses show that at low temperatures the accreted ice shapes are more streamlined as compared to ice shapes near the freezing point temperatures, where the horn type abrupt ice shapes are observed. Such changes in the accreted ice shapes changes the flow behavior and the resultant aerodynamic characteristics of the blade profiles. Figure B.4 & B.5 show the droplet collision efficiency and accreted ice shapes along NACA-0012 & NACA-23012 at different air temperatures.

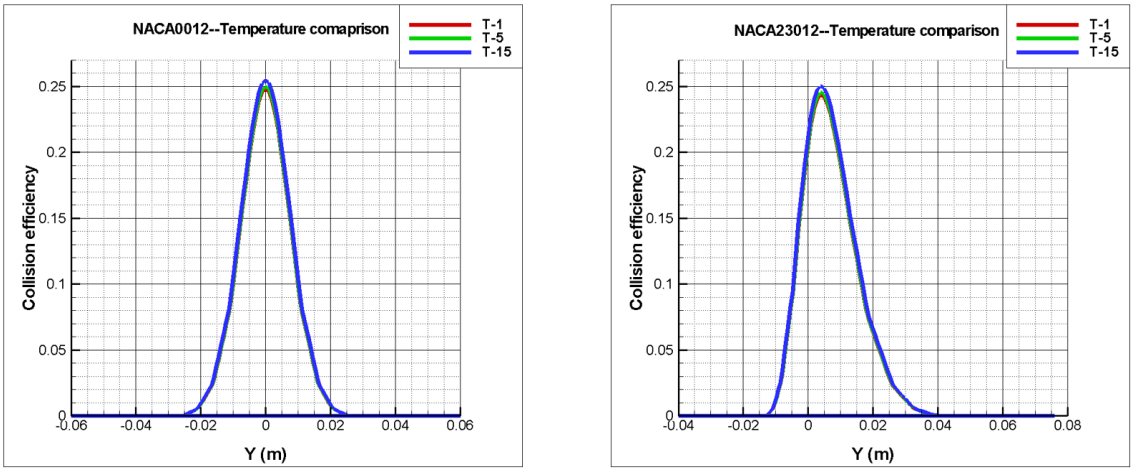

Figure B.4 – Droplet collision efficiency at different air temperatures.

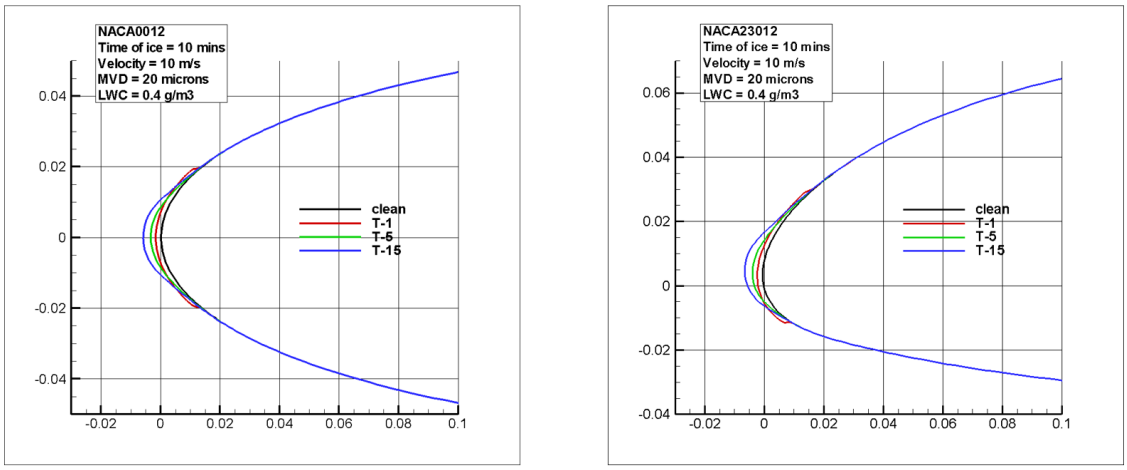

Figure B.5 – Accreted ice shapes at different air temperatures.

c) Effect of droplet size & droplet distribution spectrum

To study the effect of droplet size, numerical analyses are carried out at four different MVD's (15, 20, 40 & 60 µm). This parametric study is carried out at a constant wind velocity of 10 m/s, air temperature of -5 °C, LWC of 0.4 g/m^3 and an incoming air angle of attack of 0º. A detailed parametric study is also carried out to better understand the effects of droplet distribution spectrums, where five different droplet distributions spectrums for MVD = 20 µm (Langmuir A–E) are used for the simulations. Results show

that a change in droplet size affects the rate and shape of ice accretion. Increasing the droplet size increases the wetted surface area of the airfoil covered by the colliding droplets and consequently affects the rate and shape of ice accretion. The main reason for this can be explained by the fact that larger diameter droplets have a larger inertia compared to smaller droplets. Therefore the movements of larger droplets are less effected by the airflow and more droplets collide with the airfoil surface. The analyses show a significant increase in the droplet collision efficiency with the increase of droplet diameter. The maximum droplet collision efficiency is same for both NACA-0012 & NACA-23012 airfoils. The only observed difference is the change in the droplet impingement location in both cases. The droplet impingement location is symmetrical for NACA-0012 where in the case of NACA-23012 the droplet impingement is higher along the upper surface as compared to the lower surface. Fig. B.6 & B.7 shows the droplet collision efficiency and resultant ice shapes for both airfoils respectively.

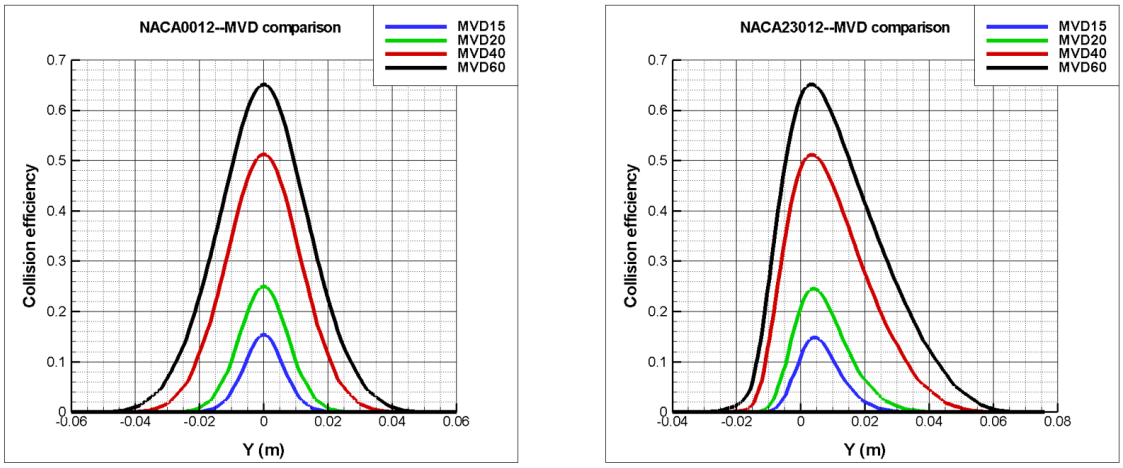

Figure B.6 – Droplet collision efficiency for different MVD.

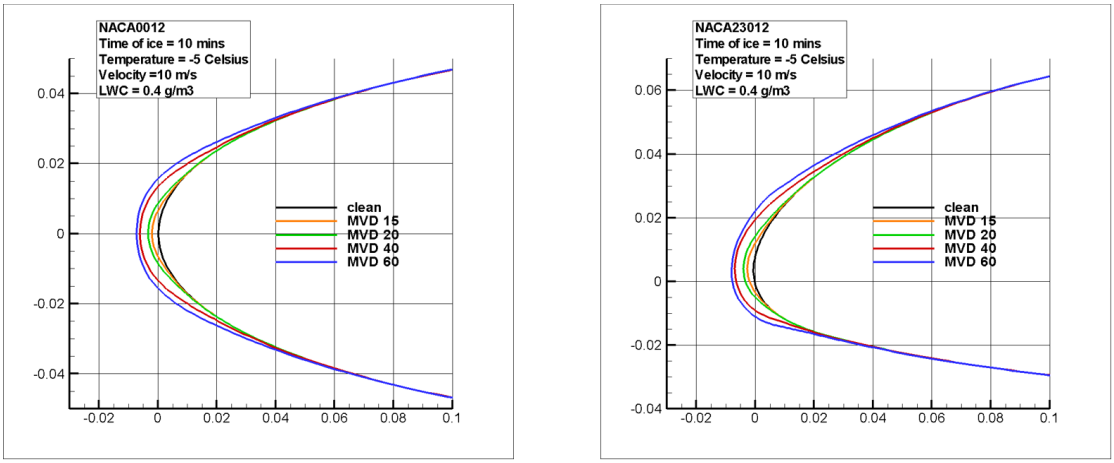

Figure B.7 – Accreted ice shapes for different MVD.

To better understand the effect of droplet distribution spectrum on ice accretion, a detailed parametric study is also carried out using five different droplet distribution spectrums (Langmuir A–E) at MVD 20 µm. The results show a change in the droplet collision efficiency and droplet impingement location with the change of the droplet distribution spectrum. A maximum droplet collision efficiency is observed for Langmuir E. The analyses show that wetted surface area where droplets collide is higher for Langmuir E distribution as compared to the Langmuir A. This difference is mainly because of the droplet's inertia

parameter (K) and the droplet impingement angle. Fig. B.8 & B.9 show the droplet collision efficiency and resultant ice shape for different droplet distribution spectrums.

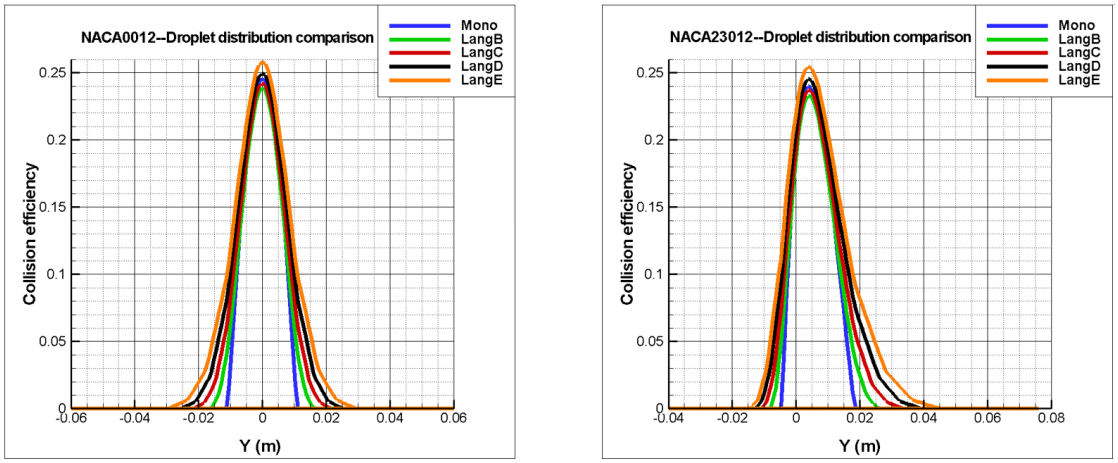

Figure B.8 – Droplet collision efficiency for different droplet distribution spectrums.

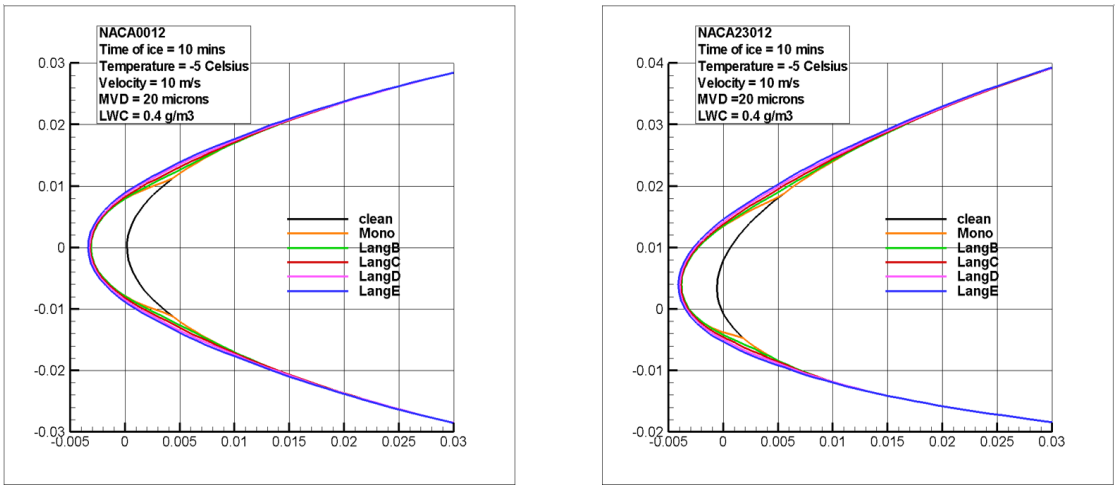

Figure B.9 – Accreted ice shapes for different droplet distribution spectrums.

B.3.2. Effects of the Geometric Parameters

To study the effect of wind turbine blade profile size variation on ice accretion, analyses are carried out using three different sizes of the NACA-0012 & NACA-23012 airfoils. Chord lengths and effective size of both airfoils are scaled up with 3 different factors. The chord length of each airfoil is represented with 1, 2 and 4 m, which represents 1 time scale, 2 times scale and 4 times scale respectively. The analyses are carried out at a constant wind velocity of 10 m/s, MVD of 20 µm for Langmuir D droplet distribution, temperatures of -5°C, LWC of 0.4 g/m^3 and an incoming air angle of attack of 0º. The results show that the droplet collision efficiency and the resultant ice growth decreases with the increase of airfoil size. Icing is less severe for larger wind turbine blade profiles both in terms of local ice mass and relative ice thickness. Fig. B.10 shows the droplet collision efficiency for each profile size.

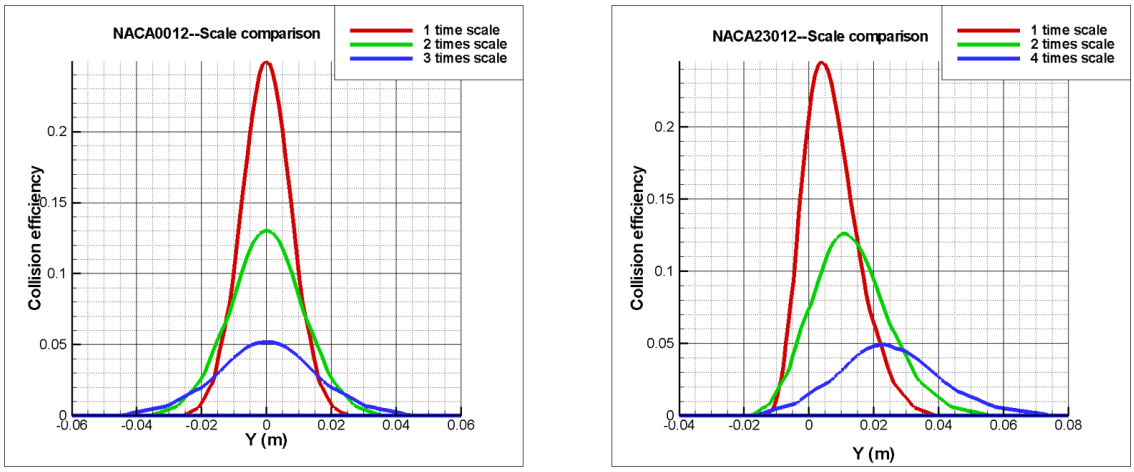

Figure B.10 – Droplet collision efficiency of different scales.

Analysis of Fig. B.11 shows that ice accretion decreases with the increase of profile size for both symmetric and asymmetric profiles. This is mainly because with the increase of profile size, the airflow and droplet behavior changes. In this case, droplet drag dominates the inertia and most of the droplets follow the streamline and does not collide with the airfoil surface, which leads to a decrease in the droplet overall collision efficiency and resultant ice growth.

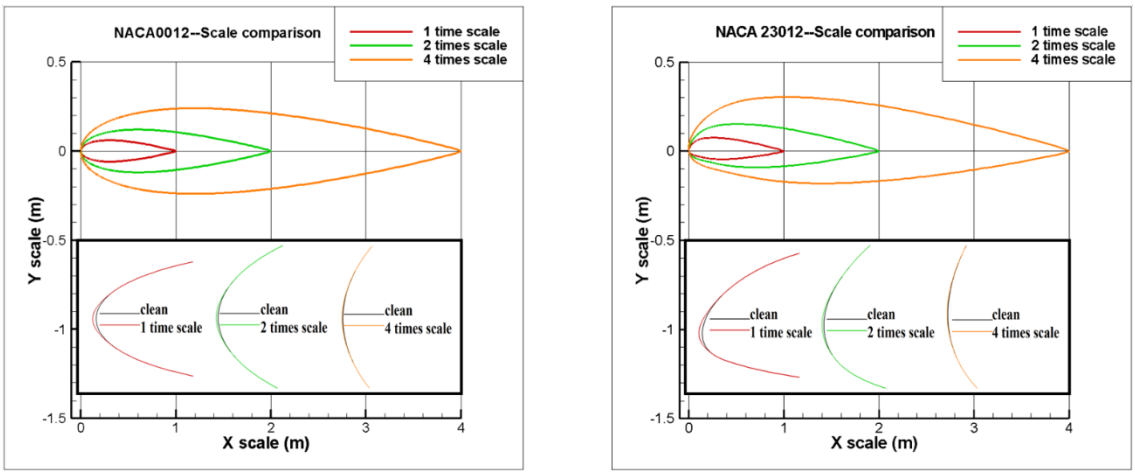

Figure B.11 – NACA-0012 and NACA-23012: Ice accumulation of different scales.

B.3.3. Effect of Ice Accretion on Aerodynamic Characteristics

A parametric study is also carried out to understand the effect of ice accretion on aerodynamic characteristics of NACA-0012 and NACA-23012 airfoils. For the iced profiles, simulated ice shapes at 0º AOA are used. A comparison is made between aerodynamic performance of clean and iced profiles. All these analyses were carried out at Re = 3×10^6. For clean airfoils results are also compared with the experimental data. Fig. B.12 shows the lift and drag coefficients for iced and clean airfoils [26] for AOA= -12, -4, 0, 4, 12 ° and Fig. B.13 shows the streamlines of NACA-0012 and NACA-23012 for iced and clean airfoils in this case.

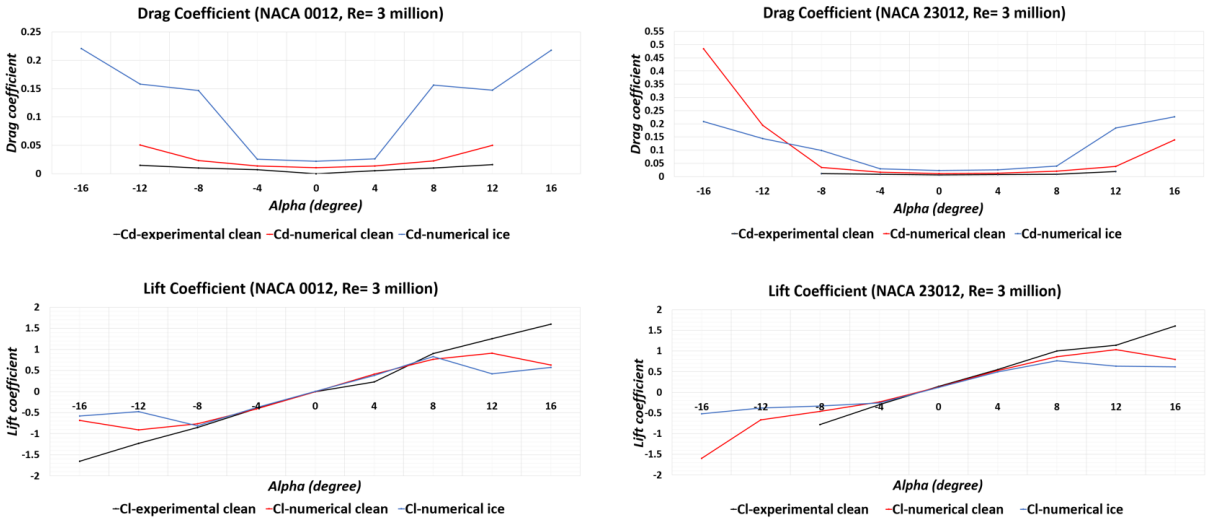

Figure B.12 – Lift and drag coefficient comparison in different AOA.

The analysis of Fig. B.12 shows a decrease in the aerodynamic characteristics of the iced airfoils when it is compared with the clean airfoil. This change in the aerodynamic characteristics is mainly due to a change in the iced airfoil shape and surface roughness, which affects the flow behavior. From an aerodynamic perspective, it is clear that the iced shapes have a significant influence on the airfoil aerodynamic characteristics, when the absolute value of the angle of attack is increased. The analysis of the flow behavior shows a significant change in the velocity and pressure distribution along the iced airfoils. A shift in position of the stagnation point is observed, which affects the velocity and pressure distribution. Results show that for the positive angles of attack a high velocity zone appears along the upper surface of the iced profiles near the leading edge, whereas a flow recirculation zone is found near the trailing edge along the upper surface of the iced profiles. For the negative angles of attack the flow separation zone appears along the pressure side of the iced airfoils. Fig. B.13 shows the velocity streamline along both clean and iced airfoils.

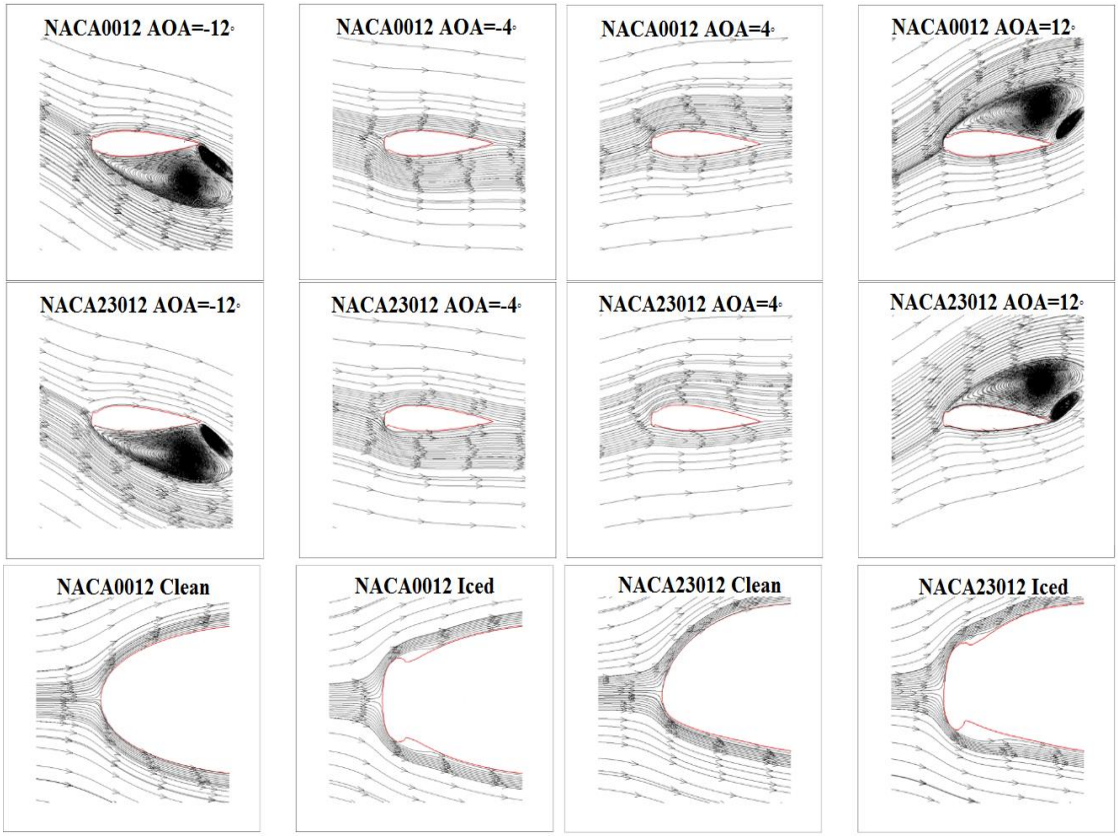

Figure B.13 – Streamlines at AOA= -12, -4, 0, 4, 12 °.

B.3.4. Comparison of Accreted Ice Mass and Thickness

Table B.2 shows a comparison of accreted ice growth rate and maximum ice thickness for both airfoils at different operating and geometric conditions used in this parametric study.

Table B.2 – Ice growth rate and thickness.

Parameterization		Max Ice Growth (kg/m^2)		Max Ice Thickness (mm)		Droplet Impingement Location Length (m) Along Leading Edge	
		NACA-0012	NACA-23012	NACA -0012	NACA -23012	NACA-0012	NACA-23012
	V5	0.995	0.955	1.047	1.008	-0.021 to 0.021	-0.010 to 0.030
	V10	3.598	3.536	3.431	3.419	-0.026 to 0.026	-0.013 to 0.040
	V30	17.588	21.329	12.125	12.202	-0.032 to 0.032	-0.017 to 0.048
	V50	36.768	45.057	18.374	19.287	-0.036 to 0.036	-0.017 to 0.054
	T-1	1.718	1.835	1.769	1.879	-0.026 to 0.026	-0.013 to 0.040
	T-5	3.598	3.536	3.431	3.419		
	T-15	3.669	3.607	6.060	6.115		
	MVD15	2.216	2.138	2.222	0.594	-0.021 to 0.021	-0.010 to 0.030
	MVD20	3.598	3.536	3.431	3.419	-0.026 to 0.026	-0.013 to 0.040
	MVD40	7.123	7.113	6.289	6.354	-0.038 to 0.038	-0.020 to 0.057
	MVD60	8.516	8.958	7.430	7.471	-0.046 to 0.046	-0.026 to 0.063

Operating parameters	**Langmuir A**	3.540	3.460	3.388	3.342	-0.011 to 0.011	-0.005 to 0.020
	Langmuir B	3.440	3.354	3.279	3.253	-0.017 to 0.017	-0.008 to 0.027
	Langmuir C	3.491	3.416	3.353	3.311	-0.020 to 0.020	-0.011 to 0.033
	Langmuir D	3.598	3.536	3.451	3.419	-0.026 to 0.026	-0.013 to 0.040
	Langmuir E	3.714	3.668	3.540	3.539	-0.030 to 0.030	-0.015 to 0.046
Geometric parameters	**1 time scale**	3.598	3.536	3.431	3.419	-0.026 to 0.026	-0.013 to 0.040
	2 times scale	1.881	1.816	1.982	1.916	-0.037 to 0.037	-0.018 to 0.058
	4 times scale	0.745	0.707	0.805	0.767	-0.046 to 0.046	-0.019 to 0.079

The results in Table B.2 show that the maximum ice growth and thickness increases significantly with the increase of air velocity, median volume diameter (MVD) and atmospheric temperature. This is mainly due to a change in the flow behavior and airfoil surface thermodynamics. For example, the analysis shows an increase in the droplet collision efficiency and droplet impingement location with the increase of air velocity. At v = 5 m/s, the droplet impingement surface length is 0.042 m along the leading edge, whereas at v = 50 m/s it increases to 0. 072 m. There is also a small change in the droplet impingement surface length for symmetric and asymmetric airfoils, which is mainly due to a change in the stagnation point location. For NACA-0012 airfoil, the stagnation point is at the center of the leading edge, whereas for NACA-23012 the stagnation point is not at the center of the leading edge, which changes the droplet behavior and resultant impingement location. The analyses at different operating temperatures show that the ice thickness and the ice rate change significantly with the change of atmospheric temperature. Higher ice thickness is observed at T = -15 °C as compared to T = -1 °C, which is mainly due to a higher droplet freezing fraction at -15 °C. Similarly results shows a significant increase in ice thickness with the increase of median volume diameter (MVD). Results from geometric parameter study shows that accreted ice mass and thickness decreases significantly with the increase of airfoils geometric size. This is mainly due to a change in flow behavior with the profile size.

B.4. Conclusion

Ice accretion along the symmetric and asymmetric airfoils was studied at different operating and geometric conditions using a computational fluid dynamics based numerical technique. Parametric analysis of ice accretion at different operating and geometric conditions show an increase in the ice growth with the increase in air velocity and droplet size, whereas a change in the atmospheric temperature significantly affects the ice shapes. A significant decrease in accreted ice mass and thickness is observed with the increase of airfoil geometric size. Results show that the airfoil shape has an effect on the rate and shape of the ice accretion. Streamline ice shapes are observed in case of symmetric airfoil as compared to asymmetric airfoil. Aerodynamic characteristics of the iced airfoils decrease as compared to the clean airfoil. The results show that the blade's airfoil geometric shape affects the ice accretions. More streamlined ice shapes are found in case of a symmetric airfoil, which highlights the possibility of controlling the accreted ice growth by optimizing the blade profile geometry. This

preliminary study needs to be extended in the future as this can possibly help to reduce the need for anti/de-icing systems on the wind turbine blades installed in the cold regions, which can lead to a significant reduction on OPEX and CAPEX of wind turbine operations in icing conditions.

Acknowledgement

The work reported in this research paper is funded by the WindCoE (*Nordic Wind Energy Centre*) (201533) project within the Interreg IVA Botnia−Atlantica, as part of European Territorial Cooperation (ETC) and University of Tromsø Ph.D. project no 381100/74104.

References

1. Neil Davis, A.H.H., Zagar, M., 2014. Icing Imparcts on Wind Energy Production DTU.
2. Yirtici, Ozcan, Tuncer, Ismail H., Ozgen, S., 2016. Ice accretion prediction on wind turbinrs and comsequent power losses. J. Phys. 753.
3. Ronsten, G., 2004. Sevenska Erfarenheter Av Vindkraft I Kallt Klimat Nedisning.
4. Hudecz, Adriana, H.M.O.L., Battisti, Lorenzo, Villumsen, Arne, 2014. Icing Problems of Wind Turbine Blades in Cold Climates. Department of Wind Energy. Technical University of Denmark pp. DTU Wind Energy PH.D.-0031(EN).
5. Ronsten, G., 2017. IEA R&D Wind's Task 19- wind energy in cold climate. Swdish wind energy association.
6. Sohrab, Gholahosein Pouryoussefi, Masoud, Mirzaei, Mohamed, Mahdi Nazemi, Fouladi, M., 2016. Experimental study of ice accretion effects on aerodynamic performance of NACA-23012 airfoil. Chin. J. Aeronaut. 29, 585–595.
7. Homola, Matthew C., Virk, Muhammad S., Sundsbø Per, A., Nicklasson, P.J., 2012. Performance losses due to ice accretion for a 5 MW wind turbine. Wind Energy 15 (3), 379–389.
8. Homola, Matthew C., Virk, Muhammad S., Tomas Wallenius, M.S.V., Nicklasson, Per J., Sundsbø, Per A., 2010. Effect of atmospheric temperature and droplet size variation on ice accretion of wind turbine blades. Wind Engineering and Industrial Aerodynamics 98 (12), 724–729.
9. Shin, J., Berkowitz, B., Chen, H., Cebeci, T., 1991. Prediction of ice shapes and their effect on airfoil performance. NASA Tech. Memorand. 103701.
10. Muhammd S Virk, et al., *Effect of atmospheric temperature and droplet size variation on ice accretion of wind turbine blades.* Wind Engineering and Industrial Aerodynamics, 2010.
11. Virk, Muhammad S., Homola, Matthew C., Nicklasson, P.J., 2010b. Effect of rime ice accretion on aerodynamic characteristics of wind turbine blade profiles. Wind Enegineering 34, 13.
12. Jasinski, W.J., Noe, S.C., Selig, M.S., Bragg, M.B., 1998. Wind turbine performance under icing conditions. Transactions of the ASME, Journal of solar energy engineering 120, 60–65.
13. Tammelin, B., Stuke, M., Seifert, H., Kimura, S., 1998. Icing effect on power production of wind turbines. In: Proceedings of the BOREAS IV Conference. Finnish Meteorological Institute.
14. Marjaniemi, M., Peltola, E., 1998. Blade heating element design and practical experiences. In: Proceedings of the BOREAS IV Conference. Finnish Meteorological Institute.
15. Marjaniemi, M., Makkonen, L., Laakso, T., 2000. Turbice - the wind turbine blade icing model. In: Proceedings of the BOREAS V Conference. Finnish Meteorological Institute.
16. Bak, C., Fuglsang, P., Sørensen, N., 1999. Airfoil Characteristics for Wind Turbines. Risø National Laboratory, Roskilde.
17. Ferrer, E., Munduate, X., 2007. Wind turbine blade tip comparison using CFD. J. Phys. Conf. 75.
18. Chi, X., Zhu, B., Addy, H.E., 2004. CFD analysis of the aerodynamics of a business-jet airfoil with leading- edge ice accretion. In: 42nd Aerospace Sciences Meeting and Exhibit, Reno,Nevada.

19. Kwon, O., Sankar, L.N., 1997. Numerical simulation of the flow about a swept wing with leading-edge ice accretions. Comput. Fluids 26, 183–192.
20. Mirzaei, M., Ardekani, M.A., Doosttalab, M., 2009. Numerical and experimental study of flow field characteristics of an iced airfoil. Aero. Sci. Technol. 13, 267–276.
21. Zhu, Z., Wang, X., Liu, J., Liu, Z., 2007. Comparison of predicting drag methods using computational fluid dynamics in 2d/3d viscous flow. Sci. China E 50, 534–549.
22. Muhammad S Virk, Matthew C Homola, and P.J. Nicklasson., *Effect of rime ice accretion on aerodynamic chractristics of wind turbine blade profiles.* Wind Enegineering, 2010. 34(2): p. 13.
23. Etemaddar, M., H.M.O.L., Moan, T., 2014. Wind Turbine Aerodynmic response under atmospheric icing conditions. Wind Energy 17, 241–265.
24. Clift, R., Grance, J.R., Weber, M.E., 1978. Bubbles, Drops and Particles. Academic Press, New York.
25. Manual, N.S.U. 2010, NTI.
26. E, I.H.A.a.A., 1949. Theory of wing Sections. Dover Publications, ing., New York.

Paper C

Experimental Study of Ice Accretion on S826 & S832 Wind Turbine Blade Profiles

Jia Yi Jin and Muhammad Shakeel Virk

Cold Regions Science and Technology, 2019, Volume 169.

Doi: 10.1016/j.coldregions.2019.102913

Author's Contribution

Jia Yi Jin has contributed substantially in the proposal of conceptualization, data curation, formal analysis, investigation, methodology, resources, software, visualization, validation, and writing of the paper.

C. Experimental study of ice accretion on S826 & S832 wind turbine blade profiles

This is a reprint

Jia Yi Jin and Muhammad Shakeel Virk

Arctic Technology and Icing Research Group
Institute of Industrial Technology
Faculty of Engineering Science and Technology
UiT- The Arctic University of Norway
Norway

Abstract

To optimize the aerodynamic performance and reduce production losses of wind turbine operating in icing conditions, it is necessary to better understand the ice accretion physics along wind turbine blade. This paper describes a case study of ice accretion physics and its effects on aerodynamic performance of S826 and S832 airfoils for dry and wet ice conditions. Both these airfoils have different geometric characteristics and are suitable for horizontal axis wind turbine blade. Icing tunnel experiments are carried out at Cranfield University to understand and simulate the ice accretion on both profiles. Results show that difference in geometric characteristics of both airfoils affects the ice accretion and more complex ice shapes are observed in case of S832 profile compared to S826. Analysis show that ice thickness is higher in case of dry rime ice conditions as compared to wet ice, whereas more complex ice shapes are observed for wet ice conditions. Computational Fluid Dynamics (CFD) based numerical analysis are carried out to study the airflow and droplets behaviour and to estimate the aerodynamic performance of both clean and iced profiles. No numerical simulations of ice accretion are carried out. CFD analysis show a change in airflow behaviour for iced profiles which leads to a decrease in aerodynamic performance, when compared with the clean profiles. The change in aerodynamics performance is higher for S832 than S826 particularly for wet ice conditions.

Keywords:
S832 airfoil; S826 airfoil; Icing wind tunnel; CFD; Aerodynamics; Wind turbine.

C.1. Introduction

In recent years, wind energy in ice prone cold regions has gained more interest due to the availability of good wind resources, but atmospheric icing is considered as hindrance in proper utilization of these good wind resources. Accreted ice on wind turbine blade changes its geometric shape, which affects the aerodynamic performance and leads to the power production losses. [1] In some cases, such losses have been reported to lead up to a 17% decrease in Annual Energy Production (AEP) and 20% to 50% in the aerodynamic performance. [2] Growing interest in better utilization of good wind resources in ice prone cold regions highlights the need of better understanding of ice accretion physics and finding innovative technological solutions for wind turbines operation in icing conditions to reduce the Capital Expenditure (CAPEX) and the Operational Expenditure (OPEX). In order to make the wind energy competitive with energy from fossil fuels, there has been a growing trend in the wind industry to scale up the turbine size to improve energy captured by a single wind turbine and thereby bring down the cost of power generation by economies-of-scale factors. In recent years, the cost of wind turbine has dropped significantly, which shows that, *"It has become more economical to install wind power plants than using fossil fuels"*. [3] This trend also highlights the importance of better understanding of ice accretion physics for wind turbines operation in wind rich cold regions.

Atmospheric ice accretion on wind turbine blades mainly occurs due to the impingement of super-cooled water droplets, which may freeze on blade surface immediately or after a short delay. [4] Ice accretion on wind turbine blade mainly occurs along leading edge, which affects the airflow and droplet behaviour and reduces its aerodynamic performance. [5] VTT technical research centre of Finland conducted a study to estimate the performance losses due to ice accretion for NREL 5MW wind turbine and found a decrease of 27% in its performance due to ice accretion. [6-7] Ice accretion depends on both operating and geometric characteristics of the wind turbine blade. On same operating conditions, blade profiles with different geometry will result in different accreted ice shapes. Most investigations about ice accretion effects on wind turbine aerodynamic performance has been performed by using ordinary wind tunnel with artificial ice templates attached. [8] Results from icing wind tunnel are more accurate, but due to complex setup and higher experimental cost, not many icing tunnel studies has been carried out to simulate the ice accretion on wind turbine blade profiles. NASA has conducted many studies about ice accretion on aircraft wing profiles using icing tunnels from 1940 to 1960, which has provided a useful insight to researcher about ice accretion physics. [9] In recent years, CFD based numerical simulations have also begun to play a significant role in simulating and determining the performance of wind turbine blade profiles under icing conditions. [10-13]

S-Family airfoils are designed by National Renewable Energy Laboratory (NREL) with a focus to use for different size of wind turbine blades. Due to good aerodynamic characteristics, S family airfoils are being used by wind turbine blade designers. For this study, analysis has been carried out using S826 & S832 airfoils, which are suitable for horizontal axis wind turbine blades. NREL has performed a series of ordinary wind tunnel experiments to study the aerodynamic performance of different un-iced (clean) 'S family' (S825, S826, S830, S831, S832) airfoils. [14-16] However, there is not any published data available about icing tunnel experimental study of these profiles. Researchers from Norwegian University of Science and Technology (NTNU) have performed CFD simulations and ordinary wind tunnel experimentation of S826 airfoil, where they first used CFD simulations to simulate the accreted ice shapes and then manufactured the ice templates to attached them with clean S826 airfoil to study the aerodynamic characteristics using ordinary wind tunnel. [17-18]

This paper presents an icing tunnel experimental study of ice accretion on S826 and S832 airfoils to better understand the ice accretion physics for dry and wet ice conditions and its effects on aerodynamic performance. Icing tunnel experiments are carried out at Cranfield University UK, whereas to study the airflow and droplets behaviour for iced and clean airfoils, CFD−based numerical study is performed using ANSYS−FENSAPICE−FLUENT, which also provided an insight of aerodynamic performance comparison for clean and iced profiles.

C.2. Icing Tunnel Experimental Study

C.2.1. Experimental Setup

The experimental study is carried out at the icing tunnel laboratory of Cranfield University (CU), UK. [19] Both profiles are manufactured with the span of 758 mm and the chord length of 500 mm. The surfaces of these profiles are made of galvanized steel (VGAL.V.D×SID+Z275) with average surface roughness of 1 microns. Icing wind tunnel facility at CU has test section size (761×761 mm) and can create realistic icing conditions for Median Volume Diameter (MVD) ranging from 15 to 80 µm, Liquid Water Content (LWC) from 0.05-3 g/m^3 and air temperature from -30 to +30 °C. Figure 1 shows the schematic view of the experimental setup of icing tunnel with mounting of the blade profile.

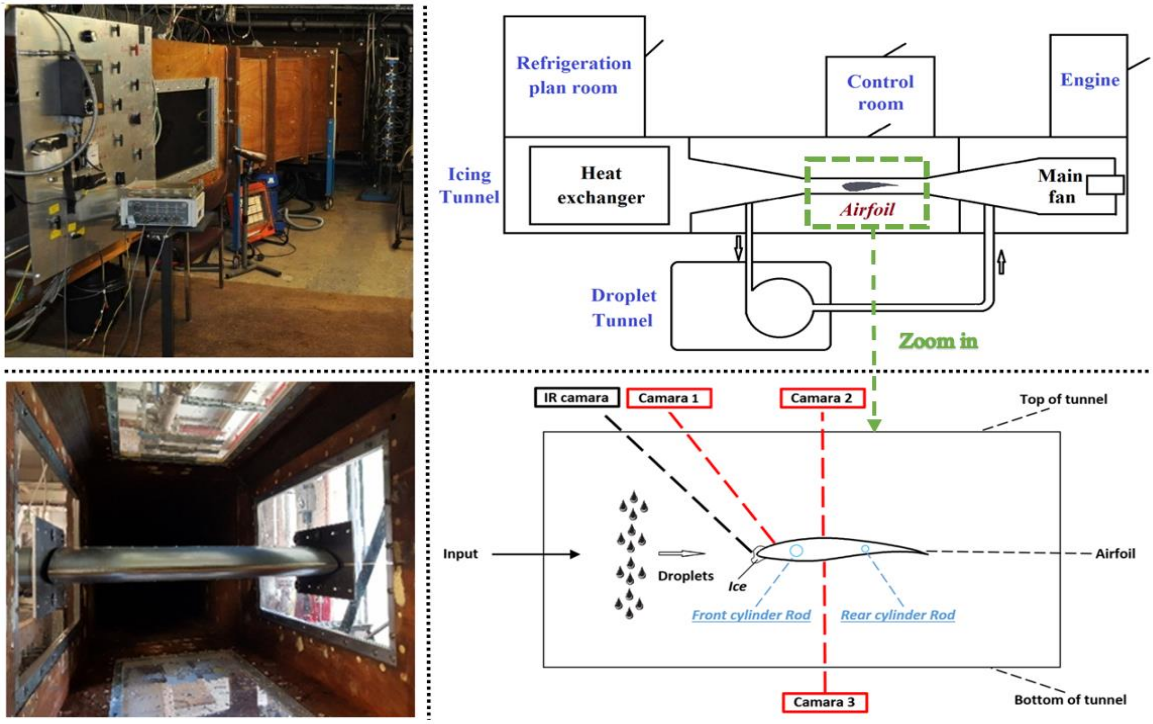

Figure C.1 – CU icing tunnel experimental setup.

To closely monitor the ice accretion along each profile, three High Definition cameras (*two for side view and one from top view*) are used for video recording and pictures. Accreted ice shapes are extracted and sketched manually after each experiment. These experiments are carried out at Reynolds number = 3×10^6 and angle of attack (AOA) = 0° for both dry (rime) and wet (glaze) ice conditions. Table C.1 presents the operating conditions used for this experimental study.

Table C.1 – Icing tunnel experimental conditions.

Airfoil	Test	Ice Type	Velocity (m/s)	Temperature (°C)	LWC (g/m^3)	MVD (microns)	AOA (degree)	Time (mins)
S826	1	Wet	77	-5	0.35	20	0	15
	2	Dry	70	-20				
S832	3	Wet	77	-5				
	4	Dry	70	-20				

In order to better monitor the icing tunnel operation, various operating parameters of icing tunnel are also closely monitored to ensure the smooth operation. Droplet MVD of 20 µm is used with the droplet distribution spectrum consisting of 60 bins. Figure C.2 shows the droplet distribution spectrum used for this study in addition to the variations in wind speed and total temperature at the icing tunnel test section for both dry and wet ice conditions.

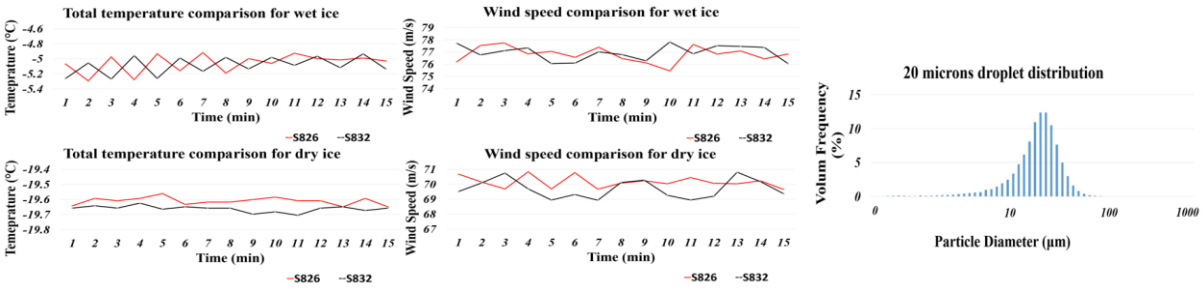

Figure C.2 – Icing tunnel operating conditions variation & droplet distribution spectrum used.

C.2.2. Experimental Results

During each experiment, ice accretion was monitored from three different views using HD cameras. Figures C.3 & C.4 show the ice growth along both profiles for dry and wet ice conditions during the experimental time span.

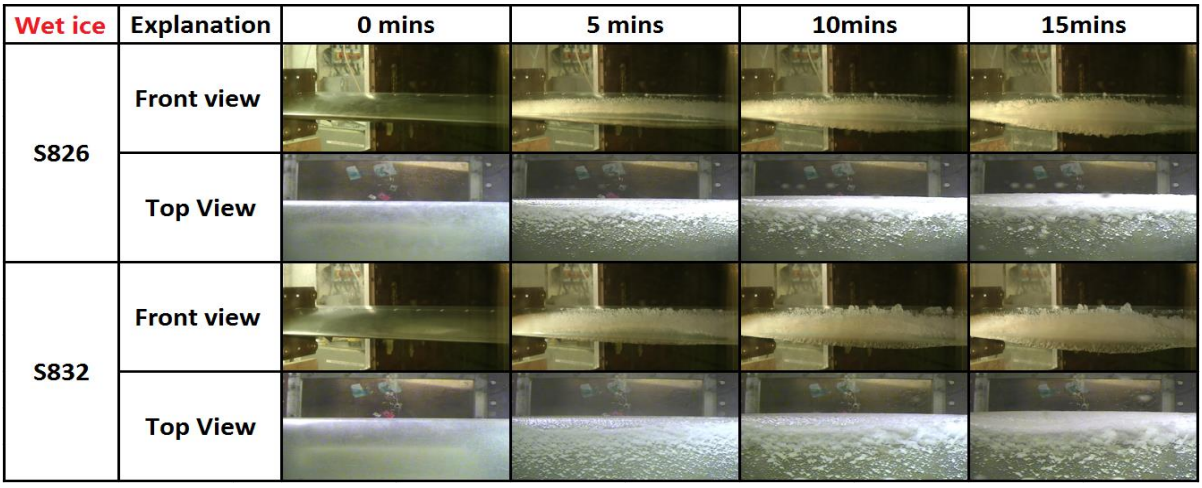

Figure C.3 – Overview of wet ice growth along S826 and S832 profiles.

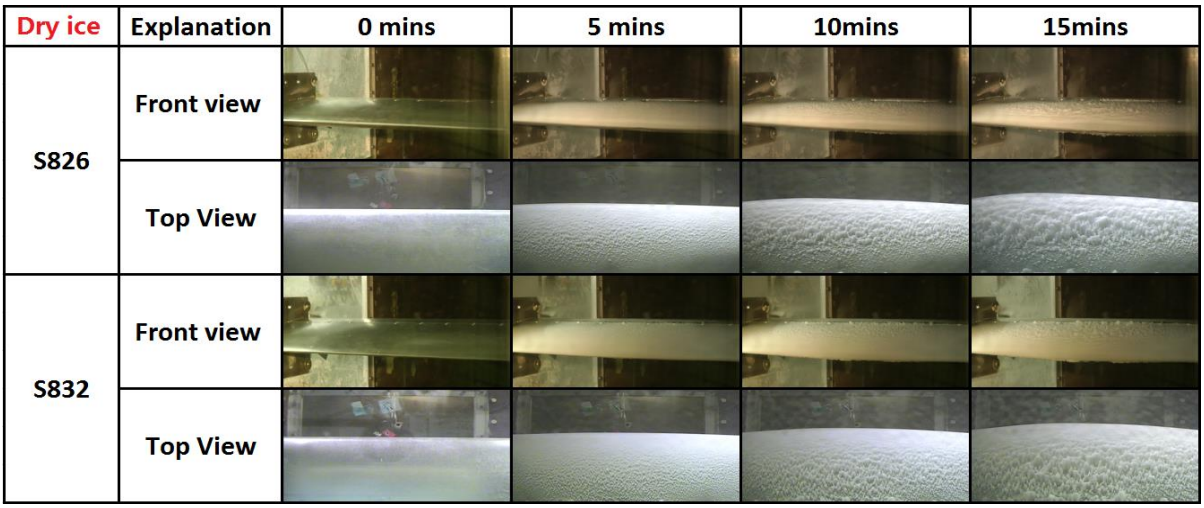

Figure C.4 – Overview of dry ice growth along S826 and S832 profiles.

To get the accreted ice shapes after each experiment, the ice chunks were cut from centre section of each profile. Figure C.5 shows the cut-out cross section and resultant ice shape from each experiment. These ice shapes were sketched manually from each cut out on grid paper and then was digitalized using computer aided design software – SolidWorks.

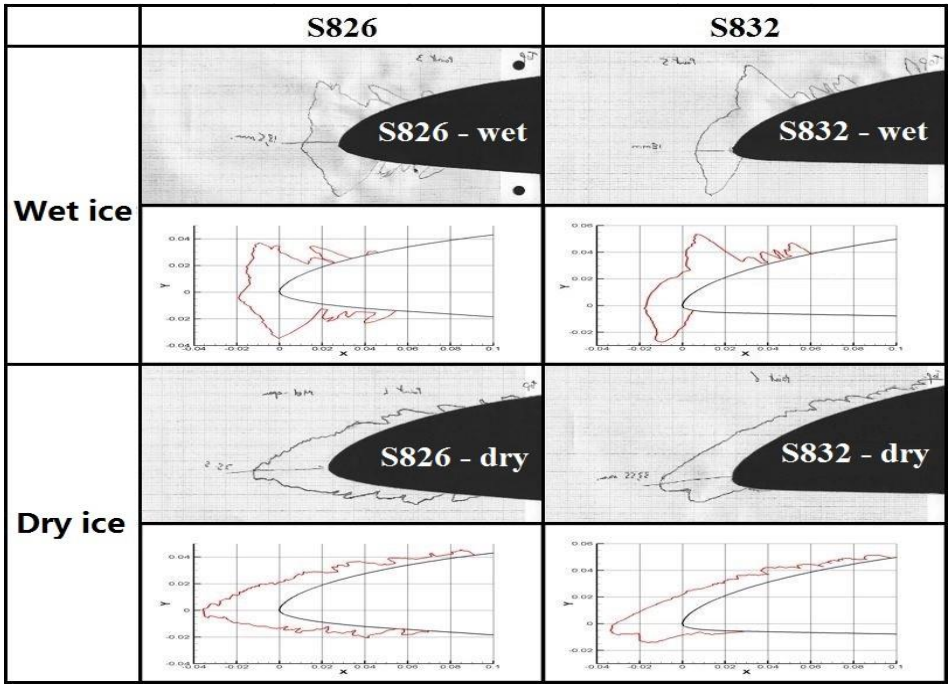

Figure C.5 – Experimental ice shapes for dry and wet ice conditions.

Both these airfoils have different geometric shapes, where S826 has more curvature along pressure side, whereas in case of S832 pressure side is having very small curvature and looks almost flat. Due to difference in the geometric characteristics, accreted ice shapes and wetted surface area covered by ice along pressure and suction sides of both profiles is different. For both profile sections, ice mainly accreted along leading edge, but distribution of ice is different along pressure and suction sides. For S826, ice accretion is extended on both sides almost equally, where as in case of S832, ice is mainly accreted along suction side of the profile and very less ice is accreted along pressure side.

Large individual ice feathery spikes pointing perpendicular to the profile surface are observed. For S826 profile section, the feathery spikes of ice are concentrated, connected and densely packed with direction of feather growing parallel to the airflow, while for S832 airfoil, the feathery spikes are loosely connected to the direction of growth being perpendicular to the profile surface. Results show that for wet ice conditions, the ice shapes are more complex along leading edge when compared with the dry ice conditions. This is mainly due to the low freezing rate of the super cooled water droplets impinging along the profile surface. For wet ice conditions, high aerodynamic forces along stagnation line of the blade profile push the non-freezing water droplets towards upper and lower sides of the profile surface, which resulted in horn shape ice along leading edge. For dry ice conditions, all impinged droplets freeze, which resulted in more streamlined ice shapes. For case of wet ice conditions, experimental results show that ice accumulation extended along chord length about 5%−10% for S826 profile and 15%−20% for S832 profile section, whereas for the dry ice conditions, ice accumulation extends towards the chord length approximately up to 25% for both S826 and S832 profiles. To avoid side wall effects of icing wind tunnel, these measurements were taken from centre section of the blade profiles. Table C.2 shows the maximum ice thickness for each profile.

Table C.2 – Maximum ice thickness.

	Max ice thickness (mm)	
	S826	**S832**
Wet Ice	18.5	18
Dry Ice	35.5	33.55

C.3. Numerical Study

CFD−based numerical analyses are carried out using ANSYS−FENSAPICE−FLUENT. The objective of this numerical study is to analyse the airflow and droplet behaviour along clean and iced profiles obtained from icing tunnel experiments and study the aerodynamic characteristic. No numerical simulations of ice accretion are carried out. These CFD simulations provided an insight of the airflow and droplet behaviour, which was not easy to study from experiments. The numerical study of airflow behaviour is performed by solving nonlinear partial differential equations for the conservation of mass, momentum and energy.

$$\frac{\partial \rho_{\alpha_1}}{\partial t} + \vec{\nabla}\left(\rho_{\alpha_1}\overrightarrow{\boldsymbol{v}_{\alpha_1}}\right) = 0 \tag{C.1}$$

$$\frac{\partial \rho_{\alpha_1}\overrightarrow{\boldsymbol{v}_{\alpha_1}}}{\partial t} + \vec{\nabla}\left(\rho_{\alpha_1}\overrightarrow{\boldsymbol{v}_{\alpha_1}}\ \overrightarrow{\boldsymbol{v}_{\alpha_1}}\right) = \vec{\nabla}.\sigma^{ij} + \boldsymbol{\rho_{\alpha}}\,\vec{g} \tag{C.2}$$

$$\frac{\partial \rho_{\alpha_1} E_{\alpha_1}}{\partial t} + \vec{\nabla}\left(\rho_{\alpha_1}\overrightarrow{\boldsymbol{v}_{\alpha_1}} H_{\alpha_1}\right) = \vec{\nabla}\left(\kappa_{\alpha}\left(\vec{\nabla}\,T_{\alpha}\right) + \nu_i \tau^{ij}\right) + \boldsymbol{\rho_{\alpha}}\,\vec{g}\,\overrightarrow{\boldsymbol{v}_{\boldsymbol{\alpha}}} \tag{C.3}$$

Where ρ is the density of air, v is the velocity vector, subscript α_1 refers to the air solution, T refers to the air static temperature in Kelvin, σ^{ij} is the stress tensor, E and H are the total initial energy and enthalpy respectively. Two phase flow (air and water droplets) is simulated using the Eulerian approach, where super cooled water droplets are assumed to be spherical. The Eulerian two phase fluid model consists of the Navier-Stokes equation with the water droplets continuity and momentum equation. The

water droplet drag coefficient is based on the empirical correlation for the flow around the spherical droplets described by Clift et al. [20]

$$\frac{\partial \alpha_2}{\partial t} + \vec{\nabla}\left(\alpha_2 \overrightarrow{V_d}\right) = 0 \tag{C.4}$$

$$\frac{\partial\left(\alpha_2 \overrightarrow{V_d}\right)}{\partial t} + \vec{\nabla}\left(\rho_{\alpha_2} \overrightarrow{V_d} H_d\right) = \frac{C_D Re_d}{24k}\, \alpha_2\left(\overrightarrow{V_{\alpha_2}} - \overrightarrow{V_d}\right) + \alpha_2\left(1 - \frac{\rho_{\alpha_2}}{\rho_d}\right)\frac{1}{Fr^2}\vec{g} \tag{C.5}$$

$$Fr = \frac{u_0}{\sqrt{g_0 l_0}} \tag{C.6}$$

Where α_2 is the water volume fraction, $\overrightarrow{V_d}$ is the droplet velocity, C_D is the droplet drag coefficient and Fr is the Froude number, u_0 is a characteristic flow velocity, g_0 is in general a characteristic external field, and l_0 is a characteristic length. The numerical analyses are carried out using custom droplet diameters distribution spectrums used in CU icing tunnel for MVD = 20 µm.

Mesh sensitivity study was carried out using coarse, medium and fine meshes to accurately determine the boundary layer characteristics (shear stress and heat flux). During mesh sensitivity analysis, number of mesh elements and y+ value less than 1 for first cell layer was selected based upon the heat flux calculations, where a numerical check was imposed that the heat flux computed with the classical formulae dT/dn should be comparable with the heat flux computed with the Gresho's method. Mesh sensitivity study showed that the effect of mesh size on droplet solution was negligible, however some flow quantities including convective heat flux on the blade surface was sensitive to the mesh size. After mesh sensitivity analysis, C type structured numerical grid with approx. 75,000 grid cells was used. K-omega SST turbulence model is used as a compromise between acceptable computational cost and required accuracy for simulating the turbulent flow. Figure C.6 shows the numerical grid of iced profiles used in this study. The numerical simulations are carried out at operating conditions specified in Table C.3.

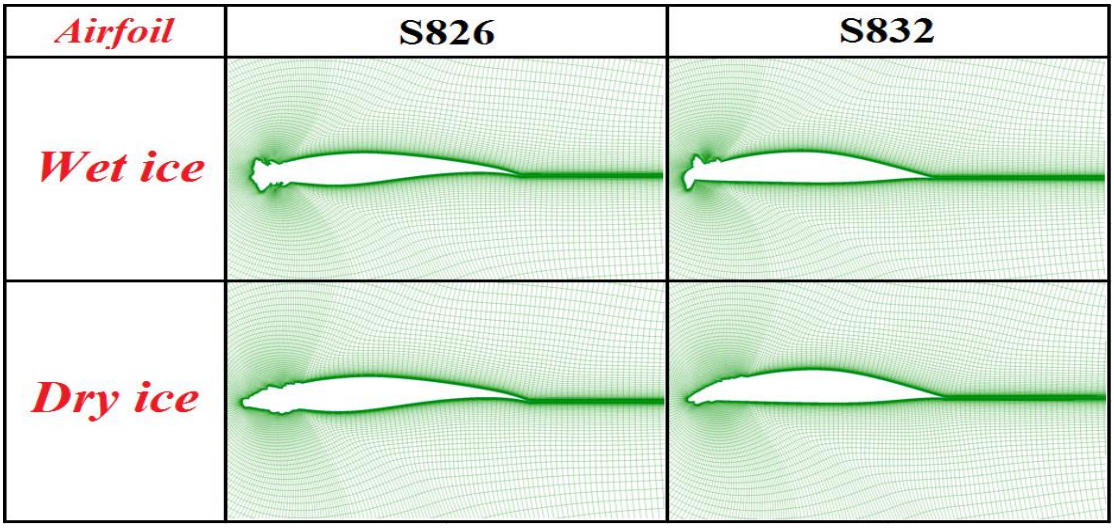

Figure C.6 – Numerical grid for iced S826 and S832 airfoils.

Table C.3 – Numerical setup.

Ice type	Wet ice	Dry ice
Chord length (m)	0.5	
Angle of attack (degree)	0	
Air velocity (m/s)	77	70
Temperature (Celsius)	-5	-20
MVD (microns)	20	
Droplet distribution	Customer distribution from CU (see Figure C.2)	
LWC (g/m^3)	0.35	

C.3.1. Numerical Results

Ice accretion along each profile changes its geometric shape, which affects the flow behaviour along pressure and suction sides of the profile and results a change in its aerodynamic performance. In this study, CFD based numerical analysis are carried out to simulate the airflow behaviour using experimental iced profile shapes. Figure C.7 shows the velocity streamlines for each case, where results show more complex flow separation for wet ice cases due to presence of ice horns along leading edge. For S826, the wet ice shape along leading edge is less complex as compared to S832, where a big ice horn is present at leading edge and ice is mainly accreted along the suction side. Due to such ice growth, airflow separation along S832 leading edge is more complex as compared to S826.

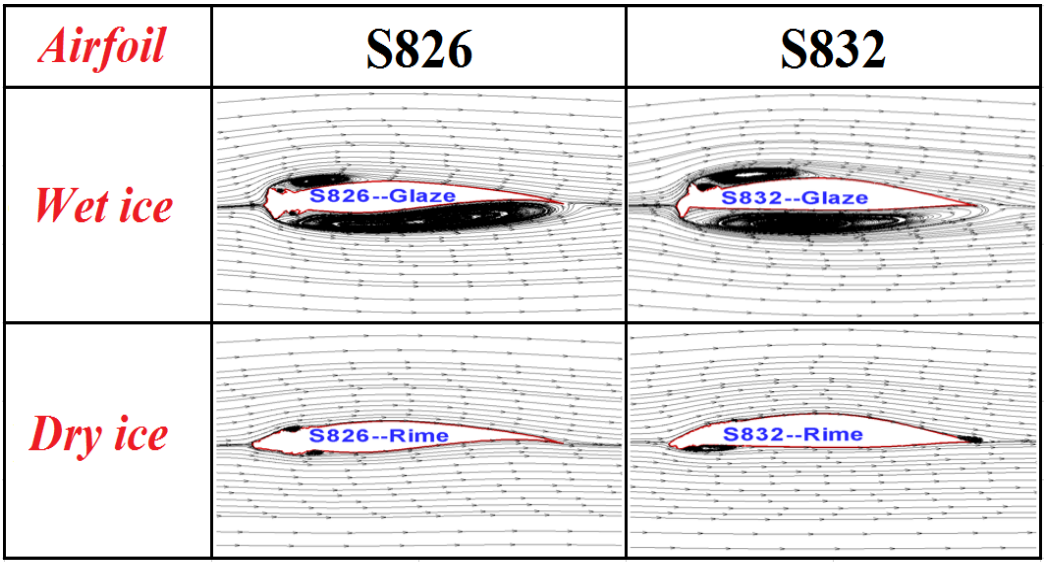

Figure C.7 – Velocity streamlines along iced profiles.

To understand the droplet behaviour along clean and iced profiles, numerical analysis are carried out to make a comparison of droplet collision efficiency. Droplet collision efficiency is the calculation of possibility of droplets impinging on the blade surface, as all droplets suspended in the air will not collide with the blade surface due to blade profile geometric features and flow behaviour. Droplet collision efficiency can be defined as the flux density of the droplets striking the surface in relation to the maximum possible. The numerical analyses are carried out using custom droplet diameters distribution spectrums used in CU icing tunnel for MVD = 20 µm. Figure C.8 shows the comparison of droplet

collision efficiency along both profiles for clean and iced conditions, where a change in droplet behaviour is observed.

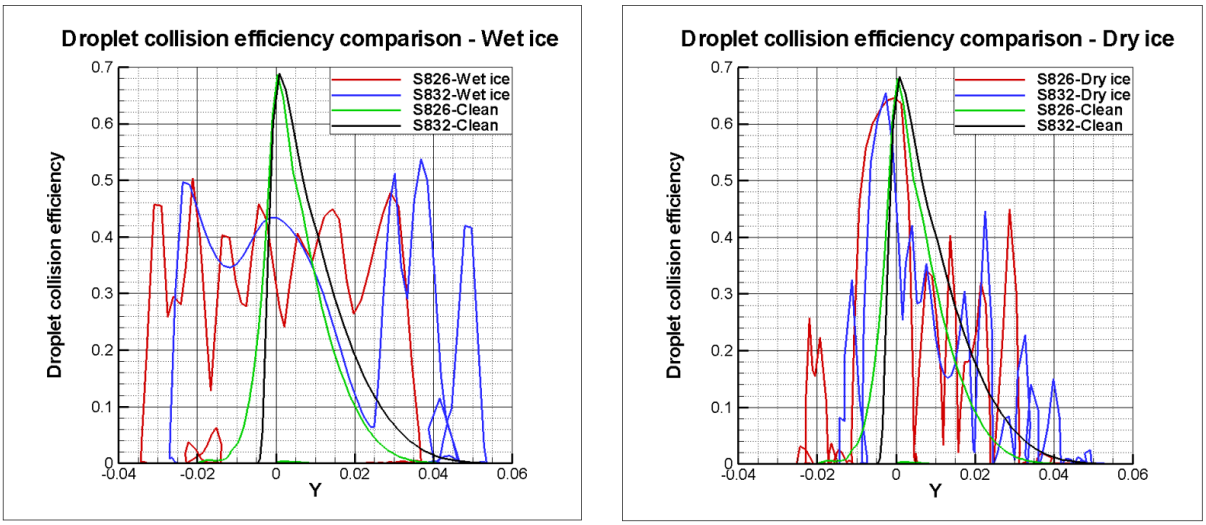

Figure C.8 – Droplet collision efficiency comparison.

Results show a decrease in maximum droplet collision efficiency for iced profiles, where as an increase in the droplet impingement area is observed, when compared with the clean profile. This change in the droplet impingement behaviour is mainly due to change in profile geometric shape after ice accretion. Figure C.9 presents a comparison of droplet impingement locations along clean and iced profiles. Results show an increase in the profile surface area under impingement of droplets in case of iced profiles.

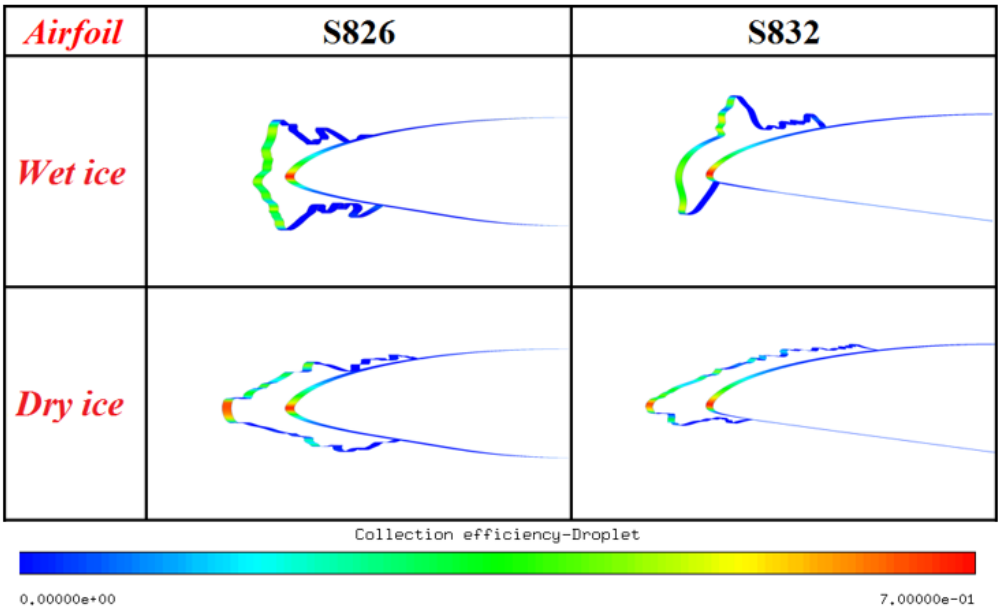

Figure C.9 – Droplet collision efficiency and impingement location along clean and iced profiles.

C.3.2. Aerodynamic Performance Analysis

To study the change in aerodynamics characteristics due to ice accretion, a detailed parametric numerical study is carried out using ANSYS−FLUENT. To validate the numerical setup, first the CFD simulations

of clean S826 & S832 are carried out to estimate the aerodynamic characteristics and results are compared with the published experimental NREL wind tunnel data of both airfoils. After that CFD simulations of airflow behaviour over ice profiles are carried out and aerodynamic characteristics are calculated and compared with the clean profile. The iced profile shapes obtained from experiments are used. Flow is simulated at different AOA's and comparison is made with the experimental aerodynamic characteristics of clean S826 and S832 airfoils. [14-15] Figure C.10 shows the aerodynamic coefficients of both clean and iced profiles, where experimental NREL clean represents the experimental results (AOA= -5° to 10°) of clean profile. [14-15] Results show a decrease in lift coefficients and increase in drag coefficient for iced profiles. This change is more significant for wet iced profiles, because of higher flow separation due to complex accreted ice shapes along leading edge.

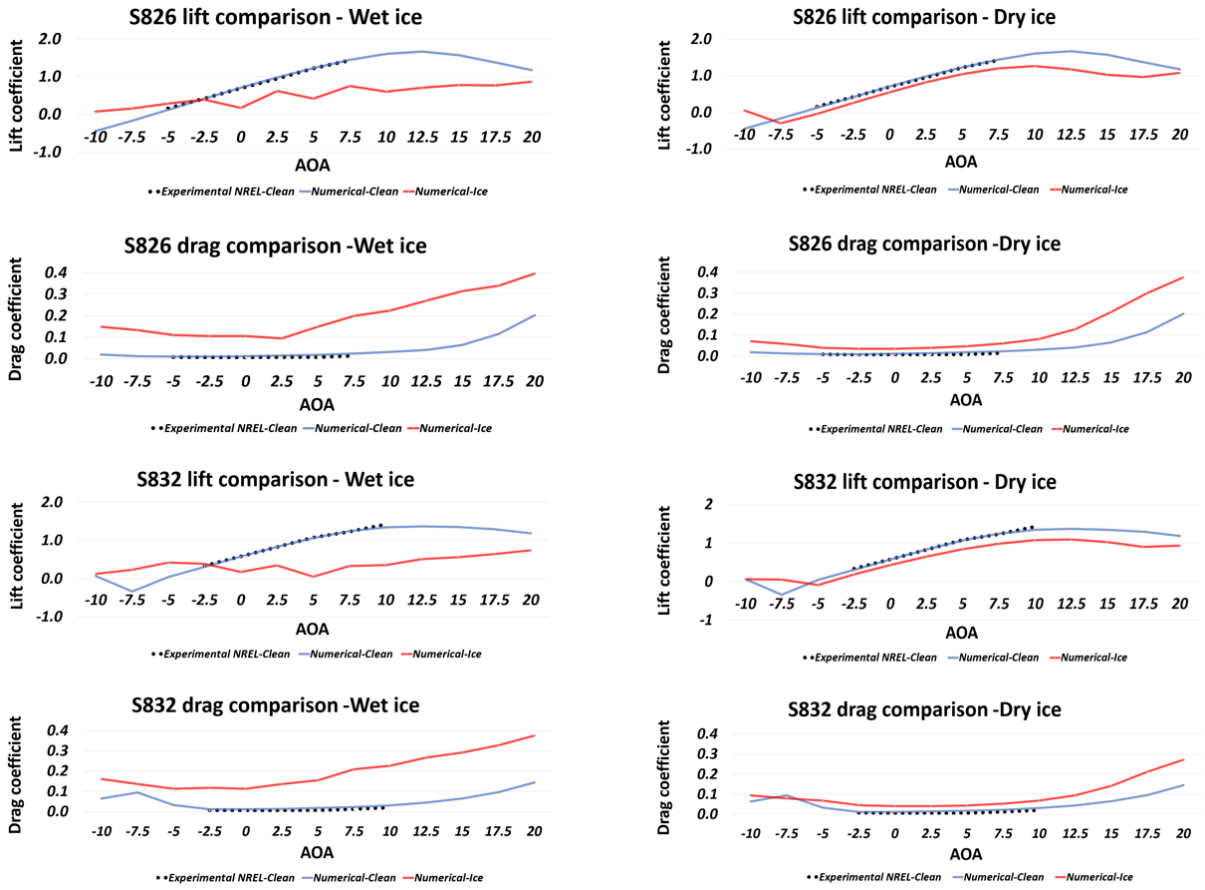

Figure C.10 – Comparison of aerodynamic performance for clean and iced profiles.

Figure C.11 presents the pressure coefficients distribution along clean and iced profiles at AOA= -5°, 0° & 5°. Results show that due to ice accretion along leading edge, the pressure coefficient of iced profile is quite different from clean profile. This change in pressure coefficient is more significant along leading edge and is quite dependent on accreted ice shape and distribution along pressure and suction sides. In case of wet ice more complex ice shapes are observed and the change in pressure coefficient is more significant.

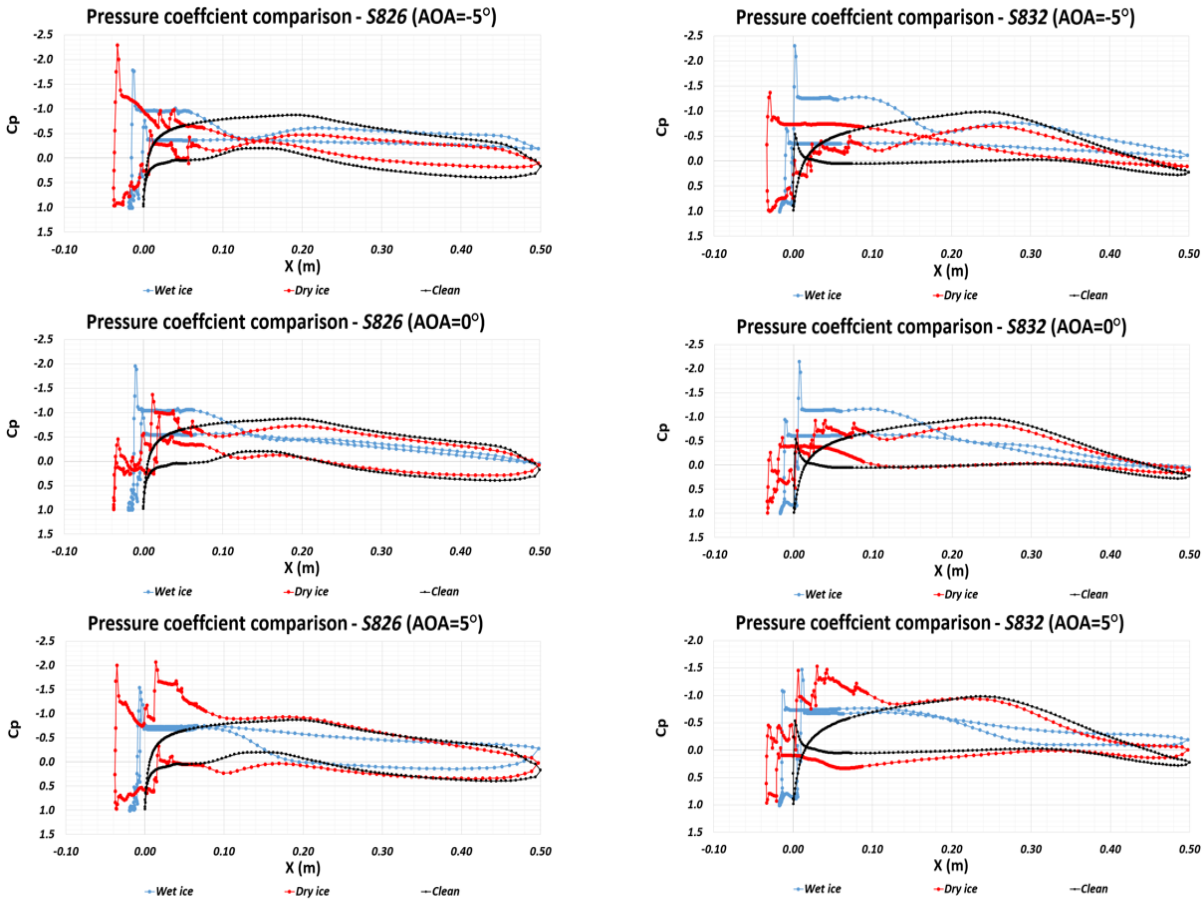

Figure C.11 – Pressure coefficient of clean and iced profiles at different AOA.

C.4. Conclusion

This study provides a good insight of ice accretion physics and its effect on aerodynamic performance of S826 & S832 airfoils. Results show that ice accreted differently along both profiles due to different geometric features. More complex ice shapes are observed in case of S832 profile when compared with S826. Horn type complex ice shapes are observed for both profiles in case of wet ice conditions mainly due to low freezing fraction and higher water run back. Analysis show that accreted ice distribution along pressure and suction sides of both profiles is different. In case of S826, for wet ice conditions, it is about 5%-10% and 15%-20% for S832 profile section, whereas for the dry ice conditions, ice accumulation extends towards the chord length approximately up to 25% for S826 and S832 airfoil. This is useful information for design of anti/de-icing systems for the wind turbine blades consisting of S826 or S832 airfoils. Numerical analysis of experimental iced profiles show a decrease in the aerodynamic characteristics of iced airfoils when it is compared with the clean airfoils. Changes in aerodynamic characteristics for S832 are higher than S826 particularly for wet ice conditions.

Acknowledgement

This work is supported by the University of Tromsø PhD project [no−381100/74104]. Authors would also like to acknowledge Mr. Pavlo Sokolov from UiT and Dr. David Hammond, Dr. Hugo Pervier and Mr. Peter West from Cranfield University, UK for assisting during icing tunnel experiments.

References

1. Davis, Neil, 2014. Icing Impacts on Wind Energy Production. DTU: DTU Wind Energy.
2. Yirtici, O., Tuncer, I.H., Ozgen, S., 2016. Ice accretion prediction on wind turbines and consequent power losses. J. Phys. Conf. Ser. 753.
3. Bleich, Katherine, Guimaraes, R.D., 2016. Renewable Infrastructure Investment Handbook: A Guide for Institutional Investors. World Economic Forum, Switzerland.
4. Pouryoussefi, S.G., Masoud, M., Nazemi, M.M., Fouladi, M., Doostmahmoudi, A., 2016. Experimental study of ice accretion effects on aerodynamic performance of NACA-23012 airfoil. Chin. J. Aeronaut. 29 (3), 585–595.
5. Lamraoui, F., Fortin, G., Benoit, R., Perron, J., Masson, C., 2014. Atmospheric icing impact on wind turbine production. Cold Reg. Sci. Technol. 100, 14.
6. Baring-Gould, I., Tallgaug, L., Ronsten, G., Hordaty, R., Cattin, R., Laakso, R., Durstewitz, M., Lacroix, A., Peltola, E., Wallenius, T., 2010. Recommendations for Wind Energy Projects in cold climates. VTT Technical Research Center, Finland, pp. 64.
7. Laakso, Timo, Baring-Gould, Ian, Durstewitz, Michael, Horbaty, Robert, Lacroix, Antoine, Peltola, Esa, Ronsten, Göran, Tallhaug, Lars, Wallenius, Tomas, 2010. State-of-The- Art of Wind Energy in Cold Climate. VTT Technical Research Center, Finland, pp. 71.
8. Shaw, R., Sotos, R., solano, F., 1982. An experimental study of airfoil icing characteristics. Twentieth Aerospace Sciences Conference.
9. Shin, Jaiwon, Bond, Thomas H., 1992. Results of an icing test on a NACA0012 airfoil in the NASA Lewis Icing Research Tunnel. In: 30th Aerospace Sciences Meeting and Exhibit. Reno, Nevada, pp. 23.
10. Virk, M.S., Homola, M.C., Nicklasson, P.J., 2010. Effect of rime ice accretion on aerodynamic chracteristics of wind turbine blade profiles. Wind Eng. 34 (2), 207–218.
11. Homola, M.C., Virk, M.S., Wallenius, T., Nicklasson, P.J., Sundsbø, P.A., 2010. Effect of atmospheric temperature and droplet size variation on ice accretion of wind turbine blades. J. Wind Eng. Ind. Aerodyn. 98 (12), 724–729.
12. Homola, Matthew C., Muhammad, S.Virk, Nicklasson, Per J., Sundsbø, Per Arne, 2012. Performance losses due to ice accretion for a 5 MW wind turbine. Wind Energy 15 (3), 379–389.
13. Jin, J.Y., Virk, M.S., 2018. Study of ice accretion along symmetric and asymmetric airfoils. J. Wind Eng. Ind. Aerodyn. 179, 10.14.
14. Somers, Dan M., 1995. The S825 and S826 Airfoils. NREL.
15. Somers, Dan M., 2002. The S830, S831, and S832 Airfoils. NREL.
16. Bertagnolio, F., Sørensen, Niels N., Johansen, Jeppe, Fuglsang, P., 2001. Wind Turbine Airfoil Catalogue. DTU-Risø National Laboratory, Roskilde, Denmark.
17. Etemaddar, M., 2013. Offshore Wind Turbine Operation under Atmospheric Icing and Controller System Faults. Department of Marine Technology, NTNU-Trondheim Norway CeSOS Conference Highlights.
18. Oggiao, Luca, 2014. CFD simulations on the NTNU wind turbine rotor and comparison with experiments. In: Renewable Energy Research Conference.
19. Cranfield University, 2019. Icing Tunnel. https://www.cranfield.ac.uk/facilities/icingtunnel.
20. Clift, R., Grace, J.R., Weber, M.E., 1978. Bubbles, Drops and Particles. New York.

Paper D

Study of Ice Accretion and Icing Effects on Aerodynamic Characteristics of DU96 Wind Turbine Blade Profile

Jia Yi Jin and Muhammad Shakeel Virk

Cold Regions Science and Technology, 2019, Volume 160. p. 119-127.

Doi: 10.1016/j.coldregions.2019.01.011

Author's Contribution

Jia Yi Jin has contributed substantially in the proposal of conceptualization, data curation, formal analysis, investigation, methodology, resources, software, visualization, validation, and writing of the paper.

D. Study of ice accretion and icing effects on aerodynamic characteristics of DU96 wind turbine blade profile

This is a reprint

Jia Yi Jin and Muhammad Shakeel Virk

Arctic Technology and Icing Research Group
Institute of Industrial Technology
Faculty of Engineering Science and Technology
UiT- The Arctic University of Norway
Norway

Abstract

In order to optimize the large wind turbines operation in ice prone cold regions, it is important to better understand the ice accretion physics and its effects on aerodynamic performance and power production losses. This paper describes a case study of ice accretion on DU96-W-180 airfoil, which has been used for large wind turbine blades such as NREL 5MW. Analysis has been carried out for glaze and rime ice conditions using icing tunnel experimental data and multiphase Computational Fluid Dynamics (CFD) based numerical approach. Results show a difference in profile surface roughness and heat fluxes during rime and glaze ice accretion process, which leads to a significant change in rate and shape of ice accretion. More complex ice shapes are observed in case of glaze ice conditions that affects the aerodynamic performance differently from rime ice conditions. Numerical results are compared with the experimental data, where a good agreement is found. Results show higher aerodynamic performance degradation for glaze ice conditions particularly at higher angles of attack.

Keywords:
Ice accretion; Wind turbine; Aerodynamic; Icing tunnel; Surface roughness; CFD.

D.1. Introduction

In recent years, activities regarding wind energy projects in ice prone cold regions have increased due to availability of good wind resources, but atmospheric icing on wind turbine blades is considered as a potential hazard in proper utilization of these good wind resources. Atmospheric icing affects the wind turbine aerodynamic performance, which leads to a decrease in wind energy production [1]. Worldwide, installed wind energy capacity in ice prone regions is expected to reach 123 GW in year 2020 [2]. Wind energy production losses due to icing have been reported to lead up to a 17% decrease in Annual Energy Production (AEP) and 20−50% in aerodynamic performance [3]. This highlights the importance of finding the innovative solutions for wind turbine operations in icing conditions. There is a growing need to improve knowledge about aerodynamic design and performance of large wind turbine rotor blades for optimal operations in icing conditions. The icing conditions within cold climates are insufficiently included in the design limits presently covered by the national and international standards for wind turbine design. The International Energy Agency (IEA) Task 19: 'Wind energy in cold climates' has also urged the development of new methods to enable better understanding of the effects of ice accretion on wind turbine performance and energy production [4].

Atmospheric ice accretion on wind turbine blades is caused by the impingement of super-cooled water droplets. Atmospheric ice is mainly classified as dry rime and wet glaze ice. Rime ice is soft and less dense and happens at very low temperature, when 100% impinging droplets freeze, whereas glaze ice is harder and denser. Glaze ice happens close to freezing temperature, when freezing fraction of impinging droplet is not 100% and some droplets run along blade surface as very thin water film. Accreted ice has a range of shapes resulting from different temperatures and heat balance situations that causes different levels of aerodynamic performance losses. Duncan et al. [5] made differentiation between rime and glaze ice shapes and found that glaze ice caused larger loss than rime ice. Virk et al. [6] found that the ice mainly accretes along leading edge of the blade and reduces torque. This effects the wind turbine aerodynamic performance and results in Annual Energy Production (AEP) losses. The parameters causing wind turbine blade aerodynamic penalty can be divided into three categories: small-scale surface roughness, large-scale surface roughness and ice geometry. The shape of the accreted ice along the wind turbine blade depends upon many variables such as point of operation, the geometry of the wind turbine blade, relative wind velocity, atmospheric temperature, droplet diameter and the liquid water content [7]. Better understanding of ice accretion effects on the blade aerodynamics can help to optimize its design and reduce the AEP losses.

Ice accretion physics and its effects on wind turbine's aerodynamic performance can be analysed using both experimental and numerical approaches. In recent years, advance CFD based numerical techniques have begun to play a significant role both in simulating and determining the performance of wind turbine blades under icing conditions [8-13]. Lab based icing tunnel experimenters provide more accurate picture of ice accretion, however, it have limited insight of the air flow and droplet behaviour, whereas CFD simulations can provide the economical insight details of air flow physics and droplet behaviour, which is difficult to obtain from icing tunnel experiments.

DU96-W-180 airfoil has been an attractive choice for large wind turbine blades and has been used for NREL 5MW wind turbine. This is an asymmetric profile with 18% thickness and has aerodynamic features, such as high-lift-to-drag ratio, insensitivity to contaminations and low noise [14-16]. Many researchers have carried out analysis to investigate DU series wind turbine blade profiles using experimental and numerical techniques [6, 17]. Linyue Gao et al. have done the experimental study of

ice mitigation for DU96-W-180 airfoil. [16, 18], but not much work has been carried out by the researchers to study the performance of DU96 airfoil under icing conditions. Matthew C. Homola et al. [19] have done CFD based numerical study to simulate the ice on DU96 airfoil as part of NREL 5MW wind turbine study, but no published work is available regarding icing tunnel experimentation of DU96 airfoil.

This paper is focused on better understating of ice accretion physics and its resultant effects on aerodynamic performance of DU96-W-180 airfoil. Both icing tunnel experiments and CFD based numerical simulations have been carried out to better investigate the ice accretion physics and resultant rate and shapes of accreted ice for both rime and glaze ice conditions. Icing tunnel experiments are carried out at Cranfield University UK, whereas CFD based numerical simulations are carried out using ANSYS-FENSAP ICE and FLUENT.

D.2. Experimental Analysis

D.2.1. Experimental Setup

The experimental study is carried out at icing wind tunnel laboratory of Cranfield University (CU), UK. DU96 wind turbine blade profile model with a span of 758 mm and chord length of 500 mm was used. The surface of blade profile model was made of Galvanized steel (VGAL.V.D×SID+Z275) with an average surface roughness of 0.9 µm. Icing wind tunnel facility of CU is able to create natural icing conditions. This icing tunnel has test section (761×761 mm) and can operate for Medium Volume Diameter (MVD) ranging from 15 to 80 microns, Liquid Water Content (LWC) from 0.05−3 g/m^3 and air temperature from -30 to +30 °C. Figure D.1 shows the icing wind tunnel setup and test cross section.

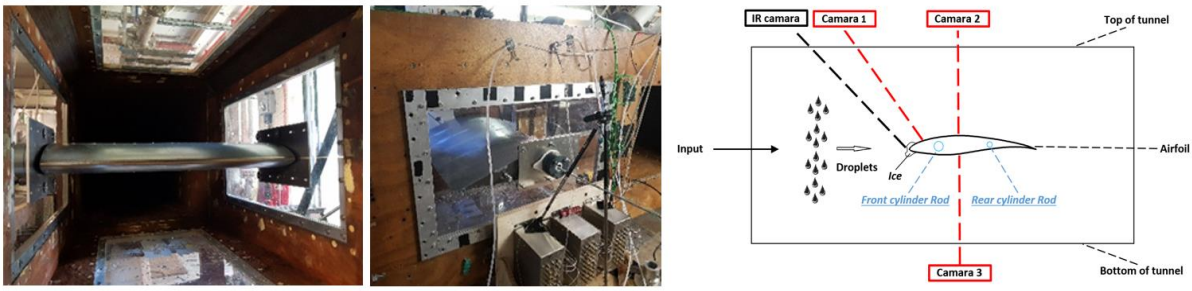

Figure D.1 – CU icing wind tunnel setup.

To closely monitor the ice accretion on the blade profile, three different High Definition (HD) cameras (one for side, one for top and one for top view) were used for video recording and images. Accreted ice shapes were extracted and sketched after each experiment. These experiments were carried out at Reynolds number = 3×10^6 for both dry rime and wet glaze ice conditions. Table D.1 shows the operating conditions used for the experiments.

Table D.1 – Icing tunnel operating conditions.

Test	Ice Type	Velocity (m/s)	Temperature (^{0}C)	LWC (g/m^3)	MVD (microns)	AOA (degree)	Icing time (mins)
1	Glaze	77	-5	0.35	20	0	15
2	Rime	70	-20				

To closely monitor the icing tunnel operations, various operating parameters of icing tunnel are closely monitored to make sure the smooth operations. MVD of 20 µm is used with the droplet distribution spectrum consists of 60 bins. Figure D.2 shows the droplet distribution spectrum, variation of icing tunnel air speed and total air temperature at tunnel test section for both rime and glaze ice conditions.

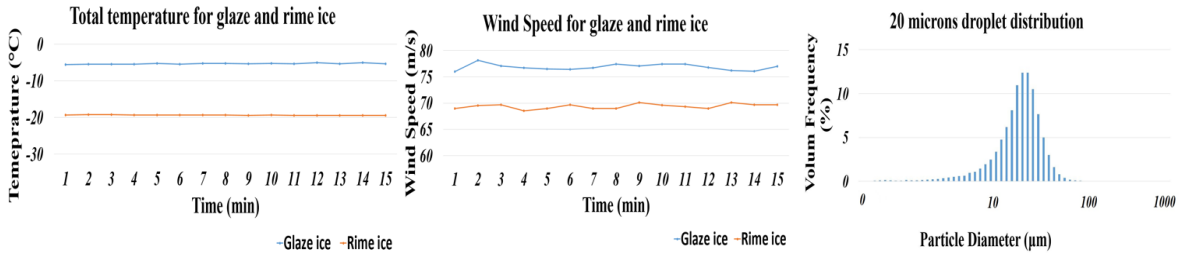

Figure D.2 – Variation of wind speed, temperature and droplet distribution spectrum in CU icing tunnel.

D.2.2. Experimental Results

Figure D.3 shows the experimental ice growth with time where results show a significant difference in ice growth for both rime and glaze ice conditions. Views from three different HD cameras were used to monitor the ice growth for this study.

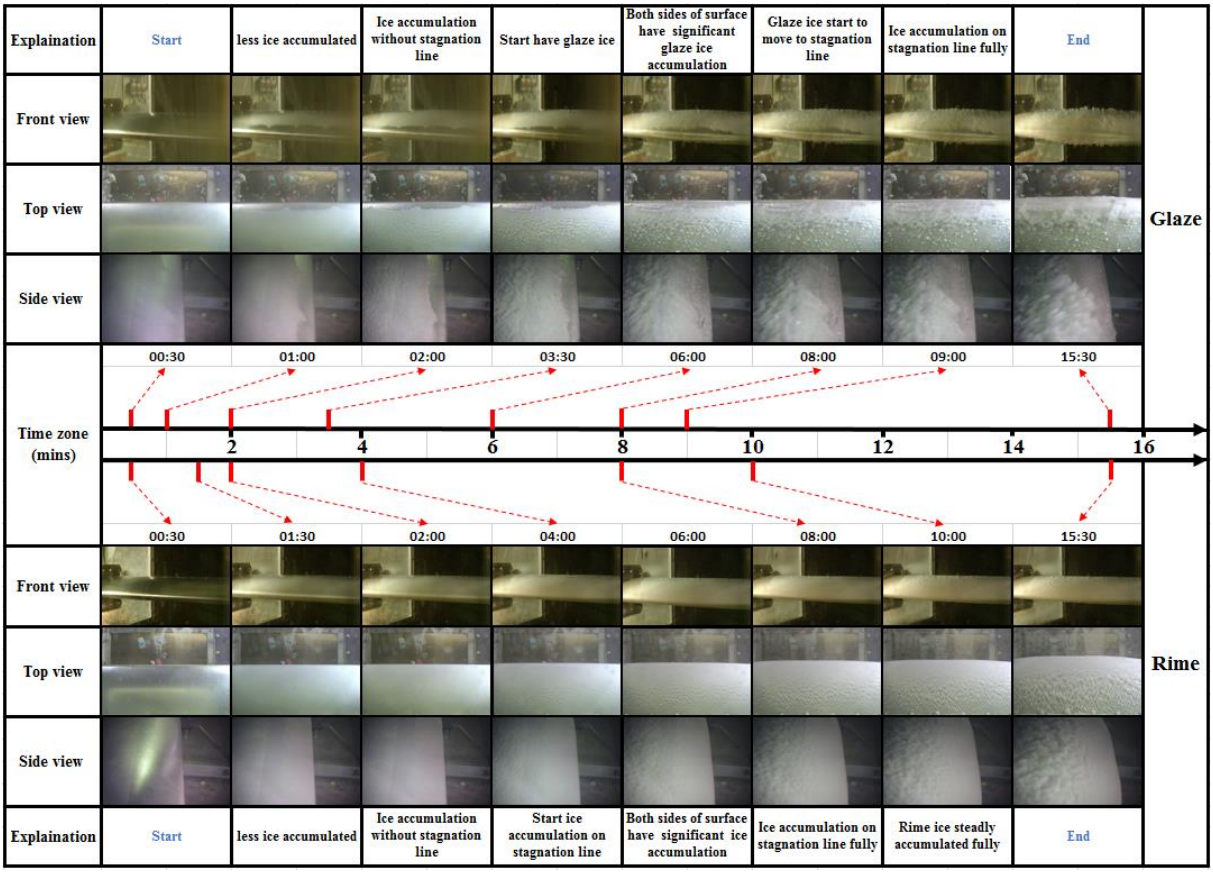

Figure D.3 – Overview of experimental ice growth at various time steps for 15 minutes.

Figure D.3 shows the ice accretion process at different time intervals for both rime and glaze ice conditions. Results show that ice mainly accreted along leading edge of the blade profile. Analysis shows that for rime conditions, accreted ice was dense and its shape along stagnation line was smooth. Further down from leading edge, tight grain hard rime ice with direction of feather growing parallel to the flow is observed. For rime conditions, ice accretion extended till 20−25% of the profile chord length. For glaze conditions, clear ice is observed along stagnation line with horn shape. Large individual feathery spikes, pointing perpendicular to the profile surface is observed. After each experiment, the ice shapes were extracted from center section of the blade profile. Experimental ice shapes with cut-outs and ice thicknesses are shown in Figure D.4. Streamline ice shapes are observed for the rime ice conditions, whereas complex horn type shapes are found in case of glaze ice conditions.

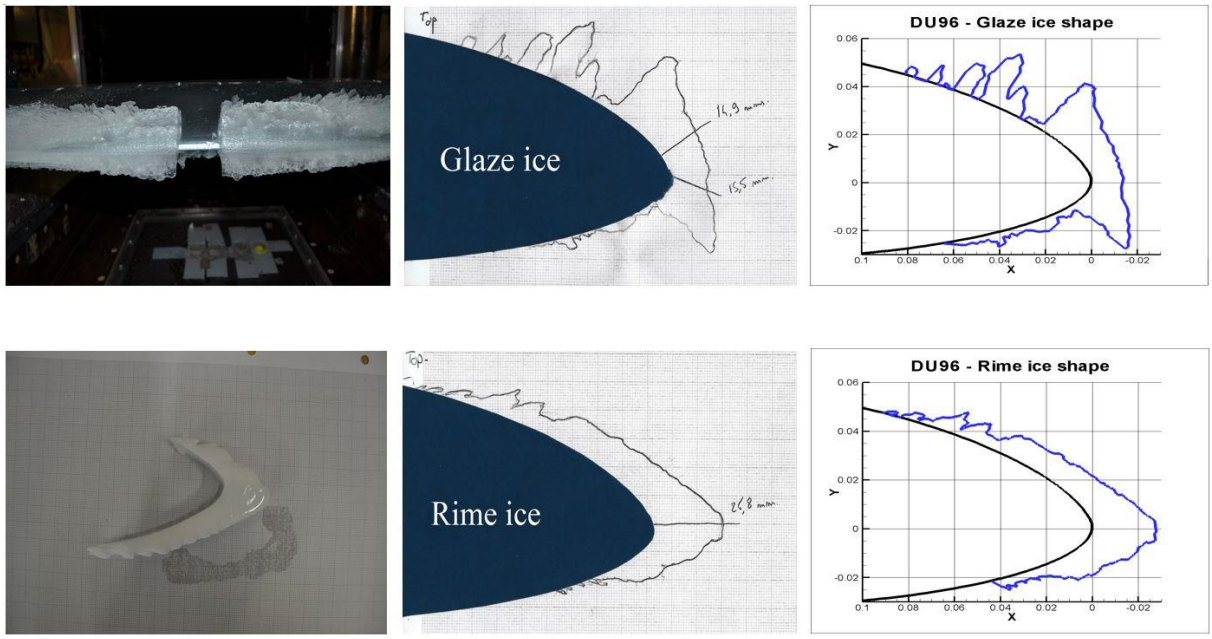

Figure D.4 – Experimental ice shapes for glaze and rime ice conditions.

D.3. Numerical Analysis

D.3.1. Numerical Setup

CFD based multiphase numerical simulations are carried out using ANSYS-FENSAP and FLUENT to study the airflow behaviour, droplet behaviour and to simulate the surface thermodynamics and resultant ice accretion. Aerodynamic coefficients (C_L and C_D) of clean and iced profiles are calculated and compared. Ice shapes form numerical simulations are compared with the experimental data. CFD simulations provided a detailed overview of the airflow and droplet behavior, which is not easy to study from experiments. Atmospheric ice accretion on blade profile can be numerically simulated by means of integrated thermo-fluid dynamic models, which involve the fluid flow simulation, droplet behaviour, surface thermodynamics and phase changes. Airflow behaviour is simulated by solving the nonlinear partial differential equations for the conservation of mass, momentum and energy.

$$\partial \rho_\alpha / \partial t + \vec{\nabla}(\rho_\alpha \overrightarrow{\boldsymbol{v_\alpha}}) = 0 \tag{D.1}$$

$$\partial \rho_\alpha \overrightarrow{\boldsymbol{v_\alpha}} / \partial t + \vec{\nabla}\,(\rho_\alpha \overrightarrow{\boldsymbol{v_\alpha}}\ \overrightarrow{\boldsymbol{v_\alpha}}) = \vec{\nabla}.\sigma^{ij} + \boldsymbol{\rho_\alpha}\,\vec{g} \tag{D.2}$$

$$\partial \rho_\alpha E_\alpha / \partial t + \vec{\nabla}\,(\rho_\alpha \overrightarrow{\boldsymbol{v_\alpha}} H_\alpha) = \vec{\nabla}\left(\kappa_\alpha \left(\vec{\nabla}\, T_\alpha\right) + \nu_i \tau^{ij}\right) + \boldsymbol{\rho_\alpha}\,\vec{g}\,\overrightarrow{\boldsymbol{v_\alpha}} \tag{D.3}$$

Where ρ is the density of air, *v* is the velocity vector, subscript α refers to the air solution, T refers to the air static temperature in Kelvin, σ^{ij} is the stress tensor and E and H are the total energy and enthalpy, respectively. The sand grain roughness for the iced surface is calculated using following Shin et al. roughness model [20].

$$[(k_s/c)/((k_s/c)_{base})]_{MVD} = \begin{cases} 1, & MVD \le 20 \\ 1.667 - 0.0333(MVD), & MVD \ge 20 \end{cases} \tag{D.4}$$

Where MVD is the droplet Median Volume Diameter (in microns), whereas the corresponding value of sand-grain roughness is obtained:

$$k_s = 0.6839[(k_s/c)/((k_s/c)_{base})]_{LWC} \\ [(k_s/c)/(k_s/c)_{base}]_{T_s}[(k_s/c)/((k_s/c)_{base})]_{MVD}(k_s/c)_{base}c \quad (D.5)$$

Two phase flow (air and water droplets) is numerically simulated using the Eulerian approach, where the super cooled water droplets are assumed to be spherical. The Eulerian two phase fluid model consists of the Navier-Stokes equation with the water droplets continuity and momentum equation. The water droplet drag coefficient is based on the empirical correlation for the flow around the spherical droplets described by Clift et al. [21]

$$\partial\alpha/\partial t + \vec{\nabla}\left(\alpha\overrightarrow{V_d}\right) = 0 \quad (D.6)$$

$$\partial\left(\alpha\overrightarrow{V_d}\right)/\partial t + \vec{V}\left(\rho_\alpha\,\overrightarrow{V_d}H_d\right) = C_D Re_d/24k\;\alpha\left(\overrightarrow{V_a} - \overrightarrow{V_d}\right) + \alpha(1-\rho_a/\rho_d)\,1/(Fr^2)\,\vec{g} \quad (D.7)$$

Where α is the water volume fraction, V_d is the droplet velocity, C_D is the droplet drag coefficient and Fr is the Froude number. The numerical study is carried out for custom droplet distribution spectrums at MVD of 20 µm. Surface thermodynamics is calculated using the mass and energy conservation equations, considering the heat flux due to convective and evaporative cooling, heat of fusion, viscous and kinetic heating.

$$\rho_f\left[\partial h_f/\partial t + \vec{\nabla}\left(\bar{V}_f h_f\right)\right] = V_\infty LWC\beta - \dot{m}_{evap} - \dot{m}_{ice} \quad (D.8)$$

$$\rho_f\left[\left(\partial h_f c_f \dot{T}_f\right)/\partial t + \dot{\nabla}\left(\partial h_f c_f \dot{T}_f\right)\right] = \left[c_f\left(\tilde{T}_\infty - \tilde{T}_f\right) + \left(\left\|\vec{V}_d\right\|^2\right)/2\right]V_\infty LWC\beta - L_{evap}\dot{m}_{evap} + \\ \left(L_{fusion} - c_s\tilde{T}\right)\dot{m}_{ice} + \sigma\varepsilon(T_\infty^4) - T_{f^4} - c_h\left(\tilde{T}_f - \tilde{T}_{ice,rec}\right) + Q_{anti-icing} \quad (D.9)$$

The coefficients ρ_f, c_f, c_s, σ, ε, L_{evap}, L_{fusion} are physical properties of the fluid. The reference conditions $\tilde{T}_\infty$, V_∞, LWC are the airflow and droplets parameters. 3D grid is generated by extruding a single cell layer in the span wise direction. ALE (Arbitrary Langrangian Eulerian) formulation is used for the grid displacement during ice accretion, which adds the grid speed terms to the Navier-Stokes equations to account for the mesh velocity [22]. Mesh sensitivity study was carried out using coarse, medium and fine meshes to accurately determine the boundary layer characteristics (shear stress and heat flux). For each case, the mesh was automatically displaced after each time shot to account for the ice growth without any change in mesh size. During mesh sensitivity analysis, number of mesh elements and y+ value < 1 for first cell layer was selected based upon the heat flux calculations, where a numerical check was imposed that the heat flux computed with the classical formulae dT/dn should be comparable with the heat flux computed with the Gresho's method. Mesh sensitivity study showed that the effect of mesh size on droplet solution was negligible, however some flow quantities including convective heat flux on the blade surface was sensitive to the mesh size, resulting in higher instantaneous ice growth in regions with higher convective heat loss. After mesh sensitivity analysis, O type structured numerical grid with y+ value < 1 and total 48,450 hexahedral elements was used for final simulations, shown in Figure D.5.

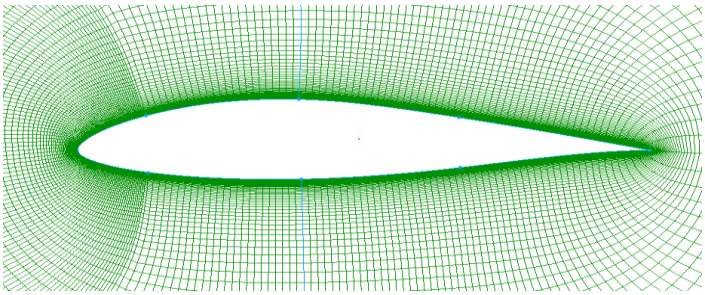

Figure D.5 – Numerical grid for DU96-W-180 airfoil.

K-omega SST turbulence model is used as a compromise between acceptable computational cost and required accuracy for simulating the turbulent flow. Sand grain roughness height for the iced surface was calculated with an empirical correlation described by Shin and Bond [20]. Numerical simulations are carried out at conditions specified in Table D.2.

Table D.2 – Numerical setup.

Chord length (m)	0.5
Angle of attack (AOA, degree)	0
Air velocity (m/s)	70 (rime), 77 (glaze)
Temperature (Celsius)	-20 (rime), -5 (glaze)
MVD (microns)	20
Droplet distribution	Custom distribution from CU (see Figure D.2)
LWC (g/m^3)	0.35
Icing time (mins)	15

D.3.2. Numerical Results

Numerical simulations have been carried out to study the ice accretion physics and its effects on airflow and droplet behaviour. In this numerical study, air flow and droplet behaviour is analyzed at different time intervals during ice accretion, which is not easily possible during icing tunnel experiments. Quasi-steady state multi-shot numerical simulations approach is used where total icing duration (15 minutes) is divided in 23 time steps. Detailed analysis have been carried out to analyses the results at each time step.

D.3.2.1. Airflow behavior

Analysis of airflow behavior show a change in velocity and pressure distribution along pressure and suction sides of the blade profile. A shift in the position of stagnation point is observed as ice accretes along leading edge. Not much flow separation is observed in case of rime ice conditions as compared to the glaze ice conditions. Figure D.6 shows the velocity contours along leading edge for glaze and rime ice conditions at different time steps.

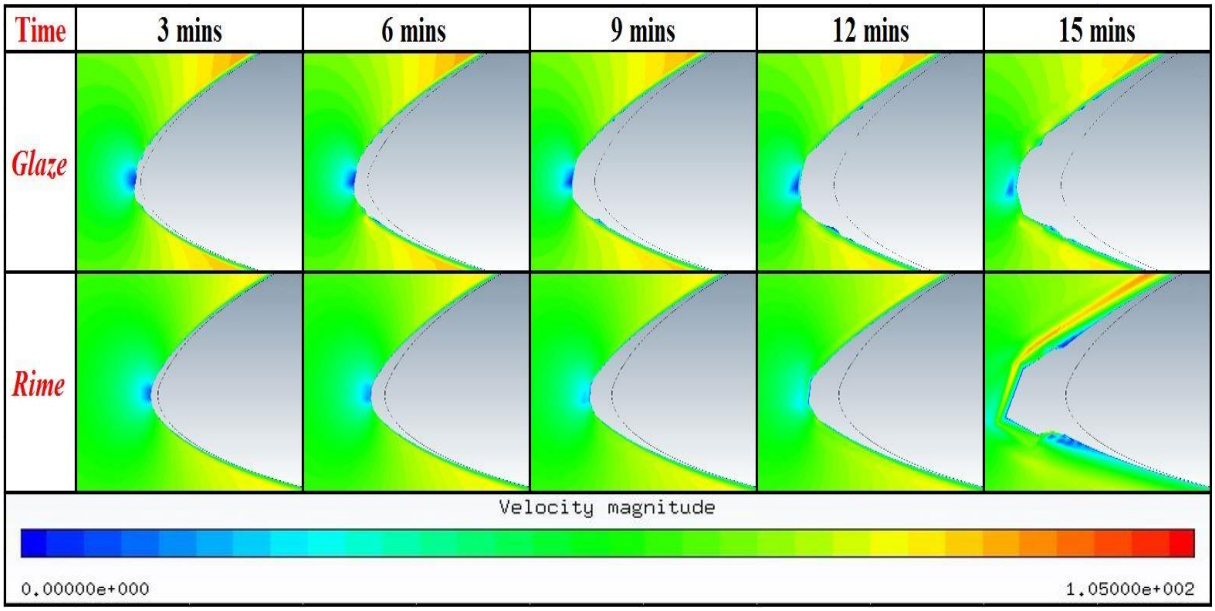

Figure D.6 – Velocity magnitude at different time steps.

During the ice accretion process, the surface roughness of the blade profile changes significantly, which effects the shear stresses and heat fluxes. This leads to a change in the boundary layer thickness which influences the convective heat transfer and droplet sticking efficiency along the blade surface. To better understand the effects of surface roughness change on shear stress and heat flux, analysis has been carried out. Figure D.7 shows the surface roughness change during the ice accretion process whereas Figure D.8 shows the heat transfer comparison for both rime and glaze ice conditions.

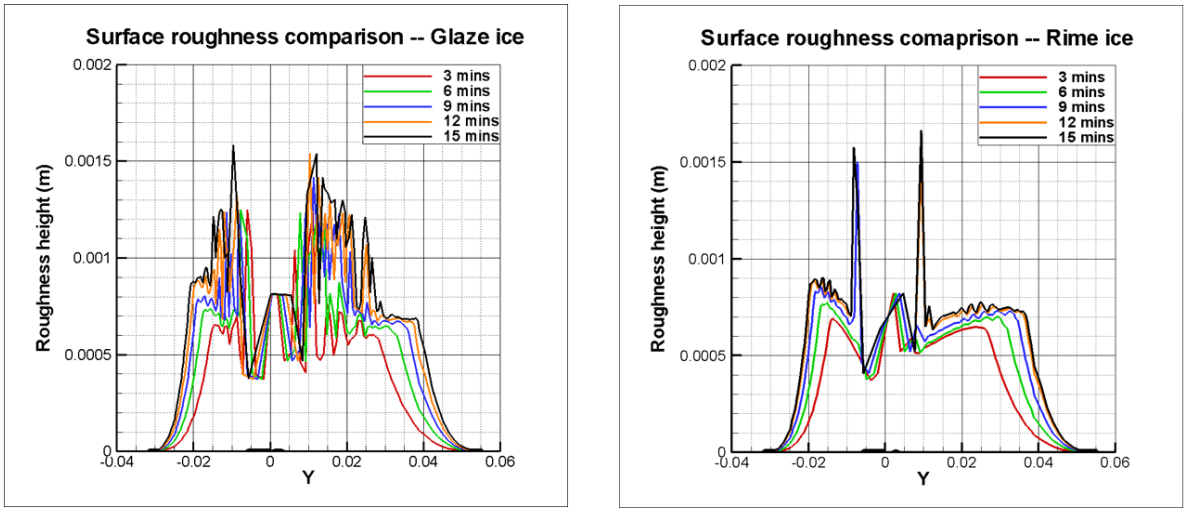

Figure D.7 – Surface roughness variation during ice accretion.

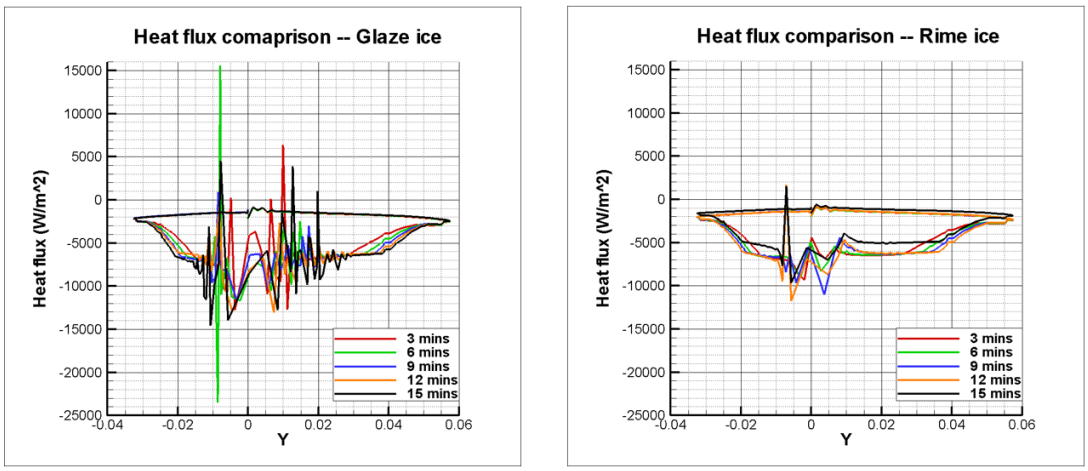

Figure D.8 – Heat flux variation during ice accretion.

Analysis shows that surface roughness and heat flux increases as ice accretion process progresses. Results show higher values of the surface roughness along leading edge of the blade profile, mainly due to higher droplet collision which leads to more ice accretion. Leading edge sections with higher surface roughness also shows higher values of surface heat transfer during ice accretion.

D.3.2.2. Droplet Behavior

The droplet behavior at each time step is analysed, where results show a change in droplet collision efficiency with the change of blade profile shape during ice accretion process. Figure D.9 shows the droplet collision efficiency variation at five different time intervals for rime and glaze ice conditions. Results show that droplet collision efficiency is higher at start of the ice accretion process, but as ice accretes, a decrease in the droplet collision efficiency is observed. This change in droplet collision is mainly due to change in blade profile shape particularly at leading edge. Along leading edge significant ice accretes due to higher droplet collision efficiency, whereas water runback process also occurs during ice accretion particularly for glaze ice conditions which results in small patches/feathers of ice along other areas of the blade profile. This leads to a change in droplet collision efficiency along blade profile during ice accretion process. Figure D.9 shows the droplet collision efficiency variation during ice accretion process for both rime and glaze ice conditions.

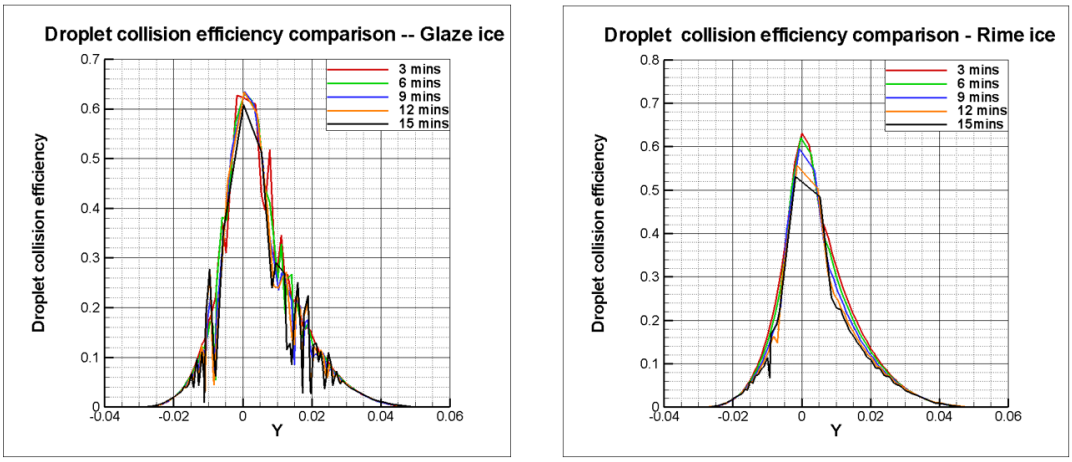

Figure D.9 – Droplet collision efficiency at different time intervals.

D.3.2.3. Ice Accretion

Figure D.10 shows the water run back film thickness variation along blade profile surface during ice accretion process. Due to very low temperature for rime ice conditions, the droplet freezing fraction is 100% due to which no water run back phenomena is observed for rime ice conditions, whereas for glaze ice conditions, analysis shows water run back along profile section. Figure D.11 shows the ice shapes of DU96 blade profile obtained from experimental and numerical simulations. A reasonably good agreement is found for the ice shapes particularly for the ice growth along stagnation point of the blade profile for both rime and glaze ice conditions. For glaze ice conditions, due to water run back and high aerodynamic heat flux along leading edge, complex horn shapes are obtained during the experiments. These ice horns are not captured very well in the numerically simulated ice shapes. For glaze ice conditions, when high speed water droplets collide with the airfoil surface, they do not get enough time to freeze and following droplets hit. Incoming airflow pushes these droplets further away from the stagnation line which leads to accumulation of these droplets along upper and lower sides of the airfoil as thin water film. This phenomena is not easy to capture during numerical simulations. To better understand this, water film thickness was simulated at each time step, shown in Figure D.10, where results show a clear trend of thick water film along leading edge.

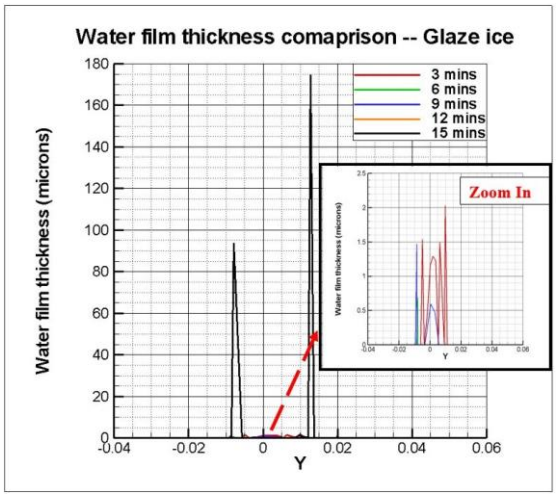

Figure D.10 – Water runback film thickness for glaze ice conditions.

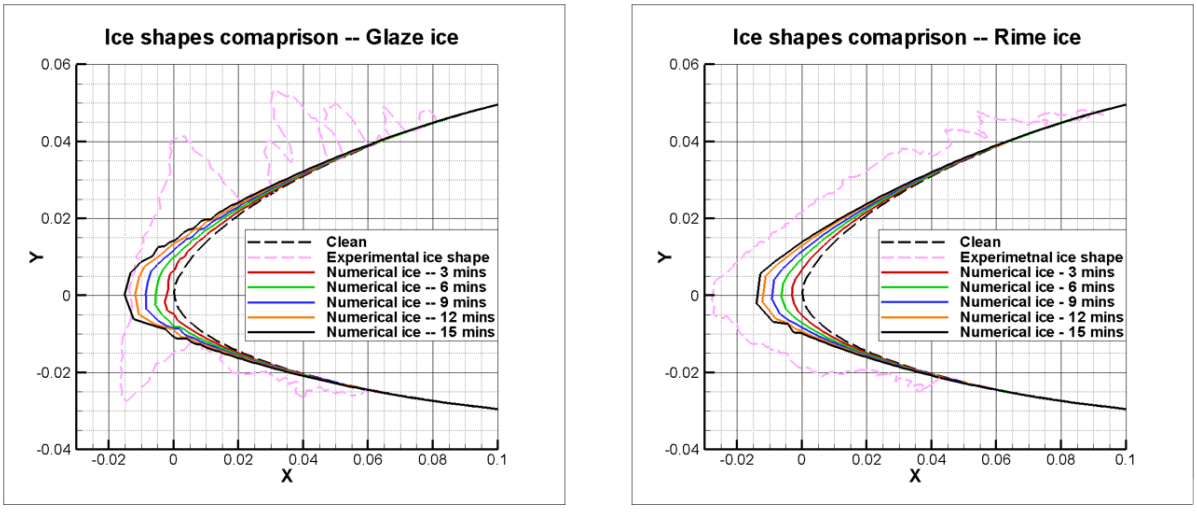

Figure D.11 – Accreted ice shapes comparison for rime and glaze ice conditions.

D.4. Aerodynamic Analysis of Experimental Ice Shape Profiles

Airflow and droplet behaviour along blade profile surface is influenced by the accreted ice shape. During ice accretion process the shape of the blade profile surface changes significantly, which also changes the flow behavior and leads to a change in aerodynamic performance of the blade profile. This section presents a detailed numerical study to analyze the change in aerodynamic performance of the DU96. Experimental ice shapes (after 15 mins) are used for this study, where a comparison is made between aerodynamic characteristics of the clean and experimental iced blade surfaces. Figure D.12 shows the velocity streamlines along the experimental ice shape obtained from rime and glaze ice conditions.

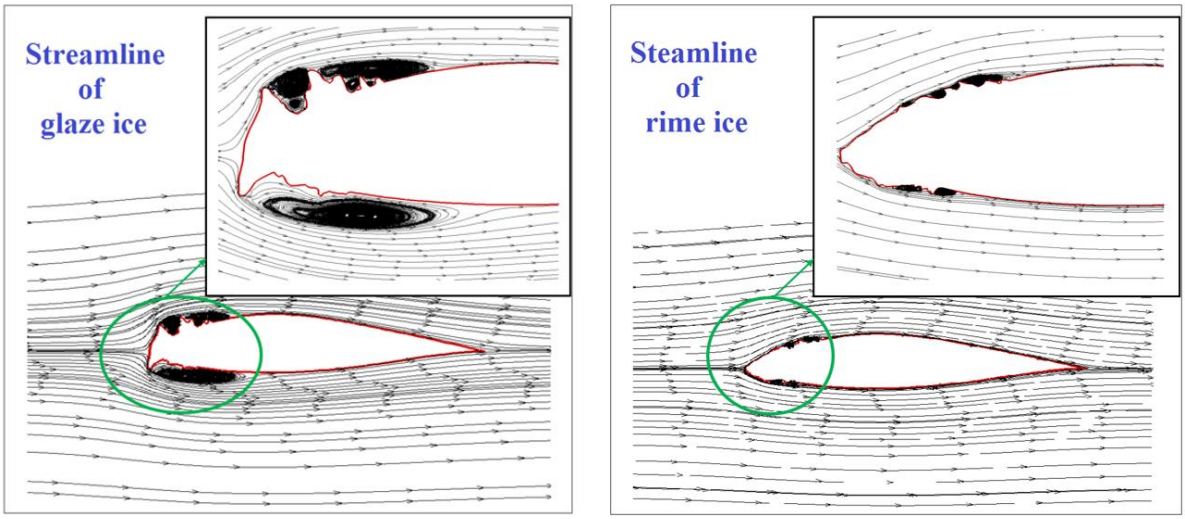

Figure D.12 – Velocity streamlines along iced DU96 blade profiles.

To analyse the change in aerodynamics characteristics of the iced profile, a detailed parametric study has been carried out at different angles of attack. The iced profile shapes obtained from experiments are used where the flow is simulated at different AOA and comparison is made with the aerodynamic characteristics of clean DU96 airfoil. These simulations are carried out using ANSYS-FLUENT. Figure D.13 shows the lift and drag coefficients comparison.

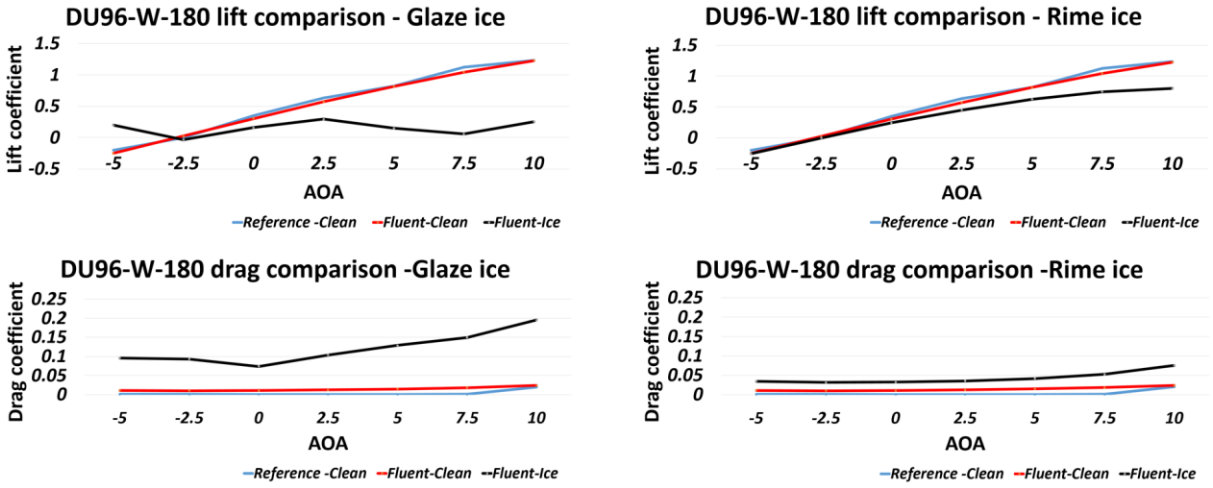

Figure D.13 – Comparison of lift and drag coefficients.

Analysis of Figure D.13 shows a decrease in the aerodynamic characteristics of ice profile when it is compared with the clean profile. This change in the aerodynamic characteristics is mainly due to a change in the blade profile aerodynamic shape due to ice and surface roughness, which affects the boundary layer flow behaviour. At all angles of attack, a significant increase in the drag coefficient is observed due to flow separation. As an overall, higher drag coefficient is found for glaze ice shapes, which leads to higher aerodynamic performance loss.

D.5. Conclusion

This ice accretion study for DU96 airfoil showed more streamlined ice shape for dry rime ice conditions, whereas complex horn type ice shape was found for case of glaze ice. This is mainly due to difference in droplet freezing fraction, as due to low freezing fraction for glaze ice conditions, higher water run back and aerodynamic heat flux along leading edge is observed which resulted in complex horn type ice shapes. This phenomenon is difficult to capture during numerical simulations and requires further improvements in the existing numerical models of wet ice accretion. Numerical results showed that blade profile surface roughness and heat flux changes significantly during ice accretion process which effects the airflow and droplet behavior. The change in accreted ice shape effects the airflow behavior and aerodynamics performance. Analysis show a decrease in the aerodynamic characteristics of the iced airfoils when it is compared with the clean. This degradation in aerodynamic performance is higher in case of glaze ice, as compared to the rime iced profile. Icing tunnel experiments provided a good overview of the ice accretion process, but it is not easy and economical to study the airflow and droplet behaviour during ice accretion process in experimental study. Therefore CFD based numerical techniques can be a good tool to study the change in air flow and droplet behaviour during ice accretion process.

Acknowledgement

This work is supported by the University of Tromsø PhD project [no 381100/74104] and WindCoE (Nordic Wind Energy Centre) project (no 338/2015) within the Interreg IVA Botnia−Atlantica, as part of European Territorial Cooperation (ETC). Authors would like to acknowledge Dr. David Hammond, Dr. Hugo Pervier and Mr. Peter West from Cranfield University, UK for assisting during icing tunnel experimentation.

References

1. Virk, Muhammad S., 2011. Atmospheric ice accretion on non-rotating circular cylinder. J. Comput. Multiphase Flow 3, 197–205. https://doi.org/10.1260/1757-482X.3.4.197.
2. Dvorak, Paul, 2013. Navigant research releases latest wind report: World Market Update2012, Ed. 18. Navigant Research, Copenhagen, Denmark.
3. Yirtici, Ozcan, Tuncer, Ismail H., Ozgen, Serkan, 2016. Ice accretion prediction on wind turbines and consequent power losses. J. Phys. Conf. Ser. 753. https://doi.org/10. 1088/1742-6596/753/2/022022.
4. Laakso, Timo, Talhaug, Lars, Ronsten, Göran, Horbaty, Robert, Baring-Gould, Ian, Lacroix, Antoine, Peltola, Esa, Wallenius, Tomas, Durstewitz, Michael, 2009. Task 19 Wind Energy in Cold Climates.

5. Duncan, T., LeBlanc, M., Morgan, C., Landberg, L., 2008. Underestanding Icing Losses and Risk of Ice Trhow at Operating Wind Farms, Windterwind 2008. Norrköping, Sweden.
6. Virk, Muhammad S., Homola, Matthew C., Nicklasson, Per J., 2010. Effect of rime ice accretion on aerodynamic chracteristics of wind turbine blade profiles. Wind Eng. 34, 207–218. https://doi.org/10.1260/0309-524X.34.2.207.
7. Peter, Drage, 2009. Numerical simulation of ice accretion on wind turbines. IWAIS 2009.
8. Timmer, W.A., 2010. Aerodynamic characteristics of wind turbine blade airfoils at high angle-of-attack. In: Proceedings of the 3rd EWEA Conference-Torque 2010: The Science of Making Torque from Wind.
9. Han, Woobeom, Kim, Honghwa, Kim, Bumsuk, 2018. Study on correlation between wind turbine performance and ice accretion along a blade tip airfoil using CFD. J. Renew. Sustain. Ener. 10https://doi.org/10.1063/1.5012802. 023306(2018).
10. Tagawa, Gitsuzo D., Morency, François, Beaugendre, Héloïse, 2018. CFD study of airfoil lift reduction casused by ice roughness. In: Proceedings of the 2018 Applied Aerodynamics Conference, https://doi.org/10.2514/6.2018-3010.
11. Jin, Jia Yi, Virk, Muhammad Shakeel, 2018. Study of ice accretion along symmetric and asymmetric airfoils. J. Wind Eng. Ind. Aerod. 179, 240–249. https://doi.org/10. 1016/j.jweia.2018.06.004.
12. Sokolov, Pavlo, Jin, Jia Yi, Virk, Muhammad S., 2018. Accreted ice mass ratio (k-factor) for rotating wind turbine blade profile and circular cylinder. Wind Energy. https:// doi.org/10.1002/we.2298.
13. Liang, Jian, Liu, Maolian, Wang, Ruiqi, Wang, Yuhang, 2018. Study on the glaze ice accretion of wind turbine with various chord lengths. In: Proceedings of the Earth and Environmental Science, https://doi.org/10.1088/1755-1315/121/4/042026.
14. Timmer, W.A., van Rooij, R.P.J.O.M., 2003. Summary of the Delft University wind turbine dedicated airfoils. J. Sol. Energy Eng. 125, 488–496. https://doi.org/10.1115/1.1626129.
15. van Rooij, R.P.J.O.M., Timmer, W.A., 2003. Roughness sensitivity considerations for thick rotor blade airfoils. J. Sol. Energy Eng. 125, 468–478. https://doi.org/10.1115/1.1624614.
16. Gao, Linyue, Liu, Yang, Hui, Hu, 2017. An experimental study on icing physics for wind turbine icing mitigation. In: Proceedings of the 35th Wind Energy Symposium. AIAA SciTech Forum. https://doi.org/10.2514/6.2017-0918.
17. Timmer, W.A., van Rooij, R.P.J.O.M., 2001. Some aspects of high angle-of-attack flow on airfoils for wind turbine application. In: Proceedings of the EWEC.
18. Gao, Linyue, Yang, Liu, Kolbakir, Cem, Hu, Hui, 2018. An experimental investigation on an electric-thermal strategy for wind turbine icing mitigation. In: Proceedings of the2018 Atmospheric and Space Environments Conference, https://doi.org/10.2514/6. 2018-3658.
19. Homola, Matthew C., Virk, Muhammad S., Nicklasson, Per J., Sundsbø, Per A., 2012. Performance losses due to ice accretion for a 5MW wind turbine. Wind Energy 15, 379–389. https://doi.org/10.1002/we.477.
20. Shin, Jaiwon, Bond, Thomas H., 1992. Experimental and computational ice shapes and resulting drag increase for a NACA 0012 airfoil. In: Proceedings of the 5th Symposium on Numerical and Physical Aspects of Aerodynamic Flows. 105743 United States.
21. Clift, R., Grace, J.R., Weber, M.E., 1978. Bubbles, Drops and Particles, New York.
22. Manual, NSU, 2010. NTI.

Paper E

Study of Ice Accretion on Horizontal Axis Wind Turbine Blade Using 2D and 3D Numerical Approach

Jia Yi Jin, Muhammad Shakeel Virk, Qin Hu and Xingliang Jiang

IEEE Access, 2020 (1-12), Volume 8, p. 166236-166245.

Doi: 10.1109/ACCESS.2020.3022458

Author's Contribution

Jia Yi Jin has contributed substantially in the proposal of conceptualization, data curation, formal analysis, investigation, methodology, resources, software, visualization, validation, and writing of the paper.

E. Study of Ice Accretion on Horizontal Axis Wind Turbine Blade Using 2D and 3D Numerical Approach

This is a reprint

Jia Yi Jin, Muhammad Shakeel Virk, Qin Hu and Xingliang Jiang

1. Arctic Technology and Icing Research Group
Institute of Industrial Technology
Faculty of Engineering Science and Technology
UiT- The Arctic University of Norway
Norway
2. State Key Laboratory of Transmission and Distribution Equipment
& System Security and New Technology
Chongqing University
China

Abstract

In order to optimize the wind turbine operation in ice prone cold regions, it is important to better understand the ice accretion process and how it affects the wind turbine performance. In this paper, Computational Fluid Dynamics (CFD) based 2D and 3D numerical techniques are used to simulate the airflow/droplet behaviour and resultant ice accretion on a 300 kW wind turbine blade. The aim is to better understand the differences in the flow behaviour and resultant ice accretion between both approaches, as typically the study of ice accretion on the wind turbine blade is performed using simple 2D simulations, where the 3D effects of flow (air & droplet) are ignored, which may lead to errors in simulated ice accretion. For 2D simulations, nine sections along a 300 kW wind turbine blade are selected, whereas for 3D study, a full-scale blade is used. The obtained results show a significant difference in the ice accretion for both approaches. Higher ice growth is observed in 2D approach when compared with the full-scale 3D simulations. CFD simulations are carried out for three different icing conditions (typical, moderate and extreme), in order to estimate the extent of differences the different operating conditions can introduce on the ice accretion process in the 2D and the 3D simulations. Complex ice shapes are observed in case of extreme ice conditions, which affect the aerodynamic performance of the blade differently from typical and moderate ice conditions.

Keywords:
Wind turbine blade; Ice accretion; Droplet; CFD; Aerodynamics.

E.1. Introduction

The primary appeal for the wind energy in cold climate regions are the higher air densities and wind speeds, which provide significant benefits to power production. However, the low temperatures and the risk for atmospheric icing associated with them poses additional challenges for wind turbine systems, when compared with the warmer climate [1]. According to the WindPower Monthly report, 127GW of installed wind power capacity was located in cold climate regions at the end of 2015, with an expected total installed capacity reaching 186GW in 2020, which would be a remarkable 30% share of the global forecasted wind capacity [2]. However, atmospheric ice accretion can be one of the primary hazards for the design and safety of wind turbine [3, 4]. This highlights the need to better understand the ice accretion process on wind turbine blades with the aim to improve safety and to reduce the Capital Expenditure (CAPEX) and Operational Expenditure (OPEX) related to wind turbine operations in the cold regions.

Atmospheric ice accretion on wind turbine blade mainly occurs due to the impingement of super-cooled water droplets, which may freeze on blade surface [5]. The accreted ice changes the blade geometry and increases its surface roughness, thus altering the aerodynamic performance of wind turbine blade [6, 7]. This primarily results in the decrease of lift force and increase of drag force, which leads to reduction in the aerodynamic performance of blade and overall power production. The accreted ice shape along the blade's leading edge depends upon many variables, such as the geometry of wind turbine blade and operating conditions, most important being the relative wind velocity, atmospheric temperature, droplet size, droplet distribution spectrum and liquid water content [8].

The ice accretion process and its effects on wind turbine's aerodynamic performance can be studied using both the experimental and the numerical approaches. Along with the field measurements, the advanced multiphase CFD simulations have become an important tool for simulating and determining the performance of wind turbine blade under icing conditions [9-14]. In 2011, Barber et al. [15] analyzed the ice accretion process on the wind turbine blades and its effects on the turbine performance using both CFD and the field measurement data. They found that the ice accretion at higher altitude sites can cause an AEP lose up to 17% and the outer section (95 – 100% of the blade length) are the most severely iced. Moreover, Lamaraoui et al. [16] found that the majority of power production loss due to atmospheric icing is primarily happening at the 80% of the blade section close to tip. Thus, the tip section of the blade is typically used in studying the atmospheric ice accretion and its effects on the wind turbine performance.

The existing codes for ice accretion such as LEWICE and CANICE [17] were developed strictly for aviation with redundant features analyses, while FENSAP-ICE is a second-generation, state-of-the-art CFD icing code capable of 2D and 3D icing simulations for a large variety of applications. CFD simulations of atmospheric icing on wind turbine blades can be performed using 2D blade "planes" and 3D full blade approach. FENSAP has been tested for icing on rotating components such as helicopter rotors and engines. This highlights the possibility to use this code for wind turbine rotor blade also. Modern CFD tools such as LEWICE [18-20], CANICE-WT [21], TURBICE [22], and FENSAP-ICE [23, 24] are capable for modelling the icing using both 2D and 3D techniques of wind turbine. The differences of these software including operational environment, prolonged exposure of the wind machine to icing, and temporal variations in the external meteorological parameters. Etemaddar et al. [25] have studied the effects of atmospheric and system parameters on the 2D icing simulated with the LEWICE code for different sections along the blade and estimated aerodynamic coefficients using

FLUENT after ice accretion, following with the validation of obtained results against experimental results of NREL 5MW wind turbine. Switchenko et al. have performed a series of 2D and 3D simulations of complex wind turbine icing events in Canada, using the FENSAP-ICE and compared with the experimental data [26]. Study of ice accretion on wind turbine blade shows that smaller wind turbines can be more adversely affected by the atmospheric icing than the larger ones.

Currently there are large number of wind farms are being built at high-altitude mountainous areas. When compared to the European sites, the icing characteristics of the Chinese sites such as the accreted ice shapes, ice density and its adhesion to the surface is quite different, mostly due to different climatic characteristics[12-14] . Thus, studying the ice accretion in such regions presents a unique opportunity. Chongqing University (CQU) is one of the major research institute, which has carried out various studies on the atmospheric ice accretion and its effect on the wind turbine operations in China, especially due to the access to the Xufeng Mountain natural icing test station [15, 18, 19, 27]. The researchers at CQU have carried out the CFD simulation of airflow behaviour along full scale wind turbine blade using 3D approach using ANSYS-FLUENT and have found that higher wind speeds lead to more abrupt flow separations, especially for glaze ice [28]. They have not performed any icing simulations, rather used ice template shapes along wind turbine blade and simulated the airflow behaviour to estimate the aerodynamic performance. In order to extend the results from the previous CQU study, the focus of this paper is to better understand the differences in the ice accretion process on the CQU 300kW wind turbine using both 2D and 3D numerical techniques. For the 2D analysis, nine sections have been selected along the blade, whereas for 3D analysis the entire blade is used in full scale.

E.2. Wind Turbine Specifications

The work in this paper is performed using 300kW wind turbine blade. This wind turbine is installed at Xufeng Mountain natural icing test station, which is situated in the Southwest Hunan Province of China (27.1258 °N, 110.5606 °E). The wind turbine is located on a complex terrain at the average elevation of 1400 m.a.s.l. at the top of the Xufeng Mountain, which has an annual average precipitation of 1810 mm that belongs to the typical micro-topography icing prone region [29]. Figure E.1 shows the terrain and the installation location of CQU 300kW wind turbine, where typically more than 90 days annually of ice cover and high humidity are observed.

Parameter	Value	Parameter	Value
Power production (kW)	300	Blade length (m)	14.6
Rotating speed (RPM)	44	Hub height (m)	31
Wind speed (m/s)	13	Tower height (m)	30
Cut-in speed (m/s)	3	Tower radius (m)	1.6
Cut-off speed(m/s)	25	Overhang (m)	3
Rotor diameter (m)	31	Inclination (°)	4

Figure E.1 – Overview of Xufeng mountain nature icing test station and 300kW wind turbine. [26]

E.3. Design of Experiment

Typical procedure for the numerical modelling of atmospheric ice accretion on wind turbines is to perform the CFD simulation on the 2D blade profile sections (airfoils), primarily to estimate its aerodynamic performance. The main advantage of 2D approach is the simplicity and computational efficiency of the setup. However, the main drawback of the 2D simulations is its inability to provide information about the flow in the z-direction, which can be crucial if more "physics-rich" processes are expected to occur that may influence the results. Therefore, this study investigates the potential differences in the ice accretion process on the CQU 300 kW wind turbine using both 2D and the 3D CFD simulations. The design of experiment section consists of following three parts: geometry, mesh and the CFD setup.

E.3.1. Geometry Model

For simplicity, it is assumed that the structural model is limited to a surface representation of the wind turbine blade and the surface in question is assumed to be composed from a collection of airfoil shapes that are lofted in the blade axis directions. In order to extend the previous CQU research, [29] the focus is on the full scale blade geometry and the chosen nine cutting planes, situated from root to tip in the ascending order 14.6 m long blade is attached to the hub with a radius of 3 m, which gives the total rotor radius of 17.6 m. The on-site observations at the Xufeng Mountain icing test station show that the outer section of the wind turbine blade near tip often has the largest ice thicknesses, thus, the majority of the chosen planes in this 2D study are located close to the tip section of the blade. The blade is composed of 15 airfoils which are shown in Figure E.2. The main geometric parameters for these nine chosen sections are summarized in Table E.1.

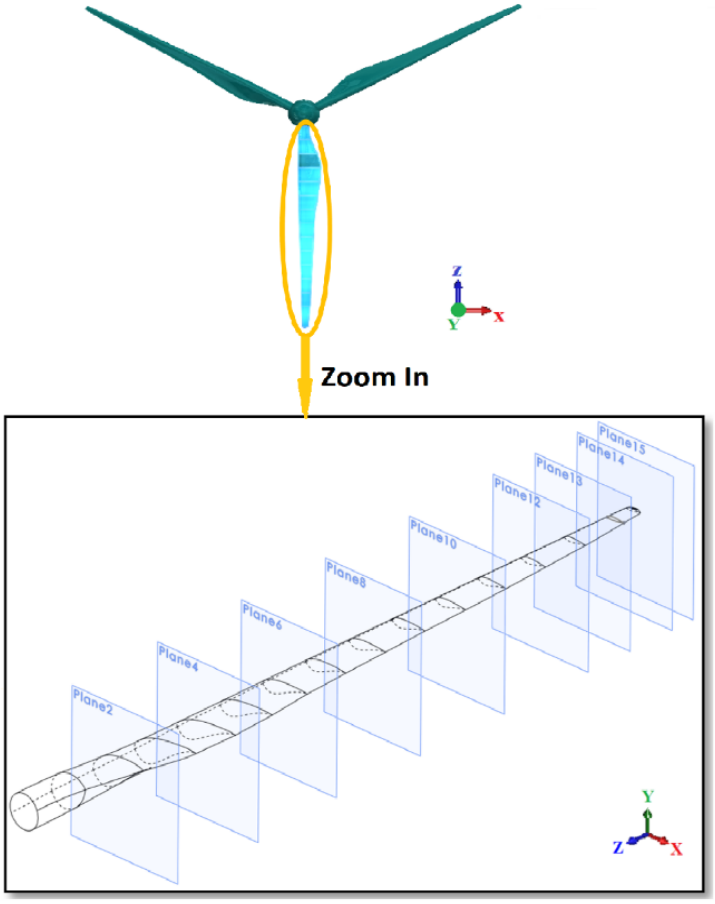

Figure E.2 – CQU wind turbine blade model and nine chosen planes.

Table E.1 – The geometric parameters for the nine chosen planes.

Cutting plane	Z (m)	Chord length (m)	r/R	Twist angle (°)	Max Thickness (m)
Plane 2	2.0	1.20	14%	19.96	0.54
Plane 4	4.0	1.31	27%	13.94	0.34
Plane 6	6.0	1.00	41%	9.50	0.24
Plane 8	8.0	0.82	55%	6.58	0.19
Plane 10	10.0	0.69	68%	4.65	0.15
Plane 12	12.0	0.55	82%	3.56	0.11
Plane 13	13.0	0.47	89%	3.17	0.08
Plane 14	14.0	0.36	96%	2.86	0.06
Plane 15	14.5	0.32	99%	2.81	0.05

E.3.2. Mesh

Numerical mesh is generated using Pointwise for 2D airfoils and the ANSYS Workbench for 3D blade. Fine meshes are made in order to accurately determine the boundary layer characteristics (shear stresses

and heat fluxes) of the turbine blade. Mesh sensitivity study was carried out using coarse, medium and fine meshes to accurately determine the boundary layer characteristics (shear stress and heat flux). During mesh sensitivity analysis, number of mesh elements and y+ value less than 1 for first cell layer was selected based upon the heat flux calculations, where a numerical check was imposed that the heat flux computed with the classical formulae dT/dn should be comparable with the heat flux computed with the Gresho's method. Mesh sensitivity study showed that the effect of mesh size on droplet solution was negligible, however some flow quantities including convective heat flux on the blade surface was sensitive to the mesh size. 2D airfoil meshes use the C-type structured numerical grid while 3D mesh of full-scale blade is generated using unstructured tetrahedral mesh. For 2D mesh the total number of hexahedral elements, ranges from 75761 to 84056 and approximate 4.88 million grid cells were used for full-scale 3D analysis. The examples of these meshes are shown in Figures E.3 and E.4.

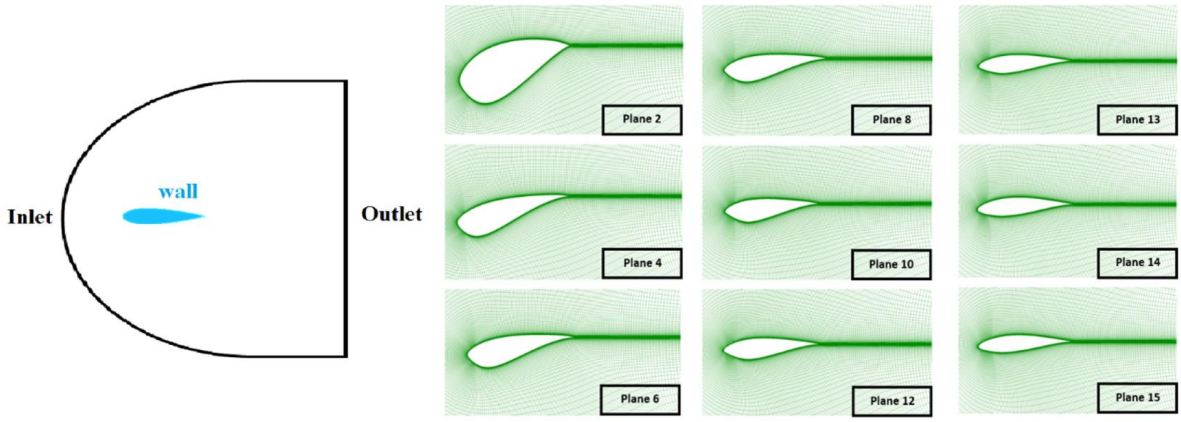

Figure E.3 – Two-dimensional numerical grid for airfoils.

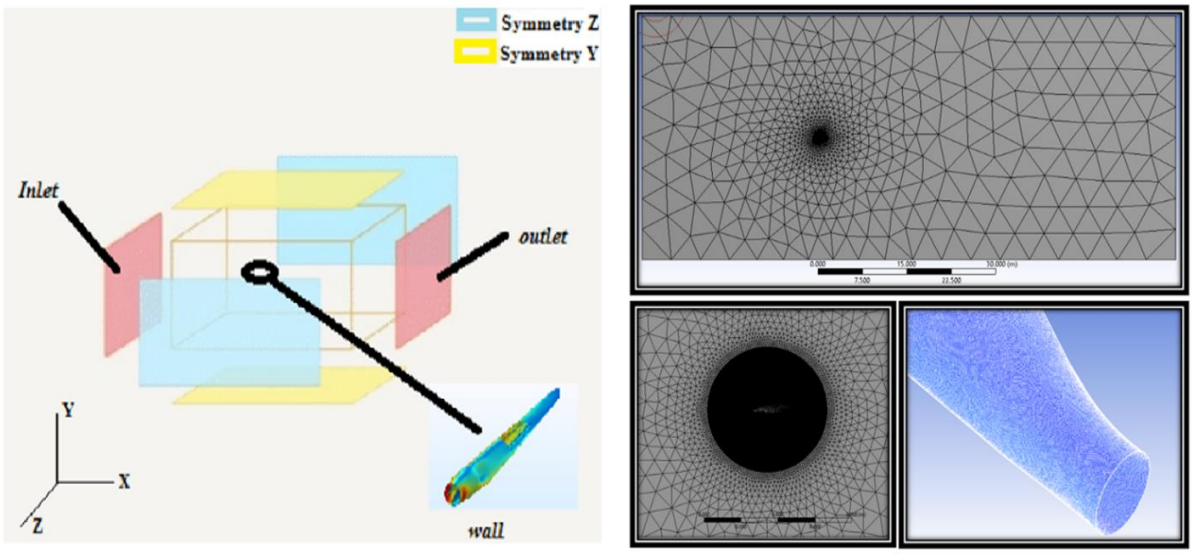

Figure E.4 – Three-dimensional numerical grid for full-scale wind turbine blade.

E.3.3. CFD Model

CFD based multiphase numerical simulations are carried out using ANSYS FENSAP-ICE, which uses the finite element method Navier-Stokes analysis with Eulerian water droplet impingement solver to

analyses the steady flow field around the turbine blade. Atmospheric ice accretion on a wind turbine blade can be numerically simulated by means of integrated thermo-fluid dynamic models, which involve the fluid flow simulation, droplet behavior, surface thermodynamics and phase changes. Airflow behavior is simulated by solving the nonlinear partial differential equations for the conservation of mass, momentum and energy.

$$\partial \rho_\alpha / \partial t + \vec{\nabla}(\rho_\alpha \overrightarrow{\boldsymbol{v_\alpha}}) = 0 \tag{E.1}$$

$$\partial \rho_\alpha \overrightarrow{\boldsymbol{v_\alpha}} / \partial t + \vec{\nabla}\left(\rho_\alpha \overrightarrow{\boldsymbol{v_\alpha}}\ \overrightarrow{\boldsymbol{v_\alpha}}\right) = \vec{\nabla}.\sigma^{ij} + \boldsymbol{\rho_\alpha}\, \vec{g} \tag{E.2}$$

$$\partial \rho_\alpha E_\alpha / \partial t + \vec{\nabla}\left(\rho_\alpha \overrightarrow{\boldsymbol{v_\alpha}} H_\alpha\right) = \vec{\nabla}\left(\kappa_\alpha\left(\vec{\nabla}\, T_\alpha\right) + \nu_i \tau^{ij}\right) + \boldsymbol{\rho_\alpha}\, \vec{g}\, \overrightarrow{\boldsymbol{v_\alpha}} \tag{E.3}$$

Where ρ is the density of air, v is the velocity vector, subscript α refers to the air solution, T refers to the air static temperature in Kelvin, σ^{ij} is the stress tensor and E and H are the total initial energy and enthalpy, respectively. The sand grain roughness for the iced surface is calculated using following Shin and al. roughness model.

$$[(k_s/c)/((k_s/c)_{base})]_{MVD} = \begin{cases} 1, & MVD \leq 20 \\ 1.667 - 0.0333(MVD), & MVD \geq 20 \end{cases} \tag{E.4}$$

Where MVD is the droplet mean diameter (in microns), whereas, the corresponding value of sand-grain roughness is obtained in Equation E-5:

$$\begin{gathered} k_s = 0.6839[(k_s/c)/((k_s/c)_{base})]_{LWC} \\ [(k_s/c)/(k_s/c)_{base}]_{T_s}[(k_s/c)/((k_s/c)_{base})]_{MVD}(k_s/c)_{base} c \end{gathered} \tag{E.5}$$

Two-phase flow (*air and water droplets*) is numerically simulated using the Eulerian approach, where the super cooled water droplets are assumed to be spherical. The Eulerian two-phase fluid model consists of the Navier-Stokes equation with the water droplets continuity and momentum equation. The water droplet drag coefficient is based on the empirical correlation for the flow around the spherical droplets described by Clift et al. [30]

$$\partial \alpha / \partial t + \vec{\nabla}\left(\alpha \overrightarrow{V_d}\right) = 0 \tag{E.6}$$

$$\partial\left(\alpha \overrightarrow{V_d}\right)/\partial t + \vec{\nabla}\left(\rho_\alpha\, \overrightarrow{V_d} \otimes \overrightarrow{V_d}\right) = C_D Re_d / 24k\ \alpha\left(\overrightarrow{V_a} - \overrightarrow{V_d}\right) + \alpha(1 - \rho_a/\rho_d)\, 1/(Fr^2) \tag{E.7}$$

$$\rho_f\left[\partial h_f / \partial t + \vec{\nabla}\left(\bar{V}_f h_f\right)\right] = V_\infty LWC\beta - \dot{m}_{evap} - \dot{m}_{ice} \tag{E.8}$$

Equation E-9 expresses the conservation of energy:

$$\begin{gathered} \rho_f\left[\left(\partial h_f c_f \dot{T}_f\right)/\partial t + \dot{\nabla}\left(\partial h_f c_f \dot{T}_f\right)\right] = \left[c_f\left(\tilde{T}_\infty - \tilde{T}_f\right) + \left(\left\|\vec{V}_d\right\|^2\right)/2\right] V_\infty LWC\beta - L_{evap}\dot{m}_{evap} + \\ \left(L_{fusion} - c_s\tilde{T}\right)\dot{m}_{ice} + \sigma\varepsilon(T_\infty^4) - T_{f^4} - c_h\left(\tilde{T}_f - \tilde{T}_{ice,rec}\right) + Q_{anti-icing} \end{gathered} \tag{E.9}$$

The coefficients ρ_f, c_f, c_s, σ, ε, L_{evap}, L_{fusion} are physical properties of the fluid. The reference conditions$\tilde{T}_\infty$, V_∞, LWC are the airflow and droplets parameters. Equation E.10 express the Jones (glaze) formula:

$$\rho_s = \begin{cases} 0.21R_M 0.53, & R_M < 10 \\ R_M/(1.15R_M + 2.94), & 10 \le R_M \le 60 \ (\text{in g/cm}^3) \\ R_M/(1.15R_M + 2.94), & R_M \ge 60 \end{cases} \quad (E.10)$$

where

$$R_M = \left(d \cdot \|\vec{V}_d\|\right)/\left(2\tilde{T}_{wall}\right)$$

d is the droplet diameter in microns, $\vec{V}_d$ is the droplet impact velocity (m/s) and $\tilde{T}_{wall}$ is the wall temperature (Celsius). ALE (Arbitrary Langrangian Eulerian) formulation is used for the mesh displacement during ice accretion. This approach adds the grid speed terms to the Navier-Stokes equations to account for the mesh velocity [31].

Table E.2 – Numerical setup.

Icing type	**Typical**	**Moderate**	**Extreme**
LWC (g/cm3)	0.2	0.5	1
MVD (μm)	17	25	35
Temperature (°C)	–5		
Freestream Velocity (m/s)	13		
AOA (°)	0		
Icing duration (min)	60		
Turbulence model	k – ω SST		
Droplet distribution spectrum	Langmuir D		
Icing model	Glaze (with beading)		
Icing density parameterization	Jones (Glaze)		

E.4. Results and Discussion

Ice accretion along wind turbine blade changes its geometric shape, which effects the flow behaviour along pressure and suction sides of the blade and results a change in its aerodynamic coefficient and overall performance. In this study, CFD based numerical analysis are carried out to simulate the airflow behavior, droplet behaviours and ice shapes using CQU clean and iced single airfoils (2D) and full scale blade (3D).

E.4.1. Airflow Behaviour Comparison

Figure E.5 shows the velocity vectors and the pressure coefficient distribution for the full-scale blade in the 3D numerical simulations, while Figures 6 shows the comparison of velocity magnitudes and the pressure coefficients on the nine chosen planes in the 2D and the 3D CFD simulations, respectively. The 3D planes in Figure E.6 are extracted from full-scale 3D simulations of the blade using plane-cutting option in CFD post processing. A clear difference in the airflow behaviour is observed in both cases.

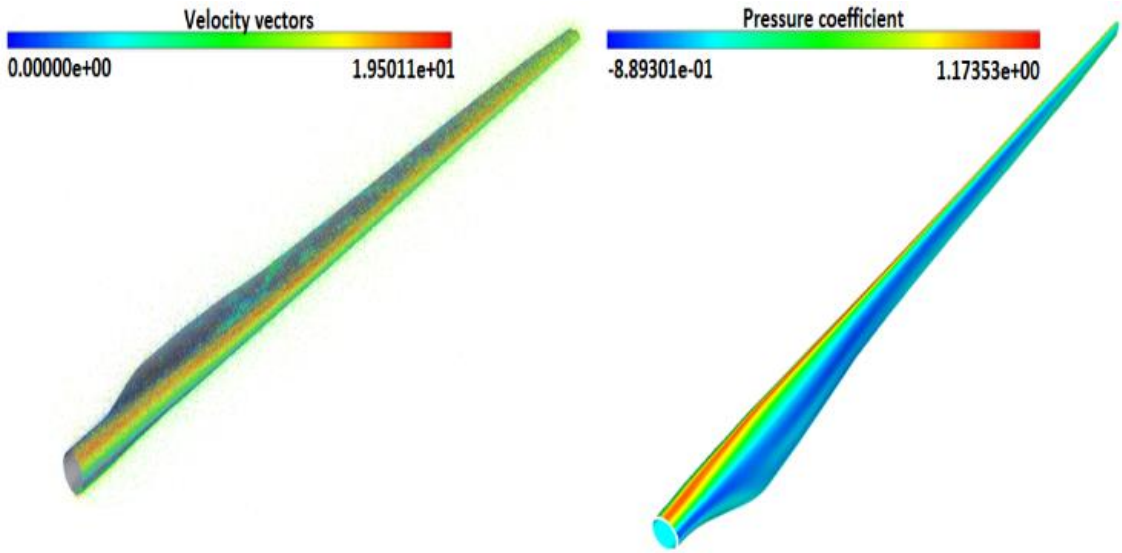

Figure E.5 – Velocity vectors and pressure coefficient for the 3D full-scale blade.

The first immediate observation when comparing the results between 2D and 3D simulations is that the 2D simulations have significantly higher values of the velocity magnitudes. This implies that the flow separation in the 2D case occurs more abruptly than in the 3D case, which results into sharp pressure gradients. Moreover, there is a significant change in the vorticity patterns, occurring behind the trailing edge when comparing the results for the velocity magnitudes between 2D and 3D case. In the 3D case, the vorticity is present in all nine planes of interest, with the sections, closer to the root of the blade having a non-zero value of the velocity magnitudes in said vortices, which gradually reaches values close to zero in the section closer to the tip. In comparison, the results from the 2D simulation show more extreme vorticity in sections closer to the root (Plane 2, 4 and 6) with velocity magnitudes being close to zero, while the sections closer to the tip do not have vorticity in the wake at all. This suggests that the flow velocity magnitude in the 3D case has a significant non-zero component in the z-direction along the blade, which can cause complex fluid-structure interactions and as a result a more complicated flow pattern. The same sort of interaction is absent from the 2D cases simply by virtue of them having no extrusion in the z-direction. The primary explanation for this difference is the asymmetry of the blade in the 3D, mainly due to twist angle between different sections of the blade, such as Plane 8 have no vortex in 2D case but in 3D case it shows vorticity pattern.

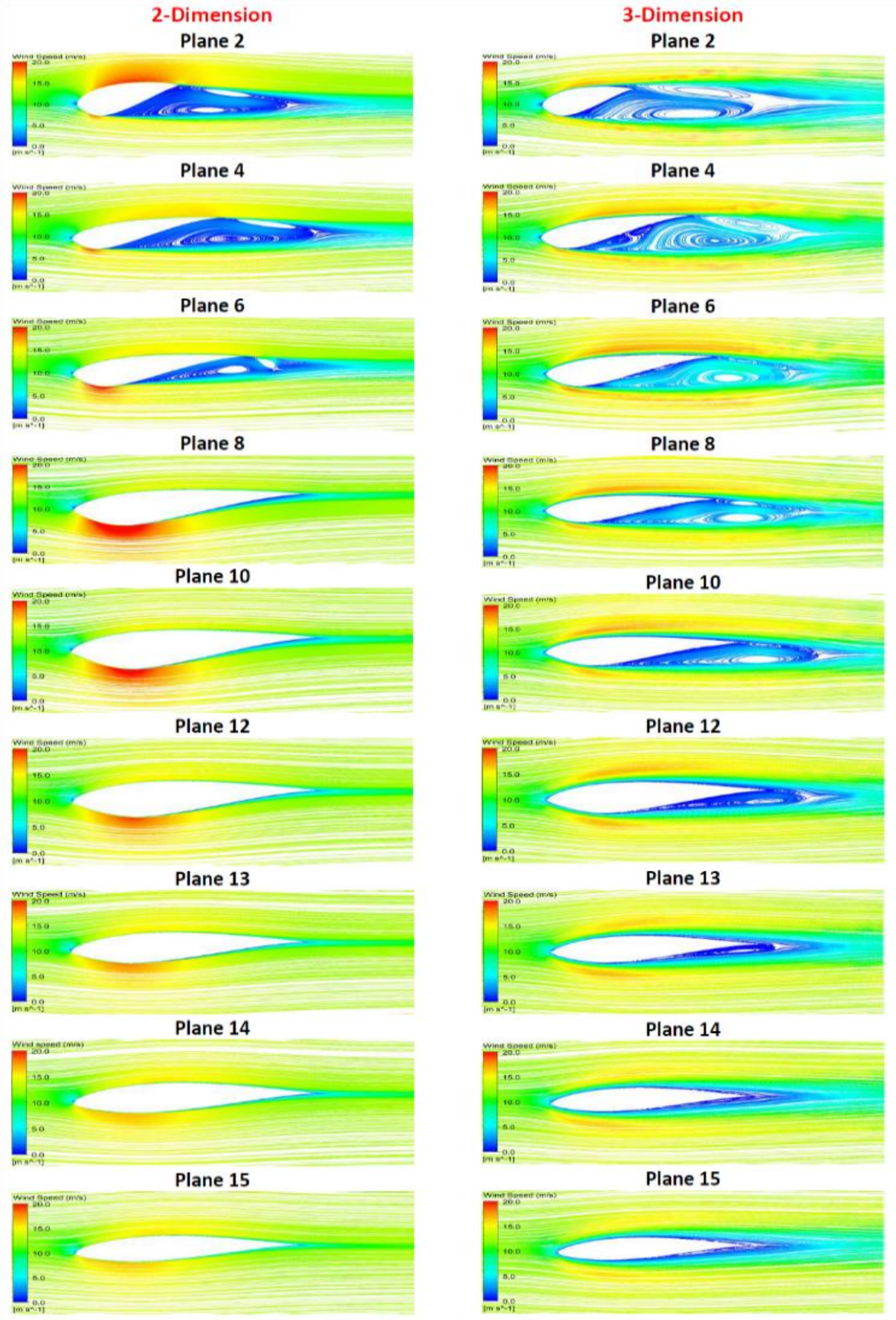

Figure E.6 – Velocity streamlines along clean wind turbine blade profiles sections (2D and extracted planer section from 3D full-scale blade).

Thus, based on 2D and 3D separation study of aerodynamic characteristics, the comparison of pressure coefficient (Cp) for both 2D-airfoil and 3D-plane cases have carried out in Figure E.7 for clean and iced conditions. The good agreement between single airfoil and single blade cutting planes are found in most cases, especially in leading edge. Reversing point are carried out more forward in single blade's most cutting planes, due to the lift and drag forces have effects the flow behaviours which affect Cp, however, the uncommon trends is found in the 3D mid section (Plane 6, 8,10 and 12) because of flow effects and wake effects. Compared with 3D simulation results, 2D results have smaller Cp range because the windward and leeward have different lift and drag force due to the shadow regions and aerodynamic changes. Icing types leads a big difference in 2D simulation, however for the 3D simulation the difference not obvious. It may be the reason that the flow behaviours are difference from 2D and 3D due to the higher and lower artificial viscosity respectively.

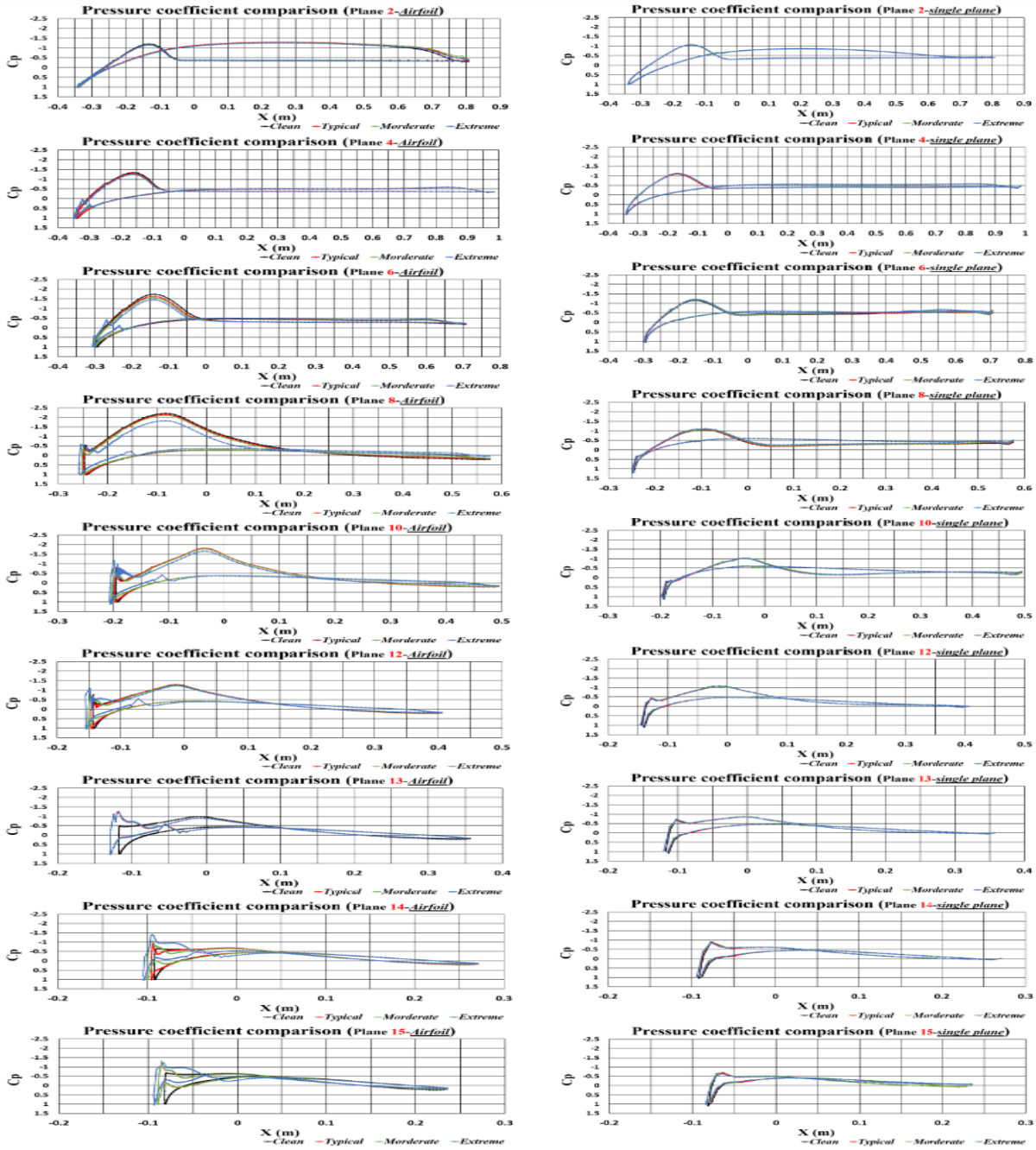

Figure E.7 – Pressure coefficient comparison between 2D and 3D cases in clean and iced profiles.

E.4.2. Droplet Behavior Comparison

Figure E.8 shows the droplet collision efficiency comparison for the moderate, typical and extreme icing conditions in the 2D and the 3D simulations. Since the droplet impingement simulations have been performed with the Langmuir D distribution, which is a seven-bin distribution, only the spectrum-averaged results are presented, in order to streamline the comparison.

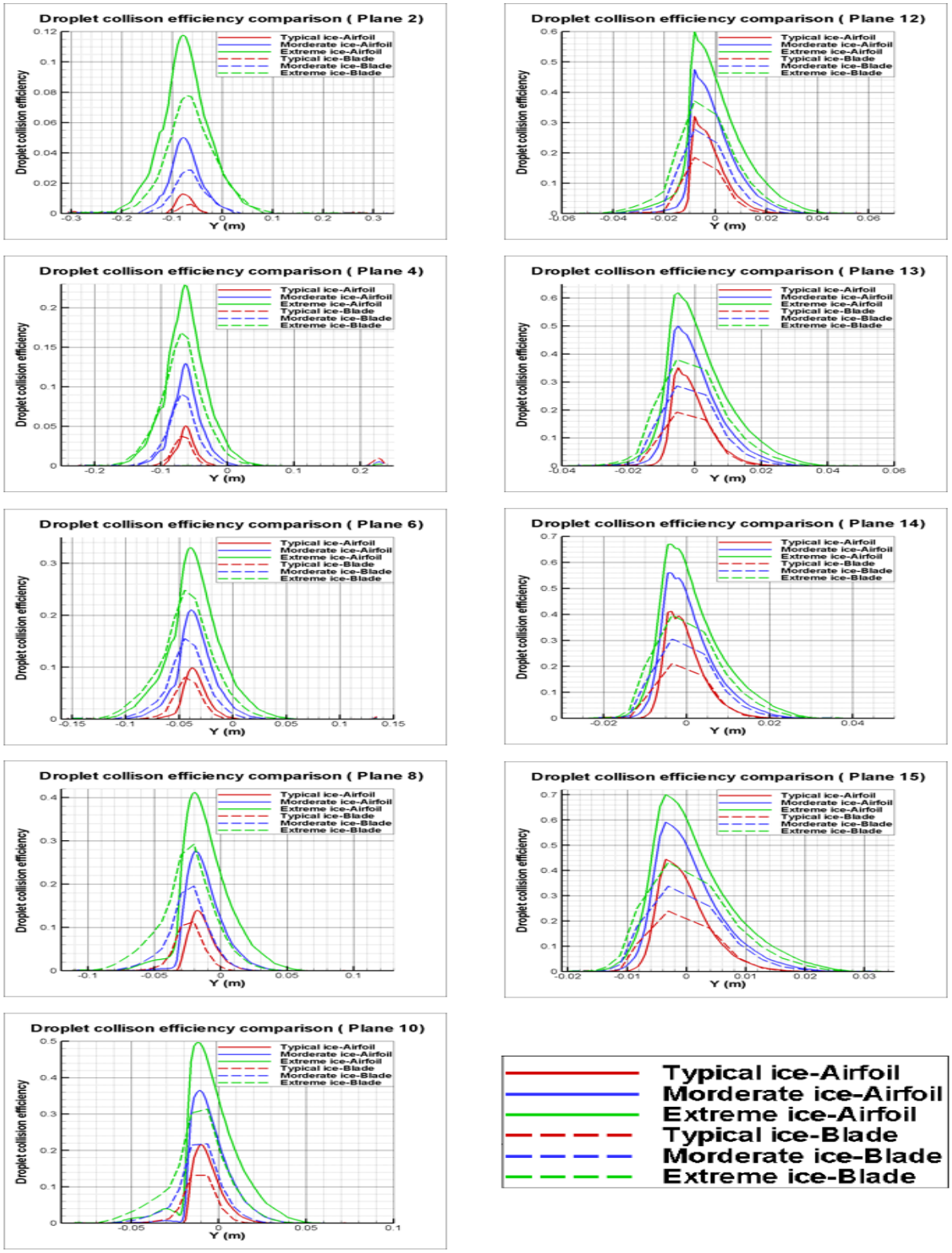

Figure E.8 – Droplet collision efficiencies comparison.

Since the operating conditions for the different icing types in Table E.2 are constant with the exception of the MVD and LWC values, the differences in the droplet behaviour will be primarily influenced by the droplet inertia, which depends on the airflow velocity magnitude distributions and the MVD values as a function of parameter Vd^2 where 'd' is the droplet diameter. Thus, the preceding discussion on the differences in the velocity magnitudes between the 2D and the 3D numerical simulations, is also relevant for the droplet collision efficiencies comparison, as the higher velocity magnitudes in the 2D case will directly result in the increase in the droplet inertia, which will in turn will increase the overall and local collision efficiencies, maximum impingement angles and the droplet impact velocities. This effect in terms of the local collision efficiencies and the maximum impingement angles is clearly visible in Figure E.8, where the results from 2D simulations displays higher values of the local collision efficiencies and the maximum impingement angles, when compared with the 3D results. This will directly result in more accreted ice masses, thicker ice shape, covering larger area and higher accreted ice densities, as they are a function of the droplet inertia in the Jones (glaze) icing density formulation, in the 2D simulations. These conclusions are applicable for all three tested icing types – *typical*, *moderate* and *severe*, as the 2D simulations show consistently higher values of the local collision efficiencies and the maximum impingement angles for all planes and at all icing types. The only thing which will change with the change in icing type is the "ratio" of the droplet collision efficiencies between the 2D and the 3D simulations, however, due to non-linear dependence of the droplet collision efficiencies on the droplet inertia the exact "ratio" will also be highly non-linear.

E.4.3. Ice Accretion Comparison

Tables E.3 and E.4 show the comparison of accreted ice densities and the maximum ice thicknesses for the nine planes of interest in the 2D and the 3D simulations, while Figure E.9 shows the ice accretion on full scale blade for three different icing conditions, whereas Figure E.10 provides the comparison of the accreted ice shapes after 60 minutes of ice accretion.

Table E.3 – Maximum ice densities comparison.

Maximum Ice density (kg/m^3)	**Ice types**					
	Typical		**Moderate**		**Extreme**	
	2D	**3D**	**2D**	**3D**	**2D**	**3D**
Plane 2	785.1	840.0	814.0	840.0	840.0	840.0
Plane 4	787.5	840.0	840.0	840.0	840.0	840.0
Plane 6	793.5	479.7	840.0	840.0	840.0	840.0
Plane 8	800.7	840.0	840.0	840.0	840.0	840.0
Plane 10	795.2	840.0	840.0	840.0	840.0	840.0
Plane 12	790.5	840.0	840.0	840.0	840.0	840.0
Plane 13	787.9	840.0	840.0	840.0	840.0	840.0
Plane 14	796.7	840.0	840.0	840.0	840.0	840.0
Plane 15	784.3	840.0	840.0	840.0	840.0	840.0

Table E.4 – Maximum ice thicknesses comparison.

Maximum Ice thickness (mm)	Ice types					
	Typical		Moderate		Extreme	
	2D	3D	2D	3D	2D	3D
Plane 2	1.01	0.51	4.13	0.85	5.07	1.11
Plane 4	2.55	1.02	3.43	1.12	7.26	1.57
Plane 6	3.19	0.79	5.16	1.45	9.03	2.05
Plane 8	3.36	1.43	6.44	1.84	10.78	2.55
Plane 10	3.44	1.44	7.64	1.81	11.59	2.50
Plane 12	3.67	1.92	8.38	2.27	12.52	3.04
Plane 13	3.67	2.28	8.45	2.64	12.20	3.41
Plane 14	3.86	1.90	8.52	2.43	12.63	3.25
Plane 15	4.01	2.17	8.56	2.59	12.67	3.44

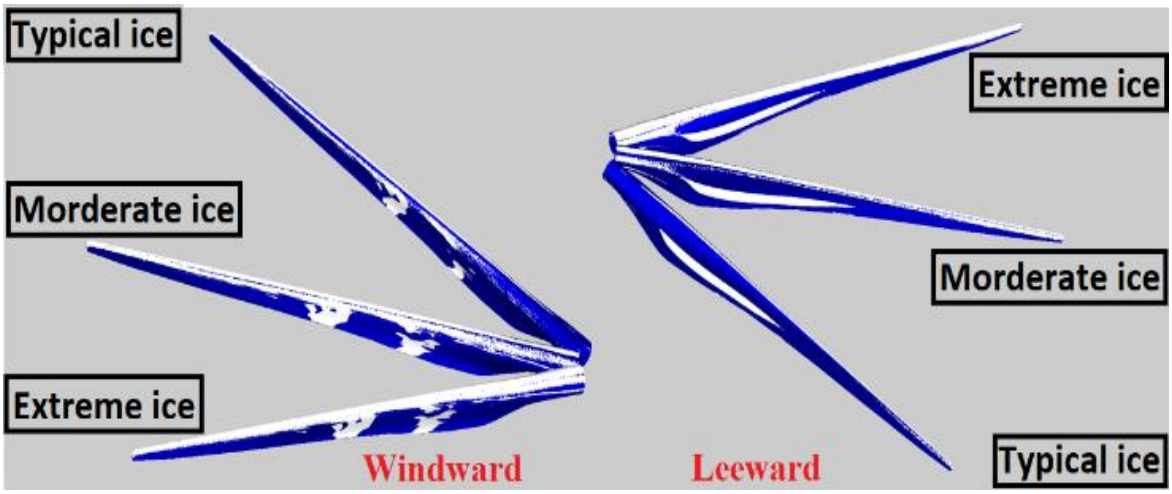

Figure E.9 – Ice accretion for the 3D full-scale blade.

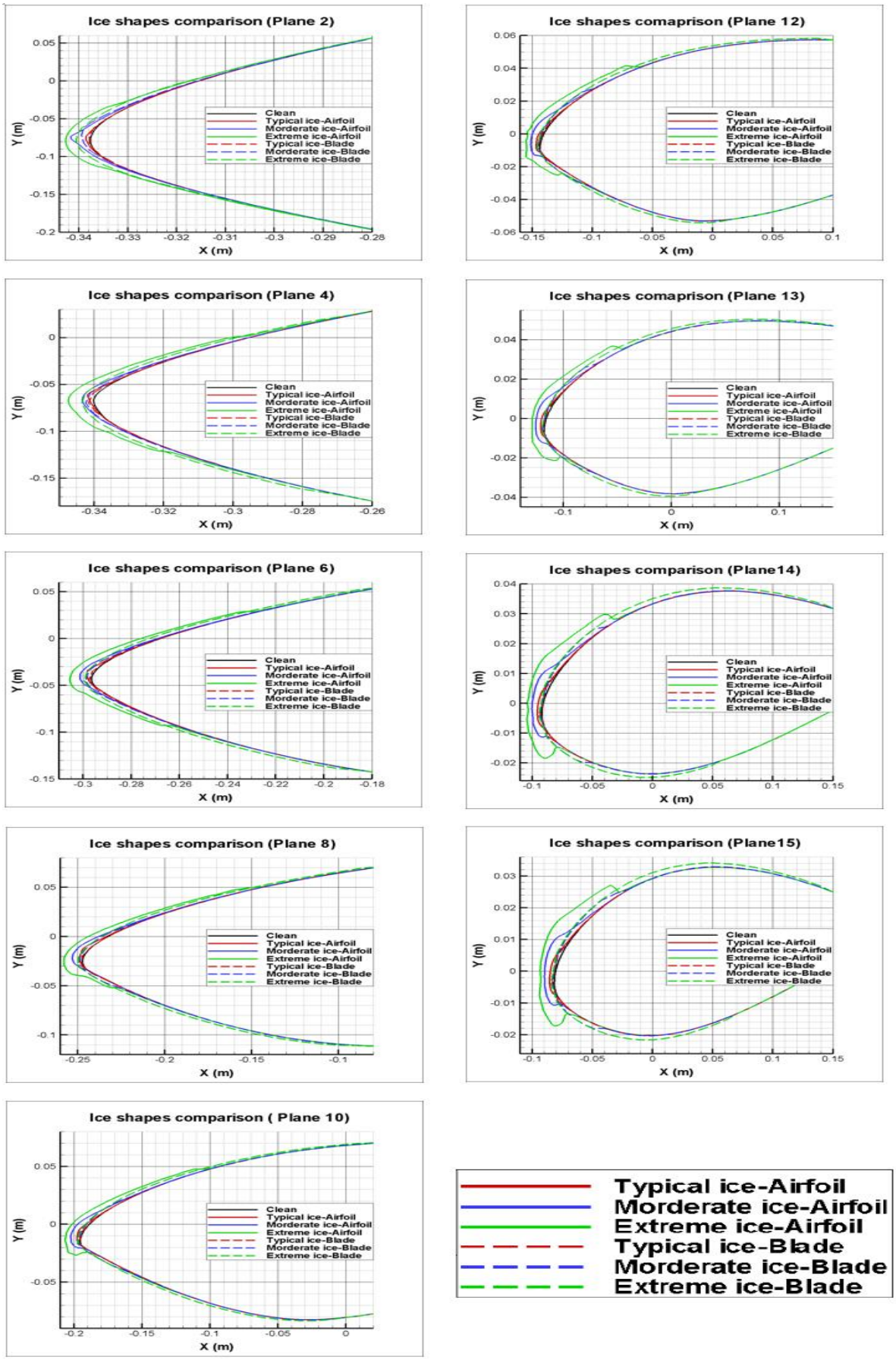

Figure E.10 – Accreted ice shapes comparison for 2D and 3D study.

The primary observation from the Table E.3 is that for the typical icing conditions the ice density values are higher in the 3D simulations than in 2D. For the rest of the cases the values of accreted ice densities are equal at 840 kg/m^3. The difference in values for the typical icing conditions is peculiar, considering that from the comparison of the droplet collision efficiencies it follows that in 2D cases the droplet collision efficiencies and the maximum impingement angles are higher than in the 3D simulations, thus implying that the droplet inertia is higher in 2D simulations and by extension, the droplet impact velocities should also be higher, which would result in higher accreted ice densities. However, the higher values of the accreted ice densities for the typical icing conditions in the 3D cases suggest that the surface temperature must be lower in the 2D cases possibly as a result of a difference in the heat fluxes between the 2D and the 3D simulations. When it comes to the maximum ice thicknesses from Table E.4 and the accreted ice shapes from Figure E.10, it is obvious that the CFD simulations in the 2D cases accrete significantly more ice than the 3D simulations for all tested icing conditions. This coupled with the fact that the velocity magnitude and pressure coefficient distributions imply that the airfoils in 2D may experience higher magnitude of lift and drag forces than 3D simulations, and may results in the airfoils in the 2D simulations being more significantly affected by the accreted ice.

E.5. Conclusion

Within this study, a series of multiphase CFD simulations on a 300 kW wind turbine blade have been performed using 2D and 3D numerical simulations. The 2D simulations were performed on the nine blade sections of interest, while the 3D simulations were performed on the entire wind turbine blade in full scale. The primary objective of this paper was comparison of the multiphase flow behaviour between the 2D and the 3D CFD simulations, primarily in connection with the atmospheric ice accretion. The obtained results show that in 3D simulations there is a significant velocity component and flow interactions in the z-direction, which are obviously absent from the 2D simulations. As a result of this flow interaction in the third dimension, the velocity magnitudes are reduced in the 3D simulations when compared to the 2D simulations. This, in turn, affects the ice accretion process, as the higher velocity magnitudes in the 2D cases result in the higher droplet inertia, collision efficiencies and the maximum impingement angles, which results in more ice mass accreted along with the thicker and larger ice shapes present in the 2D simulations. Coupled with the airflow velocity magnitudes, the result suggest that the airfoils in the 2D simulations are more aerodynamically loaded than the full blade in 3D, and the higher ice accretion values will affect the aerodynamic performance of the airfoils more significantly in the 2D simulations when compared to the 3D results. The primary reason behind such differences is believed to be the asymmetry of the wind turbine blade in 3D, primarily due to the twist angle, which causes the complex flow patterns to arise in the first place.

Acknowledgment

Authors would like to acknowledge Professor Jiang Xingliang and his research group from Chongqing University, China for providing the wind turbine blade models and field data from Xufeng mountain natural icing test station. In addition, Authors would also like to acknowledge Mr. Pavlo Sokolov from UiT for assisting during the data analysis.

References

1. A. K. Ville Lehtomäki, Pieter Jan Jordaens,Charles Godreau,Neil Davis,Zouhair Khadiri-Yazami,Rolv Erlend Bredesen,Göran Ronsten,Helena Wickman,Saskia Bourgeois,Till Beckford, *IEA Wind TCP Task 19 - Avaliable Technologies for Wind Energy in Cold Climates, 2nd Edition*, IEA Wind Task 19, 2018.
2. V. Lehtomaki, Emerging from the cold, WindPowerMonthly, 2016.
3. Neil Davis, "Icing Impacts on Wind Energy Production," DTU, DTU Wind Energy, 2014.
4. A. B. B. Tammelin, M. Cavaliere, H. Holttinen, C. Morgan, H. Seifert, K. Säntti, P. Vølund, Wind energy production in cold climate (WECO), Finnish Meteorological Institute, Helsinki, 2000.
5. M. M. Sohrab Gholahosein Pouryoussefi, Mohamed Mahdi Nazemi,Mojtaba Fouladi, Alreza Doostmahmoudi, "Experimental study of ice accretion effects on aerodynamic performance of NACA-23012 airfoil," Chinese Journal of Aeronautics, vol. 29, no. 3, pp. 585-595, 2016.
6. F. Lamraoui, Fortin, G., Perron, J., and Benoit, R., "Canadian icing envelopes near the surface and its impact on wind energy assessment," Cold Regions Science and Technology, vol. 120, pp. 76-88, 2015.
7. B. Tammelin, Cavaliere, M., Holttinen, H., Morgan, C., Seifert, H., and Säntti, K., Wind energy production in cold climate (WECO), UK DTI, 1999.
8. Drage Peter, Numerical simulation of Ice Accretion on Wind Turbines IWAIS 2009, 2009.
9. W. A. Timmer, "Aerodynamic characteristics of wind turbine blade airfoils at high angle-of-attack," in 3rd EWEA Conference-Torque 2010: The Science of Making Torque from Wind, Heraklion, Crete, Greece, 2010.
10. H. K. Woobeom Han, Bumsuk Kim, "Study on correlation between wind turbine performance and ice accretion along a blade tip airfoil using CFD," Journal of Renewable and Sustainable Energy, vol. 10, no. 2, 2018.
11. F. M. Gitsuzo d. Tagawa, Héloïse Beaugendre, "CFD study of airfoil lift reduction casused by ice roughness," in 2018 Applied Aerodynamics Conference, Atlanta, Georgia, 2018.
12. M. S. V. Jia Yi Jin, "Study of ice accretion along symmetric and asymmetric airfoils," Journal of wind engineering & industrial aerodynamics, vol. 179, pp. 10, 2018.
13. J. Y. J. Pavlo Sokolov, Muhammad S Virk, "Accreted ice mass ratio (k-factor) for rotating wind turbine blade profile and circular cylinder," Wind Energy, 2018.
14. M. L. Jian Liang, Ruiqi Wang, Yuhang Wang, "Study on the glaze ice accretion of wind turbine with various chord lengths," in Earth and Environmental Science, 2018.
15. Y. W. S. Barber, S. Jafari, "The Impact of Ice Formation on Wind Turbine performance and Aerodynamics," Journal of Solar Energy Engineering, vol. 133, no. 1, pp. 311-328, 2011.
16. G. F. F. Lamaraoui, R. Benoit, "Atmospheric icing impact on wind turbine production," Cold Regions Science and Technology, vol. 100, no. 4, pp. 36-49, 2014.
17. F. Saeed, "State-of-the-Art Aircraft Icing and Anti-Icing Simulation," ARA Journal, Vol. 2000-2002, No. 25-27, January, 2002.
18. W. Wright, "User manual for the NASA Glenn Ice Accretion code LEWICE version 2.2.2," NASA, ed., 2002.
19. W. Wright, "Validation Results for LEWICE 3.0," NASA, ed., 2005.
20. C. S. B. a. M. G. Potapczuk, "Users Manual for the NASA Lewis Three-dimensional Ice Accretion Code (LEWICE3D)," NASA, ed., 1993.
21. V. Patreau, "MODÉLISATION &QUE DWN SYSTÈME ÉLECTROTHERMIQUE DE DÉGIVRAGE DES PALES D~ÉOLIENNE À AXE HORIZONTAL," Thèse de maîtrise, École Polytechnique de Montréal, December 1998.
22. C. Son and T. Kim, "Development of an icing simulation code for rotating wind turbines," Journal of Wind Engineering and Industrial Aerodynamics", Vol. 203, 104239, August, 2020.
23. ANSYS, "ANSYS FENSAP-ICE," 2016.
24. F. M. a. W. H. H. Beaugendre, "FENSAP-ICE's Three-Dimensional In-Flight Ice Accretion Module : ICE3D," Jounal of Aircraft, vol. 40, no. 2, pp. 239-247, 2003.
25. [25] M. O. L. H. a. T. M. M. Etemaddar, "Wind Turbine aerodynamic response under atmospheric icing conditions " Wind Energy, vol. 17, pp. 241-265, 2014.

26. W. G. H. David Switchenko, Guido Baruzzi and Isik Ozcer, “Fensap-ice simulation of complex wind turbine icing events, and comparison to observed performance data,” in 32nd ASME Wind Energy Symposium, National Harbor, Maryland, 2014.
27. G. F. Fayçal Lamraoui, Robert Benoit, Jean Perron and Christian Masson “Atmospheric icing impact on wind turbine production,” Cold Regions Science and Technology, vol. 100, pp. 14, 2014.
28. H. L. Lichun Shu, Qin Hu, Xingliang Jiang, Gang Qiu, Gaohui He, Yanqing Liu, “3D numerical simulation of aerodynamic performance of iced contaminated wind turbine rotors,” Cold Regions Science and Technology, vol. 148, pp. 13, 2018.
29. H. Li, “Power Performance and Its Computational Model of Wind Turbine Under Icing Conditions,” Department of Electrical Engineering, Chongqing University, Ph.D. thesis, 2018.
30. J. R. G. R Clift, Weber., M.E., "Bubbles, drops and particles ", 1978.
31. [31] N. S. U. Manual, NTI, 2010.

Paper F

Wind Turbine Ice Detection Using AEP Loss Method – A Case Study

Jia Yi Jin, Timo Karlsson and Muhammad Shakeel Virk

Submitted (Under Review), 2021.

This copy is reprinted with permission from co-authors.

Author's Contribution

Jia Yi Jin has contributed substantially in the proposal of conceptualization, data curation, formal analysis, investigation, methodology, resources, software, visualization, validation, and writing of the paper.

F. Wind Turbine Ice Detection Using AEP Loss Method – A Case Study

This is a reprint

Jia Yi Jin[1], Timo Karlsson[2] and Muhammad Shakeel Virk[1]

1. Arctic Technology and Icing Research Group
Institute of Industrial Technology
Faculty of Engineering Science and Technology
UiT- The Arctic University of Norway
Norway
2. VTT Technical Research Centre of Finland,
Espoo, Finland.

Abstract

Ice detection of wind turbine and estimating the resultant production losses Wind resource assessment in cold regions is challenging, but very important, as wind energy project decisions in cold regions are based on these estimated results. This paper describes the comparison of a statistical and numerical case study of wind resource assessment of a wind park in ice prone cold region. Three years Supervisory Control and Data Acquisition (SCADA) data from a wind park located in arctic region is used for this study. T19IceLossMethod based statistical analysis and Computational Fluid Dynamics (CFD) based numerical simulations are carried out for wind resource assessment and estimation of resultant Annual Energy Production (AEP) due to ice. Both statistical and numerical results are compared with the field SCADA data, where a good agreement is found. Statistical analysis shows that the relative power loss due to icing related stops is the main issue for this wind park. To better understand the wind flow physics and estimation of the wind turbine wake losses, Larsen wake model is used for the numerical CFD simulations, where results show that it is important to use the wake loss model for CFD simulations of wind resource assessment and AEP estimation of a wind park. A preliminary case study about wind park layout optimization has also been carried out which shows that AEP can be improved by optimizing the wind park layout and CFD simulations can be a good tool in this regards.

Keywords:
Wind resource assessment; SCADA; T19IceLossMethod; CFD; Wake effect; Wind park optimization.

F.1. Introduction

Due to increasing demand of electrical power and needs of protecting the environment, there has been a growing need of rapid expansion and better use of renewable energy resources to reduce the carbon emissions. Cold regions have good wind resources, but environmental challenges such as icing has been recognized as hindrance in proper utilization of these good wind resources. Worldwide, installed wind energy capacity in ice prone cold regions in 2015 was 86.5 GW, which is expected to reach 123 GW in year 2020.[1] Therefore, wind resource assessment in cold regions is important both for the operation of wind parks and also to provide more accurate wind energy production forecasts.2 The assessment of wind resources at cold climate sites is challenging and include aspects as terrain topology of the area where the wind park is to be located, wind behaviour, type of buildings or any other human intervention around the wind park location that may induce changes in the terrain roughness as well as the geometry of the wind turbine and its expected performance in the calculation of the tested scenarios. Low temperatures and icing climate set additional challenges for wind resource assessment in cold regions.

The International Energy Agency (IEA) T19 set out a statistical method to assess production losses due to icing based on standard SCADA data available from modern wind parks, named 'T19IceLossMethod' and developed by international expert group IEA Wind TCP Task 19. [2] T19IceLossMethod is the standardized open source Python code model [3] for assessment of wind power production loss [2] and compared different sites with a systematic analysis method, as well as evaluate the effectiveness of various blade heating systems. [4] The scope of work includes a detailed historical SCADA data analysis using 10-minute averages from four different wind turbine models and analysis of icing conditions on sites. [5]

CFD based wind resource assessment can provides improved agreement with the field measurements, when compared with the statistical flow models. Gravdahl et al. [6] performed CFD analysis for wind resource assessment and wind park design layout optimization, where they found that design of a wind park layout based upon CFD simulations can help to increase the wind energy production. Wind turbine wake effects are important for the wind resource assessment and can be responsible for approximately 10-20% losses of the AEP. [7] Wind turbine wake effects on neighboring turbines effects the flow behavior, which also effects the wind turbine performance and power production. The development of models to describe wind turbine wake effects on energy production, include different initiatives of simplified or linearized models such as Jensen model [8] or more complex such as the eddy viscosity together with Gaussian shape, [9-10] or second order model combined with the Prandtl's assumption of velocity been function of the distance power -1/3, [11] or considering turbulence on the wake recovery as function of the distance from the wind turbine. [12] Wake structure creates a flow disturbance behind the wind turbine as well as in front of the turbine, which differ from the flow around an idealized turbine, [13] as shown in Figure F.1.

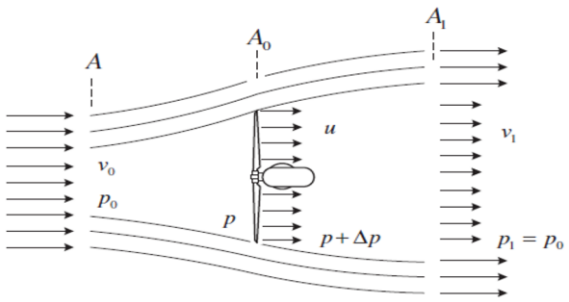

Figure F.1 – Air flow near idealized wind turbine rotor. [13]

Wake losses and aerodynamic behavior of wind turbine can be better addressed once the flow over the wind park site is better understood. Wind flow over steep slopes and ridges causes flow separation which is hard to capture and simulate using mesoscale models such as WRF. Furthermore, the atmospheric stability influences the wind flow. [14] This paper describes the statistical and numerical case study of wind resource assessment and wind park design layout effects on energy production in icing climate. T19IcelossMthod based statistical analysis and CFD based numerical simulations are carried out in comparison with the three years (2013-2015) wind park SCADA data. To better understand the wind turbine wake effects on flow behavior and resultant power production, Larsen wake model is used to calculate the AEP of each wind turbine.

F.2. Wind Park Terrain & Layout

Wind park used for this study consists of 14 wind turbines located at 400 m a.s.l in the arctic region of Norway. Three years (2013-2015) Supervisory Control and Data Acquisition (SCADA) from all wind turbines is collected and sorted for this study. This data mainly includes wind speed, wind direction, temperature and power production. Wind park terrain is hilly and is mainly covered with grass in summer and snow in winter. Figure F.2 shows the wind park layout, terrain and wind rose map.

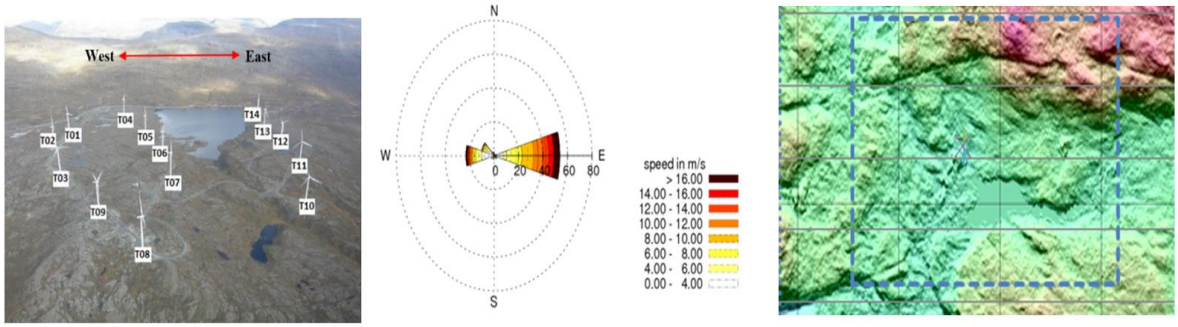

Figure F.2 – Wind park layout & wind rose map.

Wind direction is divided in 12 sectors, where first sector is oriented directly north. Wind climatology is presented as a wind rose, giving the average wind speed distribution divided in the velocity intervals (bins) and wind directions (sectors). The frequency distribution has been fitted to a Weibull distribution. Results of wind climatology for all 12 sectors are given in Table F.1.

Table F.1 – Average wind speed, frequency and Weibull shape (k) and scale (A) parameters.

		Wind speed (m/s)			Frequency (%)			Weibull shape, k			Weibull scale, A		
Year		*2013*	*2014*	*2015*	*2013*	*2014*	*2015*	*2013*	*2014*	*2015*	*2013*	*2014*	*2015*
Sector	**01**	1.62	2.63	6.30	1.14	1.84	33.08	0.92	1.23	2.16	1.70	2.84	7.46
	02	1.02	2.59	14.28	0.66	1.20	3.52	1.00	1.25	8.39	1.08	2.81	16.47
	03	8.51	1.44	2.30	24.32	0.92	1.39	2.79	1.15	0.64	10.12	1.64	1.37
	04	6.39	9.29	9.36	44.19	56.45	34.37	2.12	2.05	1.52	7.70	10.60	9.97
	05	1.94	7.29	6.19	0.98	12.08	4.72	1.06	1.57	1.56	2.02	8.45	6.90
	06	1.83	2.36	4.40	0.88	0.45	0.27	1.17	1.24	0.90	1.91	2.52	3.60
	07	2.91	2.10	3.73	0.61	0.47	0.18	1.03	1.42	0.67	2.78	2.26	2.17
	08	3.62	3.78	4.07	1.38	1.10	3.17	1.43	1.51	1.44	4.09	4.31	4.56
	09	3.79	3.33	3.22	7.08	1.59	4.82	1.10	1.34	0.89	3.94	3.68	3.13
	10	4.36	4.60	5.48	16.08	11.63	10.40	1.62	0.89	1.18	5.16	3.99	5.48
	11	2.90	3.99	4.27	2.16	9.93	3.78	1.04	1.38	0.93	3.22	4.44	3.82
	12	1.96	3.95	3.39	0.52	2.35	0.29	1.06	2.03	1.33	1.80	4.72	3.69

F.3. Model Setup

F.3.1. Statistical Model

SCADA based T19IceLossMethod is the statistical model developed to minimize the required inputs and to create a solution that would not require any external measurements, such as ice detectors. Iced wind turbine power losses are defined by comparing the performance to the calculated power curve using heated anemometers from nacelle and the measured reference, expected power curve. In general, the method can be divided into three main steps [2] and site air density and air pressure are used to calibrate the nacelle wind speed as equation F.1:

$$\omega_{site} = \omega_{std} \times \left(\frac{\rho_{std}}{\rho_{site}}\right)^{\frac{1}{3}} =$$

$$\omega_{std} \times \left(\frac{\frac{\rho_{std}}{T_{std}}}{\frac{\rho_{site}}{T_{site}}}\right)^{\frac{1}{3}} = \omega_{std} \times \left(\frac{T_{std}}{T_{site}}\left(1 - 2.25577 \times 10^{-5} \times h\right)^{5.25588}\right)^{\frac{1}{3}} \quad \text{(F. 1)}$$

where ω_{site} is calibrated nacelle wind speed, ω_{std} measured nacelle wind speed, T_{site} is nacelle temperature [15] and T_{std} is standard temperature of 15ºC, which resulting to air density of 1.225 kg/m3 at sea level $P_{std} = 101325$ Pa ambient air pressure, h is site elevation in meters above sea level. [16] In order to detect production loss, a baseline needs to be established. Icing event is defined as a period of time when the output power of wind turbine is below a set limit in cold temperature. These limits are calculated form a subset of the data where temperature is high enough so that it is reasonable to assume that there is very little icing. The detailed setup is described in Table F.2.

Table F.2 – Setup of T19IceLossMethod.

Site elevation (m)	400.0
Wind speed bin size (m/s)	1.0
Reference temperature (°C)	+1
Power curve lower limit	P10 (10% of power in the bin)
Power curve upper limit	P90 (90% of power in the bin)

The statistical model uses the 10th percentile of the power curve to trigger an icing alarm. The percentile method was chosen mainly due to robustness and simplicity of the definition. [16] This method classifies icing events into three main categories: Class a means the reduced production due to icing, Class b means the stop caused by icing and Class c is apparent over production. [5]

Most common icing effect on turbine operation is production loss, and the production losses are caused by degraded aerodynamics of the blade caused by ice accretion along the blade surface. If turbine stops during an icing event, it is assumed that the icing event is considered to be a contributing factor to the stop, where an icing induced stop is assumed to be ended once turbine output power is above the icing alarm limit again. In some cases turbine seems to be producing more than expected, this can happen if for example an anemometer is experiencing icing. An iced cup anemometer will show lower wind speeds than what the actual wind speeds are. This in turn will result in apparent overproduction in SCADA.

F.3.2. Numerical Model

CFD based numerical simulations are carried out using WindSIM software, which is a modern Wind Park Design Tool (WPDT) that helps to optimize the wind park energy production by using non-linear mathematical methods. 3D terrain model of the wind park is generated where the domain is discretized using hexahedral numerical grid. Iterative numerical simulations of air flow behavior are performed by solving Reynolds Averaged Naiver-Stokes equations (RANS). The energy equation is neglected during this study, as temperature is assumed constant in the region close to the ground surface. So, the exchange of heat and water vapour at the Earth's surface is neglected. In order to account for surface roughness in the numerical simulations, Wieringa's classification is used. RNG-based k-ε turbulence model is used due to its better agreement with the flow profiles and length of the separated flow region. The detailed setup is shown in Table F.3.

Table F.3 – Solver setting for CFD simulations.

Height of boundary layer (m)	500.0
Speed above boundary layer (m/s)	10.0
Boundary condition at the top	fix pressure
Potential temperature	No
Turbulence model	RNG k-ε

The default value of terrain surface roughness heights is read from the grid file in WindSIM, or, alternatively a constant roughness height can also be imposed in the model by specifying a non-zero

value for the roughness height. The roughness height is used in the velocity profile log-law, given in equation F.2:

$$\frac{u}{u^*} = \frac{1}{\kappa} \ln z/z_0 \qquad \text{(F. 2)}$$

where u is the wind velocity; u* is the friction velocity, κ is von Kármán constant (κ = 0.435); z is the coordinate in vertical direction; z0 is the roughness height. Wind park digital terrain layout used for the CFD simulations is shown in Figure F.3.

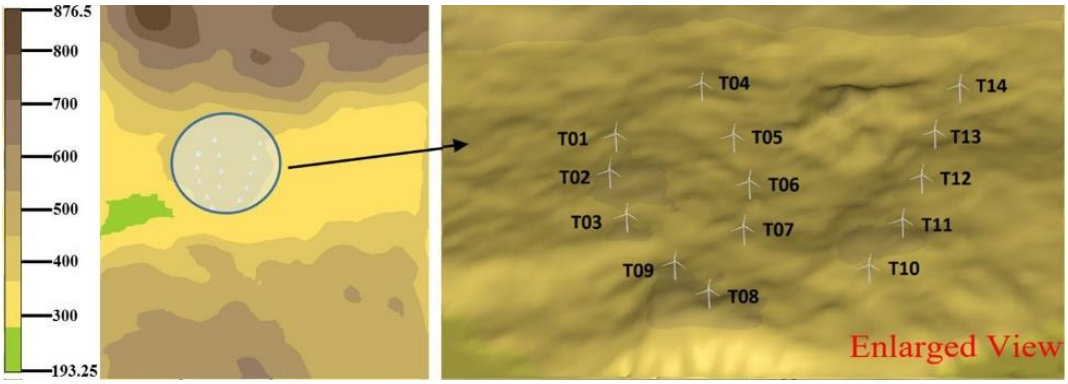

Figure F.3 – Digital terrain (m) of wind park layout.

In this study, the wind park terrain corresponds to mesoscale topology of the region around the wind park. The areas selected for the wind flow simulations is the section that involves different sizes in the direction of the flow to determine the influence of the natural formation of the region on the wind profile. In the wind park terrain, the presence of a natural channel along the mountain line west-east oriented at the north side and water body at the south represent a challenge for the selection of the domain to do the numerical simulations. Estimation of latitudinal and longitudinal extension of the domain is quite important because the wind behavior will be directly affected by the surface shape, following the mass and momentum conservation equations. For a fixed latitude range that cover the top of the mountain and a more flatter area to the south, three different territorial domains based on the variation of the starting point of the domain in the longitudinal direction are tested in this numerical study. Mesh sensitivity analysis are carried out, where a final refined mesh by default placed in the centre of the domain and the cell distribution is uniform within the refined area with an increasing cell size towards the borders with cell resolution of 28m is selected for the numerical study. Figure F.4 shows the numerical mesh used for this study, the grid spacing, and cells is described in Table F.4.

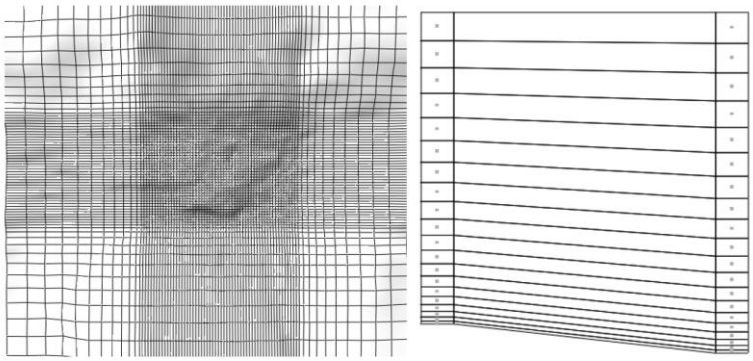

Figure F.4 – Horizontal layers (left) and vertical layers (right) of the 3D model, used for grid generation.

Table F.4 – Gird Spacing and cells.

	East	North	z	Total
Grid spacing (m)	61.8-454.8	61.0-439.0	Variable	-
Number of cells	78	64	20	99840

Larsen et al. wake loss model [9] is used for this study. This wake loss model is based on calculating the normalized velocity deficit and rotational axisymmetric along the x-axis, δV, as described in equation F.3:

$$\delta V = \frac{U - V}{U} \tag{F.3}$$

where, U is the free stream velocity, and V is air velocity at some point after the turbine rotor. This model is derived from the turbulent boundary layer equations and a similarity assumption. Shows as equation F.4:

$$\delta V = \frac{1}{9}\left(C_T A_r x^{-2}\right)^{\frac{1}{3}}\left\{r^{\frac{3}{2}}\left(3{C_1}^2 C_T A_r x\right)^{-\frac{1}{2}} - \left(\frac{35}{2\pi}\right)^{\frac{3}{10}}\left(3{C_1}^2\right)^{-\frac{1}{5}}\right\}^2 \tag{F.4}$$

where, C_T is the thrust coefficient, and the constant A_r and variable C_1 based on rotor diameter (m) D, are described in equation F.5 and F.6:

$$A_r = \frac{\pi D^2}{4} \tag{F.5}$$

$$C_1 = \left(\frac{D}{2}\right)^{\frac{5}{2}}\left(C_T A_r x_0\right)^{-\frac{5}{6}} \tag{F.6}$$

where, x_0 is described in equation F.7, and referred to R_{95} which described by using R_{nb} that correlated with the ambient turbulence intensity at hub height, I_a, as shown in equation F.8 and F.9:

$$x_0 = \frac{9.5D}{\left(\frac{2R_{95}}{D}\right)^3} - 1 \tag{F.7}$$

$$R_{95} = 0.5\left(R_{nb} + min(h, R_{nb})\right) \tag{F.8}$$

$$R_{nb} = \max(1.08D, 1.08D + 21.7D(I_a - 0.05)) \tag{F.9}$$

F.4. Results and Discussion

F.4.1. Ice Detection

Result from T19IceLossMethod are compared with the field SCADA data from the wind park. All three categories of icing events: Class a, Class b and Class c are used as relative production losses due to icing (% of kWh), relative losses due to icing related stops (% of kWh) and over production hours (% of total hours) respectively. The results from this statistical model are shown in Table F.5, and the calculation

of losses time of all icing events is illustrated in Table F.6. The maximum values are shown with pink color and the minimum values are shown with green color.

Table F.5 – Classification of icing events detected by T19IceLossMethod.

	Class a			**Class b**			**Class c**		
Year	***2013***	***2014***	***2015***	***2013***	***2014***	***2015***	***2013***	***2014***	***2015***
01	2.1	0.3	0.2	8.9	1.3	13.4	0.4	3.0	2.6
02	0.5	0.3	0.2	9.1	3.4	8.8	0.7	3.0	1.0
03	0.3	0.2	0.3	5.3	1.6	4.9	1.7	3.8	1.6
04	0.2	0.2	0.1	2.3	1.3	2.1	3.0	3.7	4.2
05	0.2	0.2	0.1	2.6	0.8	1.6	2.6	3.1	2.6
06	0.2	0.2	0.2	2.1	1.5	1.6	1.6	3.1	2.4
07	0.2	0.2	0.4	2.0	1.3	1.2	1.0	3.8	2.2
08	0.2	0.2	0.5	2.4	3.5	2.8	1.0	3.6	2.0
09	0.2	0.2	0.3	3.4	2.8	2.9	2.6	4.2	2.2
10	0.2	0.1	0.1	4.3	1.5	2.0	1.3	4.0	1.8
11	0.1	0.2	0.2	5.2	1.8	1.9	1.1	2.1	1.2
12	0.1	0.1	0.2	3.0	1.1	3.9	2.4	3.6	1.6
13	0.1	0.2	0.1	4.4	29.6	4.1	0.5	3.1	2.8
14	0.1	0.2	0.1	2.1	3.1	4.3	1.6	3.1	1.6

Table F.6 – Classification of losses time (hour) of icing events detected by T19IceLossMethod.

	Class a of time			**Class b of time**			**Class c**			**% loss of total hour**		
Year	***2013***	***2014***	***2015***	***2013***	***2014***	***2015***	***2013***	***2014***	***2015***	***2013***	***2014***	***2015***
01	6.6	2.3	0.4	12.2	6.6	3.0	0.4	12.2	2.6	19.2	11.9	15.5
02	1.4	2.1	0.7	11.5	8.7	3.0	0.7	9.5	1.0	13.6	13.8	12.0
03	1.3	1.5	1.7	10.8	6.8	3.8	1.7	6.6	1.6	13.8	12.1	9.5
04	1.0	1.6	3.0	10.7	7.5	3.7	3.0	6.6	4.2	14.7	12.8	11.5
05	0.6	1.0	2.6	11.4	8.5	3.1	2.6	7.0	2.6	14.6	12.6	10.1
06	0.7	1.0	1.6	11.5	10.1	3.1	1.6	7.3	2.4	13.8	14.2	10.4
07	1.0	1.1	1.0	12.0	9.2	3.8	1.0	7.3	2.2	14.0	14.1	10.4
08	1.0	1.6	1.0	11.4	10.2	3.6	1.0	7.0	2.0	13.4	15.4	10.4
09	0.8	1.5	2.6	11.4	8.4	4.2	2.6	6.4	2.2	14.8	14.1	9.8
10	0.8	1.0	1.3	11.4	9.5	4.0	1.3	7.8	1.8	13.5	14.5	10.4
11	0.8	1.1	1.1	13.6	9.1	2.1	1.1	7.4	1.2	15.5	12.3	9.6
12	0.7	1.2	2.4	11.8	8.9	3.6	2.4	7.9	1.6	14.9	13.7	10.4
13	0.4	1.1	0.5	11.5	19.6	3.1	0.5	7.4	2.8	12.4	23.8	11.0
14	0.6	1.5	1.6	9.8	8.3	3.1	1.6	9.7	1.6	12.0	12.9	11.6

According to the statistical method, the yellow zones are where the maximum power losses in each icing event categories, which means annual power production is not ideal in these turbines, and need to optimize the wind turbine sites or operation methods to improve the actual wind power productions. Whereas the green zones are the minimum power losses where the actual wind energy production is ideal in these turbines. To consider the operating hours of each turbines during year 2013 to 2015, turbine 01 are the maximum loss of total hours in 2013 and 2015. However, turbine 01 in 2014 has the minimum and turbine 13 has the maximum loss of total operating hours. Results of maximum ice loss detection on wind power production for turbine 01 and turbine 13 are shown in Figure F.5 by using 10th (P10) and 90th (P90) percentile of power in the bin compared with standard power production with median output power in the bin.

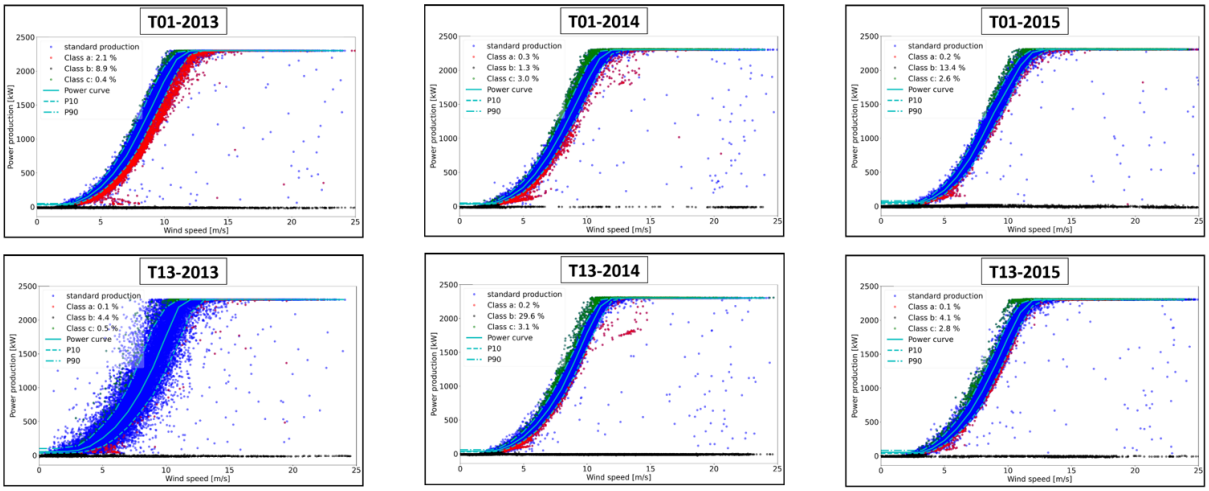

Figure F.5 – Ice detection of T01 and T13 during 2013 to 2015.

Analysis shows that the maximum reduced power production due to icing with T01 is 2.1% in 2013, 0.3% in 2014 and T08 is 0.5% in 2015, whereas the maximum ice loss with class a for all 14 wind turbines. Analysis about the maximum stop caused by icing with T02 is 9.1% in 2013, T13 is 29.6% in 2014 and T01 is 13.4% in 2015 respectively, where the maximum ice loss with class b for all 14 wind turbines. For the ice loss with class c for all 14 turbines, analysis shows that T04 is 3.0% in 2013, T09 is 4.2% in 2014 and T04 is 4.2% in 2015 with the maximum apparent overproduction. In total, added up ice losses in different categories of all 14 wind turbines, class b is the maximum ice detection category for all three years of the wind park, with 57.1%, 54.6% and 55.5% respectively, whereas class a is the minimum ice detection category during 2013 to 2015 with ice loss 4.7%, 2.8% and 3.0% separately. In other words, the relative power losses due to icing related stops are the main issue for this wind park.

F.4.2. Wind Resource Assessment

Results from CFD simulations are compared with the field SCADA data from the wind park. Both simulated and measured results of average wind conditions are used for AEP estimation. For the CFD simulations, three hub heights (35, 80 & 125 m) which equal the lower and upper tip height and the hub height are used for the comparison. Wind resource maps for all three hub heights are shown in Figure F.6, where simulation results show that the wind park locates and operates in rich wind resources area. The results from wind resource map also shows that wind speed at the hub height of 125m is the highest and 35m is the lowest in all three years. The main reason for it is the planetary boundary layer effects, i.e. the friction near the surface, due to no-slip condition, which results in some mass flux of the air

being displaced into layers at higher altitudes, which by mass-conservation principle will result in adjacent layers slowing down. In addition, according to the pioneer research work [17] and the topographic characteristics of actual wind park with specific surface roughness height study in this paper, when the airflow through the mountain and lake, the flow will form a recirculation zone. If the wind speed is high or the atmosphere structure is unstable, a strong vortex motion will appear on the leeward side of the mountain. This vortex motion may cause the wind speed to rotate at a certain height, thus showing the phenomenon that wind speed decreases with height. This affects the velocity deficit in near-surface layers that result in change of wake and associated power losses.

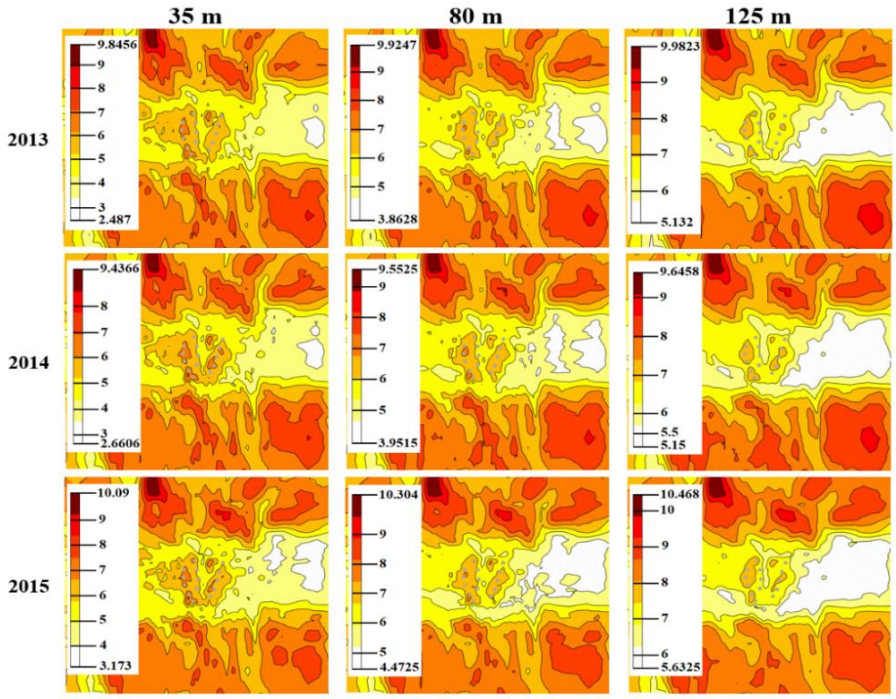

Figure F.6 – Wind resource map at hub height of 35, 80 & 125 m.

F.4.3. AEP Estimation and Comparison

Numerical analysis are carried out based on the geographical long-term conditions in order to calculate the AEP of the wind park using Larsen wake loss model with actual surface roughness height. Each year SCADA data is further analyzed and compared by T19IceLossMethod statistical model and CFD simulation. This approach is used to get the better estimate of energy based availability within field SCADA data, statistical model and numerical simulations of the wind park. In 2013 and 2015, both statistical and CFD results showed overestimated AEP values when compared with the SCADA data, whereas the underestimated AEP values show mostly in 2014 for CFD simulations. In other words, the wind park have better estimation of energy power production compare in year 2013 and 2015. Then further CFD analysis are carried out by taking into account the wind turbine wake losses. Results of this parametric study are shown in Table F.7 and Figure F.7.

Table F.7 – Energy based availability (%) of SCADA with statistical and numerical model.

%	SCADA/T19IceLossMethod			SCADA/gross-CFD			SCADA/wake loss-CFD		
Year	***2013***	***2014***	***2015***	***2013***	***2014***	***2015***	***2013***	***2014***	***2015***
01	87.90	96.98	60.23	79.71	101.50	50.51	83.55	105.90	52.01
02	89.49	94.03	89.77	72.43	101.21	77.95	75.50	104.86	80.62
03	85.84	95.44	91.81	80.44	109.20	80.79	83.72	113.26	83.57
04	97.18	97.87	97.93	93.92	104.18	85.58	95.56	105.99	86.84
05	97.12	98.50	101.61	90.76	118.54	85.10	94.61	123.04	87.88
06	96.77	97.63	98.63	91.22	111.06	82.17	95.93	116.07	85.45
07	96.82	97.36	99.45	90.86	101.07	88.01	95.53	105.48	91.90
08	97.23	96.57	98.15	88.55	97.44	85.90	90.49	99.20	87.13
09	96.03	96.27	97.15	90.43	105.40	80.80	93.56	108.40	82.93
10	94.78	98.48	95.42	80.07	94.68	72.08	81.43	95.78	72.96
11	93.96	97.86	97.59	80.03	90.87	81.77	80.79	92.18	83.83
12	95.92	98.14	96.68	85.97	101.75	73.44	86.74	102.76	74.41
13	95.70	76.40	95.31	85.43	82.49	86.60	86.11	83.47	88.13
14	97.07	95.35	67.01	101.86	125.23	64.46	102.53	126.00	64.80

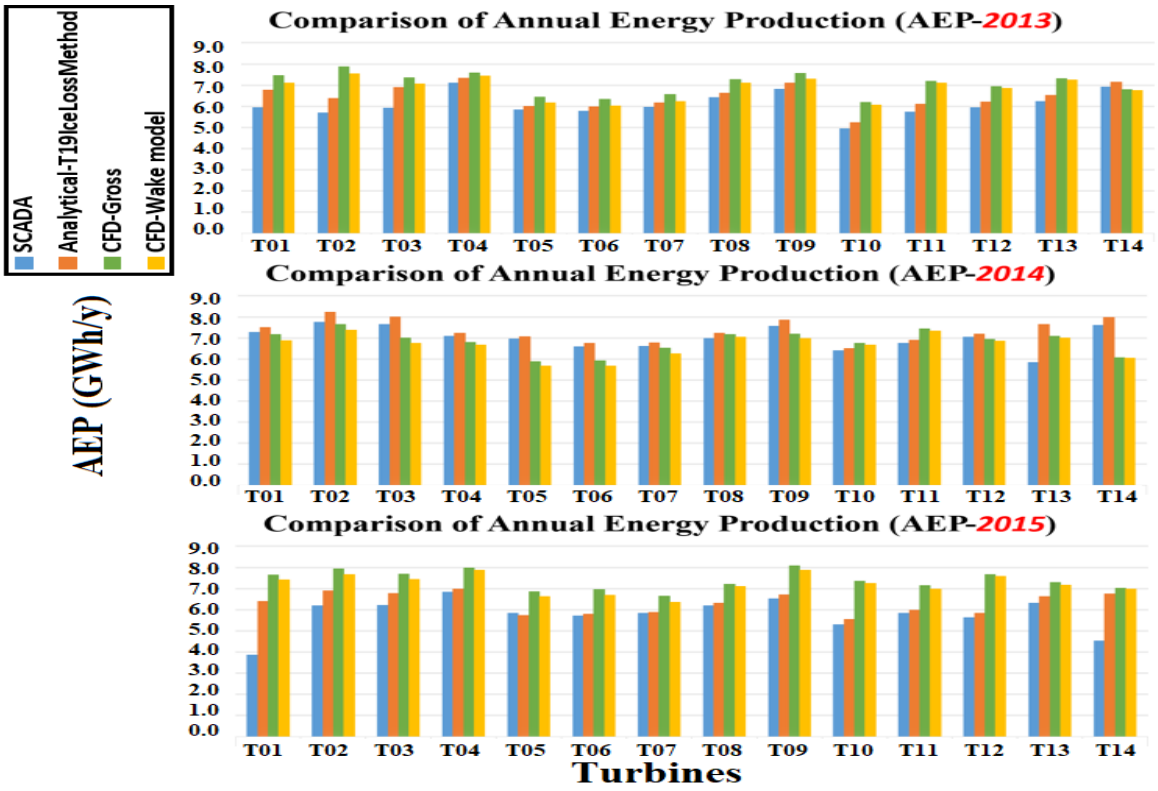

Figure F.7 – AEP comparison within SCADA, T19IceLossMethod and CFD simulation with or without wake effects for each wind turbine.

Analysis show that CFD results without use of wake model overestimated the AEP in comparison to SCADA data, whereas CFD results with the use of Larsen wake loss model is found in better agreement

with the SCADA data in 2013 and 2015, whereas for 2014 are in reverse. This case study highlights that it is important to use the proper wind turbine wake model for CFD analysis while performing the wind resource assessment.

F.4.4. Wind Park Layout Optimization

To further improve the AEP and reduce wake loss effects of the wind park, a preliminary numerical case study is carried out to optimize the existing wind park layout (wind turbine locations). WindSIM Park Optimizer is used for this purpose. Park optimizer is a numerical tool coupled with the WindSIM that helps to maximize the wind farm profitability by optimizing the wind park layout. Park optimizer uses two type of optimization approaches, 1) basic optimization, 2) WFD (wind farm design) optimization. The basic optimization is based on heuristic algorithm which gives near optimal results. Algorithms such as genetic algorithm, simulated annealing and similar trial-and error algorithms for the wind park layout design also provide good results but they are slow in process and do not provide information about the quality. The WFD optimizer is highly innovation approach based on formal research operation methods and is derived from state of art optimization solver. For this case study, we have used WFD optimizer. Results from CFD simulations of year 2014 presented in previous section are used as input to the WFD optimizer, where WFD optimizer optimally relocated the wind turbines with respect to the highest average wind speed and wind energy. Figure F.8 shows the optimized layout of the wind park in comparison to existing layout.

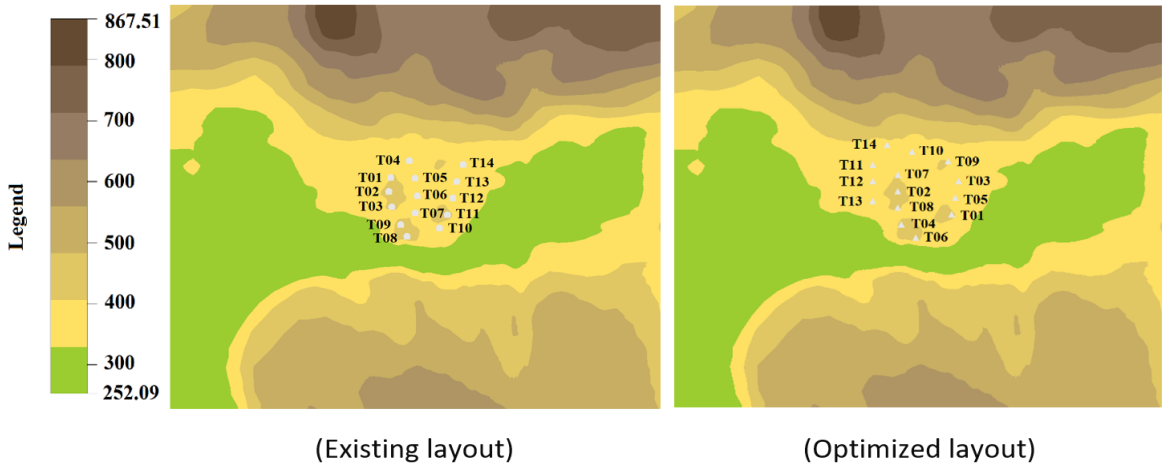

Figure F.8 – Existing wind turbines location and optimized wind turbines location.

Table F.8 – Comparison of gross AEP and total wake loss for optimized design layout of the wind park.

	Gross AEP (GWh/y)	Total wake loss (%)
SCADA	98.13	-
CFD – before optimization	95.61	35
CFD – after optimization	112	28

To verify that how much AEP is increased after optimization of the wind park layout, CFD simulations for optimized wind park layout are carried out. Larsen wake model is used for this study. Table F.8 shows the AEP and total wake loss results of the Wind Park. Before optimization of the wind park layout design, gross AEP from CFD analysis has been calculated as 95.61 GWh/y, whereas after optimizing

the wind park layout the gross AEP calculations from CFD simulations shows a value of 112 GWh/y. Comparison of AEP for optimized design layout of the wind park shows that 16.39 GWh/y energy increased as compared to the existing layout design. Moreover, the CFD based on Larsen wake model have decreased 7% in total wake loss compare before and after optimization used WFD optimizer. This shows that CFD based numerical optimization approach can be a good way to better simulate the wind resources and optimize the wind park layout and the power production.

F.5. Conclusion

SCADA data analysis, T19IceLossMehtod and CFD simulations are carried out for a wind park located in arctic region. AEP from SCADA data is compared with statistical and CFD simulations, where a good agreement is found. Statistical analysis shows the relative power loss due to icing related stops (Class b) is the main issue for this wind park from 2013 to 2015. While the CFD analysis shows that it is important to use the proper wake loss model for better estimation of the wind resources using numerical simulations. Analysis also show that CFD results without use of wake loss model can over/under-estimate the AEP in comparison to SCADA data, whereas CFD results with the use of wake loss models are in good agreement with the SCADA data. Analysis shows the phenomenon that wind speed decreases with height increase due to the wind park have a strong vortex motion appear on leeward side of the mountain and affects the velocity deficit in near-surface layers, which result in change of wake and associated power losses. Moreover, study about wind park layout optimization shows that AEP can be optimized by optimizing the wind park layout and CFD simulations can be used as a tool in this regards.

Acknowledgement

The work reported in this paper is supported by the University of Tromsø PhD project no (381100/74104). Authors would also like to thanks Dr. Matthew Carl Homola for technical support in this study.

References

1. Neil Davis, Andrea H Hahmann, and M. Zagar., Icing Impacts on Wind Energy Production. 2014, DTU: Denmark.
2. IEA Wind TCP Task 19: Available Technologies for Wind Energy in Cold Climates. IEA Wind, October 2018, 2nd edition.
3. IEA Wind Task 19, T19IceLossMethod: Method for estimating icing losses from wind turbine SCADA data, 2019.[Online] Available: https://github.com/IEAWind-Task19/T19IceLossMethod. [Accessed: 15-Nov-2019].
4. Ville Lehtomäki, Timo Karlsson and Simo Rissanen, Wind Turbine Ice Protection System Benchmark Analysis, VTT Technology, 341, VTT Technical Research Centre of Finland.
5. Task 19 Ice Loss Release 2.2 tutorial, IEA Wind Task 19, Nov.07. 2019.
6. Davis, N., Identifying and characterizing the impact of turbine icing on wind farm power generation. Wind Energy. 2016;19:1503-1518.
7. Bilal, M., Wind Energy at Nygårdsfjellet- Norway : Wind field characterization and modelling. 2016, University of Tromsø, Norway: Tromsø.
8. I. Katic, J. Højstrup, and N.O. Jensen, A Simple Model for Cluster Efficiency, in EWEC Proceedings. 1986: Rome, Italy.

9. Anderson, M., Simplified solution to the Eddy-viscosity wake model, in RES document 01327-202,. 2009.
10. Renke, D.J., Validation of wind turbine wake models. Using wind farm data and wind tunnel measurements. Delft University of Technology: Netherland.
11. Larsen, G.C., A Simple Wake Calculation Procedure. 1988, Risø National Laboratory: Denmark.
12. Ishihara, T., A. Yamaguchi, and Y. Fujino. Development of a New Wake Model Based on a Wind Tunnel Experiment. in Glob. Wind Power. http://windeng.t.u-tokyo.ac.jp/ishihara/e/. 2004.
13. Francisco Gonzalez-Longatt, Wake Effect in Wind Farm Performance Steady-State and Dynamic Behaviour. Renewable Energy. 2012; 39(1):329-338.
14. Muhammad Bilal, et al., Wind flow over complex terrain in Nygårdsfjell, Norway, in ASME 2015-Energy solution for a sustainable future. 2015, ASME: San Diego, USA.
15. Warning: Some nacelle temperature sensors have shown a constant bias of +2. . . 3 °C due to radiation heat of nacelle. Investigating this bias is recommended (compare to met mast, weather models etc)
16. Engineering ToolBox, (2003). Altitude above Sea Level and Air Pressure. [online] Available at: https://www.engineeringtoolbox.com/air-altitude-pressure-d_462.html.
17. Min Liu, Jie Sun, Hongqing Yang and Yechang Yuan, The Study on Wind Speed Change with Hight Under Different Terrain Conditions in Hubei Province. Methorolygical Monthly. 2010; 36 (4): 63-67.